

STRUCTURAL BASIS OF ANTIBODY RECOGNITION OF VIRUSES

Thesis by
Shannon Rose Esswein

In Partial Fulfillment of the Requirements for
the degree of
Doctor of Philosophy

The logo for the California Institute of Technology (Caltech), featuring the word "Caltech" in a bold, orange, sans-serif font.

CALIFORNIA INSTITUTE OF TECHNOLOGY
Pasadena, California

2022
(Defended July 14, 2021)

© 2022

Shannon Rose Esswein
ORCID: 0000-0002-5142-0190

ACKNOWLEDGEMENTS

I would like to thank my advisor, Professor Pamela Bjorkman, for her guidance throughout my PhD and for facilitating unique opportunities to collaborate with multiple virologists, immunologists, and structural biologists across the country. I appreciate her incredible attention to detail, inspirational dedication to pursuing science with rigor and integrity, and support for my career endeavors.

I thank Professor Victoria Orphan for generously giving me the opportunity to pursue my interdisciplinary project ideas and expand my skillset into a new area of virus research. I enjoyed working with her creative and supportive research group and appreciated assistance from Alon Philosoof, Aditi Narayanan, Fabai Wu, and Stephanie Connon.

A highlight of my PhD training was the wonderful opportunity to visit Rockefeller University to learn techniques in virology and immunology in the laboratories of Professors Margaret MacDonald, Charlie Rice, and Michel Nussenzweig. I am extremely grateful to Avery Peace, Andrea Jurado, Marianna Agudelo, Tania Kapoor, and Professor Davide Robbiani for the fantastic collaborations.

Furthermore, I thank Professor Richard Kuhn for hosting me at Purdue University for our collaboration investigating flavivirus breathing. Analyzing virus structures with cryo-electron microscopy was one of the most interesting and challenging projects I had the opportunity to work on, and I am grateful for guidance and help provided by Madhu Sevvana, Thomas Klose, Steve Wilson, and Geeta Buda.

I am also thankful to my candidacy and thesis committee members, Professors Doug Rees, Victoria Orphan, Dave Tirrell, and Marianne Bronner, for their support. I also appreciate the guidance of my advisors, Professors David Dawson and David Chan, in the UCLA-Caltech Medical Scientist Training Program.

Thank you to current and former Bjorkman lab members, including Jennifer Keeffe, Christopher Barnes, Anthony West, Andrew Flyak, Harry Gristick, Priyanthi Gnanapragasam, Beth Huey-Tubman, Marta Murphy, Erica Lee, Semi Rho, Lynda Llamas, Han Gao, Pauline Hoffman, Alisa Voll, Kim Dam, Morgan Abernathy, Zhi Yang, Alex Cohen, Magnus Hoffmann, Claudia Jette, Haoqing Wang, Leesa Kakutani, Nick Koranda, Andy DeLaitsch, Beth Stadtmueller, Stormy Ruiz, and Chengcheng Fan for help in ways big and small throughout my PhD. I also appreciate guidance and assistance from Lauren Ann Metskas, Tom Haralabos, Dr. Jost Vielmetter at the Caltech Protein Expression Center, Dr. Jens Kaiser at the Caltech Molecular Observatory, and Dr. Songye Chen, Dr. Andrey Malyutin, Dr. Welison Floriano, and Dr. Alasdair McDowall in the Caltech Cryo-EM Facility.

My former advisors and mentors, Professors David Eisenberg, Sir Thomas Blundell, and Duilio Cascio, instilled my fascination with using structural biology to investigate protein structures. I am immensely grateful for their role in shaping my research endeavors, their confidence in my abilities as a scientist, and for their continuing support. I am also thankful for the advice and support from former laboratory colleagues and friends, including Boris Brumshtein, Lorena Saelices, Pascal Krotee, and Mike Sawaya.

I thank all the other wonderful staff, collaborators, and friends during my time at Caltech, including, but not limited to Sarah Gillespie, Cai Tong Ng, Elise Tookmanian, James McGehee, Eric Liaw, Anya Afasizheva, Leilani Terrell, Felicia Hunt, Liz Ayala, Courtney Oaida, Sophie Miller, Elliot Mackrell, Professor Kathrin Plath, and Thomas Allison.

Furthermore, I appreciate the support of the NIH NIAID F30 Fellowship, Josephine de Karman Fellowship, and Chen Graduate Innovator Award to pursue my research ideas.

I thank Julian West for thoughtful discussions and always supporting me.

Finally, I thank my parents, Denise and Robert, for their dedication to helping others and for inspiring me to pursue a career in science and medicine to make a positive impact on the world.

ABSTRACT

The Zika epidemic in 2015-2016 and COVID-19 pandemic in 2019-2021 are the latest reminders of the enormous impact of viruses on the world. Zika, a flavivirus transmitted by mosquitos, can cause severe neurodevelopmental abnormalities including microcephaly in the newborns of the infected mothers. Vaccine design is complicated by concern that elicited antibodies may also recognize other epidemic-causing flaviviruses that share a similar envelope protein, such as dengue virus, West Nile Virus, and yellow fever virus. This cross-reactivity, if non-neutralizing, may worsen symptoms of a subsequent infection through antibody-dependent enhancement (ADE). To better understand the neutralizing antibody response and risk of ADE, we compared germline and mature antibody binding to Zika and other flaviviruses. We showed that affinity maturation of the light chain variable domain is important for strong binding of *VH3-23/VK1-5* neutralizing antibodies to Zika virus envelope domain III (EDIII) and identified interactions that contribute to weak, cross-reactive binding to West Nile Virus EDIII. These findings informed our design of EDIII-conjugated mosaic nanoparticles as a pan-flavivirus vaccine candidate. Sera from immunization trials with nanoparticles displaying EDIIIs of Zika and dengue serotypes 1-4 showed cross-reactive binding to Zika, dengue 1-4, and West Nile Virus, a promising step towards the development of safe and effective flavivirus vaccines.

Coronaviruses are another group of viruses responsible for widespread morbidity and mortality, including the severe acute respiratory syndrome coronavirus (SARS-CoV) and Middle East Respiratory Syndrome coronavirus (MERS-CoV) epidemics and current SARS-CoV-2 pandemic. Given concerns regarding new SARS-CoV-2 variants and the possibility for additional zoonotic betacoronaviruses to cause future outbreaks, we investigated how the epitopes on the SARS-CoV-2 receptor binding domain (RBD) targeted by *VH3-30*-derived antibodies correlate with their neutralization potency and breadth of betacoronavirus recognition. Analyses showed how variations in antibody light chains and CDRH3 lengths facilitate the diverse RBD epitopes, cross-reactivity, and neutralization profiles of *VH3-30* Abs, illustrating their importance for vaccine design and therapeutic antibody development.

PUBLISHED CONTENT AND CONTRIBUTIONS

Esswein SR, Gristick HB, Jurado A, Peace A, Keeffe JR, Lee YE, Voll AV, Saeed M, Nussenzweig MC, Rice CM, Robbiani DF, MacDonald MR, Bjorkman PJ. Structural basis for Zika envelope domain III recognition by a germline version of a recurrent neutralizing antibody. *Proc Natl Acad Sci U S A*. 2020 Apr 22. pii: 201919269. doi: 10.1073/pnas.1919269117. PubMed PMID: 32321830.

S.R.E. designed the project, performed surface plasmon resonance experiments, collected X-ray data, solved and analyzed the crystal structures, analyzed the data, and prepared the manuscript.

Van Rompay KKA, Coffey LL, Kapoor T, Gazumyan A, Keesler RI, Jurado A, Peace A, Agudelo M, Watanabe J, Usachenko J, Singapuri A, Immareddy R, Ardeshir A, Stuart JB, Bournazos S, Ravetch JV, Balderes PJ, Lorenz IC, Esswein SR, Keeffe JR, Bjorkman PJ, Wang Q, Rice CM, MacDonald MR, Nussenzweig MC, Robbiani DF. A combination of two human monoclonal antibodies limits fetal damage by Zika virus in macaques. *Proc Natl Acad Sci U S A*. 2020 Apr 7;117(14):7981-7989. doi: 10.1073/pnas.2000414117. Epub 2020 Mar 24. PubMed PMID: 32209664; PubMed Central PMCID: PMC7149495.

S.R.E. performed reporter viral particle neutralization assays.

Barnes CO, Jette CA, Abernathy ME, Dam K-M A, Esswein SR, Gristick HB, Malyutin AG, Sharaf NG, Huey-Tubman KE, Lee YE, Robbiani DF, Nussenzweig MC, West AP, and Bjorkman PJ. SARS-CoV-2 neutralizing antibody structures inform therapeutic strategies. *Nature*. 2020 Dec;588(7839):682-687. doi: 10.1038/s41586-020-2852-1. Epub 2020 Oct 12. PMID: 33045718; PMCID: PMC8092461.

S.R.E. processed cryo-electron microscopy data for the C144 Fab–SARS-CoV-2 spike complex.

Abernathy ME*, Dam KA*, Esswein SR*, Jette CA*, Bjorkman PJ. How antibodies recognize pathogenic viruses: Structural correlates of antibody neutralization of HIV-1, SARS-CoV-2, and Zika. *Viruses*. 2021 Oct; 13(10), 2106. doi: 10.3390/v13102106. *co-first authors

S.R.E. wrote, edited, and prepared figures for the manuscript.

TABLE OF CONTENTS

ACKNOWLEDGEMENTS	III
ABSTRACT	V
PUBLISHED CONTENT AND CONTRIBUTIONS	VI
TABLE OF CONTENTS	VIII
LIST OF FIGURES	X
LIST OF TABLES	XII
CHAPTER 1	1
INTRODUCTION	1
<i>Flaviviruses</i>	1
<i>Flavivirus structure, fusion mechanism and life cycle</i>	2
<i>Flavivirus breathing</i>	5
<i>Zika virus</i>	5
<i>Antibody-dependent enhancement</i>	6
<i>Coronavirus epidemics</i>	8
<i>The SARS-CoV-2 spike protein</i>	8
<i>Summary</i>	9
CHAPTER 2	12
STRUCTURAL BASIS FOR ZIKA ENVELOPE DOMAIN III RECOGNITION BY A GERMLINE VERSION OF A RECURRENT NEUTRALIZING ANTIBODY	12
<i>Abstract</i>	12
<i>Significance Statement</i>	13
<i>Introduction</i>	14
<i>Results</i>	17
<i>Discussion</i>	30
<i>Materials and Methods</i>	35
<i>SI Appendix</i>	43
CHAPTER 3	70
TARGETING PAN-FLAVIVIRUS NEUTRALIZATION WITH MOSAIC NANOPARTICLE IMMUNIZATION	70
<i>Abstract</i>	70
<i>Significance Statement</i>	71
<i>Introduction</i>	72
<i>Results</i>	75
<i>Discussion</i>	81
<i>Materials and Methods</i>	83
CHAPTER 4	87

CAPTURING THE BREATHING CONFORMATION OF FAB-BOUND ZIKA VIRUS WITH CRYO-ELECTRON MICROSCOPY	87
<i>Summary</i>	87
CHAPTER 5	92
VH3-30 ANTIBODIES THAT TARGET THE SARS-COV-2 RBD SHOW DIVERSE NEUTRALIZATION AND CROSS-REACTIVITY PROFILES	92
<i>Abstract</i>	92
<i>Significance Statement</i>	93
<i>Introduction</i>	94
<i>Results</i>	97
<i>Discussion</i>	109
<i>Materials and Methods</i>	115
<i>SI Appendix</i>	121
CHAPTER 6	131
QUANTIFICATION OF VIRAL PRODUCTION IN MARINE SEDIMENT NEAR A METHANE SEEP USING BIO-ORTHOGONAL NON-CANONICAL AMINO ACID TAGGING	131
<i>Abstract</i>	131
<i>Introduction</i>	132
<i>Results</i>	135
<i>Future directions</i>	147
BIBLIOGRAPHY	149

LIST OF FIGURES

FIGURE 1.1. MATURE AND IMMATURE ZIKV STRUCTURES.	2
FIGURE 1.2. SCHEMATIC OF ZIKV LIFE CYCLE AND FUSION MECHANISM.....	3
FIGURE 1.3. ZIKV E PROTEIN.....	4
FIGURE 1.4. SEQUENCE DIVERGENCE OF THE FLAVIVIRUS E PROTEINS.	7
FIGURE 1.5. SCHEMATIC OF ANTIBODY-DEPENDENT ENHANCEMENT.	7
FIGURE 1.6. SCHEMATIC OF ‘OPEN’ AND ‘CLOSED’ SARS-COV-2 S TRIMER CONFORMATIONS.....	9
FIGURE 2.1. ALIGNMENTS OF V_H AND V_L SEQUENCES OF MATURE AND IGL VERSIONS OF ABS ISOLATED FROM PATIENTS EXPOSED TO ZIKV.....	19
FIGURE 2.2. SPR BINDING ASSAYS WITH ZIKV EDIII.	20
FIGURE 2.3. COMPARISON OF QUALITATIVE ZIKV AND DENV EDIII BINDING TO IGL ABS.	21
FIGURE 2.4. RECOGNITION OF ZIKV EDIII BY Z004 IGL AND MATURE FABS.	24
FIGURE 2.5. COMPARISON OF FAB–EDIII BINDING INTERFACES.....	25
FIGURE 2.6. CROSS-REACTIVE RECOGNITION OF WNV EDIII BY Z032 _{MATURE} FAB.	28
FIGURE S2.1. ALIGNMENTS OF V_H AND V_L SEQUENCES OF ALL 20 MATURE <i>VH3-23/VK1-5</i> CLASS ABS ISOLATED FROM DONOR MEX 18.	43
FIGURE S2.2. ALIGNMENTS OF V_H AND V_L SEQUENCES OF ALL 15 MATURE <i>VH3-23/VK1-5</i> CLASS ABS ISOLATED FROM DONOR BRA 112.	44
FIGURE S2.3. ALIGNMENTS OF V_H AND V_L SEQUENCES OF ALL 27 MATURE <i>VH3-23/VK1-5</i> CLASS ABS ISOLATED FROM DONOR MEX 105.	45
FIGURE S2.4. SPR BINDING ASSAYS WITH DENV1 EDIII.	46
FIGURE S2.5. SPR BINDING ASSAYS WITH ZIKV EDIII.	47
FIGURE S2.6. SPR BINDING ASSAYS WITH DENV1 EDIII.	48
FIGURE S2.7. RESIDUAL PLOTS FOR BINDING MODEL FITTING TO SPR SENSORGRAMS OF ZIKV EDIII AND DENV1 EDIII BINDING TO MATURE ABS FROM TWO INDEPENDENT EXPERIMENTS.....	49
FIGURE S2.8. SPR BINDING ASSAYS WITH DENV2 EDIII.	50
FIGURE S2.9. SPR BINDING ASSAYS WITH DENV3 EDIII.	52
FIGURE S2.10. SPR BINDING ASSAYS WITH DENV4 EDIII.	53
FIGURE S2.11. SPR BINDING ASSAYS WITH WNV EDIII.	54
FIGURE S2.12. SPR BINDING ASSAYS WITH YFV EDIII.	55

FIGURE S2.13. RVP-BASED NEUTRALIZATION ASSAYS.....	56
FIGURE S2.14. RVP-BASED ADE ASSAY.....	58
FIGURE S2.15. RECOGNITION OF EDIIIS BY MATURE AND IGL FABS.....	59
FIGURE S2.16. CLOSE-UP VIEW OF FAB–EDIII INTERACTIONS.....	60
FIGURE S2.17. COMPARISON OF ZIKV EDIII BINDING TO Z004 _{MATURE} ABS WITH SITE-DIRECTED MUTATIONS IN THE V _L	62
FIGURE S2.18. SPR BINDING SENSORGRAMS AND RESIDUAL PLOTS.....	63
FIGURE S2.19. COMPARISON OF BOUND AND UNBOUND STRUCTURES OF Z032 _{MATURE}	64
FIGURE 3.1. PREPARATION OF EDIII NANOPARTICLES FOR IMMUNIZATION TRIALS.....	76
FIGURE 3.2. EDIII NANOPARTICLE IMMUNIZATIONS IN MICE ELICIT STRONG AB BINDING TO FLAVIVIRUS EDIIIS.....	80
FIGURE 4.1. <i>VH3-23/VK1-5</i> FAB BINDING TO EDIII CLASHES IN THE CRYO-EM STRUCTURE OF MATURE ZIKV.....	88
FIGURE 4.2. ELECTRON MICROGRAPHS OF Z004 FAB–MATURE ZIKV.....	89
FIGURE 5.1. NEUTRALIZATION POTENCIES AND BINDING AFFINITIES OF ANTI-SARS-COV-2 ABS.....	99
FIGURE 5.2. CRYSTAL STRUCTURES OF C133 AND C008 FABS BOUND TO SARS-COV-2 RBD.....	102
FIGURE 5.3. CRYO-EM DENSITY MAPS OF SARS-COV-2 S PROTOMERS BOUND BY C008, C027, C030, C113, C133, C149, AND CR3022 FABS.....	103
FIGURE 5.4. COMPARISON OF FAB-RBD BINDING INTERFACES.....	106
FIGURE S5.1. AB BINDING TO SARBEICOVIRUS RBDS.....	121
FIGURE S5.2. ALIGNMENT OF RBDS USED FOR CROSS-REACTIVITY STUDIES.....	122
FIGURE S5.3. ALIGNMENT FOR V _H PROTEIN SEQUENCES FOR A SET OF <i>VH3-30</i> AND/OR CLASS 4 ABS THAT BIND THE SARS-COV-2 RBD.....	123
FIGURE S5.4. ALIGNMENT FOR V _L PROTEIN SEQUENCES FOR A SET OF <i>VH3-30</i> AND/OR CLASS 4 ABS THAT BIND THE SARS-COV-2 RBD.....	124
FIGURE S5.5. SARS-COV-2 RBD PROTEIN INTERFACE RESIDUES BOUND BY ABS.....	125
FIGURE 6.1. BONCAT CLICK CHEMISTRY USING THE NON-CANONICAL AMINO ACID HPG.....	134
FIGURE 6.2. NUCLEIC ACID-STAINED VLPS IN AN ENVIRONMENTAL WATER SAMPLE DILUTION SERIES.....	136
FIGURE 6.3. VISUALIZATION OF NEWLY-PRODUCED VLPS IN BONCAT-LABELED ENVIRONMENTAL WATER SAMPLES.....	137
FIGURE 6.4. INCUBATION SETUP OF SEDIMENT SLURRY FROM MONTEREY SUBMARINE CANYON.....	139
FIGURE 6.5. VISUALIZATION AND QUANTIFICATION OF BONCAT-LABELED VLPS IN MARINE SEDIMENT.....	145
FIGURE 6.6. BONCAT-LABELED VLP QUANTIFICATION IN MARINE SEDIMENT NEAR A METHANE SEEP.....	146

LIST OF TABLES

TABLE 2.1. K_D S (NM) OF MATURE AND IGL AB BINDING TO EDIIIS DETERMINED BY SPR.	22
TABLE S2.1. X-RAY DIFFRACTION DATA AND REFINEMENT STATISTICS FOR FAB–EDIII CRYSTAL STRUCTURES.	65
TABLE S2.2. INTERACTING RESIDUES IN MATURE AND IGL FAB–EDIII COMPLEXES	67
TABLE S2.3. K_D S OF Z004 AB (MATURE, IGL, CHIMERAS, AND MUTANTS) BINDING TO ZIKV EDIII DETERMINED BY SPR.	68
TABLE S2.4. PAIRWISE SUPERIMPOSITIONS AND RMSD CALCULATIONS OF BOUND AND UNBOUND V_HV_L CHAINS IN THE Z032 _{MATURE} –WNV EDIII CRYSTAL STRUCTURE.	69
TABLE 4.1. SUMMARY OF FAB–ZIKV DATASETS COLLECTED WITH A TITAN KRIOS MICROSCOPE.....	91
TABLE 5.1. <i>VH3-30</i> AND CLASS 4 ANTI-SARS-COV-2 ABS.	100
TABLE S5.1. GERMLINE GENE ASSIGNMENTS FOR <i>VH3-30</i> AND CLASS 4 ABS THAT BIND THE SARS-COV-2 RBD.....	126
TABLE S5.2. X-RAY DIFFRACTION DATA AND REFINEMENT STATISTICS FOR FAB–RBD CRYSTAL STRUCTURES	127
TABLE S5.3. PAIRWISE SUPERIMPOSITIONS AND RMSD CALCULATIONS OF C008 V_HV_L AND RBD CHAINS IN THE C008 FAB–RBD CRYSTAL STRUCTURE	128
TABLE S5.4. PAIRWISE SUPERIMPOSITIONS AND RMSD CALCULATIONS OF C133 $VHVL$ AND RBD CHAINS IN THE C133 FAB–C119 FAB–RBD CRYSTAL STRUCTURE	129
TABLE S5.5. BSA AND INTERACTING RESIDUES FOR FAB–SARS-COV-2 STRUCTURES.....	130
TABLE 6.1. VOLUMES OF SEDIMENT SLURRY SAMPLES WITH VLPS RECOVERED FROM SEDIMENT USING CENTRIFUGATION	141
TABLE 6.2. VLP COUNTS DETERMINED BY OVERLAPPING FITC AND CY5 SIGNAL ON FIVE IMAGES PER ANODISC.....	144

CHAPTER 1

Introduction

With a count estimated at 10^{31} , viruses are the most abundant biological entities on the planet, exceeding cells by at least an order of magnitude^{1,2}. Although most viruses infect bacteria, viruses can infect all domains of life; in humans, there are over 300 trillion viruses^{1,3,4}. Although most of these are bacteriophages, humans are exposed to an average of 10 different species of human viruses (out of a panel of 206) over life⁵. Viruses are best known for their association with disease; however, some viruses show beneficial functions, such as supporting intestinal homeostasis⁶, providing immunity to bacterial infections⁶⁻⁸, conferring drought or cold tolerance in plants⁹, or informing virus-based cancer therapies¹⁰⁻¹². The intricate host-virus relationship is influenced by many factors, including viral cooperation during infection through a communication system using peptide signals¹³. With such viral diversity and complexity, greater insight into the impact of viruses on health and the environment may be achieved through interdisciplinary, collaborative approaches and methodology. Therefore, the work presented here utilizes a variety of technique in biochemistry, virology, immunology, and structural biology to increase our understanding of the immune response to flavivirus and coronavirus infection and to briefly explore techniques for quantifying virus production in marine sediment.

Flaviviruses

Flavivirus, a genus in the family *Flaviviridae*, contains over 70 different viruses, several of which are responsible for widespread morbidity and mortality in humans^{14,15}. These single-stranded, RNA-positive, enveloped viruses are often transmitted to humans by arthropods, including mosquito-borne viruses such as yellow fever virus (YFV)¹⁶, West Nile Virus

(WNV)¹⁷, dengue virus (DENV)¹⁸, and Zika virus (ZIKV)¹⁹ and tick-borne viruses such as tick-borne encephalitis virus and Powassan virus^{15,20}. The global diseases caused by flaviviruses range from mild febrile symptoms to severe hemorrhage, encephalitis, and neurological disorders^{15,20}.

Flavivirus structure, fusion mechanism and life cycle

Flaviviruses are icosahedral and contain seven non-structural proteins and three structural proteins: C (capsid), E (envelope), and M (membrane). The C protein is surrounded by a lipid membrane derived from the endoplasmic reticulum with integrated E and M proteins (in mature viruses) or E and precursor of M (prM) proteins (in immature viruses) (Figure 1.1)²¹⁻²³. Mature viruses enter cells by various receptors on the cell surface, such as $\alpha_v\beta_3$ integrins, C-type lectin receptors (CLR), and phosphatidylserine receptors TAM, (Tyro3, Axl, and Mer) and TIM (T cell immunoglobulin mucin domain)²⁴. After flaviviruses infect cells by receptor-mediated endocytosis, the acidic pH in endosomes causes a conformational change in the E protein and induces membrane fusion, thereby uncoating viral RNA (Figure 1.2)²⁵⁻²⁷.

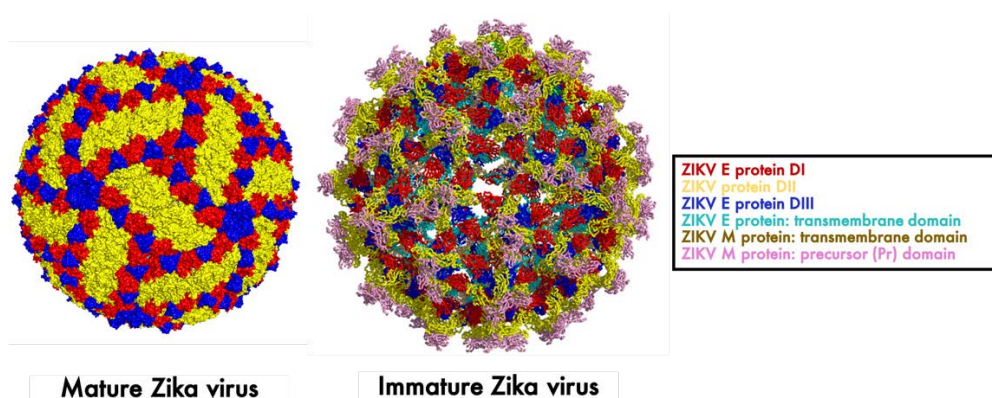


Figure 1.1. Mature and immature ZIKV structures.

Created with Pymol using PDB 6CO8²⁸ and 5U4W²¹.

Viral assembly proceeds in the endoplasmic reticulum, forming immature viruses (~60 nm) with 60 trimers of prM-E heterodimers, giving the viruses a spiky appearance²⁵⁻²⁷. During subsequent exocytosis, the prM is cleaved to M by the cellular protease furin in the slightly acidic trans-Golgi network. After the viruses are released into the neutral pH of the extracellular environment, the cleaved pr falls off, forming smooth, fully mature viruses (~50 nm) with 90 E antiparallel, homodimers arranged in 30 rafts, each with 3 sets of dimers. Subviral particles (byproducts of viral production that lack a capsid but contain prM and E) are also released from infected cells^{15,23,25-27}.

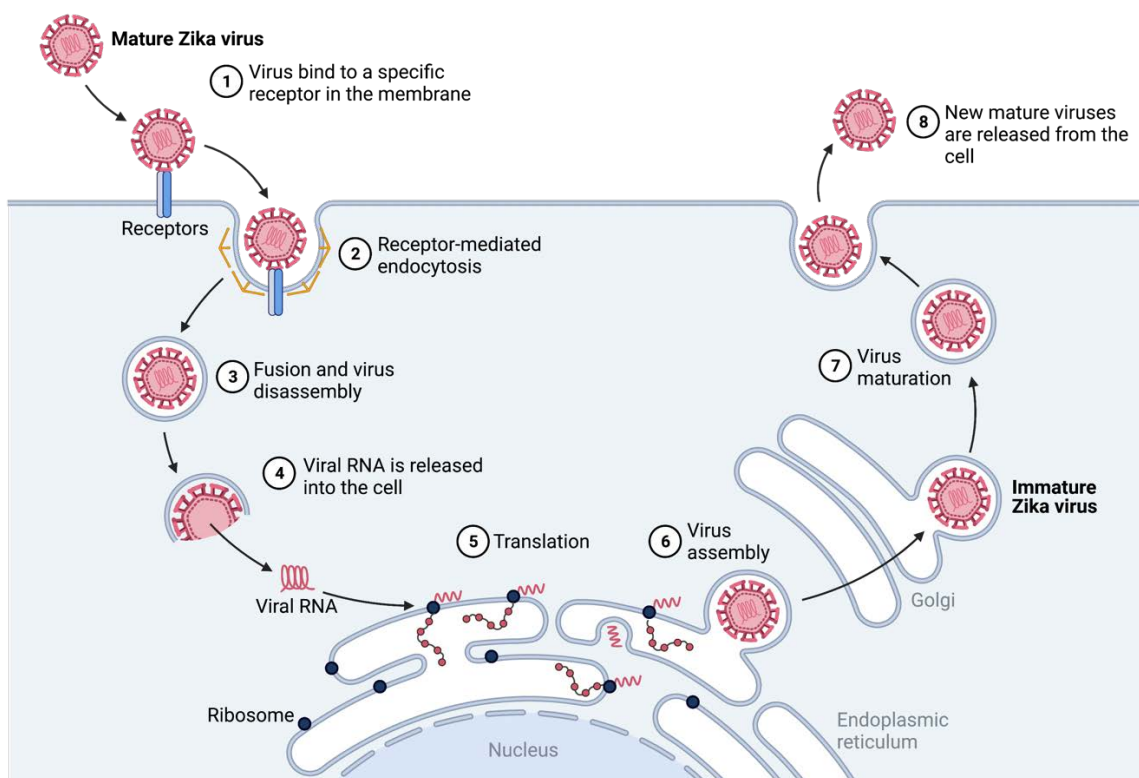


Figure 1.2. Schematic of ZIKV life cycle and fusion mechanism.

Created with BioRender.com.

E proteins contain three domains (EDI, EDII, and EDIII), two transmembrane helices that anchor E to the viral membrane, and a stem region that is partially embedded in the viral membrane (Figure 1.3)^{22,23}. DII contains a conserved fusion peptide that becomes exposed after viral entry into cells and initiates endosomal fusion, and DIII is thought to be critical for receptor binding. Flexibility of E proteins at the hinges between domains is important for the conformational changes that occur during viral assembly and maturation and is also thought to facilitate dynamic changes (known as “breathing”) in flavivirus structures^{23,29}.

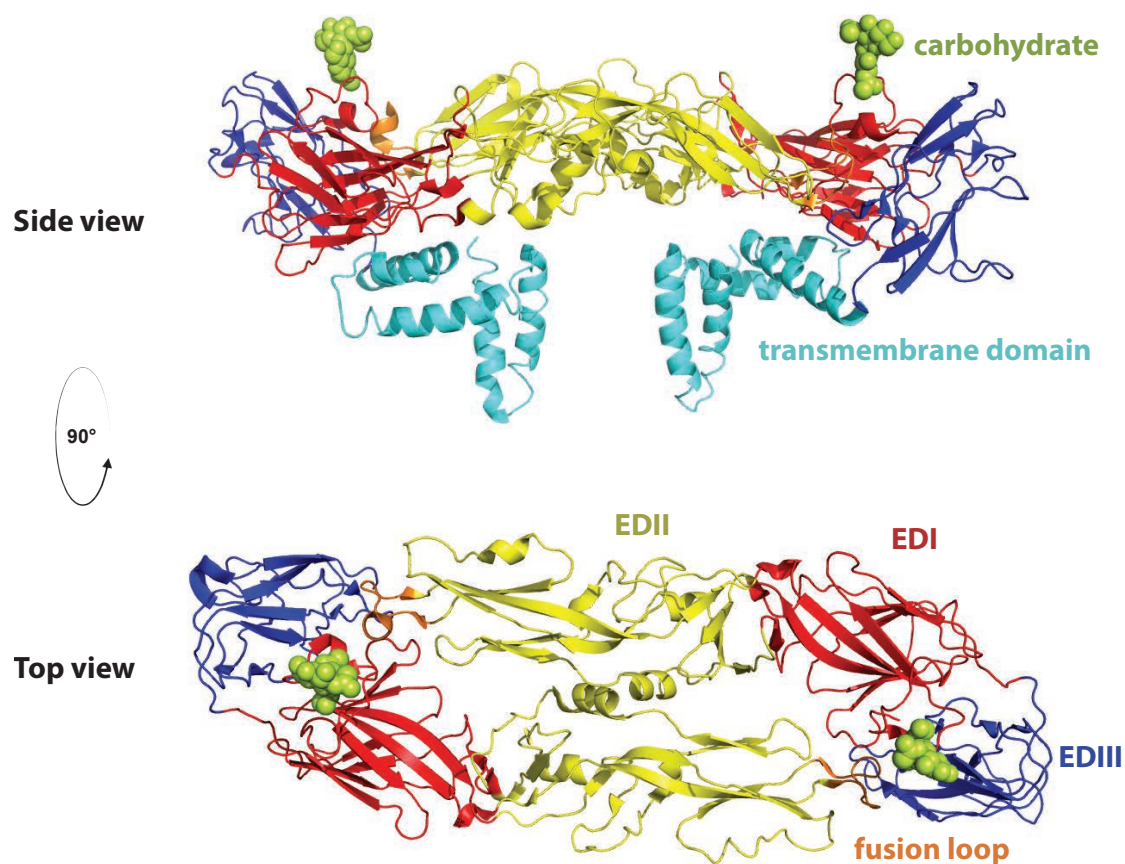


Figure 1.3. ZIKV E protein.

Created using PDB 6CO8²⁸ with Pymol.

Flavivirus breathing

While cryo-EM flavivirus structures^{21,22,28} show one static envelope structure, evidence suggests envelope proteins of both mature and immature virions are dynamic and sample different conformations³⁰⁻³². As demonstrated by antibody (Ab) neutralization at viral epitopes inaccessible in static models of virions^{29,30,33,34}, the phenomenon of flavivirus “breathing” to expose cryptic Ab epitopes may result from conformational changes of the E protein during the viral lifecycle, such as during fusion. Further evidence is provided by the finding that the potency of Abs against DENV is affected by mutations distant from the epitope, suggesting these mutations can modulate virus “breathing” and epitope accessibility²⁹. A cryo-EM “breathing” structure of DENV2 was obtained by heating the virus to 37°C³², while ZIKV remains stable in a mature conformation upon heating³⁵. Although potentially-neutralizing Abs that bind cryptic epitopes on ZIKV E proteins have been identified^{36,37}, there are no known cryo-EM structures of Fab–flavivirus complexes capturing major conformational changes. This structural information is important for understanding the virion conformations targeted by neutralizing Abs and how these Abs prevent membrane fusion and infection.

Zika virus

The flavivirus ZIKV was first discovered in 1947, the potential for an epidemic was not realized until large outbreaks occurred in 2007 and 2013-2015³⁸⁻⁴⁵. The virus can be transmitted by mosquitoes or sexually and persists in infected individuals for several months⁴⁶⁻⁴⁹. Infection is usually asymptomatic or mild, causing symptoms such as fever, rashes, conjunctivitis, arthralgia, and headaches in approximately 20% of cases. In rare cases, severe neurologic problems such as meningoencephalitis or Guillain-Barré Syndrome can occur^{41,50-52}. However, there is major concern ZIKV infection during pregnancy, which can cause severe ocular and neurodevelopmental abnormalities, including microcephaly, due to

the ability of the virus to cross the placenta^{47,53–56}. Given the demonstrated potential for large-scale spread, symptom severity, and lack of treatment or prophylaxis, a safe and effective ZIKV vaccine is urgently needed.

Since the E protein is involved in cell receptor binding and membrane fusion, it is a key target for neutralizing Abs to prevent infection^{57–59}. Epitopes for neutralizing Abs have been found on all three domains (EDI, EDII, and EDIII), between multiple domains, and across the E protein dimer; however, Abs against EDIII are often the most potently neutralizing and an important component of the Ab response that mediates protection^{15,36,60–72}. Some neutralizing Abs have cryptic epitopes that are partially buried in cryo-electron microscopy (cryo-EM) structures of ZIKV, indicating the virus structure is dynamic^{36,37}.

Antibody-dependent enhancement

Since the ZIKV E protein is similar to that of other flaviviruses, including dengue virus serotypes 1-4 (DENV1-4), West Nile Virus (WNV), and yellow fever virus (YFV)^{23,73,74} (Figure 1.4), there is concern that Abs against ZIKV may cross-react with other flaviviruses. This cross-reactivity complicates vaccine design since Abs at concentrations that are weakly neutralizing or are non-neutralizing against ZIKV and other flaviviruses could result in enhanced infection through Ab-dependent enhancement (ADE)^{23,75–79}. It is thought that ADE results from the binding of cross-reactive, but non-neutralizing Abs that promote viral entry into Fc gamma receptor (FcγR)-expressing cells, thereby enhancing infection and causing increased symptom severity^{23,76,77,80–83} (Figure 1.5). ADE is thought to underly the finding that the live attenuated tetravalent DENV vaccine, Dengvaxia, can increase the risk of severe symptoms if vaccinated individuals later becomes infected. However, this is only observed in individuals who were never previously exposed to DENV before vaccination^{84–87}. Additionally, prior DENV or ZIKV infection that results in low or intermediate Ab titers

increases the risk of worsened disease severity from a subsequent DENV infection with a different serotype⁸⁸⁻⁹⁴.

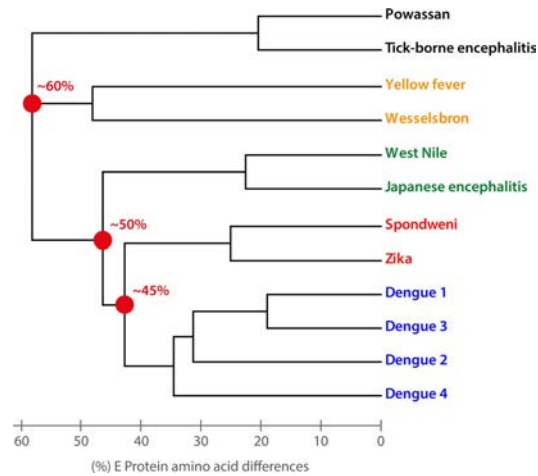


Figure 1.4. Sequence divergence of the flavivirus E proteins.

Adapted from Heinz., F.X. and Stiasny, K, *Microbio Mol Biol Rev* (2017)²³.

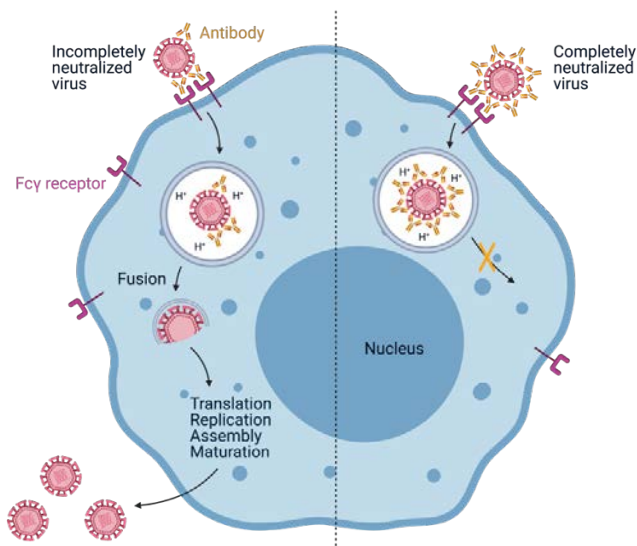


Figure 1.5. Schematic of antibody-dependent enhancement.

Created with BioRender.com.

Coronavirus epidemics

The 2003 severe acute respiratory syndrome coronavirus (SARS-CoV) epidemic throughout five continents^{95,96}, the 2012 Middle East Respiratory Syndrome coronavirus (MERS-CoV) epidemic in the Arabian Peninsula⁹⁷, and the 2019-2021 SARS-CoV-2 pandemic^{98,99} demonstrate the importance of investigating the immune response to coronavirus infection^{95-97,99,100}. These three highly pathogenic coronaviruses are from the *betacoronavirus* genus, and epidemics were caused by zoonotic transmission from animal reservoirs: MERS-CoV originated in dromedary camel^{101,102} and SARS-CoV and SARS-CoV-2 most likely originated in bats^{100,103-106}. Due to the possibility for newly-emerging zoonotic betacoronaviruses to cause future outbreaks^{104,105,107-110}, it is necessary to develop therapeutics and vaccines that provide broad protection against different SARS-like betacoronavirus (sarbecovirus) strains.

The SARS-CoV-2 spike protein

The surface of SARS-CoV-2 displays spike (S) trimer proteins that facilitate entry into host cells and are targeted by Abs during the immune response to infection. Each protomer in the S trimer comprises two subunits: S₁ and S₂. S₁ is responsible for binding to the host cell and includes the N-terminal domain (NTD) and receptor binding domain (RBD), while S₂ is responsible for fusion of the viral and cellular membranes¹¹¹⁻¹¹³. RBDs are the portions of the SARS-CoV-2 S trimer that interact with the cellular host receptor, angiotensin-converting enzyme 2 (ACE2)¹¹⁴⁻¹¹⁷; RBDs can adopt ‘up’ and ‘down’ conformations on the S trimer, but only bind ACE2 when in an ‘up’ conformation^{112-114,118-123} (Figure 1.6). Abs that target the SARS-CoV-2 RBD are an important component of the protective immune response against infection^{112-115,124-134}. The potent neutralization demonstrated by many of these Abs has been attributed to their ability to prevent viral entry by blocking the RBD from binding ACE2^{114-117,135-139}.

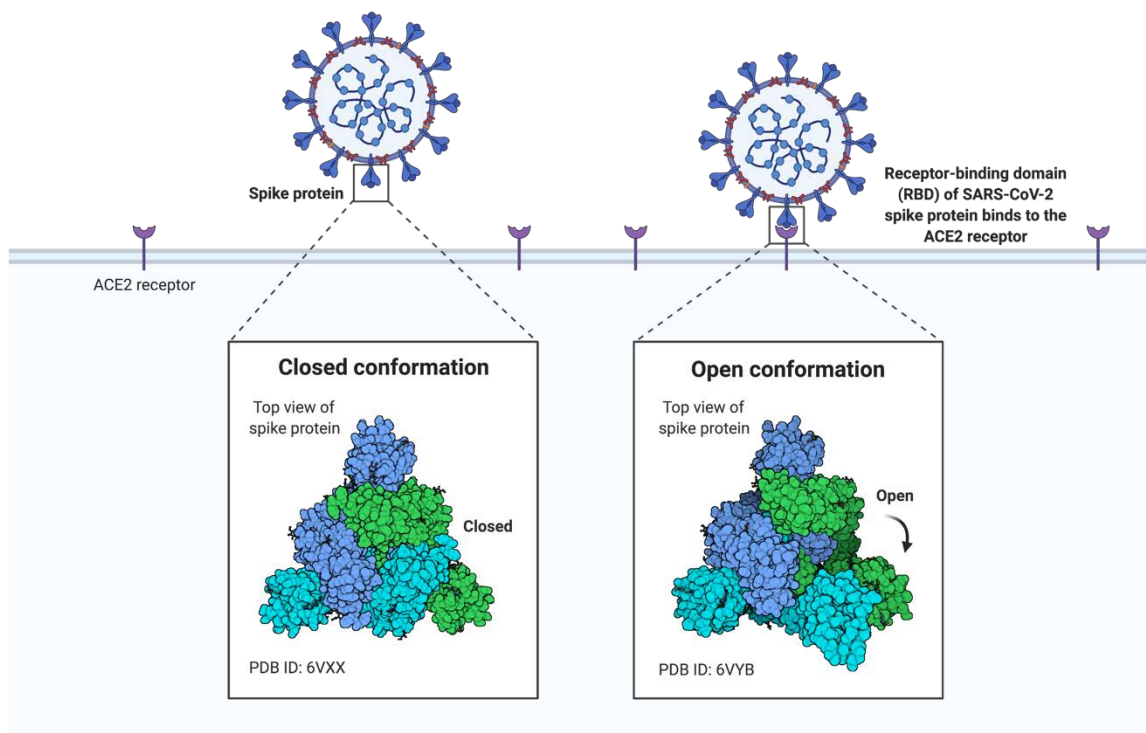


Figure 1.6. Schematic of ‘open’ and ‘closed’ SARS-CoV-2 S trimer conformations.

The SARS-CoV-2 RBD binds the ACE2 cellular receptor when in an ‘up’ conformation. Created with PDB 6VXX¹¹³ and 6VYB¹¹³ using BioRender.com.

Summary

Given the global impact and disease burden of viruses, it is important to thoroughly understand the immune response to viral infection. The work presented here utilized interdisciplinary approaches in virology, biochemistry, and structural biology to investigate the immune response to flavivirus and coronavirus infection, with an emphasis on the viruses underlying recent epidemics, ZIKV and SARS-CoV-2. Investigation of how Ab properties correlate with epitope recognition, neutralization potency, and cross-reactivity is essential for the development of safe and effective vaccines and therapeutics.

Chapter 2 presents a comparison of binding by germline and mature versions of potentially-neutralizing *VH3-23/VK1-5* Abs to ZIKV and other flaviviruses, providing insight into the affinity maturation process that gives rise to potentially-neutralizing Abs and evaluating the risk of ADE. The ability of germline versions of *VH3-23/VK1-5* Abs to bind ZIKV indicates the potential for a vaccine to successfully elicit this class of Abs. Additionally, X-ray crystal structures of Fab–EDIII complexes and site-directed mutagenesis experiments revealed that somatic hypermutation in the light chain variable domain of this class of Abs is particularly important for high affinity binding.

Chapter 3 presents a pan-flavivirus, nanoparticle-based vaccine candidate designed to elicit a cross-neutralizing response to reduce the risk of ADE. Immunization trials in mice showed that that these nanoparticles elicit a cross-reactive binding response against ZIKV, DENV1-4, and WNV, a promising step towards the development of safe and effective vaccines.

Chapter 4 presents a brief discussion of progress using cryo-EM to investigate the phenomenon of flavivirus “breathing” that exposes cryptic Ab epitopes. Determining the conformational changes of virion envelope proteins is key to understanding how neutralizing Abs prevent membrane fusion and infection.

Chapter 5 presents a structural characterization of SARS-CoV-2 Abs derived from the *VH3-30* gene segment, which is frequently enriched in convalescent COVID-19 donors. We showed that these Abs bound varied epitopes on the SARS-CoV-2 spike RBD and can induce dissociation of the spike trimer. The diverse epitopes, neutralization potencies, and cross-reactivity profiles of these Abs are an important consideration for the design of vaccines intended to elicit a protective immune response against different betacoronavirus strains.

Chapter 6 presents an exploratory project evaluating techniques to assess viral production in environmental samples. Here I quantified viruses in marine sediment incubations using biorthogonal non-canonical amino acid tagging (BONCAT).

CHAPTER 2

Structural basis for Zika envelope domain III recognition by a germline version of a recurrent neutralizing antibody

Abstract

Recent epidemics demonstrate the global threat of Zika virus (ZIKV), a flavivirus transmitted by mosquitoes. Although infection is usually asymptomatic or mild, newborns of infected mothers can display severe symptoms including neurodevelopmental abnormalities and microcephaly. Given the large-scale spread, symptom severity, and lack of treatment or prophylaxis, a safe and effective ZIKV vaccine is urgently needed. However, vaccine design is complicated by concern that elicited antibodies (Abs) may cross-react with other flaviviruses that share a similar envelope protein, such as dengue virus, West Nile virus, and yellow fever virus. This cross-reactivity may worsen symptoms of a subsequent infection through Ab-dependent enhancement (ADE). To better understand the neutralizing Ab response and risk of ADE, further information on germline Ab binding to ZIKV and the maturation process that gives rise to potentially neutralizing Abs is needed. Here we use binding and structural studies to compare mature and inferred-germline Ab binding to envelope protein domain III (EDIII) of ZIKV and other flaviviruses. We show that affinity maturation of the light chain (LC) variable domain (V_L) is important for strong binding of the recurrent *VH3-23/VK1-5* neutralizing Abs to ZIKV EDIII and identify interacting residues that contribute to weak, cross-reactive binding to West Nile virus. These findings provide insight into the affinity maturation process and potential cross-reactivity of *VH3-23/VK1-5* neutralizing Abs, informing precautions for protein-based vaccines designed to elicit germline versions of neutralizing Abs.

Significance Statement

There is concern for design of a safe vaccine for Zika virus because Abs elicited against Zika may also bind flaviviruses that share a similar envelope protein. If Abs elicited by a Zika vaccine bind, but do not effectively neutralize other flaviviruses, they may enhance virus entry into cells through the process of Ab-dependent enhancement of infection, potentially leading to more severe disease. By directly comparing how mature Zika-neutralizing Abs and their germline precursors bind different flaviviruses, we provide insight into the Ab maturation process and the molecular interactions important for strong, neutralizing binding to Zika versus weak, cross-reactive binding to other flaviviruses.

Adapted from:

Esswein SR, Gristick HB, Jurado A, Peace A, Keeffe JR, Lee YE, Voll AV, Saeed M, Nussenzweig MC, Rice CM, Robbiani DF, MacDonald MR, Bjorkman PJ. Structural basis for Zika envelope domain III recognition by a germline version of a recurrent neutralizing antibody. *Proc Natl Acad Sci U S A*. 2020 Apr 22. pii: 201919269. doi: 10.1073/pnas.1919269117. PubMed PMID: 32321830. S

Introduction

Zika virus (ZIKV) is an arthropod-borne flavivirus first discovered in 1947, with the first reported human case in 1964 and large outbreaks in 2007 and 2013-2015³⁸⁻⁴⁵. Although commonly transmitted by mosquitoes, ZIKV can also be transmitted sexually and can persist in infected individuals for up to several months⁴⁶⁻⁴⁹. Infection is either asymptomatic or causes mild symptoms, including fever, conjunctivitis, headache, rash, and arthralgia, in approximately 20% of cases, and severe neurologic problems such as meningoencephalitis or Guillain-Barré Syndrome in rare cases^{41,50-52}. There are major concerns about ZIKV infection during pregnancy, which can cause fetal neurodevelopmental abnormalities such as microcephaly^{47,53-56}. Given the large-scale spread, symptoms severity, and lack of treatment or prophylaxis, a safe and effective ZIKV vaccine is urgently needed.

The ZIKV envelope (E) protein, containing domains EDI, EDII and EDIII, is similar to the E protein of other flaviviruses, including dengue virus serotypes 1-4 (DENV1-4), West Nile virus (WNV), and yellow fever virus (YFV)^{23,73,74}. EDIII is an important target for neutralizing Abs⁵⁷⁻⁵⁹. Indeed, many Abs against the ZIKV EDIII domain are strongly neutralizing and are an important component of the response to infection^{36,60-71}. A set of recurrent Abs (commonly occurring in multiple individuals, also referred to as “public Abs”) identified from a large cohort of patients in Brazil and Mexico potentially neutralize both ZIKV and DENV1 by binding the lateral ridge of the EDIII domain³⁶. These Abs share the germline variable heavy (VH) gene segment *VH3-23* and the germline variable kappa (VK) gene segment *VK1-5*. One of these *VH3-23/VK1-5* Abs, Z004, exhibited protection against ZIKV infection in mice, and when used in combination with another Ab, Z021, reduced viremia and prevented the emergence of ZIKV escape mutations in infected macaques^{36,62}.

Strongly neutralizing anti-ZIKV Abs that are derived from known germline Ab precursors represent a potential target for a germline-targeting approach to vaccine design. Such

approaches rely on the Ab response to an antigen being initiated through antigen binding to a B cell receptor in its germline configuration, triggering B cell activation and subsequent affinity maturation through the process of somatic hypermutation¹⁴⁰. However, a potential concern for vaccine design efforts targeting the epitope for *VH3-23/VK1-5* Abs or other flavivirus epitopes is that generation of weakly neutralizing or non-neutralizing Abs against ZIKV that cross-react with different flaviviruses could result in enhanced infection through the process of Ab-dependent enhancement (ADE)^{23,75-79}. It is thought that ADE can result when the binding of cross-reactive, but non- or only poorly-neutralizing, Abs promote viral entry into Fc gamma receptor (FcγR)-expressing cells, thereby providing an alternative route of infection and causing increased virus production and symptom severity^{23,76,77,80-83}. Therefore, understanding the ability of germline Abs to bind flavivirus envelope proteins and mature into specific, potentially-neutralizing Abs is important for development of a safe vaccine.

The Ab affinity maturation process for EDIII recognition can be investigated by structural comparisons of germline and mature Ab recognition of antigen. This approach provided insights into the affinity maturation of Abs against other viruses, including an increased understanding of modes of binding and somatic hypermutation in broadly neutralizing Abs against HIV-1¹⁴¹⁻¹⁴⁵. In the case of ZIKV, knowledge of how both germline and mature versions of potentially neutralizing Abs bind flaviviruses may enhance our understanding of the interactions that give rise to potent neutralization versus weak cross-reactivity that could contribute to risk for ADE.

Here we report binding and structural studies to gain insight into affinity maturation and cross-reactivity of the *VH3-23/VK1-5* class of anti-ZIKV Abs. Through sequence alignments, surface plasmon resonance (SPR), neutralization assays, ADE assays, and structural studies, we compared mature and inferred germline (iGL) Ab binding to flavivirus EDIII domains from ZIKV, DENV1-4, WNV, and YFV. As part of this analysis, we

compared two new crystal structures, an iGL Ab bound to ZIKV EDIII and a cross-reactive mature Ab bound to WNV EDIII, with two previously-determined crystal structures of potently neutralizing mature Abs bound to ZIKV and DENV1 EDIII³⁶. These findings revealed components of germline maturation, including contributions of somatic hypermutation in the V_L domain of the Fab, important for development of *VH3-23/VK1-5* Abs that potently neutralize ZIKV and inform cross-reactivity precautions for flavivirus vaccine design and passive delivery of ZIKV Abs.

Results

Selection of anti-ZIKV Abs for binding and structural studies. Potent neutralizing and recurring *VH3-23/VK1-5* Abs against ZIKV and DENV1 were previously identified in multiple donors exposed to ZIKV in Mexico and Brazil³⁶. To investigate germline Ab maturation and cross-reactivity of *VH3-23/VK1-5* Abs, we selected a set of seven Abs identified from the memory B cells of three of the donors: Z004_{mature} from donor MEX 18; Z006_{mature} from donor MEX 105; Z031_{mature}, Z032_{mature}, Z034_{mature}, Z035_{mature}, and Z036_{mature} from donor BRA 112 (SI Appendix, Figures S2.1-S2.3). Since crystal structures were previously determined for Z004_{mature} and Z006_{mature} Fabs complexed with DENV1 EDIII and ZIKV EDIII, respectively (PDBs 5VIC and 5VIG), these Abs were of particular interest for comparison to germline versions. Additionally, Z031_{mature}, Z032_{mature}, Z034_{mature}, Z035_{mature}, and Z036_{mature}, which we term the Z03X_{mature} series, were selected since *VH3-23/VK1-5* Abs from patient BRA 112 were previously shown to neutralize ZIKV, but no structural information on EDIII recognition was known³⁶.

Design of inferred germline (iGL) versions of anti-ZIKV Abs. Z004_{iGL} and Z03X_{iGL} were constructed based on the germline gene assignments of mature *VH3-23/VK1-5* Abs identified from donors MEX 18 and BRA 112 (SI Appendix, Figures S2.1-S2.3)^{36,146}. There are 16 amino acid differences in the V_H and nine differences in the V_L of the Z004_{mature} and Z004_{iGL} sequences (Figure 2.1), some occurring in complementarity determining regions (CDRs) (three in CDR1, six in CDR2, and five in CDR3) (Figure 2.1A). Amino acid differences between the Z03X_{mature} series and the Z03X_{iGL} ranged from 13 to 23 for V_H and 8 to 11 for V_L (Figure 2.1B). The Z03X_{iGL} V_H CDR1 (CDRH1) differed from all Z03X_{mature} sequences except Z035_{mature}, and the V_L CDR1 (CDRL1) differed from all Z03X_{mature} sequences except Z031_{mature}. The Z03X_{iGL} CDRH2 differed from all Z03X_{mature} sequences by at least three amino acids, and CDRL2 was the same as all Z03X_{mature} sequences except Z034_{mature}. The

CDR3s of the Z03X_{iGL} V_H and V_L differed by at least two amino acids from all Z03X_{mature} sequences.

Assessing binding of anti-ZIKV IgGs with flavivirus EDIIIs. To investigate whether iGL versions of Abs bind ZIKV EDIIIs and whether any of the mature anti-ZIKV Abs cross-react with EDIIIs of other flaviviruses, we used surface plasmon resonance (SPR) to determine Ab binding affinities for EDIII domains. To avoid avidity effects, the monomeric EDIII domains were injected over mature and iGL versions of IgGs coupled to biosensor flow cells. The analytes included EDIIIs from ZIKV, DENV1, DENV2, DENV3, DENV4, WNV, and YFV, and the IgG ligands included Z004_{mature}, Z006_{mature}, Z031_{mature}, Z032_{mature}, Z034_{mature}, Z035_{mature}, Z036_{mature}, Z004_{iGL}, and Z03X_{iGL}.

Sensorgrams revealed strong binding of both ZIKV and DENV1 EDIII to all mature IgGs, with low nM or pM equilibrium dissociation constants (K_{DS}) (Figures 2.2A; SI Appendix, Figures S2.4A-S2.7; Table 2.1). The K_D values for Z004_{mature}, Z006_{mature}, Z032_{mature}, Z034_{mature}, Z035_{mature} and Z036_{mature} were all ~2 to 14x lower for ZIKV EDIII than DENV1 EDIII, demonstrating stronger binding to ZIKV EDIII. Z031_{mature} was the only IgG to bind more tightly to DENV1 than ZIKV EDIII. Mature IgGs showed weak binding to some of the EDIIIs; specifically, Z004_{mature}, Z006_{mature}, and Z034_{mature} with DENV2 EDIII, Z004_{mature} with DENV4 EDIII, and all mature IgGs with WNV EDIII ($K_{DS} > 100 \mu\text{M}$) (SI Appendix, Figures S2.8-S2.12; Table 2.1). Although the binding of Abs to DENV2, DENV4 and WNV is weak (SI Appendix, Figures S2.8A, S2.10A, S2.11A), it is clearly detectable compared to negative controls that show no binding (SI Appendix, Figures S2.8B, S2.9, S2.10B, S2.11B, S2.12). However, reporter viral particle (RVP)-based neutralization assays with a subset of *VH3-23/VK1-5* Abs showed mature Abs neutralize ZIKV and DENV1, but not WNV (SI Appendix, Figure S2.13). Additionally, RVP-based ADE assays showed no ability of mature Abs to induce ADE of DENV2 or WNV (SI Appendix, Figure S2.14).

A. V_H alignment

```

Z004 iGL      EVQLLESGGGLVQPGGSLRLSCAASGFTFSSYAMSWVRQAPGKLEWVSA 50
Z004 mature  .....T..T.....RD.....S 50

Z004 iGL      ISGSGGSTYYADSVKGRFTISRDNKNTLYLQMNLSRAEDTAVYYCAKDR 96
Z004 mature  Y..IDD.....S..S.H.....S.L.F..... 96

Z004 iGL      GPRGVGELFDYWGQGLTVTVSS 113
Z004 mature  .....S..... 113

```

V_L alignment

```

Z004 iGL      DIQMTQSPSTLSASVGDRTTITCRASOSISSWLAWYQQKPKGAPKLLIYK 50
Z004 mature  .....K.....T 50

Z004 iGL      ASSLESGVPSRFRSGSGGTEFTLTISLQPDFFATYYCQQYNSYPWTFGQ 100
Z004 mature  T.T.K.....HPY.V..... 100

Z004 iGL      GTKVEIK 107
Z004 mature  ..... 107

```

B. V_H alignment

```

Z03X iGL      EVQLLESGGGLVQPGGSLRLSCAASGFTFSSYAMSWVRQAPGKLEWVSAISGSGG---- 55
Z031 mature  .....V.....G..G.A.....I.S..SID---- 54
Z032 mature  .....R.....T.....P..T.....L.....G.T.DS---- 55
Z034 mature  .....A.....ET.....R..G.G.....S.YI..... 54
Z035 mature  .....I.....I.....G.....ASDN 53
Z036 mature  .....D.....T.G.A.....L.S..SVD---- 54

Z03X iGL      --STYYADSVKGRFTISRDNKNTLYLQMNLSRAEDTAVYYCAKDRISGSGGELFSSWGQ 105
Z031 mature  -P.....V.....E.....H.S..KV.....F.....N.....A... 105
Z032 mature  --.....A.....T.D.....HS.L.....Y... 105
Z034 mature  -D.....A.....S.....DR.T.....VR..IQ.....YRY... 105
Z035 mature  GA.R.....S.....V.....QK... 105
Z036 mature  -D.K...A.....R.....H.....VD.....IPH.L...YAN... 105

Z03X iGL      GTLTVTVSS 113
Z031 mature  ..... 113
Z032 mature  ..... 113
Z034 mature  ..... 113
Z035 mature  ..... 113
Z036 mature  ..... 113

```

V_L alignment

```

Z03X iGL      DIQMTQSPSTLSASVGDRTTITCRASOSISSWLAWYQQKPKGAPKLLIYKASSLESGVPS 60
Z031 mature  .....S.....F..H.....I.. 60
Z032 mature  .....N.....NQ.....F.M...T.T... 60
Z034 mature  .....M.....V.NK.....ET.I...S. 60
Z035 mature  .....A.....N.N.....F.....T...A. 60
Z036 mature  .....G.....R..MH...N.Y.... 60

Z03X iGL      RFSGSGSGTEFTLTISLQPDFFATYYCQQYNSYPWTFGQGTKVEIK 107
Z031 mature  .....NN.....H.H..... 107
Z032 mature  .....H.F..... 107
Z034 mature  .....H.HG..... 107
Z035 mature  .....H.Y...Y... 107
Z036 mature  .....H.H...Y... 107

```

Figure 2.1. Alignments of V_H and V_L sequences of mature and iGL versions of Abs isolated from patients exposed to ZIKV.

A. Z004 mature and iGL Ab. **B.** Mature and iGL Z03X Abs. CDR1, CDR2, and CDR3 are orange, blue, and red, respectively. The Kabat numbering scheme was used.

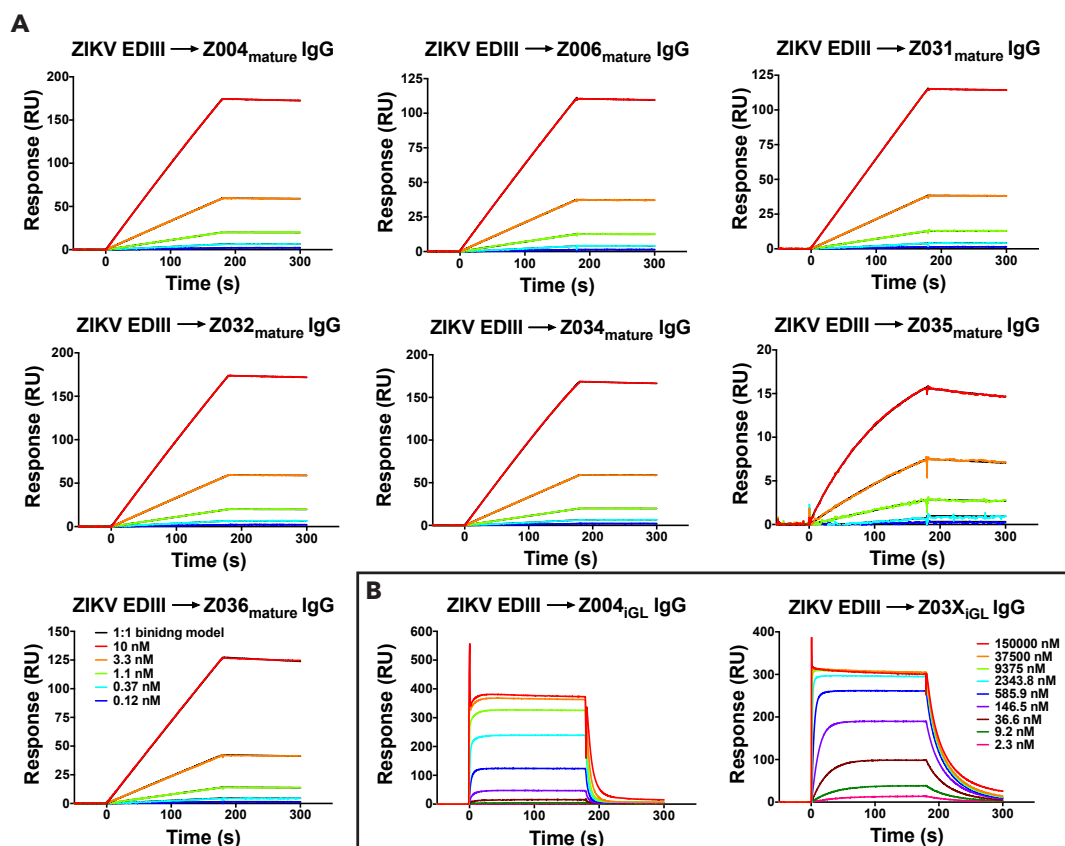


Figure 2.2. SPR binding assays with ZIKV EDIII.

IgGs were captured on a protein A biosensor chip, and the indicated concentrations of ZIKV EDIII were injected. Sensorgrams are indicated in colors representing different injected concentrations. **A.** Mature IgGs binding to ZIKV EDIII. Fits to a 1:1 binding model are in black; since the models very closely fit the data, the models are only slightly visible. The legend shown in the bottom left panel applies to all sensorgrams. Residual plots for the 1:1 binding model fitting are shown in SI Appendix, Figure S2.7A. Two independent experiments were performed; the other set of sensorgrams is shown in SI Appendix, Figure S2.5. **B.** iGL IgGs binding to ZIKV EDIII. Fitting curves for equilibrium binding responses are shown in Figure 2.3. Y-axes show response units (RU). The legend shown in the right panel applies to both sensorgrams.

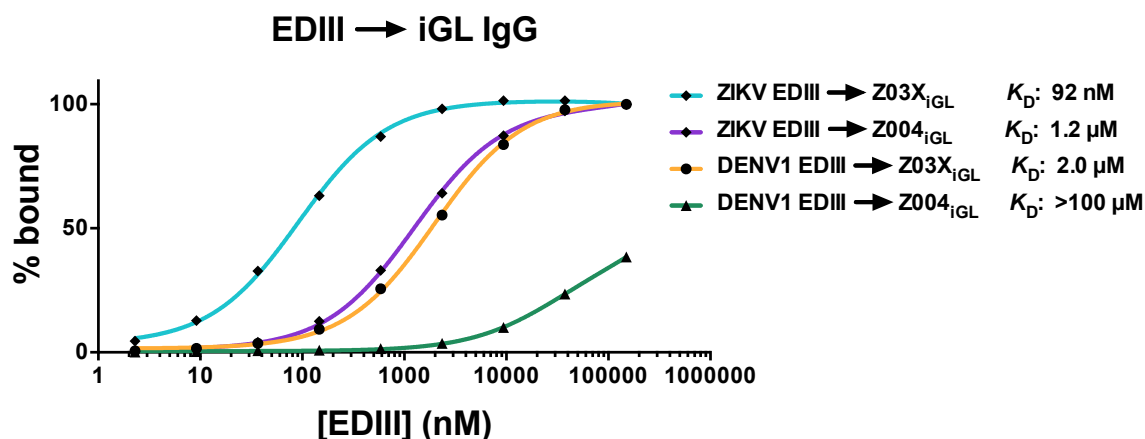


Figure 2.3. Comparison of qualitative ZIKV and DENV EDIII binding to iGL Abs.

Normalized equilibrium binding responses (R_{eq}) from the sensorgrams in Figures 2.2B and SI Appendix, Figure S2.4B are plotted versus the log of the concentration of the indicated injected proteins with best fit binding curves to the experimental data points shown as continuous lines. The standard errors (S.E.) of the fit and 95% confidence intervals (C.I.) of the K_D s are as follows: ZIKV EDIII → Z03X_{iGL} IgG (K_D : 92 nM, S.E.: 4.9 nM, C.I.: 79-100 nM), ZIKV EDIII → Z004_{iGL} IgG (K_D : 1.2 μM, S.E.: 61 nM, C.I.: 1100-1400 nM), and DENV1 EDIII → Z03X_{iGL} IgG (K_D : 2.0, S.E.: 100 nM, C.I.: 1700-2200 nM). Since DENV1 EDIII → Z004_{iGL} binding reaction did not reach equilibrium, the K_D is approximated as greater than the highest concentration of analyte injected.

As expected, the iGL IgGs bound EDIII with lower affinities (e.g., low μM to high nM K_D s for the interactions of Z004_{iGL} and Z03X_{iGL} with ZIKV and DENV1 EDIII, respectively) than the mature IgGs (Figure 2.2B; Table 2.1; SI Appendix, Figure S2.4B). The iGL IgGs bound ZIKV EDIII with ~22 to 83x higher affinity than DENV1 EDIII, similar to the trend shown by mature IgGs (Figure 2.3). The only other EDIIIs that showed detectable interactions with iGL IgGs were Z03X_{iGL}-DENV2 EDIII and Z03X_{iGL}-DENV4 EDIII (SI

Appendix, Figures S2.8, S2.10; Table 2.1). While the Z004_{iGL} and Z03X_{iGL} IgGs neutralized ZIKV RVPs (NT50s (concentration at 50% neutralization) of 8.8 ng/mL and 0.82 ng/mL, respectively) and DENV1 RVPs (NT50s: 1400 ng/mL and 40 ng/mL), these iGL IgGs also showed ability to induce some ADE of ZIKV and DENV1 (but not DENV2 or WNV) (SI Appendix, Figures S2.13-S2.14).

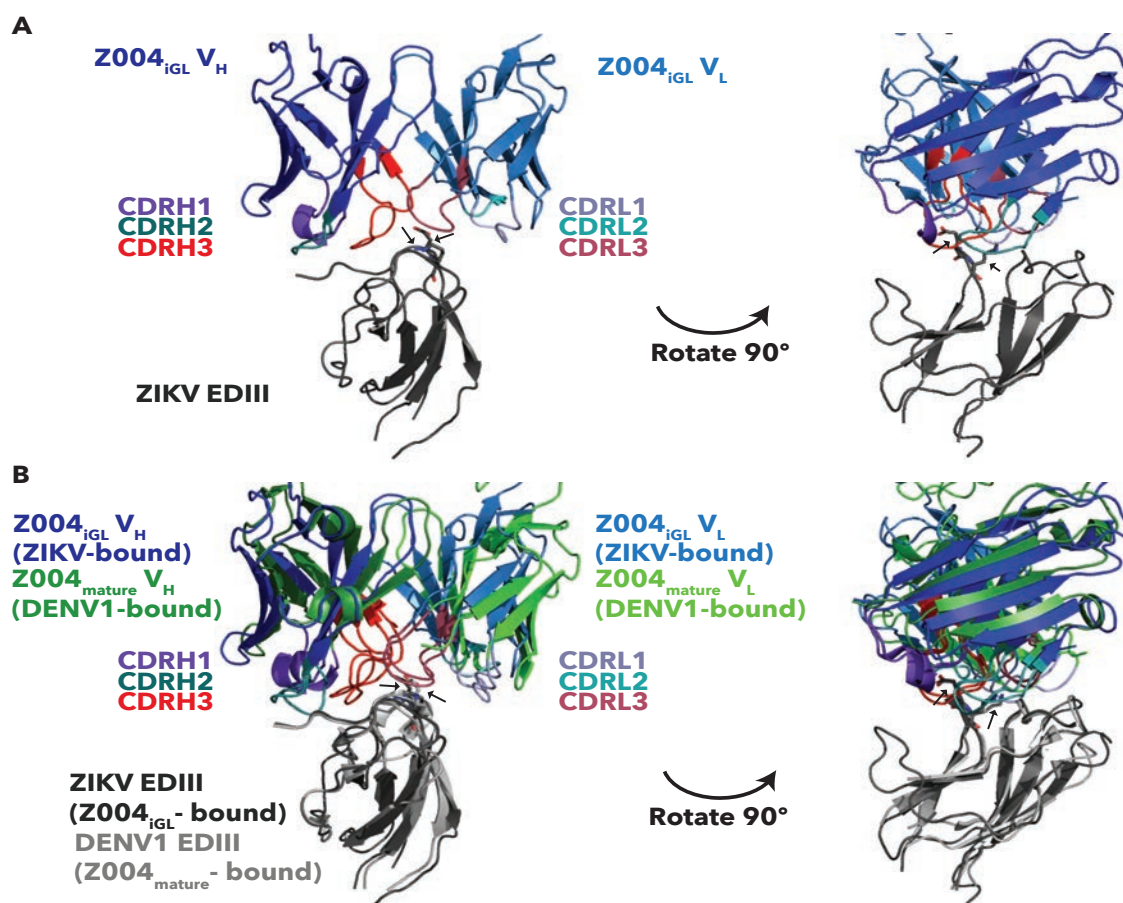
IgG	EDIII						
	ZIKV	DENV1	DENV2	DENV3	DENV4	WNV	YFV
Z004 _{mature}	0.28	0.47	>100,000	<i>n.b.</i>	>100,000	>100,000	<i>n.b.</i>
Z006 _{mature}	0.50	1.7	>100,000	<i>n.b.</i>	<i>n.b.</i>	>100,000	<i>n.b.</i>
Z031 _{mature}	3.0	0.33	<i>n.b.</i>	<i>n.b.</i>	<i>n.b.</i>	>100,000	<i>n.b.</i>
Z032 _{mature}	0.30	1.1	<i>n.b.</i>	<i>n.b.</i>	<i>n.b.</i>	>100,000	<i>n.b.</i>
Z034 _{mature}	0.059	0.80	>100,000	<i>n.b.</i>	<i>n.b.</i>	>100,000	<i>n.b.</i>
Z035 _{mature}	0.78	5.2	<i>n.b.</i>	<i>n.b.</i>	<i>n.b.</i>	>100,000	<i>n.b.</i>
Z036 _{mature}	0.29	0.53	<i>n.b.</i>	<i>n.b.</i>	<i>n.b.</i>	>100,000	<i>n.b.</i>
Z004 _{iGL}	1200	>100,000	<i>n.b.</i>	<i>n.b.</i>	<i>n.b.</i>	<i>n.b.</i>	<i>n.b.</i>
Z03X _{iGL}	92	2000	>100,000	<i>n.b.</i>	>100,000	<i>n.b.</i>	<i>n.b.</i>

n.b.: no detectable binding at concentrations $\leq 150 \mu\text{M}$.

To characterize affinity maturation of anti-ZIKV Abs and the structural correlates of Ab cross-reactivity, we set up crystallization screens for all seven Fabs and for the 31 Fab-EDIII complexes that exhibited detectable binding interactions (Table 2.1). Crystals were obtained and X-ray structures determined for two complexes: Z004_{iGL} Fab with ZIKV EDIII (3.1 Å resolution) and Z032_{mature} Fab with WNV EDIII (2.9 Å resolution) (SI Appendix, Table S2.1).

Comparing iGL and mature Fab interactions with flavivirus EDIII. Crystals of the Z004_{iGL} Fab–ZIKV EDIII complex contained two Fab–EDIII complexes in the asymmetric unit (root mean square deviation, rmsd, of 0.37 Å for 279 C α atoms in the V_H-V_L and EDIII domains) (SI Appendix, Table S2.1). The structure revealed that Z004_{iGL} binds the same epitope on the EDIII lateral ridge as Z004_{mature}. Alignment of the EDIII portions of both complexes revealed similar binding interactions, including recognition of the EDIII EK amino acid motif (E393-K394) that is central to the binding epitope in the Z004_{mature} Fab–DENV1 EDIII (PDB 5VIC) and Z006_{mature}–ZIKV EDIII (PDB 5VIG) crystal structures (Figures 2.4; SI Appendix, S2.15A, Table S2.2).

To compare the binding interfaces of the iGL and mature Abs with EDIII, we calculated buried surface areas (BSAs) on the Fab and EDIII in each complex (Figure 2.5). Increased BSA generally correlates with a larger number of interface residues and a higher binding affinity¹⁴⁷. As expected from the low affinity of the Z004_{iGL} Fab interaction with EDIII, less surface area was buried by EDIII on Z004_{iGL} Fab (~660 Å²) than on Z004_{mature} (~810 Å²) or Z006_{mature} (~890 Å²) (Figure 2.5). The difference in Fab BSA between Z004_{iGL} and Z004_{mature} was largely accounted for by interactions with V_L rather than V_H. Specifically, the V_H BSA was similar for Z004_{iGL} (~410 Å²) and Z004_{mature} (~400 Å²), whereas the V_L BSA was greater for Z004_{mature} (~410 Å²) than Z004_{iGL} (~250 Å²). There was more EDIII surface area buried by V_H than by V_L for all complexes (Figure 2.5). Since the Z004_{iGL}–ZIKV EDIII and Z004_{mature}–DENV1 EDIII structures do not directly compare iGL and mature Z004 binding to the same EDIII, we also made a homology model of Z004_{mature}–ZIKV EDIII binding by threading the sequence of ZIKV EDIII onto the structure DENV1 EDIII in the Z004_{mature}–DENV1 EDIII structure. The BSA on the Fab (770 Å²) for the Z004_{mature}–ZIKV EDIII model showed the same trend as Z004_{mature}–DENV1 EDIII: the V_H BSA of Z004_{mature} (~390 Å²) was similar to Z004_{iGL} (~410 Å²), whereas the V_L BSA was greater for Z004_{mature} (~380 Å²) than Z004_{iGL} (~250 Å²) (Figure 2.5).



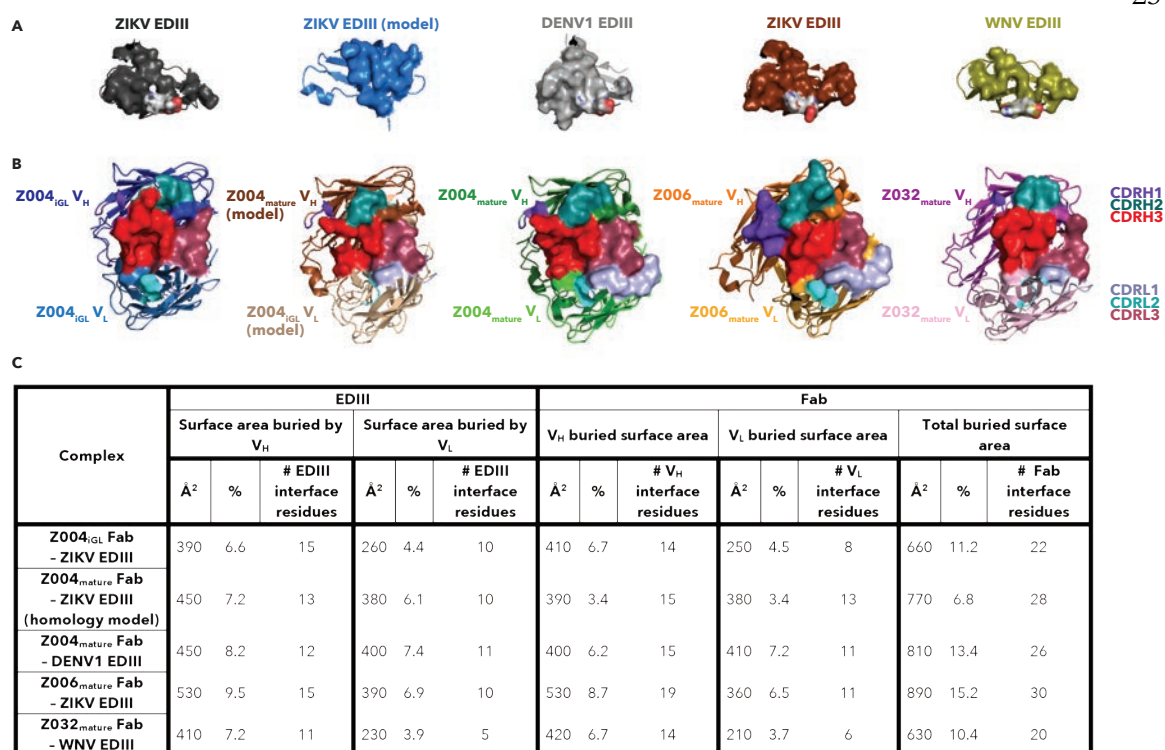


Figure 2.5. Comparison of Fab–EDIII binding interfaces.

Surface representations of the **A**. EDIII epitopes contacted by Fabs, and **B**. Fab binding epitopes contacted by EDIII in the Z004_{iGL} Fab–ZIKV EDIII (PDB 6UTA), Z004_{mature} Fab–ZIKV EDIII homology model, Z004_{mature} Fab–DENV1 EDIII (PDB 5VIC), Z006_{mature} Fab–ZIKV EDIII (PDB 5VIG), and Z032_{mature} Fab–WNV EDIII (PDB 6UTE) structures (left to right). The Z004_{mature} Fab–ZIKV EDIII homology model was made by threading the sequence of ZIKV EDIII onto the structure DENV1 EDIII in the Z004_{mature}–DENV1 EDIII structure. Binding epitopes are shown as surfaces over cartoon representations. CDRs are colored as indicated (right). **C**. Quantification of BSA (Å² and percentage of total surface area) and number of interface residues buried on the entire EDIII (left) and V_H and V_L of the Fab (right) based on the interfaces mapped in A and B. The column labeled total buried surface area for Fabs includes the sum of BSA for the V_H and V_L.

Z004_{iGL} showed only 5 residues that interact with the ZIKV EDIII antigen compared with 10 interacting residues for Z004_{mature} (with DENV1 EDIII in the crystal structure and with ZIKV EDIII in the homology model) and 13 residues in Z006_{mature} Fabs that interact with ZIKV EDIII (SI Appendix, Figure S2.16A-D, Table S2.2). The finding of fewer interacting residues is consistent with the weaker binding of Z004_{iGL} demonstrated by SPR (Figures 2.2, 3; Table 2.1). Similar to the trends with differences in BSA, differences in the number of Fab residues predicted to interact with EDIII was pronounced for V_L: 1 by Z004_{iGL} V_L, 4 by Z004_{mature} V_L (with ZIKV in the model), 5 by Z004_{mature} V_L (with DENV1), 6 by Z006_{mature} V_L (with ZIKV) (SI Appendix, Figure S2.16A-D, Table S2.2). Among Fab residues that interact with EDIII by either Z004_{iGL} or Z004_{mature}, we observe that the only residues that differ in sequence between the iGL and mature version are in the V_L CDRL3: F91_{VL}, Y92_{VL} and V94_{VL} in Z004_{mature}, compared with Y91_{VL}, N92_{VL}, and Y94_{VL} in Z004_{iGL} (SI Appendix, Figure S2.16-S2.17A, Table S2.2). Two of these residues, F91_{VL} and Y92_{VL}, interact with the ZIKV EDIII EK motif. In contrast, the only residues that interact with EDIII by both Z004_{mature} and Z004_{iGL} are in the V_H and share the same sequence: S56_{VH} (CDRH2), Y58_{VH} (FWRH3), and E100_{CVH} (CDRH3). Z006_{mature} Fab also shared one of the same V_H interacting residues: Y58_{VH} (framework region (FWR)H3) (SI Appendix, Figure S2.16, Table S2.2).

To further investigate the effects of affinity maturation in the V_H versus the V_L domain for high affinity EDIII binding, we prepared two Z004 chimeric IgGs for SPR and neutralization assay analysis: one with mature V_H and iGL V_L and the other with iGL V_H and mature V_L. The SPR sensorgrams for ZIKV EDIII binding to the Z004 chimeras were fit to a 1:1 binding model (SI Appendix, Figure S2.18) and showed 10-fold higher affinity binding to the V_{iGL} HC-V_{mature} LC chimera (K_D : 2.5 nM) than to the V_{mature} HC-V_{iGL} LC chimera (K_D : 29 nM) (Table S2.3). The V_{iGL} HC-V_{mature} LC sensorgrams appeared similar to mature V_H-V_L sensorgrams (slow off-rate), whereas the V_{mature} HC-V_{iGL} LC sensorgrams were more similar to the iGL V_H-

V_L sensorgrams (fast off-rate), consistent with the importance of light chain maturation in the development of high affinity recognition of Zika EDIII. Neutralization assays comparing the two chimeric Abs showed that while both Z004 chimeras can neutralize ZIKV and DENV1, the $V_{iGL\ HC}-V_{mature\ LC}$ chimera neutralizes just as potently (NT_{50} : 0.34) as fully mature Z004 IgG (NT_{50} : 0.55), while $V_{mature\ HC}-V_{iGL\ LC}$ chimera neutralizes with slightly lower potency (NT_{50} : 1.00) (SI Appendix, Figure S2.13).

To assess which residues are important for high affinity binding, we first prepared ZIKV EDIII with the EK motif (central to the binding epitope and involved in several interactions with Z004), mutated to alanines (E393A-K394A) for binding studies with SPR. Binding of Z004_{mature} IgG to ZIKV EDIII_{AA} mutant was nearly abolished with a K_D of $\gg 100\ \mu M$ (SI Appendix, Figure S2.17B, Table S2.3). To verify that the Z004 V_L residues that interact with EDIII and differ between Z004_{iGL} and Z004_{mature} (F91_{VL}, Y92_{VL} and V94_{VL}) are important for high-affinity binding to ZIKV EDIII, we prepared Z004_{mature} IgG variants with two or all three residues mutated to alanines. When the two EK-interacting residues were mutated (Z004_{mature} IgG: V_L F91A-Y92A), we observed 100-fold reduced binding affinity to ZIKV EDIII (K_D : 35 nM). When all three residues were mutated (Z004_{mature} IgG: V_L F91A-Y92A-V94A), we observed 1000-fold reduced binding affinity (K_D : 230 nM) (SI Appendix, Figure S2.17C-D, Table S2.3).

Structural correlates of weak Ab cross-reactivity. We were able to crystallize a complex of Z032_{mature} Fab bound to WNV EDIII despite the low affinity of this interaction ($K_D \geq 100\ \mu M$) (Table 2.1). Perhaps correlating with the low affinity of the complex, the crystallographic asymmetric unit contained one Fab–WNV EDIII complex and four unbound Fabs (Figure 2.6A; SI Appendix, Table S2.1). The four unbound Fabs were similar to each other (rmsds ranging from 0.22 Å to 0.47 Å for pairwise superimpositions of 203-214 C α residues in the V_H - V_L domains) (SI Appendix, Table S2.4). WNV EDIII-bound and unbound Fabs were also similar (rmsds ranging from 0.35 Å to 0.45 Å for pairwise superimpositions

of 210-217 C α residues in the V_H-V_L domains), indicating no major structural changes upon EDIII binding (SI Appendix, Figure S2.19, Table S2.4).

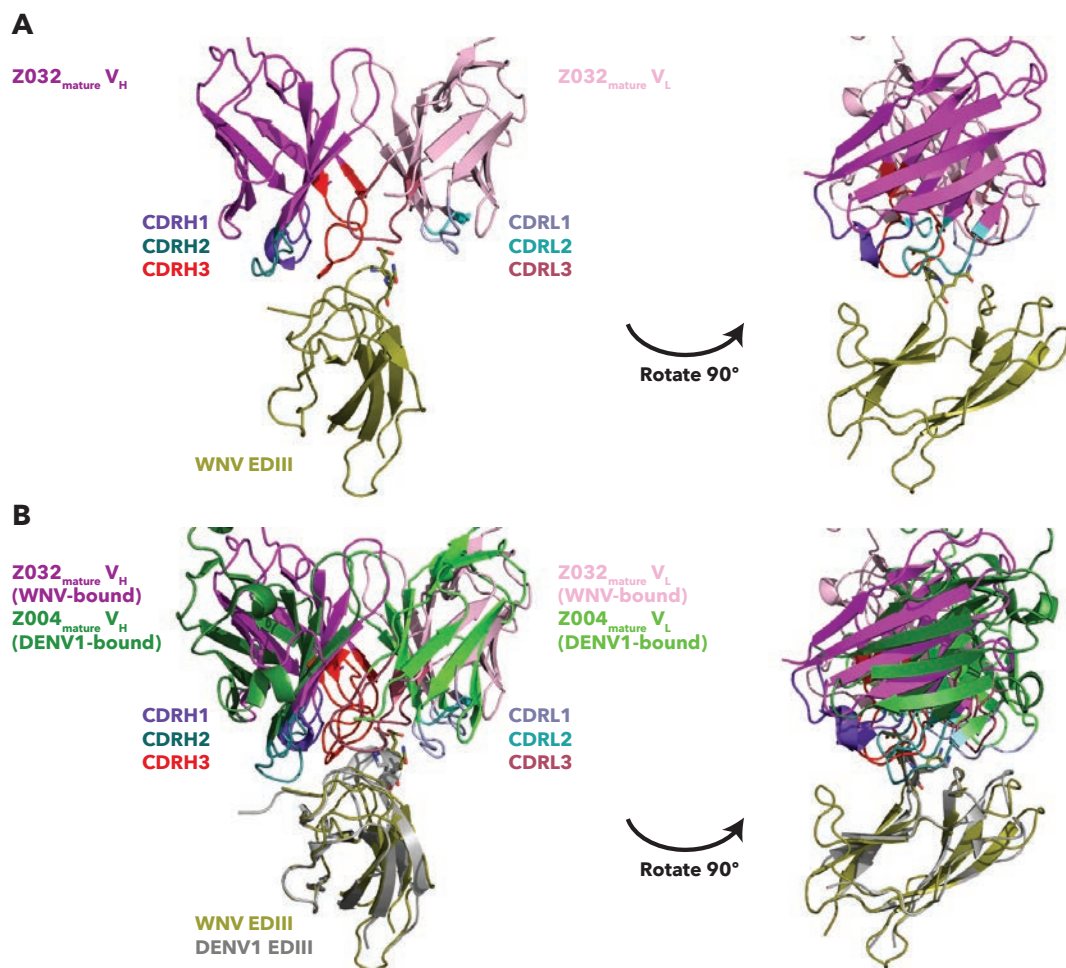


Figure 2.6. Cross-reactive recognition of WNV EDIII by Z032_{mature} Fab.

Fab-EDIII complex structures are shown as cartoon representations with Fab V_H-V_L domains only and the EQ or EK motifs of WNV and DENV1 EDIIIs highlighted as sticks (panels A and B). **A.** Z032_{mature} Fab–WNV EDIII structure. **B.** Superimposition of the Z032_{mature} Fab–WNV EDIII and Z004_{mature} Fab–DENV1 EDIII (PDB 5VIC) structures. Structures were superimposed on the EDIII domains.

The Z032_{mature} Fab–WNV EDIII structure showed that Z032_{mature} Fab interacts with WNV EDIII at the lateral ridge epitope recognized by Z004_{mature}, Z006_{mature}, and Z004_{iGL}, although with a low Fab BSA ($\sim 630 \text{ \AA}^2$) (Figures 2.5-2.6; SI Appendix, S14). Similar to Z004_{iGL}, the V_H (420 \AA^2) contributes more to the total Z032_{mature} Fab BSA than V_L (210 \AA^2). The low Fab BSA correlates with fewer interacting residues at the binding interface: only 8 Z032 Fab residues were found to interact with 6 WNV EDIII residues (SI Appendix, Figure S2.16, Table S2.2). Some Z032_{mature} Fab interacting residues were also involved in interactions in other Fab–EDIII structures: S56_{VH} (in Z004_{iGL} and Z004_{mature}), Y58_{VH} (FWR3) (in Z004_{iGL}, Z004_{mature}, and Z006_{mature}), R96_{VH} (CDRH3) (in Z004_{mature} and Z006_{mature}), E100_{CVH} (CDRH3) (in Z004_{iGL} and Z004_{mature}), Y91_{VL} (in Z006_{mature}), and Y94_{VL} (in Z004_{iGL}) (SI Appendix, Figure S2.16, Table S2.2). This suggests that these residues contribute to enhanced cross-reactivity of anti-ZIKV *VH3-23/VK1-5* Abs.

Discussion

Understanding the structural basis of Ab recognition of ZIKV and other flavivirus antigens informs considerations and precautions for vaccine design to elicit EDIII-specific Abs. Here we conducted binding and structural studies comparing interactions of mature and iGL *VH3-23/VK1-5* Abs isolated from ZIKV-exposed donors with a panel of flavivirus EDIII domains to provide insight into the affinity maturation process of this class of potentially-neutralizing ZIKV Abs. In addition to revealing interactions critical for potent binding to ZIKV, we also identified weaker interactions that may contribute to cross-reactivity and potentially ADE.

By comparing mature and iGL *VH3-23/VK1-5* Ab binding to EDIIIs, we identified the mutations introduced through somatic hypermutation that facilitate tight binding of the Z004 Ab to ZIKV. As expected, a crystal structure of a Z004_{iGL}-EDIII complex showed fewer Fab residues that interact with EDIII than observed for EDIII complexes including mature Fabs such as Z004_{mature}, Z006_{mature}, and Z032_{mature}³⁶. In a direct comparison of the Z004_{mature}-DENV1 EDIII structure and Z004_{mature}-ZIKV EDIII homology model with the Z004_{iGL}-ZIKV EDIII structure, the only three Fab residues involved in interactions with EDIII that differed in sequence between Z004_{mature} and Z004_{iGL} are in V_L. In contrast, the three interacting residues that are shared by both Z004_{mature} and Z004_{iGL} are in V_H. This suggests that affinity maturation of V_L CDRL3 may be particularly important for higher affinity binding to EDIII. This is further supported by the finding that the increased BSA on Z004_{mature} compared to Z004_{iGL} was largely accounted for by an increase in the V_L BSA. Comparison of the binding affinities and neutralization potencies of Z004 mature/iGL chimeras also suggests the importance of V_L maturation for EDIII recognition.

Through investigation of the effects of site-directed mutations in Z004_{mature} IgG and ZIKV EDIII on binding, we showed that interactions with the EDIII EK motif are critical for high affinity binding. While both V_H and V_L residues interact with the EK motif, the only EDIII-

interacting residues that differ between Z004_{mature} and Z004_{iGL} are in V_L (F91, Y92, and V94). The reduced binding affinity when these residues are mutated to alanines supports that affinity maturation of the V_L is important for high affinity binding.

The importance of V_L somatic hypermutation was also observed in a previous longitudinal analysis of a ZIKV-infected patient to trace the lineage of ZK2B10, a protective VH1-8/VL1-47 Ab against ZIKV that binds a different part of the EDIII lateral ridge¹⁴⁸. Two residues in the VL1-47 germline-coded lambda V_L, N31 (CDRL1) and S91 (CDRL3), were shown to be necessary and sufficient for functional maturation of the VH1-8/VL1-47 Ab lineage to achieve potent ZIKV neutralization. They observed low somatic hypermutation in germline-like somatic variants of V_H, concluding that restricted V_H gene segment usage, rather than somatic hypermutation in the V_H domain, was important to achieve high affinity and potency. While ZK2B10 is derived from different germline genes and binds a different part of the EDIII lateral ridge than the *VH3-23/VK1-5* Abs studied here, we observed a similar trend for the *VH3-23/VK1-5* Ab Z004: affinity maturation of V_L was important for strong binding and neutralization, while V_H interactions were restricted to residues already present in the germline gene.

Through assessment of *VH3-23/VK1-5* Ab binding to a panel of flavivirus EDIIIs using SPR, the Abs tightly bound ZIKV and DENV1 and weakly bound DENV2, DENV4, and WNV EDIII, indicating a potential for cross-reactivity. Although this class of mature Abs was shown to neutralize DENV1 in addition to ZIKV³⁶, the ability of iGL Abs to bind DENV1 EDIII as well as the apparent weak binding of both mature and iGL Abs to other flaviviruses suggests the possibility of ADE upon subsequent infection with a different flavivirus in humans. The EK motif, which is only present in ZIKV and DENV1 EDIII, likely contributes to initial recognition by germline Abs that leads to the tighter binding and neutralization of these two flaviviruses by *VH3-23/VK1-5* Abs. The importance of E393 in the EK motif for neutralization of ZIKV strains was also previously described for the *VH3-23/VK1-5* Ab

ZIKV-116³⁷. In contrast to ZIKV and DENV1, the lateral ridges of DENV2, DENV4, and WNV EDIIIs all contain motifs other than EK, yet still showed weak binding to at least one mature or iGL Ab by SPR. This suggests the interactions that contribute to cross-reactive binding of Abs to these flaviviruses are different from, or only partially overlap with, the interactions that contribute to high affinity and neutralizing binding to ZIKV and DENV1 EDIIIs. Apart from DENV1, WNV EDIII was the only flavivirus for which all seven mature *VH3-23/VK1-5* Abs showed cross-reactivity (Table 2.1). Given that binding to DENV2, DENV4, and WNV EDIIIs is weak ($K_D \geq 100 \mu\text{M}$), it is unclear whether this cross-reactivity could facilitate ADE of these flaviviruses upon infection. However, our RVP-based assays showing no ADE for DENV2 or WNV infection suggests this is of low concern. The potential for cross-reactivity of other Abs with ZIKV and WNV EDIII was shown in studies demonstrating that previous exposure to WNV enhances subsequent ZIKV infection in mice, although immunodominant DII-specific fusion loop Abs might explain this *in vivo* enhancement⁷⁶.

The crystal structure of Z032_{mature} Fab complexed with WNV EDIII provided an example of the structural basis of cross-reactive recognition. This structure shows that the Z03X Abs bind the same lateral ridge epitope as other *VH3-23/VK1-5* Abs³⁶. A few Z032_{mature} Fab-interacting residues (S56_{VH} (CDRH2), Y58_{VH} (FWRH3), R96_{VH} (CDRH3), E100C_{VH} (CDRH3), Y91_{VL} (CDRL3), and Y94_{VL} (CDRL3)) are also involved in at least one other interaction in the Z004_{iGL}, Z004_{mature}, and Z006_{mature} complexes with EDIII domains. This suggests these residues, including the one in a conserved FWR (Y58_{VH}), may contribute to cross-reactivity of *VH3-23/VK-15* Abs, potentially even precursor germline versions, with different flaviviruses. These residues are present in iGL sequences, suggesting that residues that contribute to cross-reactivity may already be present prior to affinity maturation. The weak, cross-reactive binding of Z004_{iGL} to DENV1 EDIII and of Z03X_{iGL} to DENV1, DENV2 and DENV4 further supports this suggestion. Five of the eight Z032_{mature} Fab

residues predicted to bind WNV EDIII are in the V_H , suggesting the V_H may contribute more to weak, cross-reactive binding, whereas somatic hypermutation in the V_L may contribute more to tight binding of mature *VH3-23/VK1-5* Abs to ZIKV.

Comparison of the structures of bound and unbound Z032_{mature} Fabs indicated the *VH3-23/VK1-5* class of Abs does not require major conformational changes for binding. Superimposition of the bound and unbound Z032_{mature} V_HV_L revealed a low calculated rmsd and no major differences in the backbone structure, suggesting that conformations were preformed prior to binding. This suggests that *VH3-23/VK1-5* mature Abs use a lock-and-key mode of binding, involving minimal conformational changes between the bound and unbound states of antigen and Ab¹⁴⁹⁻¹⁵¹.

Germline versions of *VH3-23/VK1-5* ZIKV-neutralizing Abs showed detectable binding to ZIKV and DENV1 EDIII in the nM and low μ M range. This was also previously observed for the germline version of the *VH3-23/VK1-5* Ab ZIKV-116, which bound (K_{DS} of 48.9 nm-10 μ M) and neutralized ZIKV and DENV1 strains³⁷. This ability of germline versions of *VH3-23/VK1-5* Abs to bind ZIKV contrasts with germline-reverted forms of most broadly neutralizing Abs against HIV-1, which generally do not bind HIV-1 envelope¹⁵². The ability of germline versions of neutralizing Abs to bind antigens is of particular interest for vaccine design, as this suggests immunogens may effectively elicit precursors of the desired Ab class, which could then mature into neutralizing Abs. Initial studies of the potential of ZIKV EDIII to serve as a safe and effective immunogen are underway, and indicate potential to elicit a specific and potent neutralizing Ab response to ZIKV in mice¹⁵³⁻¹⁵⁵.

Increased understanding of the differences in the interactions that contribute to neutralization versus cross-reactivity leading to ADE may enable strategic immunogen design. The *in vitro* ability of germline and mature¹⁵⁶ *VH3-23/VK1-5* Abs to induce some ADE for ZIKV and DENV1, but not for DENV2 or WNV suggests there may be minimal risk of ADE due to

weak cross-reactivity for this class of Abs. While this is not indicative of *in vivo* ability to enhance infection, there may be concern that Ab titers falling below neutralizing levels may be a risk for ADE. These findings indicate the importance of examining the cross-reactivity and ADE-potential of other anti-ZIKV classes of Abs under consideration for vaccine design or passive delivery. Understanding which residues contribute to cross-reactivity versus potent neutralization may also inform the necessity of modifying passively-delivered Abs to reduce cross-reactivity and prevent ADE by introducing Fc of mutations that prevent Fc γ R binding.

Materials and Methods

Design of iGL versions of Abs against ZIKV. Sequences of iGL versions of anti-ZIKV Abs are based on V, D and joining J gene segment assignments from IgBlast^{36,146}. All mature *IGHV3-23/IGKV1-5* Ab sequences from donors MEX 18 and BRA 112 were considered for design of the Z004 and Z03X iGLs, respectively. CDR1 and CDR2 of the iGLs were based on the V gene segment assignment of the mature sequences, specifically *IGHV3-23* for the HC and *IGKV1-5* for the LC. The CDRH3 of the iGL was based on a consensus of the V, D, and J gene segment assignments for the mature HC sequences, and CDRL3 of the iGL was based on a consensus of V and J gene segment assignments for the mature LC sequences (SI Appendix, Figures S2.1-S2.3).

Protein expression. Abs were produced as previously described^{36,157}. Briefly, Z006_{mature}, Z031_{mature}, Z032_{mature}, Z034_{mature}, Z035_{mature}, Z036_{mature}, and Z03X_{iGL} IgGs were expressed by transient transfection of HEK293-6E cells with equal amounts of Ig HC and LC expression vectors. After seven days, IgGs were purified from supernatants using Protein G Sepharose 4 Fast Flow (GE Healthcare). Z004_{mature}, Z004_{iGL}, and N6 IgGs were expressed by transient transfection and purified from supernatants using a HiTrap MabSelect column (GE Healthcare) and size exclusion chromatography (SEC) using a Superdex 200 column (GE Healthcare) in 20 mM Tris pH 8.0, 150 mM NaCl.

Fabs with C-terminal His-tags were produced by transient transfection of Expi293F cells with equal amounts of HC and LC expression vectors. The Fabs were purified from supernatants with Ni-NTA affinity chromatography and SEC with a Superdex 200 column in 20 mM Tris, 150 mM NaCl.

Flavivirus EDIIIs were expressed in *E. coli* and purified from inclusion bodies as previously described^{36,69,158}. Briefly, EDIII genes from ZIKV (H/PF/2013 strain, GenBank KJ776791),

DENV1 (45AZ5 strain, NCBI reference NC_001477), DENV2 (NCBI reference NC_001474), DENV3 (NCBI reference NC_001475.2), DENV4 (NCBI reference NC_002640.1), YFV (Asibi strain, Genbank KF769016), and WNV (Genbank KX547539.1) in pET21 expression plasmids were transformed into BL21 (DE3) competent cells and cultures were grown in LB with carbenicillin at 37°C. Expression was induced with IPTG at an O.D. of ~0.6, and the culture was harvested after four hours and stored overnight at -20°C. The pellet was resuspended in 20 mM Tris pH 8.0, 150 mM NaCl, cells were lysed and centrifuged at 21,000 x g for 30 minutes, and the pellet was resuspended in 6 M guanidine hydrochloride, 100 mM Tris-HCl pH 8.0. This suspension was centrifuged again at 21,000 x g for 30 minutes, and then 20 mM beta-mercaptoethanol was added to the supernatant. EDIII in the supernatant was refolded by dropwise, rapid dilution into 400 mM L-Arginine, 100 mM Tris-base pH 8.0, 2 mM EDTA, 5 mM reduced glutathione, 0.5 mM oxidized glutathione, and 10% glycerol at 4°C. The protein was then concentrated and purified by SEC with a Superdex 75 column (GE Healthcare) in 20 mM Tris pH 8.0, 150 mM NaCl, 0.02% NaN₃.

SPR binding assays. SPR experiments were performed using a Biacore T200 instrument (GE Healthcare). Binding assays were done by flowing EDIII analytes over IgG ligands bound to a protein A-coupled biosensor chip in 0.2 µm-filtered HBS-EP+ running buffer. The protein A-coupled chip was prepared from a CM5 chip (GE Healthcare) by coupling 1 µM His-tagged Protein A at pH 4.5 to each flow cell to a final density of ~3000 response units (Rus). IgGs were then injected onto each flow cell at 50 nM. An irrelevant HIV-1 Ab, N6¹⁵⁹, was used as a control on a reference flow cell. To remove IgGs from the chip between runs, a solution of 10 mM glycine 50% v/v pH 1.5/ pH 2.5, 1 M guanidine hydrochloride was applied.

For interactions with measurable on- and off-rates, kinetic constants were derived from sensorgram data using global fitting of the association and dissociation phases of binding

curves in the working set using Biacore T200 Evaluation Software (GE Healthcare). The sensorgrams were fit to a binding model that assumed a single class of non-interacting binding sites in a 1:1 binding interaction. K_D values were derived as $K_D = k_d/k_a$, the ratio of the association (k_a) and dissociation (k_d) constants. For interactions with fast on- and off-rates, K_D values were derived by nonlinear regression analysis of plots of R_{eq} (the equilibrium binding response) versus the log of the injected protein concentration. Data were fit to a 1:1 binding model, and each K_D was determined as the concentration at which half-maximal binding was observed. If a saturated binding response was not achieved at the highest injected concentration of analyte, we approximated the saturated response as the highest R_{eq} achieved.

For SPR runs used to determine K_D values, the EDIIIs for ZIKV, DENV1-4, WNV, and YFV were dialyzed into HBS-EP+ running buffer using a Slide-A-Lyzer MINI Dialysis Device with 3,500 Da molecular weight cutoff (ThermoFisher) to minimize refractive index changes between the association and dissociation phases. We used concentrations of ZIKV and DENV1 EDIII ranging from 0.04 to 10 nM in a three-fold dilution series flowed over immobilized mature IgG, and concentrations of ZIKV, DENV1 and ZIKV_{AA mutant} EDIIIs ranging from 2.3 nM to 150 μ M in a four-fold dilution series flowed over immobilized iGL IgGs or Z004_{mature} IgG and the control IgG. Concentrations of DENV2, DENV3, DENV4, WNV, and YFV EDIIIs from 2.3 nM to 150 μ M in a four-fold dilution series were flowed over immobilized mature and iGL IgGs. Concentrations of ZIKV EDIII ranging from 0.036 nM to 150 μ M in a four-fold dilution series were flowed over immobilized Z004 iGL/mature chimeric IgGs in two independent experiments. Concentrations of ZIKV EDIII ranging from 0.036 nM to 37.5 μ M in a four-fold dilution series were flowed over immobilized Z004 IgG V_L site-directed mutants. The injection flow rate was 10 μ L/minute over three minutes and the dissociation time was two minutes. For repeated SPR runs for ZIKV and DENV1 EDIII flowed over mature IgGs, concentrations of EDIII from 1.4 to 1000 nM in a three-fold dilution series were injected at a flow rate was 30 μ L/minute over one minute and a

dissociation time of five minutes (SI Appendix, Figures S2.5-S2.6). K_{DS} for mature IgG binding to ZIKV EDIII and DENV1 EDIIIs were calculated as the average of two independent experiments.

Crystallization trials. For the Z004_{iGL} Fab–ZIKV EDIII complex, Fabs and EDIII were incubated at a 1:1.8 molar ratio for three days and then purified by SEC on Superdex 200 10/300 Increase column (GE Healthcare). For the Z032_{mature} Fab–WNV EDIII complex, Fabs and EDIII were incubated at a 1:1 molar ratio for three days. Crystallization trials were set up at ~5 mg/mL (Z004_{iGL} Fab–ZIKV EDIII) and ~10 mg/mL (Z032_{mature} Fab–WNV EDIII) in sitting-drop plates with a Mosquito micro-crystallization robot and stored at room temperature. Crystals were cryo-protected with 25% glycerol. Crystallization conditions corresponding to determined structures include 1% w/v tryptone, 0.001 M sodium azide, 0.05 M HEPES sodium pH 7.0, 20% w/v polyethylene glycol 3,350 (Z004_{iGL} Fab–ZIKV EDIII) and 0.2 M sodium bromide, 20% w/v polyethylene glycol 3,350 (Z032_{mature} Fab–WNV EDIII).

X-ray structure determinations. X-ray data for the Z004_{iGL} Fab–ZIKV EDIII structure were collected at the Stanford Synchrotron Radiation Lightsource (SSRL). Data for the Z032_{mature} Fab–WNV EDIII complex were collected at the Advanced Photon Source (APS), Argonne, IL, using the GM/CA 23-ID-D beamline. Z004_{iGL} Fab–ZIKV EDIII diffraction data were processed using the XDS package¹⁶⁰, and Z032_{mature} Fab–WNV EDIII complex data were processed using iMosflm¹⁶¹. Data were scaled using Pointless and Aimless^{162,163}.

Structures were solved by molecular replacement (MR) using Phaser-MR¹⁶⁴. For the Z004_{iGL} Fab–ZIKV EDIII structure, the structure was first determined at 3.3 Å using Z004_{mature} Fab–DENV1 EDIII (PDB 5VIC) as the initial search model³⁶. This gave a partial solution with two Z004_{mature} Fab–DENV1 EDIII molecules in the asymmetric unit, with one of the Fabs containing an incorrectly placed constant (C_HC_L) domain. This C_HC_L domain was removed

and MR was repeated using the initial partial solution and one Z004_{mature} C_HC_L as search models. The structure was then determined at 3.1 Å using a similar method, except the Fab with the incorrectly placed C_HC_L domain was completely removed and MR was repeated using the initial partial solution and the corresponding Z004_{mature} Fab–DENV1 EDIII from the 3.3 Å structure as a search model. For the Z032_{mature} Fab–WNV EDIII complex, Z006_{mature} V_HV_L and Z006_{mature} C_HC_L (PDB 5VIG) domains were used as the initial search models³⁶, which produced a partial solution with four V_HV_L and four C_HC_L. MR was repeated using this partial solution and WNV EDIII (PDB 1ZTX) as search models⁶⁶. This generated a partial solution with one WNV EDIII placed correctly and three placed incorrectly, so all molecules were removed except for one Fab bound to WNV EDIII. For this Fab-EDIII partial solution, Fab residues were mutated to match the Z032_{mature} sequence, and then to generate Z032_{mature} Fab, Z032_{mature} V_HV_L, and Z032_{mature} C_HC_L search models. MR was repeated using the Z032_{mature} Fab-WNV EDIII partial solution and Z032_{mature} V_HV_L and C_HC_L as search models. This gave a partial solution with two unbound Fabs and one EDIII-bound Fab correctly placed; again, incorrectly placed molecules were removed. MR was repeated with this partial solution and Z032_{mature} Fab as a search model. This gave a partial solution with four correctly placed Fabs, one EDIII-bound and three unbound. MR was repeated with this partial solution and an additional Z032_{mature} Fab as search models, resulting in the final structure with four unbound and one EDIII-bound Fab. Protein models were refined with phenix.refine using torsion angle refinement, group B factors, and non-crystallography symmetry restraints¹⁶⁵. PDB accession codes and X-ray data collection and refinement statistics are in SI Appendix, Table S2.1.

Figures were prepared and rmsds of superimposed C α atoms were calculated using Pymol¹⁶⁶. A Z004 Fab-Zika EDIII homology model was created using SWISS-MODEL¹⁶⁷. A control for the homology model was prepared by threading ZIKV EDIII onto DENV1 EDIII in the Z021 Fab–DENV1 EDIII structure (PDB 6DFJ); comparison of V_HV_L–EDIIIs from the

Z021 Fab–ZIKV EDIII homology model and the known Z021 Fab–ZIKV EDIII structure (PDB 6DFI) resulted in an rmsd of 0.28 for 239 C α atoms⁶². Fab-EDIII binding interfaces were mapped as residues within 4 Å in Pymol. BSAs (calculated using a 1.4 Å probe) and the contact residues at Fab-EDIII interfaces (calculated using a distance of <3.89 Å and an A-D-H angle >90° for H-bonds and a distance <4 Å for salt bridges) were determined with PDBePISA¹⁶⁸.

Plasmid construction. pWNV/TX02/CprME was generated by assembly PCR. Using pZIKV/HPF/CprME (obtained from Ted Pierson, see ref.³⁶) as template and oligos RU-O-24611 (5'- CTTGACCGACAATTGCATGAAG) and RU-O-24620 (5'- CCTCTGGTTTCTTAGACATAGCCTGCTTTTTTTGTACAAAC), the CMV promoter region linked to the beginning of the WNV capsid protein was amplified. The WNV CprME region with upstream overlap with the CMV promoter was amplified using Oligos RU-O-24619 (5'- GTTTGTACAAAAAAGCAGGCTATGTCTAAGAAACCAGGAGG) and RU-O-24621 (5'- TTCGAACCGCGGCTGGGTCCTATTAAGCGTGCACGTTTCACGGAGAG) and a full length WNV strain TX02 infectious clone (obtained from Ilya Frolov¹⁶⁹) as a template. The two fragments were assembled by PCR using oligos RU-O-24611 and RU-O-24621, and the product was digested with *Sna*BI and *Sac*II and cloned into similarly digested pZIKV/HPF/CprME. All PCR derived DNA regions were verified by sequencing.

RVP production. RVPs were generated as previously described³⁶ by co-transfection of two plasmids: a luciferase-expressing WNV replicon plasmid (pWNVII-Rep-REN-IB, obtained from Ted Pierson) and a C-prM-E expression plasmid encoding structural proteins of ZIKV strain HPF with the PRVABC59 E protein (pZIKV/HPF/CprM*PRVABC59E*)¹⁷⁰, DENV1 strain WP (pDENV1/WP/CprME, obtained from Ted Pierson), DENV2 strain 16681 (pDENV2/16681/CprME, obtained from Ted Pierson), or WNV strain TX02 (pWNV/TX02/CprME). Lenti-X 293T cells were seeded at 5x10⁵ cells/well in collagen-

coated 6-well plates one day before DNA transfection. One μg of pWNVII-Rep-REN-IB (WNV replicon expression construct) and 3 μg of the flavivirus CprME expression construct were co-transfected with Lipofectamine 2000 (Invitrogen). After incubation at 37°C for 4-5 hours, media (containing lipid-DNA complexes) was removed and replaced with DMEM containing 20 mM HEPES, 3% FBS. Cells were then incubated at 34°C for 48-72 hours before supernatant (containing RVPs) was harvested, filtered through a 0.22 μm filter, and frozen at -80°C.

RVP-based neutralization assays. Abs were diluted in triplicate in Medium-199 with 17% Bovine Serum Albumin, 1% P/S (BA-1 diluent) to 40 $\mu\text{g}/\text{mL}$ and then serially diluted in BA-1 diluent using five-fold dilutions. RVPs were diluted in OPTI-MEM to a concentration that results in $\sim 1 \times 10^6$ relative light units (RLU) per 25 μL (determined based on a titration of the harvested RVPs on Huh-7.5 cells). Serially diluted Abs were mixed with equal volumes of RVPs, and incubated for 1 hour at 37°C. 50 μL of RVP-Ab complex was added to Huh-7.5 cells seeded in 96-well half-area plates at 7.5×10^3 cells/well in 50 μL the day prior. After incubation at 37°C for 24 hours, media was removed, cells were lysed in 35 μL 1X Lysis Buffer, and 20 μL was used for Renilla luciferase measurement on a FLUOstar Omega luminometer (BMG LabTech) using the Renilla Luciferase Assay System (Promega). Luciferase activity, measured as RLUs, was normalized as the percentage of luciferase activity relative to activity from RVPs incubated without Ab. Experiments were repeated twice and plotted on the same graph. The N6 Ab (negative control) was assessed at 10 $\mu\text{g}/\text{mL}$ final concentration in the well. IC_{50} values (the Ab concentration that resulted in 50% inhibition) were determined by nonlinear regression fitting of the curve in GraphPad Prism.

ADE assays. Abs were diluted in triplicate in BA-1 diluent to 40 $\mu\text{g}/\text{mL}$ and then serially diluted by three-fold dilutions. RVPs were diluted in OPTI-MEM with a goal of achieving $\sim 1 \times 10^6$ Huh-7.5 cell relative light units (RLU) per 12.5 μL (determined based on a titration of the harvested RVPs on Huh-7.5 cells in the absence of Ab). For some RVPs this goal was

not attainable and lower RLU were used. Serially diluted Abs were mixed with equal volumes of RVPs, and incubated for 1 hour at 37°C. 25 μ L of RVP-Ab complex was added to K562 cells seeded the prior day in poly-L-lysine coated 96-well half-area plates at 5.0×10^3 cells/well in 25 μ L of DMEM containing 10% FBS and 1X NEAA . Every plate included a no Ab control, an N6 negative control, and Z004 wt Ab (10 ng/mL final concentration) with the ZIKVHPF/PRVABC59*E* RVP as a positive control. Each plate also included Huh-7.5 cells seeded the day prior at 7.5×10^3 c/w in 50 μ L to serve as a positive control for RVP activity. After incubation at 37°C for 24 hours, media was removed, cells were lysed in 35 μ L 1X Lysis Buffer, and 20 μ L was used for Renilla luciferase measurement on a FLUOstar Omega luminometer (BMG LabTech) using the Renilla Luciferase Assay System (Promega). Luciferase activity, measured as RLUs, was normalized to respective RVP luciferase activity determined on fully permissive Huh-7.5 cells (positive control). Experiments were repeated twice and plotted on the same graph. The HIV-1 Ab N6 (negative control) and cross-reactive Ab Z015_{mature} (WNV positive control) were assessed at the highest concentration (10 μ g/mL). Z004_{mature} Ab (positive control¹⁵⁶) was assessed at 0.01 μ g/mL, a concentration known to show ADE for ZIKV.

Data availability. Crystallographic coordinates for structures Z004_{iGL} Fab–ZIKV EDIII and Z032_{mature} Fab–WNV EDIII are available from the Protein Data Bank under accession codes 6UTA and 6UTE.

SI Appendix

V_H alignment

```

      CDR1                CDR2                CDR3
      26 33                51 57                93
IGHV3-23*01  EVQLLESGGGLVQPGGSLRLSCAASGFTFSSTYAMSVVRQAPGKGLVHVAISG-----SGGSTYYADSVKGRFTISRDNKNTLYLQMNLSRAEDTAVYCAK-----
IGHD3-10*01  -----VLLMFGE-LL-----
IGHJ4*02  -----YFDYWGQGTIVTVSS-----
MEX18_07  EVQLLESGGGLVQPGGSLRLSCAASGFTFSSTYAMSVVRQAPGKGLVHVAISGGRGAIAGDGSIIYADSVKGRFTISRDNKNTLYLQMNLSRAEDTAVYCAKDR-----VAFDGFHVWGQGTIVTVSS
MEX18_15  EVQLLESGGGLVQPGGSLRLSCAASGFTFSSTYAMSVVRQAPGKGLVHVAISGSP-----LDGSTYYAASVKGRFTISRDNKNTLYLQMNLSRAEDTAVYCAKDRITMGVGE-LFVDMWPGQTLVSVSS
MEX18_21  EVQLLESGGGLVQPGGSLRLSCAASGFTFSSTYAMSVVRQAPGKGLVHVAISG-----LDGSTYYADSVKGRFTISRDNKNTLYLQMNLSRAEDTAVYCAKDRGPRGVGE-LFDFWGQGTIVSVSS
MEX18_24  EVQLLESGGGLVQPGGSLRLSCAASGFTFSSTYAMSVVRQAPGKGLVHVAISG-----LDGSTYYADSVKGRFTISRDNKNTLYLQMNLSRAEDTAVYCAKDRGPRGVGE-LFDFWGQGTIVSVSS
MEX18_27  EVQLLESGGGLVQPGGSLRLSCAASGFTFSSTYAMSVVRQAPGKGLVHVAISG-----VDDSTYYAESVKGRFTISRDNKNTLYLQMNLSRAEDTAVYCAKDRGPRGVGE-LFDSWGQGTIVTVSS
MEX18_36  EVQLLESGGGLVQPGGSLRLSCAASGFTFSSTYAMSVVRQAPGKGLVHVAISG-----LDGSTYYADSVKGRFTISRDNKNTLYLQMNLSRAEDTAVYCAKDRITMGVGE-LFDFWGQGTIVTVSS
MEX18_38  EVQLLESGGGLVQPGGSLRLSCAASGFTFSSTYAMSVVRQAPGKGLVHVAISG-----LDGSTYYADSVKGRFTISRDNKNTLYLQMNLSRAEDTAVYCAKDRITMGVGE-LFDFWGQGTIVTVSS
MEX18_41  EVQLLESGGGLVQPGGSLRLSCAASGFTFSSTYAMSVVRQAPGKGLVHVAISG-----LDGSTYYADSVKGRFTISRDNKNTLYLQMNLSRAEDTAVYCAKDRITMGVGE-LFDFWGQGTIVTVSS
MEX18_50  EVQLLESGGGLVQPGGSLRLSCAASGFTFSSTYAMSVVRQAPGKGLVHVAISG-----LDGSTYYADSVKGRFTISRDNKNTLYLQMNLSRAEDTAVYCAKDRITMGVGE-LFDFWGQGTIVTVSS
MEX18_54  EVQLLESGGGLVQPGGSLRLSCAASGFTFSSTYAMSVVRQAPGKGLVHVAISG-----LDGSTYYADSVKGRFTISRDNKNTLYLQMNLSRAEDTAVYCAKDRITMGVGE-LFDFWGQGTIVTVSS
MEX18_58  EVQLLESGGGLVQPGGSLRLSCAASGFTFSSTYAMSVVRQAPGKGLVHVAISG-----LDGSTYYADSVKGRFTISRDNKNTLYLQMNLSRAEDTAVYCAKDRITMGVGE-LFDFWGQGTIVTVSS
MEX18_65  EVQLLESGGGLVQPGGSLRLSCAASGFTFSSTYAMSVVRQAPGKGLVHVAISG-----LDGSTYYADSVKGRFTISRDNKNTLYLQMNLSRAEDTAVYCAKDRITMGVGE-LFDFWGQGTIVTVSS
MEX18_79  EVQLLESGGGLVQPGGSLRLSCAASGFTFSSTYAMSVVRQAPGKGLVHVAISG-----LDGSTYYADSVKGRFTISRDNKNTLYLQMNLSRAEDTAVYCAKDRITMGVGE-LFDFWGQGTIVTVSS
MEX18_80  EVQLLESGGGLVQPGGSLRLSCAASGFTFSSTYAMSVVRQAPGKGLVHVAISG-----LDGSTYYADSVKGRFTISRDNKNTLYLQMNLSRAEDTAVYCAKDRITMGVGE-LFDFWGQGTIVTVSS
MEX18_83  EVQLLESGGGLVQPGGSLRLSCAASGFTFSSTYAMSVVRQAPGKGLVHVAISG-----LDGSTYYADSVKGRFTISRDNKNTLYLQMNLSRAEDTAVYCAKDRITMGVGE-LFDFWGQGTIVTVSS
MEX18_84  EVQLLESGGGLVQPGGSLRLSCAASGFTFSSTYAMSVVRQAPGKGLVHVAISG-----LDGSTYYADSVKGRFTISRDNKNTLYLQMNLSRAEDTAVYCAKDRITMGVGE-LFDFWGQGTIVTVSS
MEX18_86  EVQLLESGGGLVQPGGSLRLSCAASGFTFSSTYAMSVVRQAPGKGLVHVAISG-----LDGSTYYADSVKGRFTISRDNKNTLYLQMNLSRAEDTAVYCAKDRITMGVGE-LFDFWGQGTIVTVSS
MEX18_89: Z004  EVQLLESGGGLVQPGGSLRLSCAASGFTFSSTYAMSVVRQAPGKGLVHVAISG-----LDGSTYYADSVKGRFTISRDNKNTLYLQMNLSRAEDTAVYCAKDRITMGVGE-LFDFWGQGTIVTVSS
MEX18_93  EVQLLESGGGLVQPGGSLRLSCAASGFTFSSTYAMSVVRQAPGKGLVHVAISG-----LDGSTYYADSVKGRFTISRDNKNTLYLQMNLSRAEDTAVYCAKDRITMGVGE-LFDFWGQGTIVTVSS
MEX18_94  EVQLLESGGGLVQPGGSLRLSCAASGFTFSSTYAMSVVRQAPGKGLVHVAISG-----LDGSTYYADSVKGRFTISRDNKNTLYLQMNLSRAEDTAVYCAKDRITMGVGE-LFDFWGQGTIVTVSS
MEX18_IGL  EVQLLESGGGLVQPGGSLRLSCAASGFTFSSTYAMSVVRQAPGKGLVHVAISG-----SGGSTYYADSVKGRFTISRDNKNTLYLQMNLSRAEDTAVYCAKDRGPRGVGE-LFDFWGQGTIVTVSS

```

V_L alignment

```

      CDR1                CDR2                CDR3
      27 32                50                89
IGKV1-5*03  DIQMTQSPSTLSASVGDRTVITCRASQSISSWLANVYQQKPKGKAPKLLIYKASLSLEGVPSRFSGSGSGTEFTLTISLQPDFDFTATYCCQQYNSYS-----
IGKJ1*01  -----NIFGQGTKEIK-----
MEX18_07  DIQMTQSPSTLSASVGDRTVITCRASQSISSWLANVYQQKPKGKAPKLLIYKASLSLEGVPSRFSGSGSGTEFTLTISLQPDFDFTATYCCQQYNSYPIPTFGQGTKEIK
MEX18_15  DIQMTQSPSTLSASVGDRTVITCRASQSISSWLANVYQQKPKGKAPKLLIYQASTLQNGVPSRFSGSGSGTEFTLTISLQPDFDFTATYCCQHYSYPIPTFGQGTKEIK
MEX18_21  DIQMTQSPSTLSASVGDRTVITCRASQSISSWLANVYQQKPKGKAPKLLIYKASTLKGVPVSRFSGSGSGTEFTLTISLQPDFDFTATYCCQHFYSVPPIPTFGQGTKEIK
MEX18_24  DIQMTQSPSTLSASVGDRTVITCRASQSISSWLANVYQQKPKGKAPKLLIYKASTLKGVPVSRFSGSGSGTEFTLTISLQPDFDFTATYCCQHYSYPIPTFGQGTKEIK
MEX18_27  DIQMTQSPSTLSASVGDRTVITCRASQSISSWLANVYQQKPKGKAPKLLIYKASTLKGVPVSRFSGSGSGTEFTLTISLQPDFDFTATYCCQHFYSVPPIPTFGQGTKEIK
MEX18_36  DIQMTQSPSTLSASVGDRTVITCRASQSISSWLANVYQQKPKGKAPKLLIYKASTLKGVPVSRFSGSGSGTEFTLTISLQPDFDFTATYCCQHYSYPIPTFGQGTKEIK
MEX18_38  DIQMTQSPSTLSAIGDRTVITCRASQSISSWLANVYQQKPKGKAPKLLIYKASTLKGVPVSRFSGSGSGTEFTLTISLQPDFDFTATYCCQHYSYPIPTFGQGTKEIK
MEX18_41  DIQMTQSPSTLSASVGDRTVITCRASQSISSWLANVYQQKPKGKAPKLLIYKASTLKGVPVSRFSGSGSGTEFTLTISLQPDFDFTATYCCQHYSYPIPTFGQGTKEIK
MEX18_50  DIQMTQSPSTLSASVGDRTVITCRASQSISSWLANVYQQKPKGKAPKLLIYKASTLKGVPVSRFSGSGSGTEFTLTISLQPDFDFTATYCCQHYSYPIPTFGQGTKEIK
MEX18_54  DIQMTQSPSTLSASVGDRTVITCRASQSISSWLANVYQQKPKGKAPKLLIYKASTLKGVPVSRFSGSGSGTEFTLTISLQPDFDFTATYCCQHYSYPIPTFGQGTKEIK
MEX18_58  DIQMTQSPSTLSASVGDRTVITCRASQSISSWLANVYQQKPKGKAPKLLIYKASTLKGVPVSRFSGSGSGTEFTLTISLQPDFDFTATYCCQHYSYPIPTFGQGTKEIK
MEX18_65  DIQMTQSPSTLSAIGDRTVITCRASQSISSWLANVYQQKPKGKAPKLLIYKASTLKGVPVSRFSGSGSGTEFTLTISLQPDFDFTATYCCQHYSYPIPTFGQGTKEIK
MEX18_79  DIQMTQSPSTLSASVGDRTVITCRASQSISSWLANVYQQKPKGKAPKLLIYKASTLKGVPVSRFSGSGSGTEFTLTISLQPDFDFTATYCCQHYSYPIPTFGQGTKEIK
MEX18_80  DIQMTQSPSTLSASVGDRTVITCRASQSISSWLANVYQQKPKGKAPKLLIYKASTLKGVPVSRFSGSGSGTEFTLTISLQPDFDFTATYCCQHYSYPIPTFGQGTKEIK
MEX18_83  DIQMTQSPSTLSASVGDRTVITCRASQSISSWLANVYQQKPKGKAPKLLIYKASTLKGVPVSRFSGSGSGTEFTLTISLQPDFDFTATYCCQHYSYPIPTFGQGTKEIK
MEX18_84  DIQMTQSPSTLSASVGDRTVITCRASQSISSWLANVYQQKPKGKAPKLLIYKASTLKGVPVSRFSGSGSGTEFTLTISLQPDFDFTATYCCQHYSYPIPTFGQGTKEIK
MEX18_86  DIQMTQSPSTLSASVGDRTVITCRASQSISSWLANVYQQKPKGKAPKLLIYKASTLKGVPVSRFSGSGSGTEFTLTISLQPDFDFTATYCCQHYSYPIPTFGQGTKEIK
MEX18_89: Z004  DIQMTQSPSTLSASVGDRTVITCRASQSISSWLANVYQQKPKGKAPKLLIYKASTLKGVPVSRFSGSGSGTEFTLTISLQPDFDFTATYCCQHYSYPIPTFGQGTKEIK
MEX18_93  DIQMTQSPSTLSASVGDRTVITCRASQSISSWLANVYQQKPKGKAPKLLIYKASTLKGVPVSRFSGSGSGTEFTLTISLQPDFDFTATYCCQHYSYPIPTFGQGTKEIK
MEX18_94  DIQMTQSPSTLSASVGDRTVITCRASQSISSWLANVYQQKPKGKAPKLLIYKASTLKGVPVSRFSGSGSGTEFTLTISLQPDFDFTATYCCQHYSYPIPTFGQGTKEIK
MEX18_IGL  DIQMTQSPSTLSASVGDRTVITCRASQSISSWLANVYQQKPKGKAPKLLIYKASLSLEGVPSRFSGSGSGTEFTLTISLQPDFDFTATYCCQQYNSYPIPTFGQGTKEIK

```

Figure S2.1. Alignments of V_H and V_L sequences of all 20 mature VH3-23/VK1-5 class Abs isolated from donor MEX 18.

Protein sequences are shown with their iGL (highlighted)³⁶. The most common germline gene assignments (top lines) determined by IgBLAST for this set of Abs are shown³⁶. For V_H, this includes the *IGHV3-23*01* V gene segment, the *IGHD3-10*01* D gene segment, and the *IGHJ4*02* J gene segment. The D gene segment is shown as one possible reading frame. For V_L, this includes the *IGKV1-5*03* V gene segment, and the *IGKJ1*01* J gene segment. The mature Ab Z004 used for binding studies corresponds to the sequence MEX18_89. The Kabat numbering scheme was used.

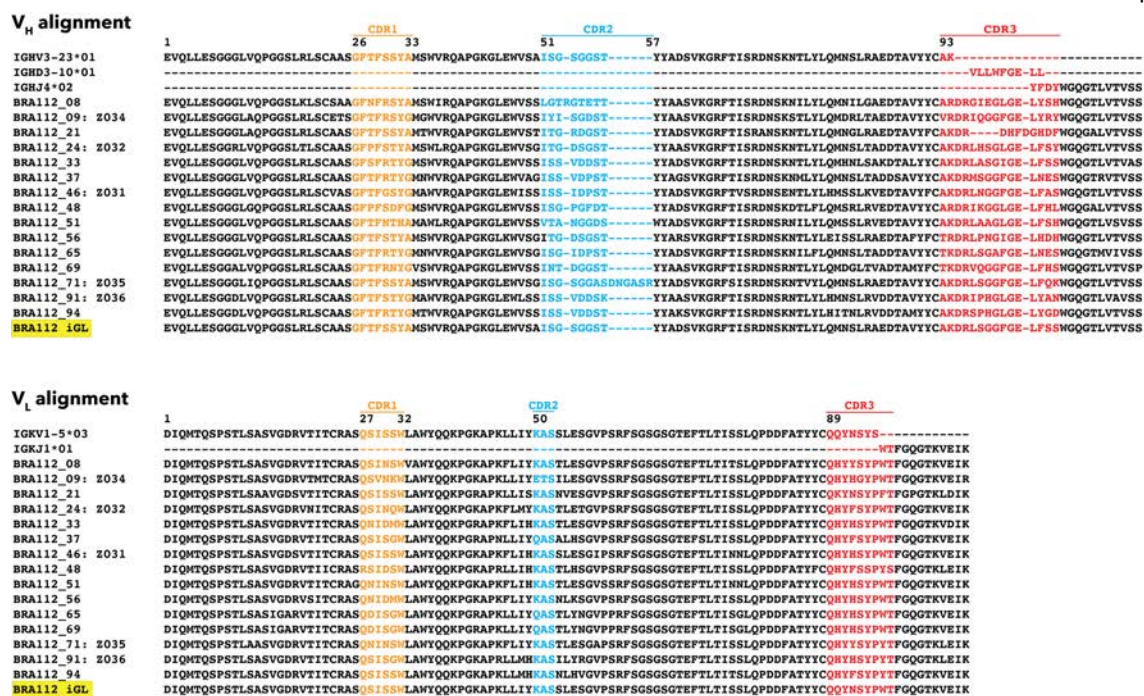


Figure S2.2. Alignments of V_H and V_L sequences of all 15 mature V_H3-23/V_K1-5 class Abs isolated from donor BRA 112.

Protein sequences are shown with their iGL (highlighted)³⁶. The most common germline gene assignments (top lines) determined by IgBLAST for this set of Abs are shown³⁶. For V_H, this includes the *IGHV3-23*01* V gene, the *IGHD3-10*01* D gene, and the *IGHJ4*02* J gene. The D gene segment is shown as one possible reading frame. For V_L, this includes the *IGKV1-5*03* V gene and *IGKJ1*01* J gene. The Z03X mature Abs (Z034, Z032, Z031, Z035, and Z036) used for binding studies correspond to the sequences BRA112_09, BRA112_24, BRA112_46, BRA112_71, and BRA112_91 respectively. The Kabat numbering scheme was used.

V_H alignment

```

1          CDR1          CDR2          CDR3
26 33          51 57          93
IGHV3-23*03  EVQLLESGGGLVPGGSLRLSCAASQFTFRRYAMAVVRQAPGKGLVSVLYGGDSTYAASVKGRFTISRDNKNTLYLQNSLRAEDTAVTTCAK-----GISGGWY-----YFDWGGQGLVTVSS
IGHB6-19*01  EVQLLESGGGLVPGGSLRLSCKASQFTFRRYAMAVVRQAPGKGLVSVLYGGDSTYAASVKGRFTISRDNKNTLYLQNSLRAEDTAVTTCAK-----GISGGWY-----YFDWGGQGLVTVSS
IGHJ4*02     EVQLLESGGGLVPGGSLRLSCKASQFTFRRYAMAVVRQAPGKGLVSVLYGGDSTYAASVKGRFTISRDNKNTLYLQNSLRAEDTAVTTCAK-----DTGMSIVDWGGQGLVTVSS
MEX105_01   EVQLLESGGGLVPGGSLRLSCKASQFTFRRYAMAVVRQAPGKGLVSVLYGGDSTYAASVKGRFTISRDNKNTLYLQNSLRAEDTAVTTCAK-----DTGMSIVDWGGQGLVTVSS
MEX105_02   EVQLLESGGGLVPGGSLRLSCKASQFTFRRYAMAVVRQAPGKGLVSVLYGGDSTYAASVKGRFTISRDNKNTLYLQNSLRAEDTAVTTCAK-----DTGMSIVDWGGQGLVTVSS
MEX105_04   EVQLLESGGGLVPGGSLRLSCKASQFTFRRYAMAVVRQAPGKGLVSVLYGGDSTYAASVKGRFTISRDNKNTLYLQNSLRAEDTAVTTCAK-----DTGMSIVDWGGQGLVTVSS
MEX105_05   EVQLLESGGGLVPGGSLRLSCKASQFTFRRYAMAVVRQAPGKGLVSVLYGGDSTYAASVKGRFTISRDNKNTLYLQNSLRAEDTAVTTCAK-----DTGMSIVDWGGQGLVTVSS
MEX105_09   EVQLLESGGGLVPGGSLRLSCKASQFTFRRYAMAVVRQAPGKGLVSVLYGGDSTYAASVKGRFTISRDNKNTLYLQNSLRAEDTAVTTCAK-----DTGMSIVDWGGQGLVTVSS
MEX105_11   EVQLLESGGGLVPGGSLRLSCKASQFTFRRYAMAVVRQAPGKGLVSVLYGGDSTYAASVKGRFTISRDNKNTLYLQNSLRAEDTAVTTCAK-----DTGMSIVDWGGQGLVTVSS
MEX105_14   EVQLLESGGGLVPGGSLRLSCKASSLSTGRYDMMVTRQAPGKGLVSVLYGGDSTYAASVKGRFTISRDNKNTLYLQNSLRAEDTAVTTCAK-----LHFDPPHMGGQGLVTVSS
MEX105_15   EVQLLESGGGLVPGGSLRLSCKASQFTFRRYAMAVVRQAPGKGLVSVLYGGDSTYAASVKGRFTISRDNKNTLYLQNSLRAEDTAVTTCAK-----DTGMSIVDWGGQGLVTVSS
MEX105_23   EVQLLESGGGLVPGGSLRLSCKASQFTFRRYAMAVVRQAPGKGLVSVLYGGDSTYAASVKGRFTISRDNKNTLYLQNSLRAEDTAVTTCAK-----DTGMSIVDWGGQGLVTVSS
MEX105_25   EVQLLESGGGLVPGGSLRLSCKASQFTFRRYAMAVVRQAPGKGLVSVLYGGDSTYAASVKGRFTISRDNKNTLYLQNSLRAEDTAVTTCAK-----DTGMSIVDWGGQGLVTVSS
MEX105_27   EVQLLESGGGLVPGGSLRLSCKASQFTFRRYAMAVVRQAPGKGLVSVLYGGDSTYAASVKGRFTISRDNKNTLYLQNSLRAEDTAVTTCAK-----DTGMSIVDWGGQGLVTVSS
MEX105_28   EVQLLESGGGLVPGGSLRLSCKASQFTFRRYAMAVVRQAPGKGLVSVLYGGDSTYAASVKGRFTISRDNKNTLYLQNSLRAEDTAVTTCAK-----DTGMSIVDWGGQGLVTVSS
MEX105_33   EVQLLESGGGLVPGGSLRLSCKASQFTFRRYAMAVVRQAPGKGLVSVLYGGDSTYAASVKGRFTISRDNKNTLYLQNSLRAEDTAVTTCAK-----DTGMSIVDWGGQGLVTVSS
MEX105_37   EVQLLESGGGLVPGGSLRLSCKASQFTFRRYAMAVVRQAPGKGLVSVLYGGDSTYAASVKGRFTISRDNKNTLYLQNSLRAEDTAVTTCAK-----DTGMSIVDWGGQGLVTVSS
MEX105_39   EVQLLESGGGLVPGGSLRLSCKASQFTFRRYAMAVVRQAPGKGLVSVLYGGDSTYAASVKGRFTISRDNKNTLYLQNSLRAEDTAVTTCAK-----DTGMSIVDWGGQGLVTVSS
MEX105_42: 2006 EVQLLESGGGLVPGGSLRLSCKASQFTFRRYAMAVVRQAPGKGLVSVLYGGDSTYAASVKGRFTISRDNKNTLYLQNSLRAEDTAVTTCAK-----SNQMSIINLMGRGLVTVSS
MEX105_45   EVQLLESGGGLVPGGSLRLSCKASQFTFRRYAMAVVRQAPGKGLVSVLYGGDSTYAASVKGRFTISRDNKNTLYLQNSLRAEDTAVTTCAK-----DTGMSIVDWGGQGLVTVSS
MEX105_48   EVQLLESGGGLVPGGSLRLSCKASQFTFRRYAMAVVRQAPGKGLVSVLYGGDSTYAASVKGRFTISRDNKNTLYLQNSLRAEDTAVTTCAK-----DTGMSIVDWGGQGLVTVSS
MEX105_50   EVQLLESGGGLVPGGSLRLSCKASQFTFRRYAMAVVRQAPGKGLVSVLYGGDSTYAASVKGRFTISRDNKNTLYLQNSLRAEDTAVTTCAK-----DTGMSIVDWGGQGLVTVSS
MEX105_51   EVQLLESGGGLVPGGSLRLSCKASQFTFRRYAMAVVRQAPGKGLVSVLYGGDSTYAASVKGRFTISRDNKNTLYLQNSLRAEDTAVTTCAK-----DTGMSIVDWGGQGLVTVSS
MEX105_54   EVQLLESGGGLVPGGSLRLSCKASQFTFRRYAMAVVRQAPGKGLVSVLYGGDSTYAASVKGRFTISRDNKNTLYLQNSLRAEDTAVTTCAK-----DTGMSIVDWGGQGLVTVSS
MEX105_60   EVQLLESGGGLVPGGSLRLSCKASQFTFRRYAMAVVRQAPGKGLVSVLYGGDSTYAASVKGRFTISRDNKNTLYLQNSLRAEDTAVTTCAK-----DTGMSIVDWGGQGLVTVSS
MEX105_64   EVQLLESGGGLVPGGSLRLSCKASQFTFRRYAMAVVRQAPGKGLVSVLYGGDSTYAASVKGRFTISRDNKNTLYLQNSLRAEDTAVTTCAK-----DTGMSIVDWGGQGLVTVSS
MEX105_66   EVQLLESGGGLVPGGSLRLSCKASQFTFRRYAMAVVRQAPGKGLVSVLYGGDSTYAASVKGRFTISRDNKNTLYLQNSLRAEDTAVTTCAK-----DTGMSIVDWGGQGLVTVSS
MEX105_78   EVQLLESGGGLVPGGSLRLSCKASQFTFRRYAMAVVRQAPGKGLVSVLYGGDSTYAASVKGRFTISRDNKNTLYLQNSLRAEDTAVTTCAK-----DTGMSIVDWGGQGLVTVSS
MEX105_87   EVQLLESGGGLVPGGSLRLSCKASQFTFRRYAMAVVRQAPGKGLVSVLYGGDSTYAASVKGRFTISRDNKNTLYLQNSLRAEDTAVTTCAK-----DTGMSIVDWGGQGLVTVSS
MEX105_88   EVQLLESGGGLVPGGSLRLSCKASQFTFRRYAMAVVRQAPGKGLVSVLYGGDSTYAASVKGRFTISRDNKNTLYLQNSLRAEDTAVTTCAK-----DTGMSIVDWGGQGLVTVSS

```

V_L alignment

```

1          CDR1          CDR2          CDR3
27 32          50          89
IGKV1-5*03  DIQMTQSPFSTLSASVGDRTVITCRASQIISISLANYTQKPGKAPKLLIYQASLSLEGVPSRFSGSGSGTEFTLTISLQPEDDPAITFCQQYSTYYS-----
IGKJ1*01    DIQMTQSPFSTLSASVGDRTVITCRASQIISISLANYTQKPGKAPKLLIYQASLSLEGVPSRFSGSGSGTEFTLTISLQPEDDPAITFCQQYSTYYS-----WFGQGTKEIK
MEX105_1   DIQMTQSPFSTLSASVGDRTVITCRASQIISISLANYTQKPGKAPKLLIYQASLSLEGVPSRFSGSGSGTEFTLTISLQPEDDPAITFCQQYSTYYS-----WFGQGTKEIK
MEX105_2   DIQMTQSPFSTLSASVGDRTVITCRASQIISISLANYTQKPGKAPKLLIYQASLSLEGVPSRFSGSGSGTEFTLTISLQPEDDPAITFCQQYSTYYS-----WFGQGTKEIK
MEX105_4   DIQMTQSPFSTLSASVGDRTVITCRASQIISISLANYTQKPGKAPKLLIYQASLSLEGVPSRFSGSGSGTEFTLTISLQPEDDPAITFCQQYSTYYS-----WFGQGTKEIK
MEX105_5   DIQMTQSPFSTLSASVGDRTVITCRASQIISISLANYTQKPGKAPKLLIYQASLSLEGVPSRFSGSGSGTEFTLTISLQPEDDPAITFCQQYSTYYS-----WFGQGTKEIK
MEX105_9   DIQMTQSPFSTLSASVGDRTVITCRASQIISISLANYTQKPGKAPKLLIYQASLSLEGVPSRFSGSGSGTEFTLTISLQPEDDPAITFCQQYSTYYS-----WFGQGTKEIK
MEX105_11  DIQMTQSPFSTLSASVGDRTVITCRASQIISISLANYTQKPGKAPKLLIYQASLSLEGVPSRFSGSGSGTEFTLTISLQPEDDPAITFCQQYSTYYS-----WFGQGTKEIK
MEX105_14  DIQMTQSPFSTLSASVGDRTVITCRASQIISISLANYTQKPGKAPKLLIYQASLSLEGVPSRFSGSGSGTEFTLTISLQPEDDPAITFCQQYSTYYS-----WFGQGTKEIK
MEX105_15  DIQMTQSPFSTLSASVGDRTVITCRASQIISISLANYTQKPGKAPKLLIYQASLSLEGVPSRFSGSGSGTEFTLTISLQPEDDPAITFCQQYSTYYS-----WFGQGTKEIK
MEX105_23  DIQMTQSPFSTLSASVGDRTVITCRASQIISISLANYTQKPGKAPKLLIYQASLSLEGVPSRFSGSGSGTEFTLTISLQPEDDPAITFCQQYSTYYS-----WFGQGTKEIK
MEX105_25  DIQMTQSPFSTLSASVGDRTVITCRASQIISISLANYTQKPGKAPKLLIYQASLSLEGVPSRFSGSGSGTEFTLTISLQPEDDPAITFCQQYSTYYS-----WFGQGTKEIK
MEX105_27  DIQMTQSPFSTLSASVGDRTVITCRASQIISISLANYTQKPGKAPKLLIYQASLSLEGVPSRFSGSGSGTEFTLTISLQPEDDPAITFCQQYSTYYS-----WFGQGTKEIK
MEX105_28  DIQMTQSPFSTLSASVGDRTVITCRASQIISISLANYTQKPGKAPKLLIYQASLSLEGVPSRFSGSGSGTEFTLTISLQPEDDPAITFCQQYSTYYS-----WFGQGTKEIK
MEX105_33  DIQMTQSPFSTLSASVGDRTVITCRASQIISISLANYTQKPGKAPKLLIYQASLSLEGVPSRFSGSGSGTEFTLTISLQPEDDPAITFCQQYSTYYS-----WFGQGTKEIK
MEX105_37  DIQMTQSPFSTLSASVGDRTVITCRASQIISISLANYTQKPGKAPKLLIYQASLSLEGVPSRFSGSGSGTEFTLTISLQPEDDPAITFCQQYSTYYS-----WFGQGTKEIK
MEX105_39  DIQMTQSPFSTLSASVGDRTVITCRASQIISISLANYTQKPGKAPKLLIYQASLSLEGVPSRFSGSGSGTEFTLTISLQPEDDPAITFCQQYSTYYS-----WFGQGTKEIK
MEX105_42: 2006 DIQMTQSPFSTLSASVGDRTVITCRASQIISISLANYTQKPGKAPKLLIYQASLSLEGVPSRFSGSGSGTEFTLTISLQPEDDPAITFCQQYSTYYS-----WFGQGTKEIK
MEX105_45  DIQMTQSPFSTLSASVGDRTVITCRASQIISISLANYTQKPGKAPKLLIYQASLSLEGVPSRFSGSGSGTEFTLTISLQPEDDPAITFCQQYSTYYS-----WFGQGTKEIK
MEX105_48  DIQMTQSPFSTLSASVGDRTVITCRASQIISISLANYTQKPGKAPKLLIYQASLSLEGVPSRFSGSGSGTEFTLTISLQPEDDPAITFCQQYSTYYS-----WFGQGTKEIK
MEX105_50  DIQMTQSPFSTLSASVGDRTVITCRASQIISISLANYTQKPGKAPKLLIYQASLSLEGVPSRFSGSGSGTEFTLTISLQPEDDPAITFCQQYSTYYS-----WFGQGTKEIK
MEX105_51  DIQMTQSPFSTLSASVGDRTVITCRASQIISISLANYTQKPGKAPKLLIYQASLSLEGVPSRFSGSGSGTEFTLTISLQPEDDPAITFCQQYSTYYS-----WFGQGTKEIK
MEX105_54  DIQMTQSPFSTLSASVGDRTVITCRASQIISISLANYTQKPGKAPKLLIYQASLSLEGVPSRFSGSGSGTEFTLTISLQPEDDPAITFCQQYSTYYS-----WFGQGTKEIK
MEX105_60  DIQMTQSPFSTLSASVGDRTVITCRASQIISISLANYTQKPGKAPKLLIYQASLSLEGVPSRFSGSGSGTEFTLTISLQPEDDPAITFCQQYSTYYS-----WFGQGTKEIK
MEX105_64  DIQMTQSPFSTLSASVGDRTVITCRASQIISISLANYTQKPGKAPKLLIYQASLSLEGVPSRFSGSGSGTEFTLTISLQPEDDPAITFCQQYSTYYS-----WFGQGTKEIK
MEX105_66  DIQMTQSPFSTLSASVGDRTVITCRASQIISISLANYTQKPGKAPKLLIYQASLSLEGVPSRFSGSGSGTEFTLTISLQPEDDPAITFCQQYSTYYS-----WFGQGTKEIK
MEX105_78  DIQMTQSPFSTLSASVGDRTVITCRASQIISISLANYTQKPGKAPKLLIYQASLSLEGVPSRFSGSGSGTEFTLTISLQPEDDPAITFCQQYSTYYS-----WFGQGTKEIK
MEX105_87  DIQMTQSPFSTLSASVGDRTVITCRASQIISISLANYTQKPGKAPKLLIYQASLSLEGVPSRFSGSGSGTEFTLTISLQPEDDPAITFCQQYSTYYS-----WFGQGTKEIK
MEX105_88  DIQMTQSPFSTLSASVGDRTVITCRASQIISISLANYTQKPGKAPKLLIYQASLSLEGVPSRFSGSGSGTEFTLTISLQPEDDPAITFCQQYSTYYS-----WFGQGTKEIK

```

Figure S2.3. Alignments of V_H and V_L sequences of all 27 mature VH3-23/VK1-5 class Abs isolated from donor MEX 105.

Protein sequences are shown with CDRs highlighted³⁶. The mature Ab Z006 used for binding studies corresponds to the sequence MEX105_42. The most common germline gene assignments (top lines) determined by IgBLAST for this set of Abs are shown³⁶. For V_H, this includes the *IGHV3-23*03* V gene segment, the *IGHD6-19*01* D gene segment, and the *IGHJ4*02* J gene segment. The D gene segment is shown as one possible reading frame. For V_L, this includes the *IGKV1-5*03* V gene segment and the *IGKJ1*01* J gene segment. The Kabat numbering scheme was used.

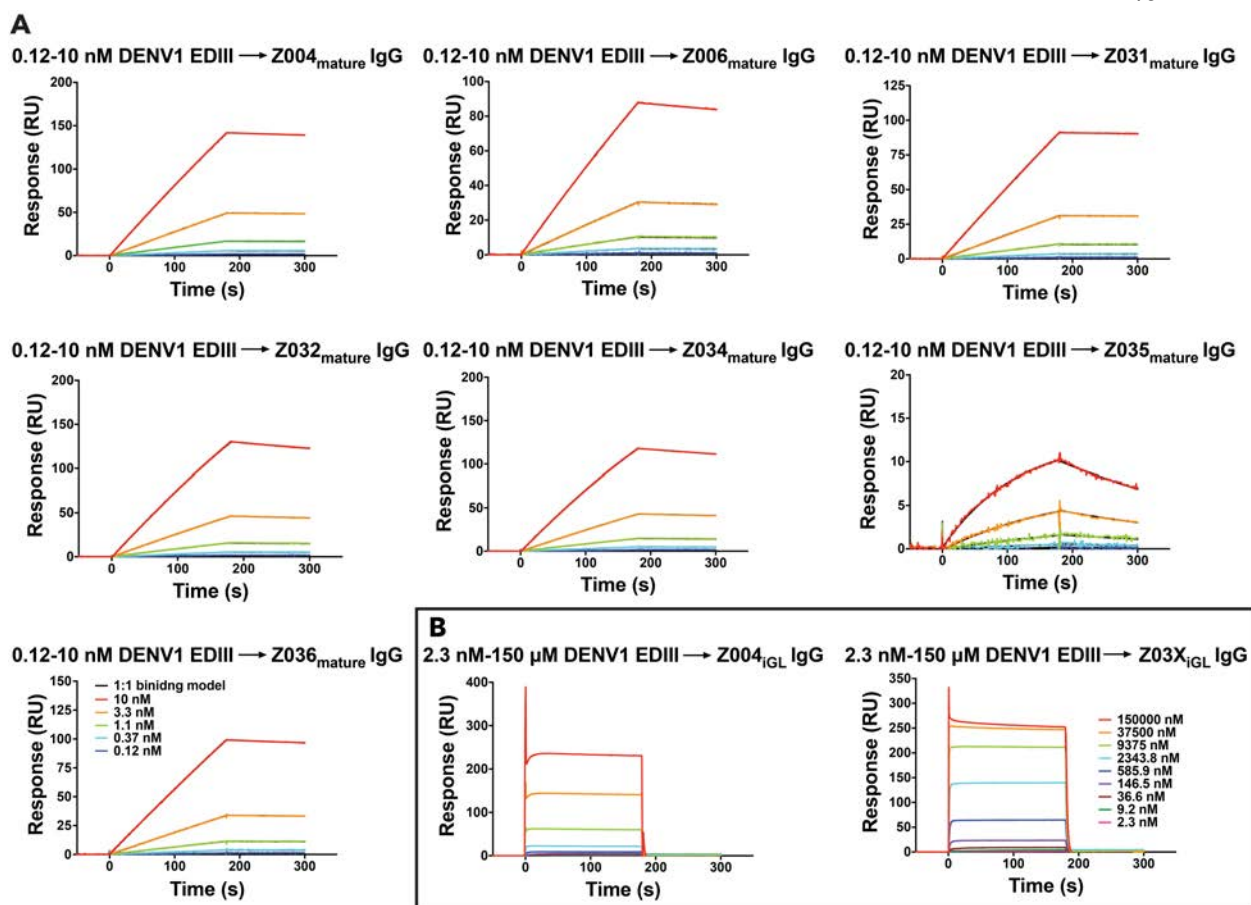


Figure S2.4. SPR binding assays with DENV1 EDIII.

IgGs were captured on a protein A biosensor chip, and the indicated concentrations of DENV1 EDIII were injected. Sensorgrams are indicated in colors representing different injected concentrations. **A.** Mature IgGs binding to DENV1 EDIII. Fits to a 1:1 binding model are in black; since the models very closely fit the data, the models are only slightly visible. Residual plots for the 1:1 binding model fitting are shown in SI Appendix, Figure S2.7A. Two independent experiments were performed; the other set of sensorgrams is shown in Si Appendix, Figure S2.6. **B.** iGL IgGs binding to DENV1 EDIII. Fitting curves for equilibrium binding responses are shown in Figure 2.3. Y-axes show response units (RU).

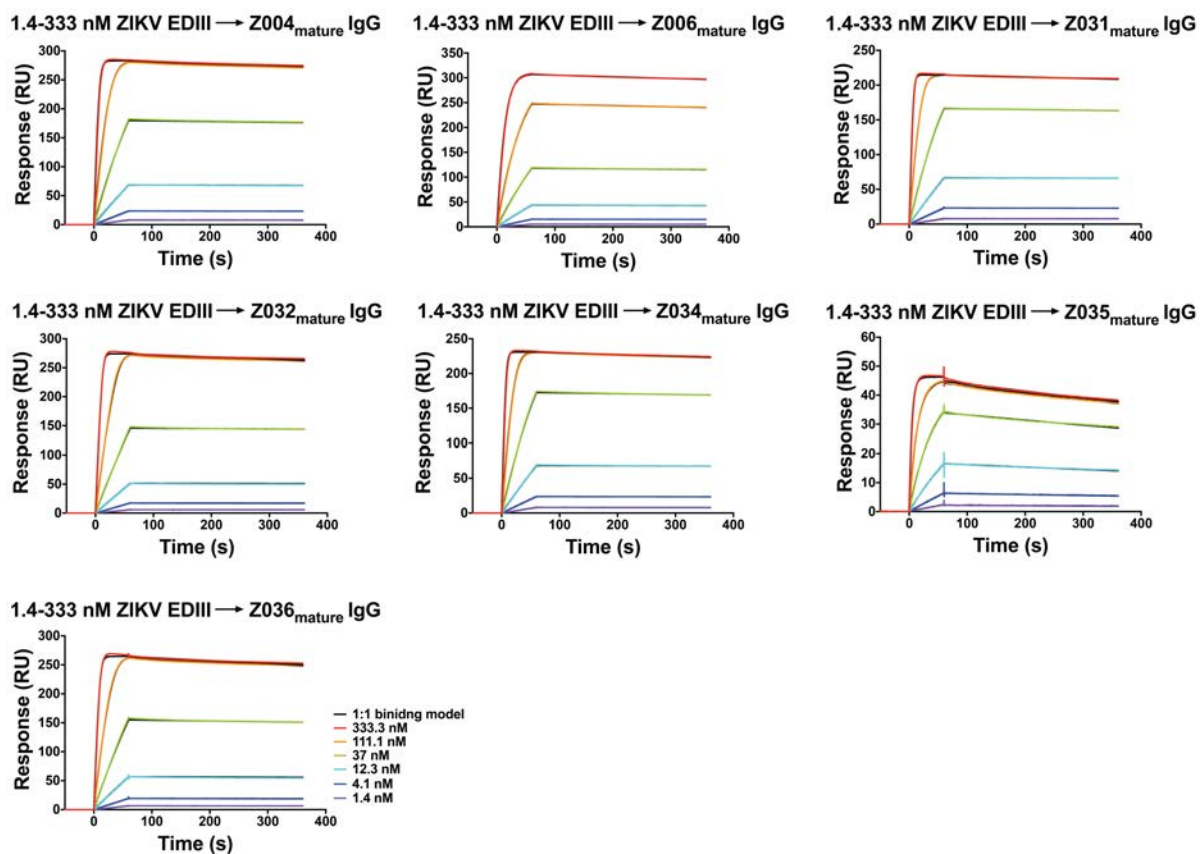


Figure S2.5. SPR binding assays with ZIKV EDIII.

IgGs were captured on a protein A biosensor chip, and the indicated concentrations of ZIKV EDIII were injected. Sensorgrams are indicated in colors representing different injected concentrations. Mature IgGs binding to ZIKV EDIII. Fits to a 1:1 binding model are in black; since the models very closely fit the data, the models are only slightly visible. Residual plots for the 1:1 binding model fitting are shown in SI Appendix, Figure S2.7B. Y-axes show response units (RU). Two independent experiments were performed; the other set of sensorgrams is shown in Figure 2.2A.

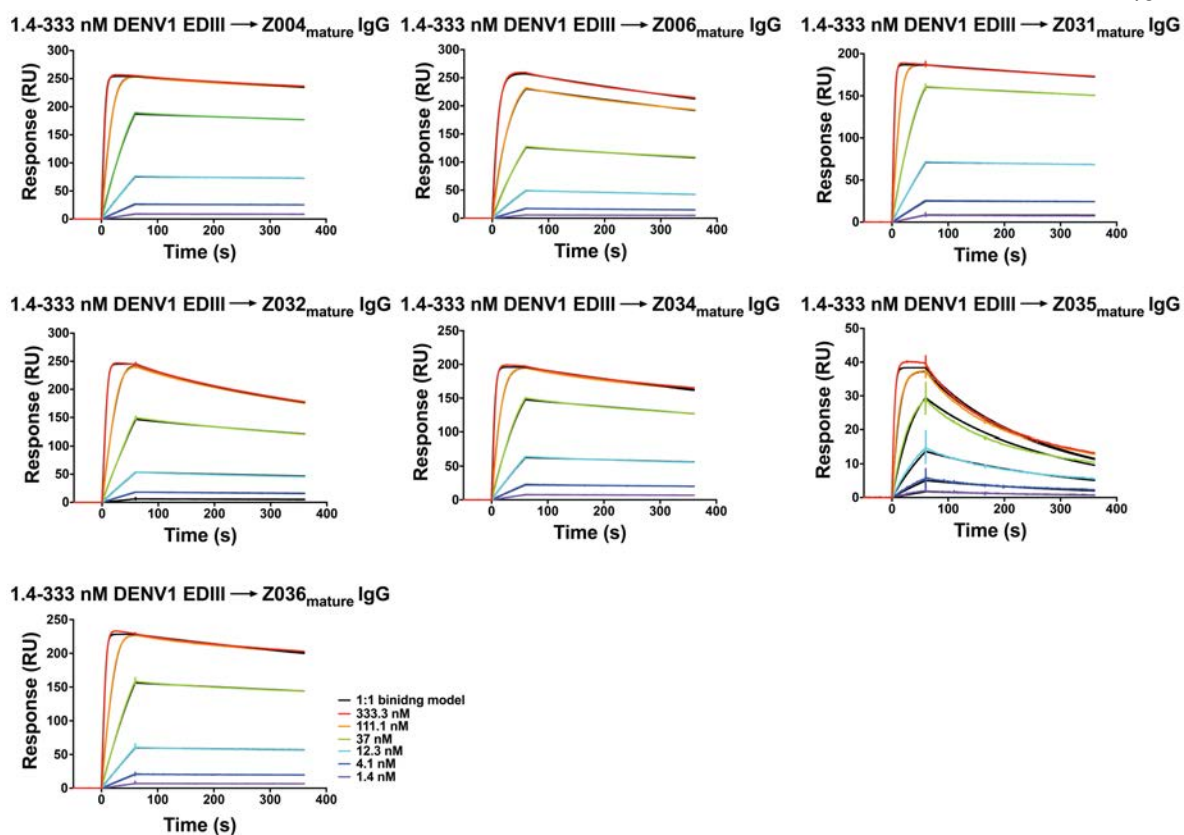


Figure S2.6. SPR binding assays with DENV1 EDIII.

IgGs were captured on a protein A biosensor chip, and the indicated concentrations of DENV1 EDIII were injected. Sensorgrams are indicated in colors representing different injected concentrations. Mature IgGs binding to DENV1 EDIII. Fits to a 1:1 binding model are in black; since the models very closely fit the data, the models are only slightly visible. Residual plots for the 1:1 binding model fitting are shown in SI Appendix, Figure S2.7B. Y-axes show response units (RU). Two independent experiments were performed; the other set of sensorgrams is shown in SI Appendix, Figure S2.4A.

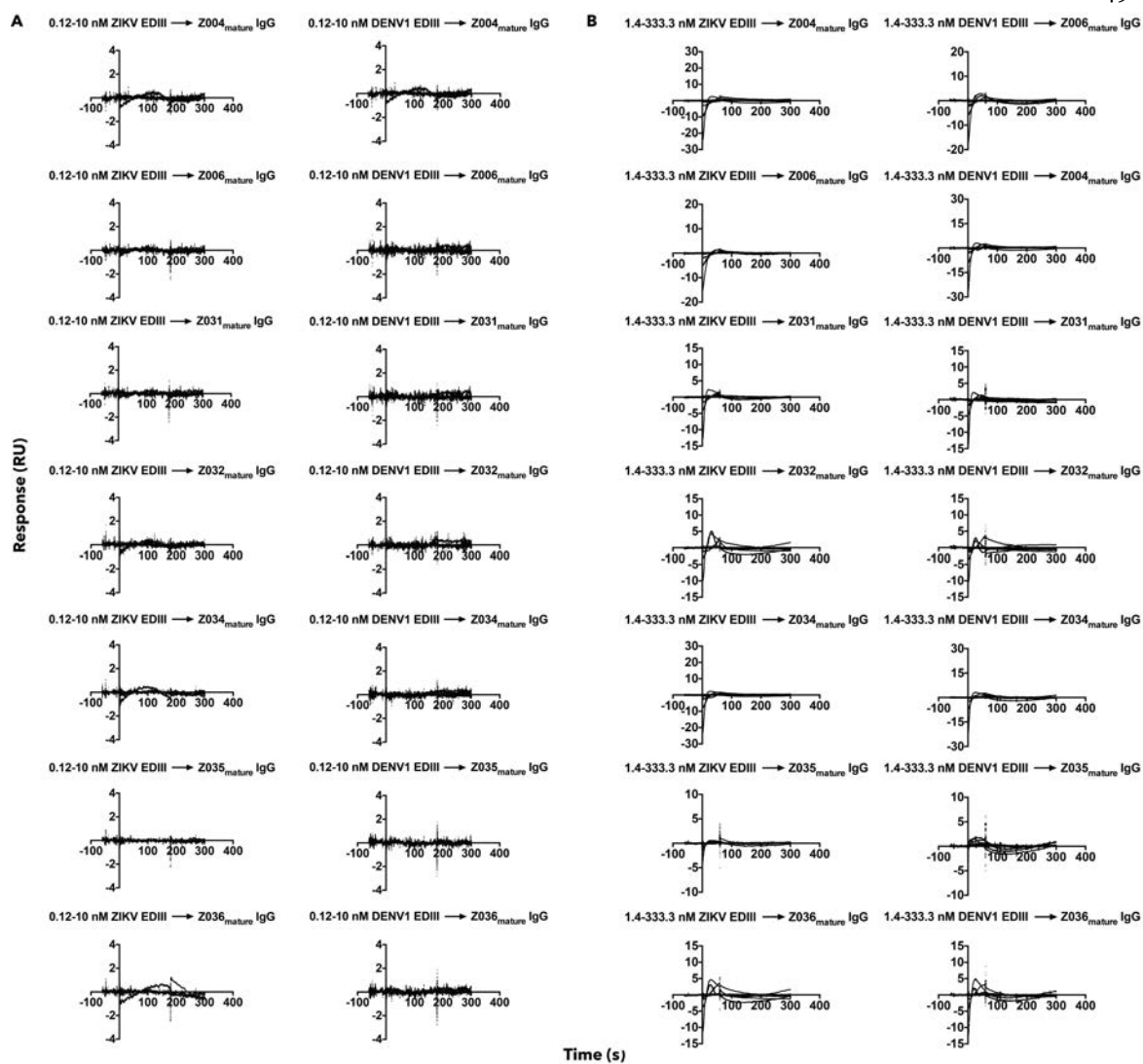


Figure S2.7. Residual plots for binding model fitting to SPR sensorgrams of ZIKV EDIII and DENV1 EDIII binding to mature Abs from two independent experiments. A. Related to Figure 2.2A and SI Appendix, Figure S2.4A. **B.** Related to SI Appendix, Figures S2.5-S2.6. Y-axis shows response units (RU).

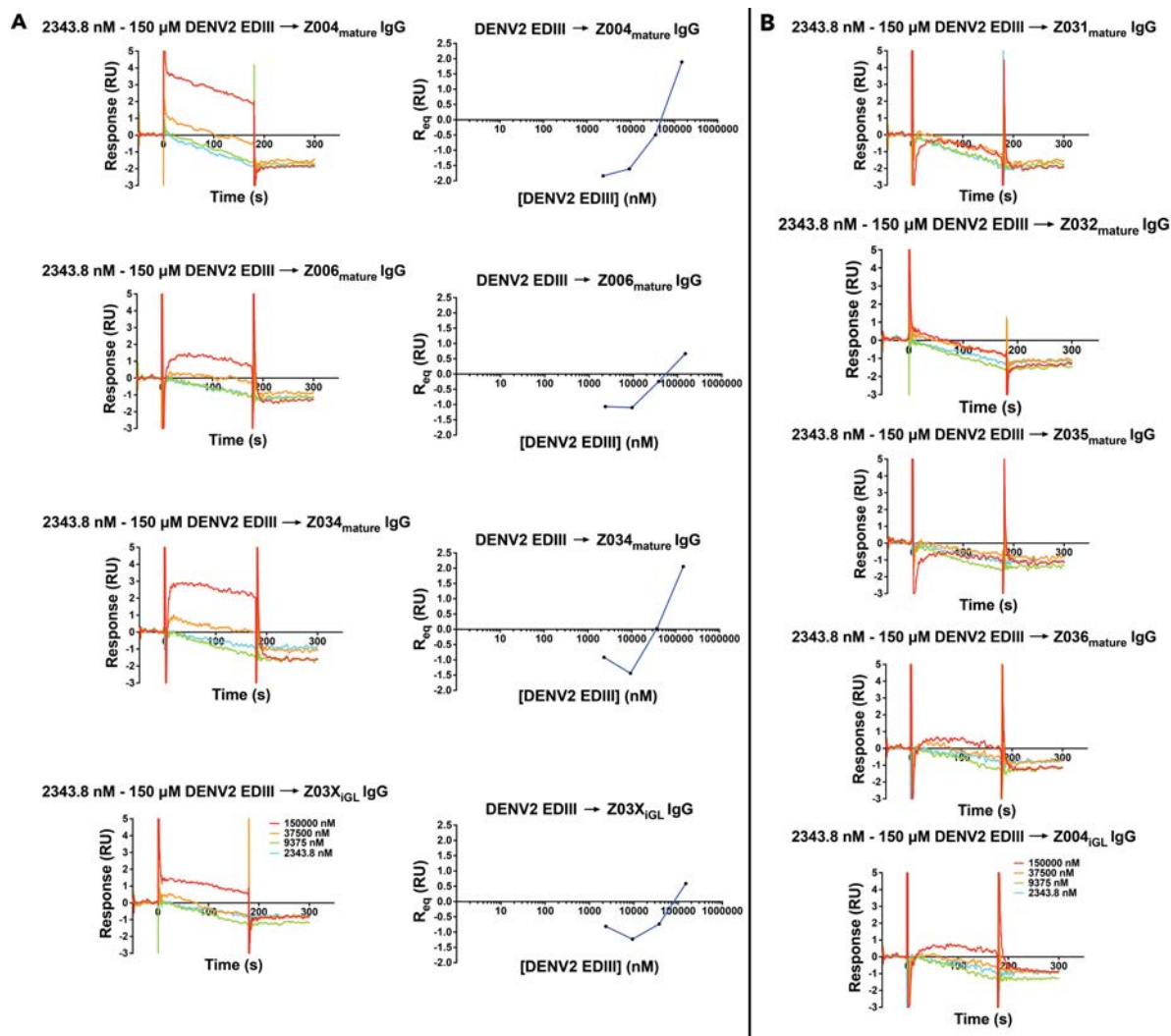


Figure S2.8. SPR binding assays with DENV2 EDIII.

IgGs were captured on a protein A biosensor chip, and the indicated concentrations of DENV2 EDIII were injected. Sensorgrams are indicated in colors representing different injected concentrations. **A.** Three mature IgG and one iGL IgG binding to DENV2 EDIII. Sensorgrams (left) and equilibrium binding curves (right) demonstrate weak binding of DENV2 EDIII to Z004_{mature}, Z006_{mature}, Z034_{mature}, and Z03X_{iGL} IgGs. **B.** Four mature IgGs and one iGL IgG showed no binding to DENV2 EDIII. No detectable binding was found for

Z031_{mature}, Z032_{mature}, Z035_{mature}, Z036_{mature}, and Z004_{iGL} at concentrations ≤ 150 μM .

Negative values indicate more DENV2 EDIII bound to the reference flow cell, HIV-1 IgG N6, than to the mature and iGL anti-ZIKV IgGs. Y-axes show response units (RU). Four independent injections were performed.

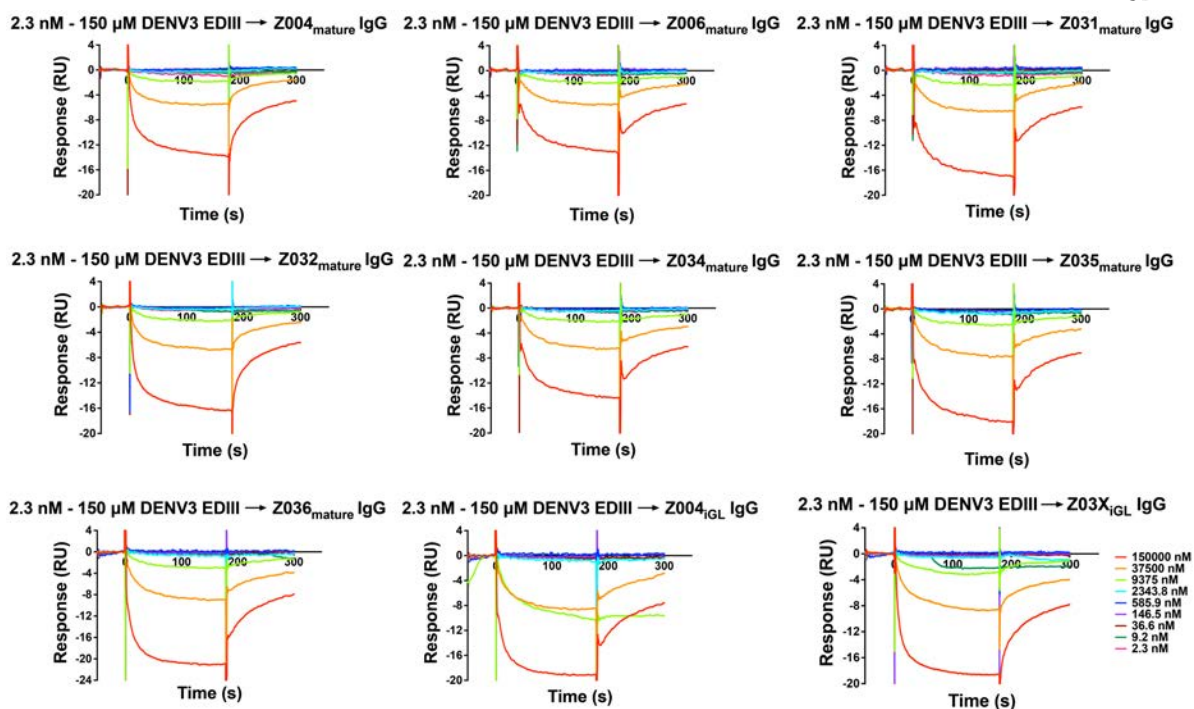


Figure S2.9. SPR binding assays with DENV3 EDIII.

IgGs were captured on a protein A biosensor chip, and the indicated concentrations of DENV3 EDIII were injected. Sensorgrams are indicated in colors representing different injected concentrations. No detectable binding was found for Z004_{mature}, Z006_{mature}, Z031_{mature}, Z032_{mature}, Z034_{mature}, Z035_{mature}, Z036_{mature}, Z004_{iGL}, and Z03X_{iGL} at concentrations $\leq 150 \mu$ M. Negative values indicate more DENV3 EDIII bound to the reference flow cell, HIV-1 IgG N6, than to the mature and iGL anti-ZIKV IgGs. Y-axes show response units (RU). Nine independent injections were performed.

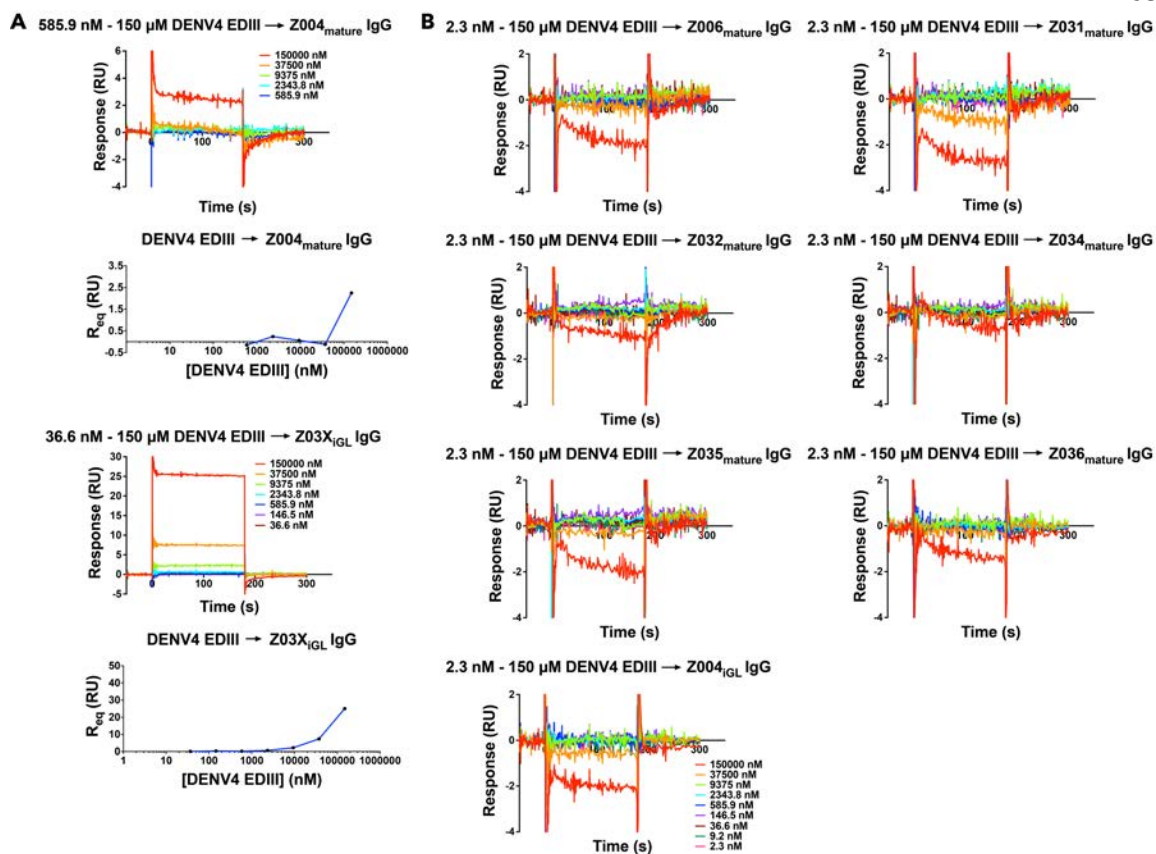


Figure S2.10. SPR binding assays with DENV4 EDIII.

IgGs were captured on a protein A biosensor chip, and the indicated concentrations of DENV4 EDIII were injected. Sensorgrams are indicated in colors representing different injected concentrations. **A.** One mature IgG and one iGL IgG binding to DENV4 EDIII. Sensorgrams (left) and equilibrium binding curves (right) demonstrate weak binding of DENV4 EDIII to Z004_{mature} and Z03X_{iGL} IgGs. **B.** Six mature IgGs and one iGL IgG showed no binding DENV4 EDIII. No detectable binding was found for Z004_{mature}, Z006_{mature}, Z031_{mature}, Z032_{mature}, Z034_{mature}, Z035_{mature}, Z036_{mature}, and Z004_{iGL} at concentrations ≤ 150 μ M. Negative values indicate more DENV4 EDIII bound to the reference flow cell, HIV-1 IgG N6, than to the mature and iGL anti-ZIKV IgGs. Y-axes show response units (RU). Five to nine independent injections were performed.

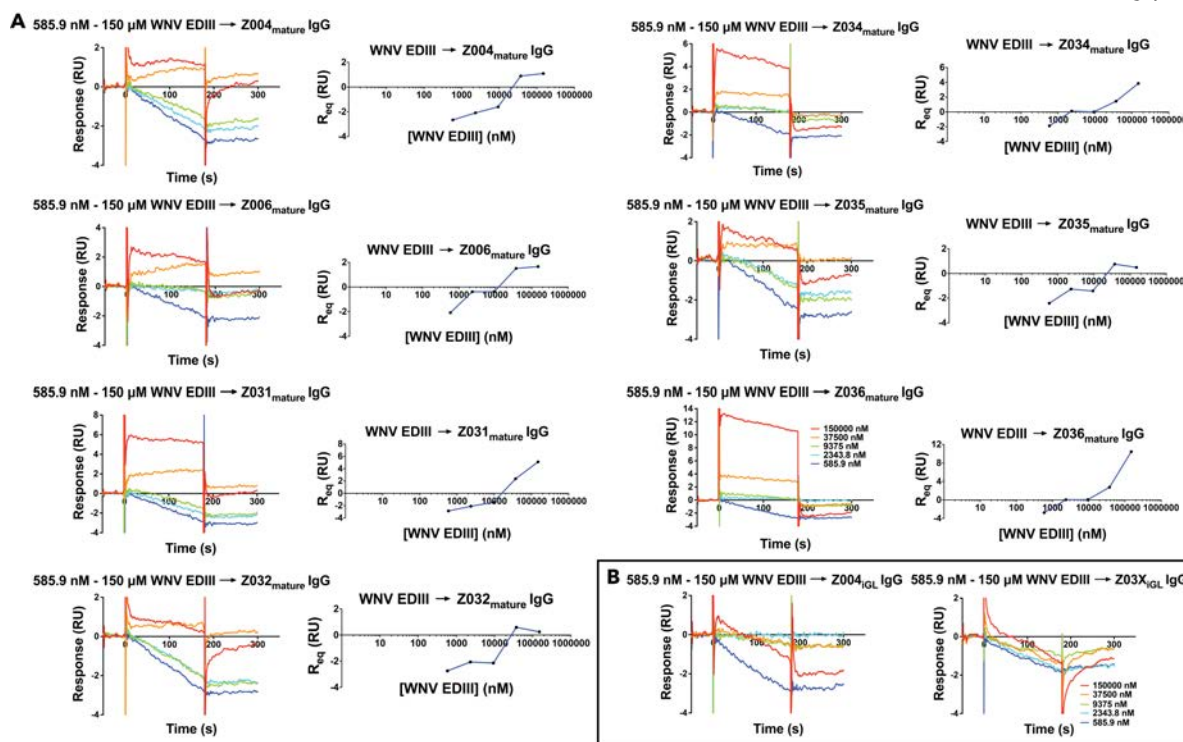


Figure S2.11. SPR binding assays with WNV EDIII.

IgGs were captured on a protein A biosensor chip, and the indicated concentrations of WNV EDIII were injected. Sensorgrams are indicated in colors representing different injected concentrations. **A.** Mature IgGs binding to WNV EDIII. Sensorgrams (left) and equilibrium binding curves (right) demonstrate weak binding of WNV EDIII to Z004_{mature}, Z006_{mature}, Z031_{mature}, Z032_{mature}, Z034_{mature}, Z035_{mature}, and Z036_{mature}. **B.** No detectable binding was found for Z004_{iGL} and Z03X_{iGL} at concentrations $\leq 150 \mu\text{M}$. Negative values indicate more WNV EDIII bound to the reference flow cell, HIV-1 IgG N6, than to the mature and iGL anti-ZIKV IgGs. Y-axes show response units (RU). Five independent injections were performed.

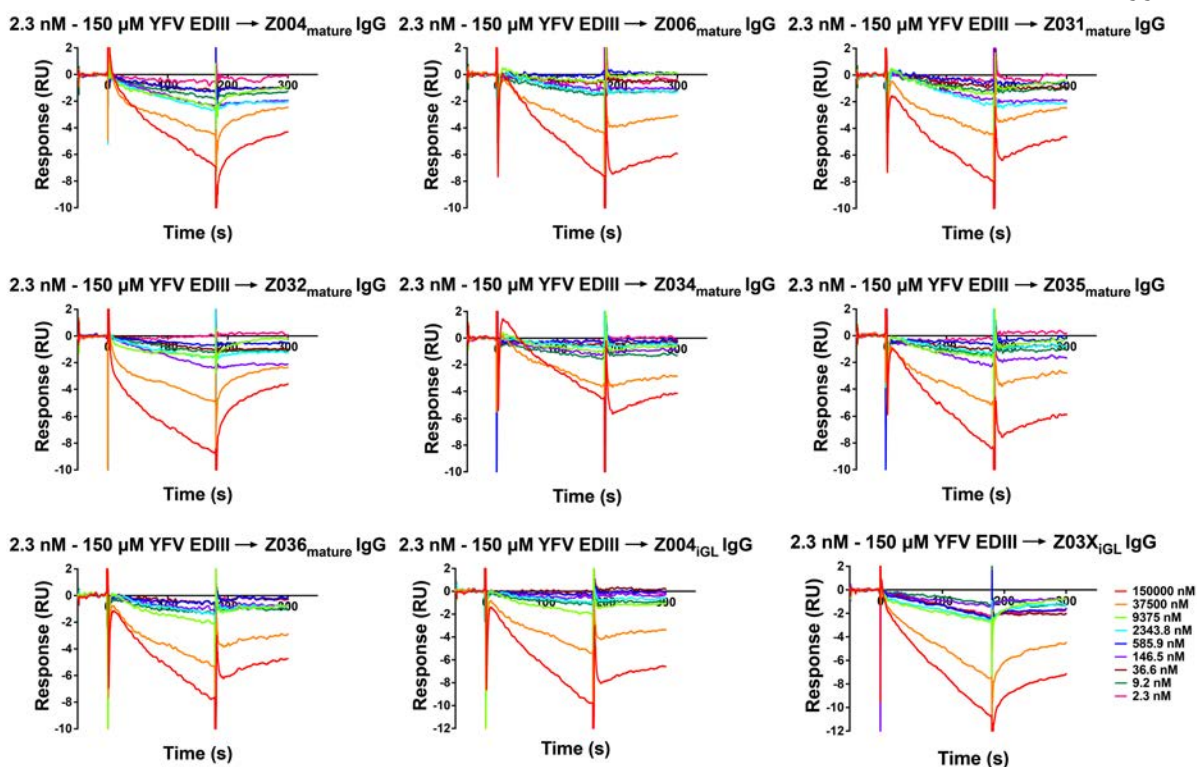


Figure S2.12. SPR binding assays with YFV EDIII.

IgGs were captured on a protein A biosensor chip, and the indicated concentrations of YFV EDIII were injected. Sensorgrams are indicated in colors representing different injected concentrations. No detectable binding was found for any IgGs at YFV EDIII concentrations $\leq 150 \mu\text{M}$. Note that negative values indicate more YFV EDIII binds to the reference flow cell, HIV-1 IgG N6, than to the mature and iGL anti-ZIKV IgGs. Y-axes show response units (RU). Nine independent injections were performed.

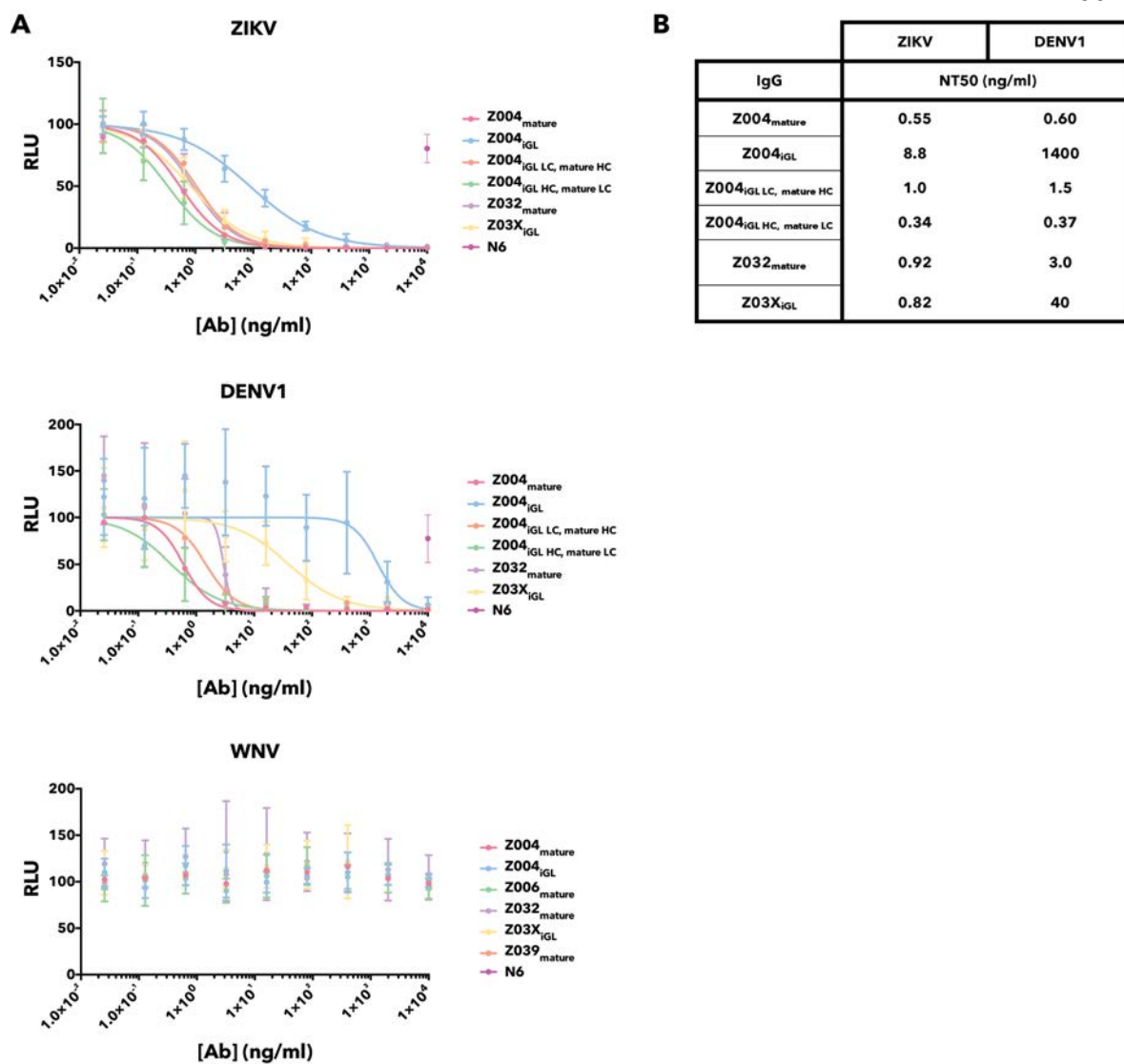


Figure S2.13. RVP-based neutralization assays.

A. Neutralization curves for Abs against ZIKV, DENV1 and WNV RVPs. Two or three independent experiments were performed and are plotted on the same graph. Y-axes show luciferase activity (relative light units, RLUs) normalized to RVP luciferase activity without Ab present. The HIV-1 Ab N6 (negative control) was assessed at the highest concentration (10 $\mu\text{g}/\text{mL}$). **B.** NT50s for Abs against ZIKV and DENV1 RVPs.

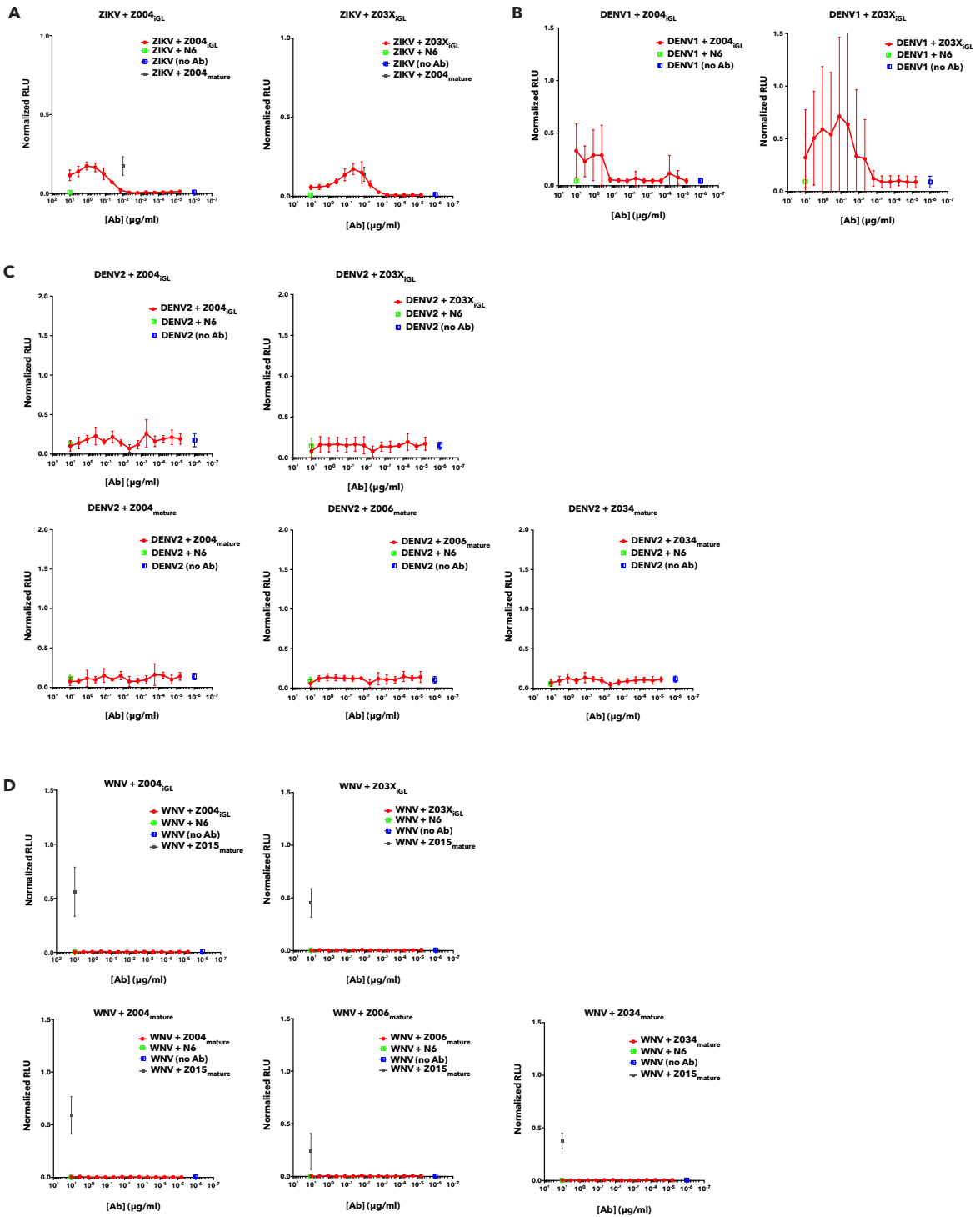


Figure S2.14. RVP-based ADE assay.

ADE assays for Abs against **A.** ZIKV, **B.** DENV1, **C.** DENV2, and **D.** WNV RVPs. Two independent experiments were performed and the normalized data were combined. Data plotted is the luciferase activity (relative light units, RLU) normalized to respective RVP luciferase activity determined on fully permissive Huh-7.5 cells (positive control). The HIV-1 Ab N6 (negative control) and cross-reactive Ab Z015_{mature} (WNV positive control) were assessed at the highest concentration (10 µg/mL). Z004_{mature} Ab (ZIKV positive control) was assessed at 0.01 µg/mL, a concentration known to show ADE for ZIKV.

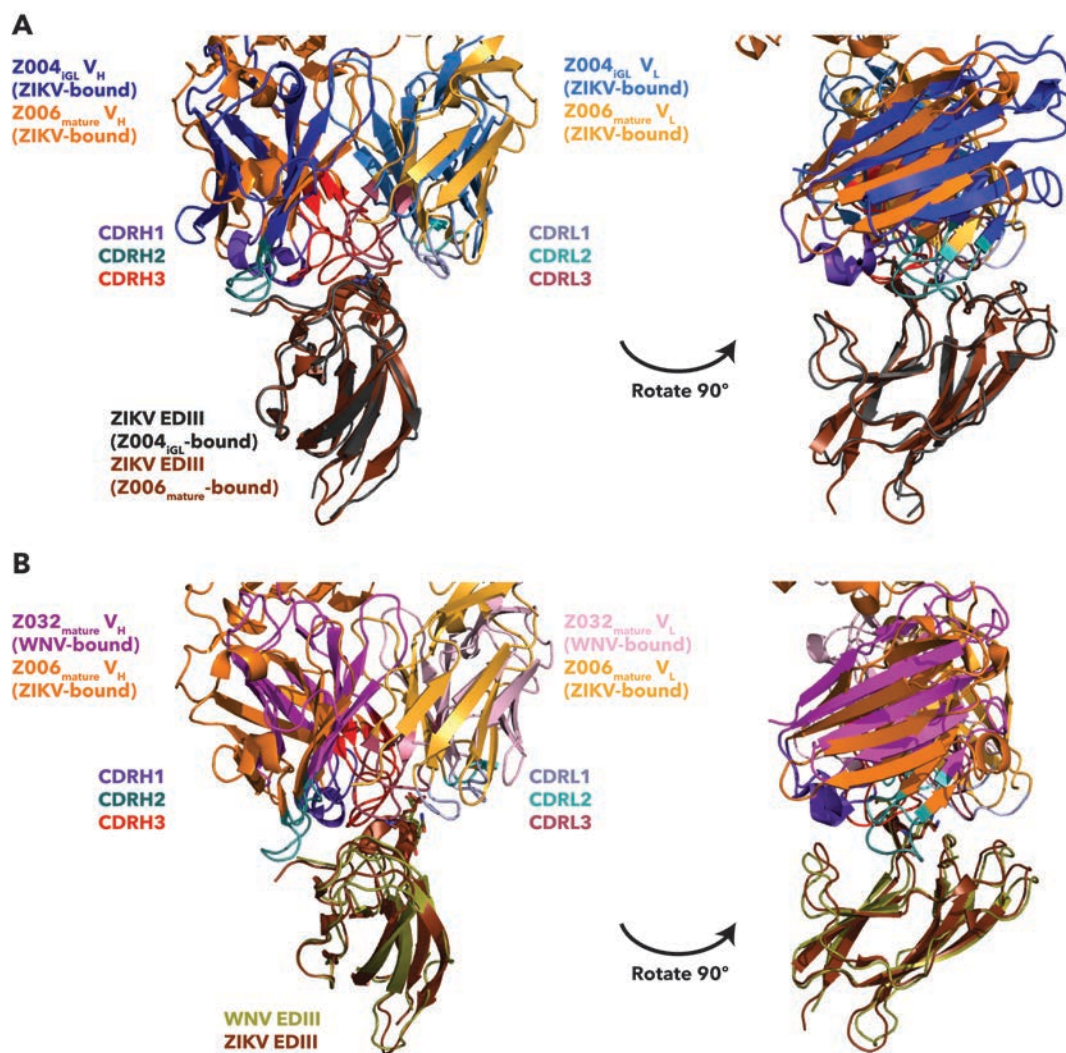


Figure S2.15. Recognition of EDIIIs by mature and iGL Fabs.

Fab V_H-V_L-EDIII structures are shown as cartoon representations. The Fab C_H-C_L domains were truncated in the figure in order to focus on the V_H-V_L interaction with EDIII. Structures were superimposed on the EDIII. The ZIKV EK and WNV EQ motifs are shown as sticks. **A.** Superimposition of Z004_{iGL} V_HV_L-ZIKV EDIII (Figure 2.4A) and Z006_{mature}-ZIKV EDIII structures. **B.** Superimposition of Z006_{mature}-ZIKV EDIII and Z032_{mature}-WNV EDIII structures.

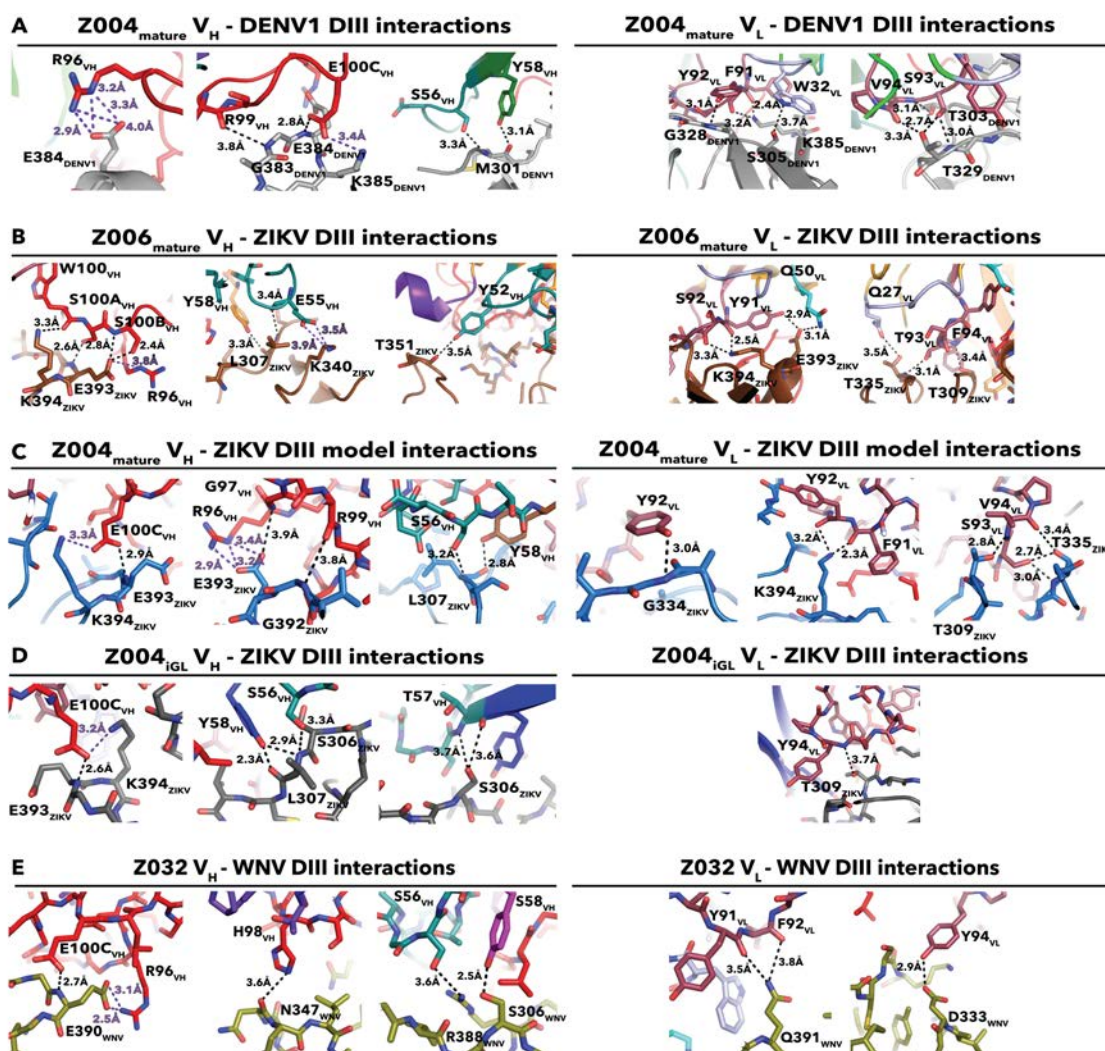


Figure S2.16. Close-up view of Fab–EDIII interactions.

Interactions with V_H are shown on the left and interactions with V_L are shown on the right. **A.** Z004_{mature}–DENV1 EDIII crystal structure (PDB 5VIC). **B.** Z006_{mature}–ZIKV EDIII crystal structure (PDB 5VIG). **C.** Z004_{mature}–ZIKV EDIII homology model. **D.** Z004_{IGL}–ZIKV EDIII crystal structure (PDB 6UTA). **E.** Z032_{mature}–WNV EDIII crystal structure (PDB 6UTE).

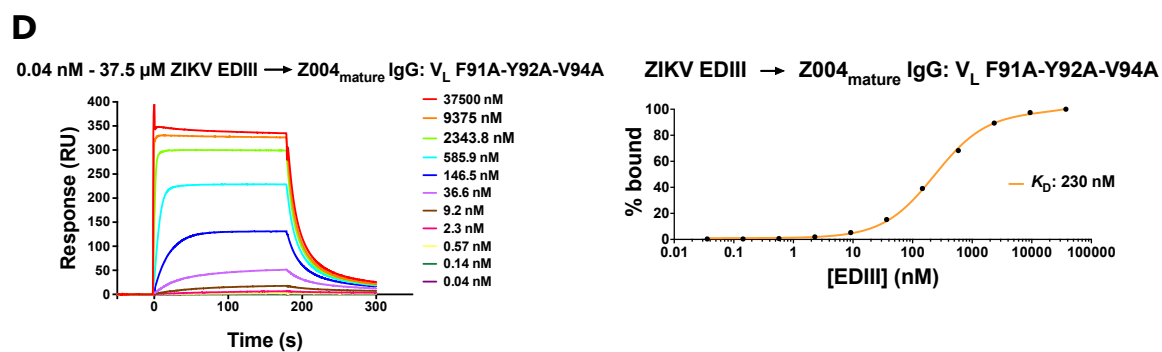
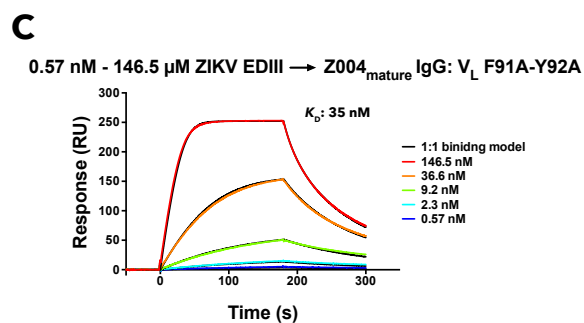
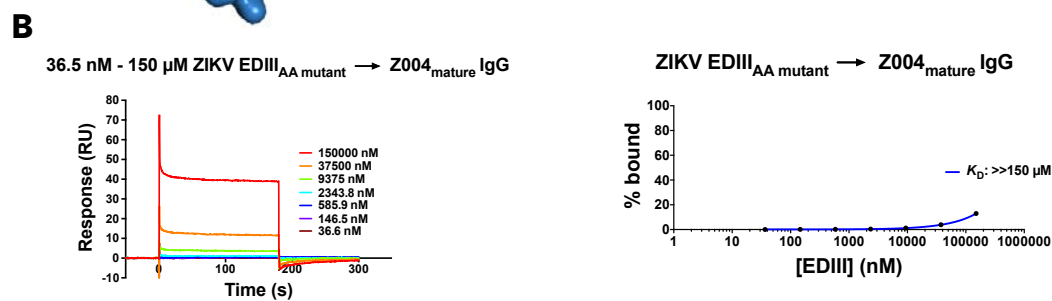
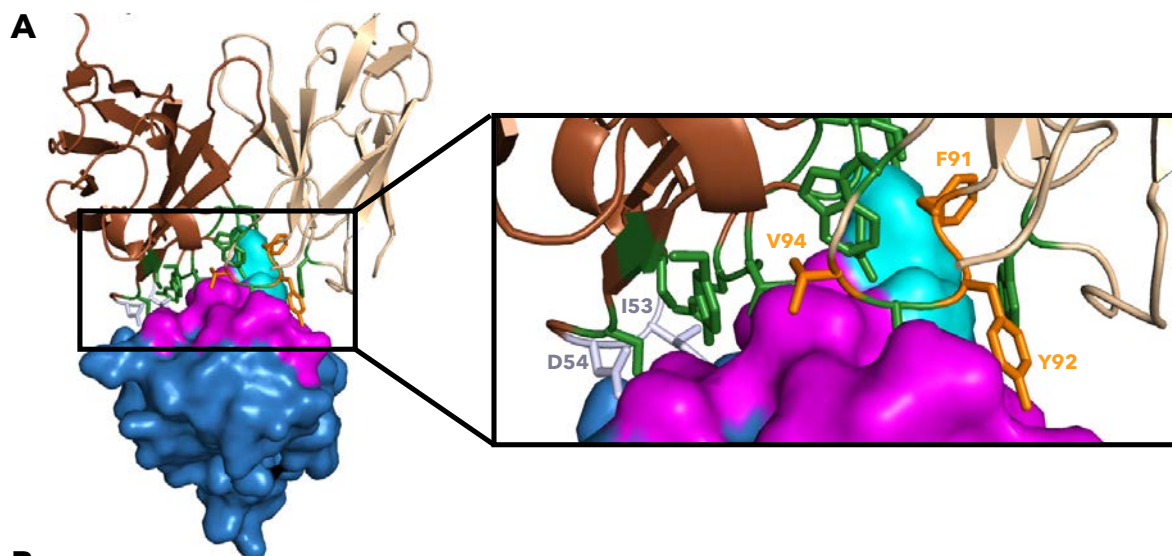


Figure S2.17. Comparison of ZIKV EDIII binding to Z004_{mature} Abs with site-directed mutations in the V_L.

A. Z004_{mature} V_HV_L-ZIKV EDIII homology model showing residues that differ between iGL and mature Z004 Fab at the EDIII-binding interface. Z004_{mature} V_HV_L (dark brown, V_H; tan, V_L) is shown as a cartoon representation and ZIKV EDIII (dark blue) is shown as a surface representation. EDIII residues within 4 Å of the V_HV_L are shown in magenta with the EK motif in teal. V_HV_L residues within 4 Å of the EDIII are shown in dark green with the V_H residues that differ between Z004_{iGL} and Z004_{mature} (but do not interact with EDIII), I53 and D54, shown in light purple and the V_L residues that differ between Z004_{iGL} and Z004_{mature} (and interact with EDIII), F91, Y92, and V94, shown in orange. **B-D.** SPR binding assays. IgGs were captured on a protein A biosensor chip, and the indicated concentrations of EDIII were injected. Sensorgrams are indicated in colors representing different injected concentrations. Y-axes show response units (RU). Five to 11 independent injections were performed. **B.** ZIKV EDIII_{AA mutant} (E393A-K394A) binding to Z004_{mature} IgG. **C-D.** ZIKV EDIII binding to Z004_{mature} IgGs with alanine mutations in the V_L: F91A-Y92A (C) and F91A-Y92A-V94A (D). **C.** Fits to a 1:1 binding model are in black; since the model fits very closely fit the data, the models are only slightly visible. The corresponding residual plot is also shown. **B,D.** Normalized equilibrium binding response (R_{eq}) from the sensorgram is plotted versus the log of the concentration of the indicated injected proteins with the best fit binding curve to the experimental data points shown as a continuous line. The standard error of the fit for the 230 nM K_D was 12 nM, with a 95% confidence of 200-260 nM for ZIKV EDIII → Z004_{mature} IgG: V_L F91A-Y92A-V94A. Since the ZIKV EDIII → Z004_{mature} IgG binding reaction did not reach equilibrium, the K_D is approximated as greater than the highest concentration of analyte injected.

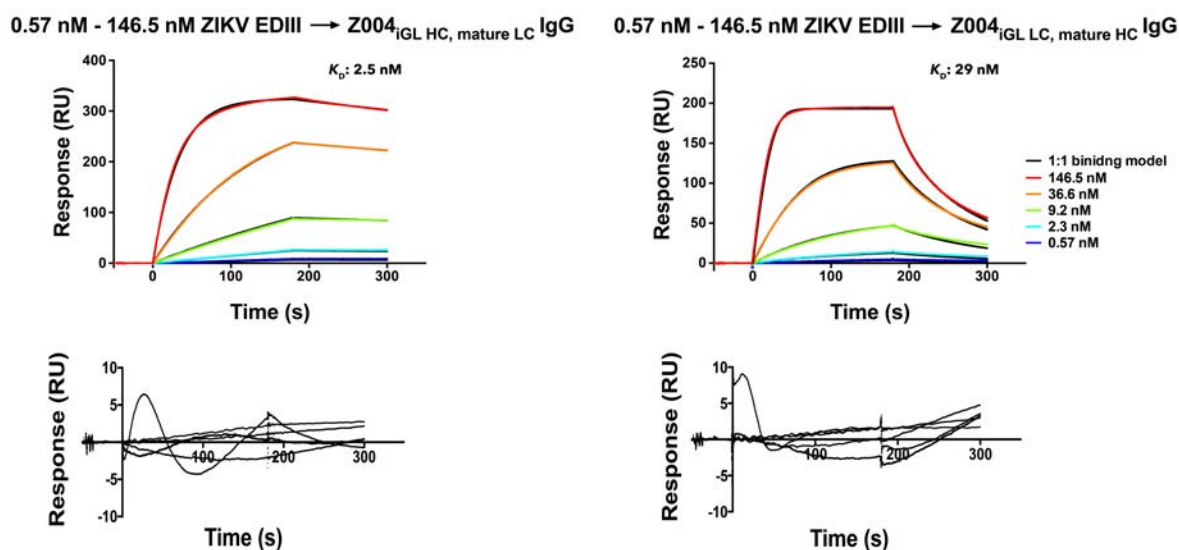


Figure S2.18. SPR binding sensorgrams and residual plots.

SPR binding sensorgrams (top; colored traces) and residual plots (bottom) for binding model fittings (top, black lines) of Z004 mature-iGL IgG chimeras (ligand) interacting with ZIKV EDIII (analyte). IgGs were captured on a protein A biosensor chip, and the indicated concentrations of ZIKV EDIII were injected. Sensorgrams are shown in colors representing different injected concentrations. Y-axes show response units (RU). Two independent experiments were performed.

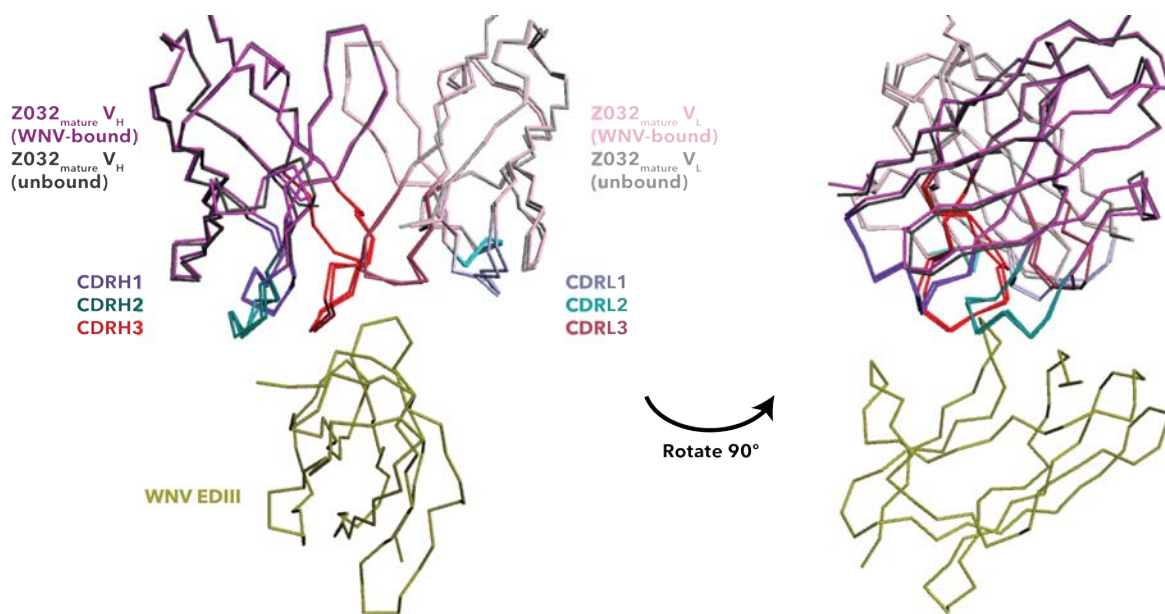


Figure S2.19. Comparison of bound and unbound structures of Z032_{mature}.

A. Superimposition of V_H-V_L domains from the structure determination of a Z032_{mature} Fab–WNV EDIII complex, in which the crystallographic asymmetric unit contained both bound (chains C and D) and unbound (chains E and F shown here) Fabs.

Table S2.1. X-ray diffraction data and refinement statistics for Fab–EDIII crystal structures.		
	Z004_{iGL} Fab–ZIKV EDIII PDB 6UTA	Z032_{mature} Fab–WNV EDIII PDB 6UTE
Data collection		
Space group	P4 ₃ 2 ₁ 2	P2 ₁
Cell dimensions		
<i>a</i> , <i>b</i> , <i>c</i> (Å)	85.91, 85.91, 327.46	96.23, 114.02, 127.26
α , β , γ (°)	90, 90, 90	90, 109.5, 90
Resolution (Å)	38.4-3.1	40.0-2.9
<i>R</i> _{pim} (%)	8.8 (49.1) *	9.5 (50.4)
<i>I</i> / σ (<i>I</i>)	9.1 (1.7)	5.6 (1.5)
Completeness (%)	93.6 (71.4)	99.7 (99.5)
Redundancy	12.4 (7.5)	3.1 (3.1)
CC(1/2)	0.99 (0.76)	0.98 (0.64)
Refinement		
Resolution (Å)	38.4-3.1	39.9-2.9
No. reflections	21817 (1618)	57390 (5694)
<i>R</i> _{work} / <i>R</i> _{free}	27.4/29.3	22.3/26.5
No. atoms		
Peptide	8060	17255
Ligand	0	30
Water	0	0
B-factors		
Peptide	62.8	58.4
Ligand	0	80.1
Water	0	0
R.M.S. deviations		
Bond lengths (Å)	0.013	0.002
Bond angles (°)	1.56	0.55
Ramachandran statistics		
Ramachandran favored (%)	90.4	95.9
Ramachandran allowed (%)	7.54	3.97
Ramachandran outliers (%)	2.10	0.18

Number of TLS Groups	6	11
----------------------	---	----

Each structure was derived from a single crystal.

*Highest resolution shell statistics shown in parentheses.

Table S2.2. Interacting residues in mature and iGL Fab–EDIII complexes

	V_H residues* that interact with EDIII	V_L residues* that interact with EDIII	EDIII residues that interact with Fab
Z004_{iGL} Fab – ZIKV EDIII	S56 _{VH} (CDRH2) T57 _{VH} (CDRH2) Y58 _{VH} (FWRH3) E100C _{VH} (CDRH3)	Y94 _{VL} (CDRL3)	S306 _{ZIKV} L307 _{ZIKV} T309 _{ZIKV} E393 _{ZIKV} K394 _{ZIKV}
Z004_{mature} Fab – ZIKV EDIII (homology model)	S56 _{VH} (CDRH2) Y58 _{VH} (FWRH3) R96 _{VH} (CDRH3) G97 _{VH} (CDRH3) R99 _{VH} (CDRH3) E100C _{VH} (CDRH3)	F91 _{VL} (CDRL3) Y92 _{VL} (CDRL3) S93 _{VL} (CDRL3) V94 _{VL} (CDRL3)	L307 _{ZIKV} T309 _{ZIKV} G334 _{ZIKV} T335 _{ZIKV} G392 _{ZIKV} E393 _{ZIKV} K394 _{ZIKV}
Z004_{mature} Fab – DENV1 EDIII	S56 _{VH} (CDRH2) Y58 _{VH} (FWRH3) R96 _{VH} (CDRH3) R99 _{VH} (CDRH3) E100C _{VH} (CDRH3)	W32 _{VL} (CDRL1) F91 _{VL} (CDRL3) Y92 _{VL} (CDRL3) S93 _{VL} (CDRL3) V94 _{VL} (CDRL3)	M301 _{DENV1} T303 _{DENV1} S305 _{DENV1} G328 _{DENV1} T329 _{DENV1} G383 _{DENV1} E384 _{DENV1} K385 _{DENV1}
Z006_{mature} Fab – ZIKV EDIII	Y52 _{VH} (CDRH2) E55 _{VH} (CDRH2) Y58 _{VH} (FWRH3) R96 _{VH} (CDRH3) W100 _{VH} (CDRH3) S100A _{VH} (CDRH3) S100B _{VH} (CDRH3)	Q27 _{VL} (CDRL1) Q50 _{VL} (CDRL2) Y91 _{VL} (CDRL3) S92 _{VL} (CDRL3) T93 _{VL} (CDRL3) F94 _{VL} (CDRL3)	L307 _{ZIKV} T309 _{ZIKV} T335 _{ZIKV} K340 _{ZIKV} T351 _{ZIKV} E393 _{ZIKV} K394 _{ZIKV}
Z032_{mature} Fab – WNV EDIII	S56 _{VH} (CDRH2) Y58 _{VH} (FWR3) R96 _{VH} (CDRH3) H98 _{VH} (CDRH3) E100C _{VH} (CDRH3)	Y91 _{VL} (CDRL3) F92 _{VL} (CDRL3) Y94 _{VL} (CDRL3)	S306 _{WNV} D333 _{WNV} N347 _{WNV} R388 _{WNV} E390 _{WNV} Q391 _{WNV}

*The Kabat numbering scheme was used.

Table S2.3. K_{DS} of Z004 Ab (mature, iGL, chimeras, and mutants) binding to ZIKV EDIII determined by SPR.		
IgG	EDIII	K_D (nM)
Z004_{mature}	ZIKV	0.28
Z004_{iGL}	ZIKV	1200
Z004_{iGL LC, mature HC}	ZIKV	29
Z004_{iGL HC, mature LC}	ZIKV	2.5
Z004_{mature}	ZIKV _{AA mutant}	>>150 μ M
Z004_{mature}: V_L F91A-Y92A	ZIKV	35
Z004_{mature}: V_L F91A-Y92A-V94A	ZIKV	230

Table S2.4. Pairwise superimpositions and rmsd calculations of bound and unbound $V_H V_L$ chains in the $Z032_{\text{mature}}$ -WNV EDIII crystal structure.

$Z032_{\text{mature}}$ $V_H V_L$ chains: Set 1	$Z032_{\text{mature}}$ $V_H V_L$ chains: Set 2	Cα atom count	rmsd (Å)
C and D (bound)	A and B (unbound)	213	0.42
C and D (bound)	E and F (unbound)	210	0.45
C and D (bound)	G and H (unbound)	217	0.35
C and D (bound)	I and J (unbound)	211	0.42
A and B (unbound)	E and F (unbound)	203	0.22
A and B (unbound)	G and H (unbound)	204	0.32
A and B (unbound)	I and J (unbound)	206	0.39
E and F (unbound)	G and H (unbound)	210	0.37
E and F (unbound)	I and J (unbound)	212	0.47
G and H (unbound)	I and J (unbound)	214	0.41

CHAPTER 3

Targeting pan-flavivirus neutralization with mosaic nanoparticle immunization

Abstract

Epidemics caused by dengue serotypes 1-4 (DENV1-4), West Nile Virus (WNV), yellow fever virus (YFV) and Zika virus (ZIKV) demonstrate the global threat of mosquito-borne flaviviruses. Due to high sequence identity of their envelope proteins, there is concern, particularly for DENV and ZIKV, that infection with one virus will elicit antibodies (Abs) that also recognize, but do not neutralize other flaviviruses. Non-neutralizing cross-reactivity can enhance viral entry into cells, leading to increased disease severity upon a subsequent flavivirus infection. This phenomenon, termed antibody-dependent enhancement (ADE), presents challenges for the design of vaccines that do not induce ADE and suggests vaccines need to elicit potent cross-reactive flavivirus neutralization to be safe. Here we designed homotypic nanoparticles displaying envelope domain III (EDIII) of ZIKV, DENV1-4, WNV and YFV individually on separate nanoparticles as well as heterotypic (mosaic) nanoparticles co-displaying all seven or just five (ZIKV, DENV1-4) of these EDIIIs on the same nanoparticles. Immunizations in mice with mosaic and mixes of homotypic nanoparticles elicited antibody responses superior to those elicited by ZIKV EDIII homotypic nanoparticles for binding to ZIKV EDIII. Additionally, mosaic nanoparticles displaying ZIKV and DENV1-4 EDIIIs showed superior cross-reactive binding responses to ZIKV, DENV1-4, and WNV EDIIIs compared to mixes of homotypic nanoparticles even though WNV EDIII was not present on the immunized nanoparticles. These findings are a promising step towards the development of a pan-flavivirus vaccine candidate that offers cross-reactive neutralization with reduced risk of ADE.

Significance Statement

Design of safe and effective vaccines for Zika, dengue and other flaviviruses is challenging due to concern that antibodies that neutralize one virus will also bind, but not effectively neutralize other flaviviruses. This non-neutralizing cross-reactivity causes risk for increased viral entry into cells through antibody-dependent enhancement of infection, which worsens the severity of disease symptoms. We developed vaccine candidates with envelope domain III of Zika and dengue viruses 1-4 displayed together on the same nanoparticles (mosaic) or individually on separate nanoparticles (homotypic) for immunization trials. In mice, immunization with mosaic nanoparticles demonstrated an advantage over mixes of homotypic nanoparticles for eliciting antibodies that showed cross-reactive binding to Zika, dengue 1-4, and West Nile Virus even though envelope domain III of West Nile Virus was not present on the immunized nanoparticle. This a promising step towards the development of a safe vaccine intended to provide pan-flavivirus neutralization to lower the risks of antibody-dependent enhancement.

Introduction

The Zika virus (ZIKV) epidemic in 2015-2016 was a reminder of the enormous global disease burden of epidemic-causing flaviviruses, including dengue serotypes 1-4 (DENV1-4), West Nile Virus (WNV), and yellow fever virus (YFV)^{20,171,172}. These flavivirus are primarily transmitted by mosquitos, particularly *Aedes aegypti*, and cause febrile disease with a broad spectrum of symptoms^{20,23,171}. Although ZIKV was first discovered in 1947^{43,44}, the potential for epidemics was not realized until large outbreaks occurred in 2007³⁹, 2013-2014^{40,41}, and when cases spread to the Americas in 2015-2016^{38,42,173}. Infection usually causes mild symptoms in approximately 20% of cases and severe neurologic problems such as Guillain-Barré Syndrome only in rare cases^{41,50-52}. However, ZIKV can cause severe fetal neurodevelopmental abnormalities such as microcephaly in the newborns of infected women^{47,53,54,56,174}. DENV infects an estimated 400 million humans each year and causes disease ranging from febrile illness with flu-like symptoms to severe hemorrhagic fever and dengue shock syndrome with plasma leakage, coagulopathy, and bleeding^{18,20,171}. WNV has spread widely throughout the western hemisphere and can cause severe neurological symptoms, including meningitis, encephalitis, and acute flaccid paralysis^{175,176}. Despite the existence of a YFV vaccine, YFV is still endemic in many parts of the world and causes febrile illness with potential for hepatitis, renal failure, hemorrhage, and shock^{20,177}. Given the global threat of ZIKV, DENV, and other flaviviruses, there is urgent need for the development of effective vaccines safe for widespread use.

Since the flavivirus envelope (E) proteins share ~40-80% amino acid sequence identity between ZIKV, DENV1-4, WNV, and YFV, and there are other highly conserved regions within the structural and non-structural proteins^{23,73,74,178}, there is concern that antibodies (Abs) elicited by infection or vaccination against one flavivirus can cross-react with other flaviviruses, but not provide potent neutralization. Non- or only weakly-neutralizing cross-reactive Abs can enhance viral entry into cells that express the Fc gamma receptor (FcγR) by

antibody-dependent enhancement (ADE), facilitating an alternative route of infection and enhancing viral production and disease severity^{23,75–82,179,180}.

The greatest observed risk of ADE is for ZIKV and DENV1-4, which are closely related, often co-circulate, and have caused widespread disease^{23,181,182}. Abs against the immunodominant fusion loop and precursor membrane (prM) proteins were found to be particularly cross-reactive and are often weak neutralizers and strong promoter of ADE^{179,183–186}. The live attenuated tetravalent DENV vaccine Dengvaxia increases the risk of severe DENV symptoms in people who were never previously exposed to any DENV infection before, limiting its safety and use^{84–87}. Prior DENV infection does not seem to increase risk of severe ZIKV symptoms in humans or cause congenital Zika syndrome in ZIKV-infected pregnant women^{187–190}, and there is some evidence that prior DENV infection may even reduce the risk of ZIKV infection and complicated symptoms^{191–193}. However, prior DENV or ZIKV infection that results in low or intermediate Ab titers increases the risk of worsened disease severity from a subsequent DENV infection with a different serotype^{88–94}. High Ab titers resulting from multiple DENV infections protects against severe subsequent DENV disease⁹⁰, suggesting a vaccine strategy with consistent boosting may be necessary to generate protective titers.

Multivalent antigen display was shown to be an effective strategy for increasing the immunogenicity of protein subunit vaccines and providing longer lasting immunity^{194,195}. Antigens can be multimerized on nanoparticles using “plug and display” approaches such as the SpyCatcher-SpyTag system^{196–198}. This system utilizes spontaneous isopeptide bonds to conjugate antigens tagged with a 13-residue peptide (SpyTag) to multiple copies of engineered protein domains (SpyCatcher) fused on a virus-like particle (VLP)^{196–199}. Antigens multimerized on nanoparticles with this approach were previously shown to elicit potent neutralizing responses^{200–204}. Additionally, the development of mosaic nanoparticles displaying heterotypic antigens from different virus strains is a strategy intended to

selectively engage B cells that tolerate antigenic variability versus strain-specific B cells^{140,202,203}. Immunizations with mosaic nanoparticles were shown to successfully elicit cross-reactive antibody response for SARS-like betacoronaviruses and influenza^{202,203}.

Several antibodies against E protein domain III (EDIII) are potently neutralizing and demonstrate less non-neutralizing cross-reactivity than antibodies against other conserved epitopes, making EDIII a target for protein-subunit based vaccine design and therapeutic antibody development^{36,57-64,64-71,205-209}. Immunization trials in mice using ZIKV EDIII or E protein vaccine candidates, some of which are VLP-based, showed promise for eliciting neutralizing ZIKV-specific Abs^{153-155,206,210-214}. Similar VLP approaches displaying WNV E protein or EDIIIs²¹⁵⁻²¹⁸ or co-displaying the EDIII or E protein of one, two or four of the DENV serotypes also showed ability to generate neutralizing Abs^{207,219-227}.

Due to concerns of ADE associated with flavivirus infection and vaccination, a ZIKV vaccine that generates an immune response that is potently cross-neutralizing against other flaviviruses may minimize the risk of ADE. Here we used the SpyCatcher-SpyTag system to multimerize Spytagged EDIIIs (EDIII-SpyTag003) of ZIKV, DENV1-4, WNV, and YFV onto SpyCatcher003-mi3 nanoparticles to evaluate whether mosaic nanoparticles can elicit cross-reactive Ab responses. We showed that mosaic nanoparticles displaying ZIKV and DENV1-4 EDIIIs (5-mosaic) elicited cross-reactive binding that is superior to that of mixes of homotypic nanoparticles. Additionally, 5-mosaic nanoparticles elicited cross-reactive binding against WNV EDIII despite this EDIII not being present on the immunized nanoparticles. These findings are a promising step for the development of safe and effective vaccines to protect against ZIKV and other flaviviruses.

Results

EDIIIs were efficiently conjugated on mi3 nanoparticles. Each of the seven EDIII-SpyTag003 constructs (ZIKV, DENV1-4, WNV, and YFV) were individually conjugated to SpyCatcher003-mi3 (up to 60 attachment sites possible) to prepare homotypic nanoparticles, and equimolar amounts of five (ZIKV, DENV1-4) or all seven EDIII-SpyTag003 constructs were combined for conjugation to SpyCatcher003-mi3 to prepare 5-mosaic or 7-mosaic nanoparticles, respectively (Figure 3.1A,C)^{204,228}. Conjugation was evaluated by purification of the nanoparticles from excess unbound EDIII-SpyTag003 by size exclusion chromatography (SEC) followed by sodium dodecyl sulfate polyacrylamide gel electrophoresis (SDS-PAGE). SDS-PAGE showed nearly 100% conjugation with similar efficiencies for each EDIII-mi3 construct, although DENV1 conjugation showed some relative reduction (Figure 3.1D). This suggests 5-mosaic and 7-mosaic nanoparticles contained approximately equimolar mixtures of different EDIIIs. Combinations of five (ZIKV, DENV1-4) or all seven homotypic nanoparticles were mixed in equimolar amounts to prepare 5-admix and 7-admix nanoparticles, respectively, for immunization trials.

Sera from immunizations shows strong binding to ZIKV, DENV1-4, and WNV EDIIIs. Immunization trials were performed in mice for the following groups of nanoparticles: homotypic ZIKV EDIII-mi3, 5-mosaic, 7-mosaic, 5-admix, 7-admix, and unconjugated SpyCatcher003-mi3. Each group had five mice except SpyCatcher003-mi3, which had three mice. Mice were injected with equal doses of nanoparticles plus adjuvant for the prime (day 0) and subsequent boosts at days 14, 28, and 42. Mice were bled before each injection and at day 60 for sera analyses (Figure 3.1B). One mouse from the 7-admix group died between the day 14 and day 28 timepoints.

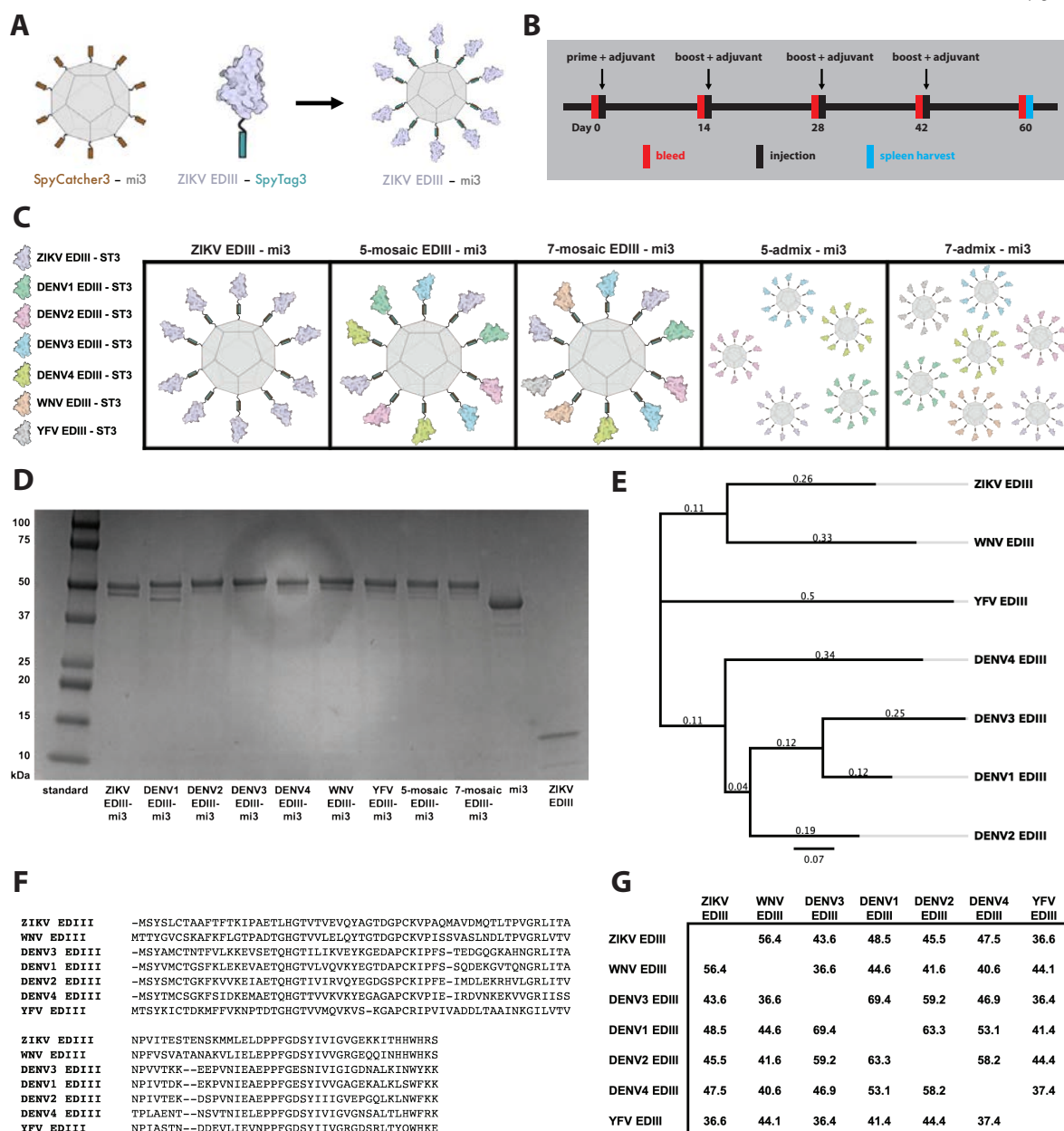


Figure 3.1. Preparation of EDIII nanoparticles for immunization trials.

A. SpyTagged EDIIIs were attached to SpyCatcher003-mi3 to prepare EDIII-mi3 nanoparticles. There are 60 potential coupling sites on the mi3; only ten conjugated EDIIIs are shown on each nanoparticle for clarity. **B.** Immunization schedule; adjuvant is AddaVax

(Invivogen). **C.** The following groups of nanoparticles were prepared: homotypic ZIKV EDIII nanoparticles (ZIKV EDIII–mi3), mosaic nanoparticles with ZIKV and DENV1-4 EDIIIs conjugated to the same mi3s (5-mosaic EDIII–mi3), mosaic nanoparticles with ZIKV, DENV1-4, WNV and YFV EDIIIs conjugated to the same mi3s (7-mosaic EDIII–mi3), a mix of homotypic ZIKV and DENV1-4 EDIII nanoparticles (5-admix–mi3), a mix of homotypic ZIKV, DENV1-4, WNV, and YFV EDIII nanoparticles (7-admix–mi3). **D.** Coomassie-stained SDS-PAGE of SEC-purified EDIII-conjugated nanoparticles (EDIII–mi3), unconjugated SpyCatcher003-mi3 nanoparticles (mi3), and unconjugated ZIKV EDIII. **E.** Phylogenetic tree of EDIII proteins. **F.** Alignments of EDIII sequences. **G.** Pairwise percent identities of EDIII proteins.

Sera were analyzed by ELISA area under the curve (AUC) for ability to bind ZIKV, DENV1-4, WNV and YFV EDIIIs. Sera from mice immunized with homotypic ZIKV EDIII–mi3 nanoparticles showed binding only to ZIKV EDIII and the response increased from day 14 (after the prime) to 42 (after 2 boosts) (Figure 3.2, red bars). The 7-admix group showed an advantage compared to the 5-admix group for binding to WNV and YFV, consistent with the presence of WNV and YFV EDIIIs on the 7-admix nanoparticles, but a comparable response was observed for these two groups for binding to ZIKV and DENV1-4 (Figure 3.2, yellow and purple bars). The 5-mosaic and 7-mosaic groups showed comparable binding to ZIKV and DENV1-4, although 5-mosaic sera showed an advantage for binding to ZIKV EDIII at day 42 (Figure 3.2, dark blue and teal bars). Interestingly, both 5-mosaic and 7-mosaic sera showed binding to WNV EDIII, despite this EDIII not being present on the 5-mosaic immunized nanoparticle. Additionally, 7-mosaic nanoparticles showed no advantage over 5-mosaic nanoparticles, except for days 28 and 60 against WNV. On the timepoint when the highest binding response was observed, day 42, the 5-mosaic and 7-mosaic sera showed comparable binding to WNV EDIII.

Notably, the 5-mosaic nanoparticles consistently showed a superior response compared to 5-admix nanoparticles for binding against ZIKV, DENV1-4, and WNV. Although there is clear binding to the EDIIIs by day 28, the consistent advantage of sera from mice immunized with 5-mosaic compared to 5-admix nanoparticles was first evident at day 42. The 7-mosaic nanoparticles also showed an advantage compared to 7-admix nanoparticles at some timepoints for binding to a few EDIIIs (days 28 and 60 for ZIKV, day 60 for DENV1, days 14 and 28 for DENV2, day 14 for DENV4, and days 28 and 60 for WNV), although this advantage was less consistent across timepoints. Of all the EDIIIs, the 5-admix, 5-mosaic, 7-admix, and 7-mosaic sera showed the strongest responses to DENV1 and DENV3. Binding to YFV EDIII was weak by all sera groups, although the 7-admix group showed an advantage compared to the mi3 control, indicating an advantage of homotypic nanoparticles for binding to YFV EDIII.

Assays to assess the neutralization potencies and ADE of the sera samples are in progress. Flow cytometry analyses of B cells from harvested spleens will also be performed to determine whether B cells show cross-reactive binding to multiple EDIIIs.

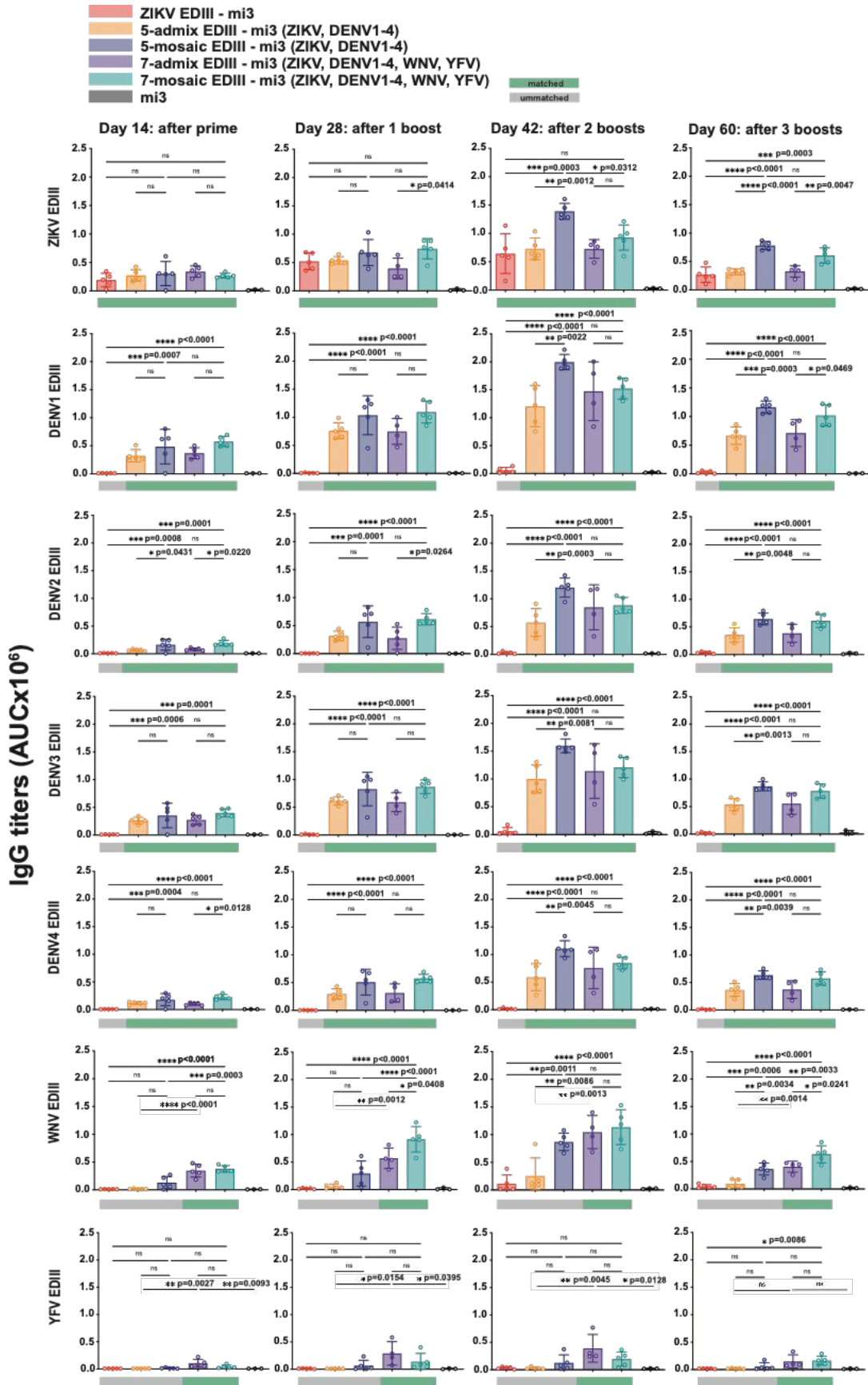


Figure 3.2. EDIII nanoparticle immunizations in mice elicit strong Ab binding to flavivirus EDIIIs.

ELISA data for mouse sera binding to flavivirus EDIIIs. ELISA data from sera IgG responses to seven different flavivirus EDIIIs, indicated on the y-axes, are shown as area under the curve (AUC). The sera is from days 14, 28, 42, and 60 as indicated at the top of each column. Sera from six immunization groups were tested; the key is shown in the legend at the top of the figure. Green and gray rectangles below ELISAs represent mismatched strains (grey: EDIII tested in the ELISA the was not present on the immunized nanoparticle) or matched strains (green: EDIII tested in the ELISA was present on the immunized nanoparticle). Each dot represents the mean of duplicate assays for serum from one animal. The means and standard deviations for vaccinated cohorts are indicated by the height of rectangles and vertical lines, respectively. Significant differences between groups linked by horizontal lines are indicated by asterisks. NS indicates ‘not significant’.

Discussion

The development of safe and effective vaccines against co-circulating mosquito-borne flaviviruses such as ZIKV and DENV is challenging due to concerns about the risk of ADE^{84,87,185,229–231}. The design and evaluation of vaccine candidates that elicit pan-flavivirus neutralization with reduced potential for ADE is critical for addressing global epidemics. Here we multimerized EDIIIs of seven flaviviruses on mosaic and homotypic nanoparticles using the “plug and display” SpyTag-SpyCatcher strategy¹⁹⁷ and showed that immunization with either mosaic nanoparticles or a mix of homotypic nanoparticles elicits pan-flavivirus sera binding to ZIKV, DENV1-4, and WNV. These initial findings show promise for using mosaic nanoparticles as a candidate for the development of safe and effective pan-flavivirus vaccines.

Notably, our findings showed a superior immune response after immunizations with 5-mosaic (ZIKV and DENV1-4) nanoparticles compared to a mix of homotypic nanoparticles for binding to ZIKV and DENV1-4 as well as for eliciting a cross-reactive response against WNV EIII (Figure 3.2). Of all the EDIII amino acid sequences, WNV EDIII is most similar to ZIKV EDIII, which is consistent with the cross-reactive sera recognition we observed (Figure 3.1E-G). Additionally, the superior response of 5-mosaic nanoparticles over ZIKV EDIII homotypic nanoparticles for binding to ZIKV EDIII reinforces the advantage of using mosaic nanoparticles. Since the strongest binding response was observed on day 42 after a prime and two boosts, this supports that a vaccination strategy with multiple boosts is favorable for generating high titers. The lack of a superior response for 7-mosaic nanoparticles over 5-mosaic nanoparticles for binding to any EDIIIs on day 42 indicates 5-mosaic nanoparticles are sufficient and advantageous for eliciting pan-flavivirus binding to ZIKV, DENV1-4, and WNV EDIIIs. Additionally, the finding that immunizations with ZIKV EDIII homotypic nanoparticles only elicited a specific binding response against ZIKV

EDIII is consistent with previous studies that performed immunizations with ZIKV EDIII^{153–155,210,214}.

The reduced binding detected for all sera samples to YFV EDIII indicates using mosaic nanoparticles or mixtures of homotypic nanoparticles is not an advantageous strategy for eliciting binding to YFV EDIII. This is consistent with the observation that the YFV EDIII amino acid sequence is the least similar to the ZIKV, DENV1, DENV3, and DENV4 sequences compared to the other EDIIIs in our panel (Figure 3.1E-G). While homotypic YFV EDIII nanoparticles are an alternative possibility that may be more effective, YFV is the only flavivirus of the seven for which a vaccine is already universally available and there is no conclusive known risk of ADE due to YFV infection in humans^{232–234}.

These initial findings show promise for development of mosaic nanoparticles as a pan-flavivirus vaccine candidate. Neutralization and ADE assays are underway to evaluate their effectiveness.

Materials and Methods

Sequence comparisons. Using Geneious 11.0.5 software, EDIII protein sequence alignments were performed with ClustalW²³⁵, the phylogenetic tree was built with the Jukes-Cantor distance model and neighbor-joining tree building method, and pairwise percent identities were calculated.

Expression of EDIII proteins. Flavivirus EDIIIs were expressed in *E. coli* and purified from inclusion bodies as previously described^{36,69,158,205}. EDIII genes from ZIKV (H/PF/2013 strain, GenBank KJ776791), DENV1 (45AZ5 strain, NCBI reference NC_001477), DENV2 (NCBI reference NC_001474), DENV3 (NCBI reference NC_001475.2), DENV4 (NCBI reference NC_002640.1), YFV (Asibi strain, Genbank KF769016), and WNV (Genbank KX547539.1) were cloned in pET21 expression plasmids with a C-terminal SpyTag003²²⁸ (RGVPHIVMVDAYKRYK) (for conjugation to SpyCatcher003-mi3) or a hexahistidine tag (for ELISAs). In brief, plasmids were transformed into BL21 (DE3) competent cells and cultures were grown using IPTG-induction. Cultures were harvested, stored overnight at -20°C, and the pellet was resuspended in 20 mM Tris pH 8.0, 150 mM NaCl. The cells were lysed and centrifuged at 21,000g for 30 minutes, and the pellet was resuspended in 6 M guanidine hydrochloride, 100 mM Tris-HCl pH 8.0. This suspension was centrifuged for 21,000g for 30 minutes, and 20 mM beta-mercaptoethanol was added to the supernatant. EDIII was refolded by dropwise, rapid dilution into 400 mM L-Arginine, 100 mM Tris-base pH 8.0, 2 mM EDTA, 5 mM reduced glutathione, 0.5 mM oxidized glutathione, and 10% glycerol at 4°C. EDIII was then concentrated and purified by SEC with a Superdex 75 column (GE Healthcare) into 20 mM Tris pH 8.0, 150 mM NaCl, 0.02% NaN₃.

Expression of mi3 nanoparticles. SpyCatcher003-mi3 nanoparticles were prepared as previously described^{200,202,236}. In brief, the pET28a SpyCatcher-mi3 gene (Addgene) was transformed into BL21 (DE3)-RIPL *E.coli* cells (Agilent) for expression. Cell pellets were

resuspended in 20 mL 25 mM Tris-HCl pH 8.5, 300 mM NaCl, 0.1 mg/mL lysozyme, 1 mg/mL cOmplete mini EDTA-free protease inhibitor (Merck), and 1 mM phenylmethanesulfonyl fluoride (PMSF) (Sigma) and lysed with a cell disruptor. Lysates were then centrifuged for 45 min. at 35,000g at 4°C, and the supernatant was passed through a 0.2- μ m filter. Ammonium sulfate (170 mg per mL of lysate) was added, and SpyCatcher003-mi3 nanoparticles were precipitated by incubation at 4°C for one hour while mixing with a stir bar at 100 rpm. Nanoparticles were centrifuged for 30 min. at 30,000g at 4°C, and the pelleted nanoparticles were resuspended in 8 mL TBS (25 mM Tris-HCl pH 8.5, 150 mM NaCl). Residual ammonium sulfate was removed by 16 hours of dialysis at 4°C against a 500-fold excess of TBS. Nanoparticles were then concentrated with a Amicon Ultra concentrator with a 30 kDa molecular-weight cutoff (Millipore Sigma) and purified by SEC with a HiLoad 16/600 Superdex 200 (GE Healthcare) column equilibrated with 25 mM Tris-HCl pH 8.0, 150 mM NaCl, 0.02% NaN₃ (TBS). SpyCatcher003-mi3 nanoparticles were stored at 4°C for up to 1 month for conjugation.

Preparation of conjugated EDIII-mi3 nanoparticles. Conjugated nanoparticles were prepared as previously described^{202,236}. SpyCatcher003-mi3 nanoparticles were incubated with a 1.2-fold molar excess of EDIII-SpyTag003 (either a single EDIII for homotypic nanoparticles or an equimolar mixture of five or seven EDIIIs to prepare mosaic nanoparticles) at room temperature overnight. Conjugated EDIII-mi3 were purified from free EDIII-SpyTag003 by SEC using a Superose 6 10/300 (GE Healthcare) column equilibrated with PBS (20 mM sodium phosphate pH 7.5, 150 mM NaCl). SDS-PAGE was used to analyze the eluted fractions corresponding to conjugated EDIII-mi3. The concentration of EDIII-mi3 was determined using a Bio-Rad Protein Assay. Admix nanoparticle mixtures were prepared by combining equimolar amounts of five or seven EDIII-conjugated homotypic nanoparticles. The schematic of EDIII-nanoparticles was created with BioRender.com.

Immunizations. Immunizations were performed using 4-6 week old male C57BL mice with three mice in the cohort immunized with SpyCatcher003-mi3 cohort and five mice in all other cohorts immunized with EDIII-mi3. Immunizations were carried out with subcutaneous injections of 5 μ g of conjugated EDIII (calculated as the mass of the EDIII, assuming 100% efficiency of conjugation to SpyCatcher003-mi3) or 5 μ g of unconjugated SpyCatcher003-mi3, in 100 μ L of 50% v/v AddaVax adjuvant (Invivogen). The mice were boosted at 14, 28, and 42 days after the prime with the same quantity of antigen in adjuvant. Animals were bled via tail veins on day 0 (before the prime) and at days 14, 28, and 42 (before each boost). On day 60, the mice were euthanized and bled via cardiac puncture and spleens were harvested. Animal experiments were performed in accordance with Protocol 18074 at Rockefeller University approved by the Institutional Animal Care and Use Committee (IACUC). Blood samples from Day 0, 14, 28 and 42 were placed in MiniCollect Serum and Plasma Tubes (Greiner) and centrifuged at 15,000 rpm for one minute to separate the red blood cells from the sera and kept at -20°C. Day 60 samples were placed in 1.5 mL microcentrifuge tubes (Eppendorf) kept on ice before centrifugation at 15,000 rpm for one minute to clot the blood. The sera was harvested, frozen in liquid nitrogen, and stored at -80°C until ELISAs were performed.

ELISAs. ELISAs were performed as previously described^{136,202,236}. Briefly, EDIIIs at 2.5 μ g/mL in 100 mM NaHCO₃ pH 9.8 were coated on Nunc MaxiSorp 384-well plates (Sigma). After incubation overnight at 4°C, plates were blocked with 3% bovine serum albumin (BSA) in 20 mM Tris pH 8.0, 150 mM NaCl, 0.02% sodium azide, 0.1% Tween20 (TBS-T) at room temperature for one hour. Blocking solution was removed before IgGs (four-fold serially diluted in 3% BSA, TBS-T from a starting concentration of 50 μ g/mL) were added to the plates. After incubation at room temperature for 3 hrs., plates were washed with TBS-T and incubated with a 1:50,000 dilution of secondary HRP-conjugated goat anti-mouse IgG H&L (ab6789; Abcam) for 45 minutes at room temperature. Plates were then washed with

TBS-T, SuperSignal ELISA Femto Maximum Sensitivity Substrate (ThermoFisher) was added, and plates were read at 425 nm. ELISAs were performed in duplicate and area under the curve (AUC) and 50% binding concentrations (IC_{50}) were determined after sigmoidal nonlinear regression (least-squares method without weighting; GraphPad Prism 9.0.0). One 7-mosaic sera sample was only assessed from a single assay for binding to DENV2 due to a technical error.

CHAPTER 4

Capturing the breathing conformation of Fab-bound Zika virus with cryo-electron microscopy

Summary

Previous cryo-EM flavivirus structures^{21,22,28} showed one static envelope structure, but evidence suggests envelope proteins of both mature and immature virions are dynamic and sample different conformations^{29,30,33,34}. As demonstrated by antibody (Ab) neutralization at viral epitopes inaccessible in static models of virions^{29,30,33,34,36}, the phenomenon of flavivirus “breathing” to expose cryptic Ab epitopes may result from conformational changes of the E protein during the viral lifecycle, such as during fusion²³⁷. Further evidence is provided by the finding that the potency of Abs against dengue virus is affected by mutations distant from the epitope, suggesting these mutations modulate virus “breathing” and epitope accessibility²⁹.

Cryo-electron microscopy (cryo-EM) structures of Zika virus (ZIKV) have been solved at resolutions as high as 3.1 Å with and without Fabs from neutralizing Abs^{21,22,28,35,61,238–241}. Known structures of Fab-bound ZIKV do not show major conformational differences from mature ZIKV unbound by Fab. However, crystal structures of Fabs of potentially neutralizing *VH3-23/VK1-5* Abs, Z004 or Z006, in complex with ZIKV envelope domain III (EDIII)³⁶ superimposed onto the cryo-EM mature^{22,28} or immature²¹ ZIKV virion structures show these Abs cannot bind to the virus in the crystallographically-observed conformations due to steric hinderance (Figure 4.1). This suggests ZIKV undergoes a conformational change, or “breathing”, upon *VH3-23/VK1-5* Fab binding. Here, I showed progress using cryo-EM to capture the “breathing” conformation of Fab-bound mature ZIKV.

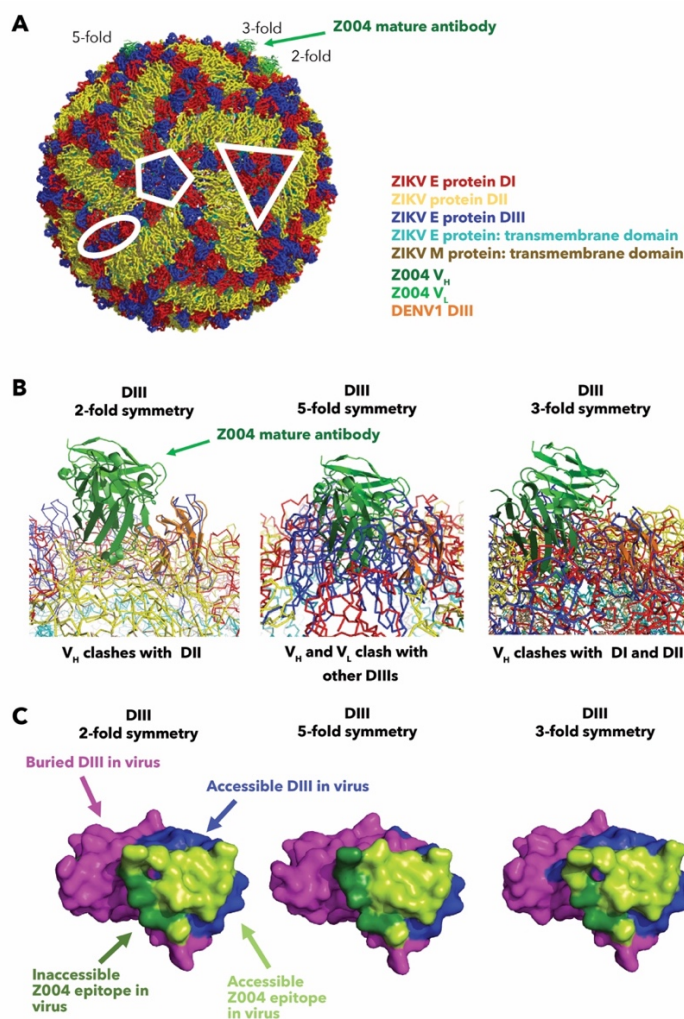


Figure 4.1. *VH3-23/VK1-5* Fab binding to EDIII clashes in the cryo-EM structure of mature ZIKV.

A. The Z004_{mature} Fab–DENV1 EDIII (green–orange) from the crystal structure is superimposed on the EDIIIs of the mature ZIKV cryo-EM structure (PDB 6CO8) corresponding to the two, three, and five-fold local symmetry environments (white). **B.** A magnified view of each Fab–EDIII superimposed on the virion EDIIIs (from part 7A) shows the Fab clashes with other domains in the virion structure. **C.** Surface representations of the

Z004_{mature} binding epitope on EDIIIs (green) showing the portion that is accessible (light green) and the portion that is buried (dark green).

Initial screening of Fab-mature ZIKV was performed for several Fabs using a Talos Arctica microscope with a 16M Ceta CMOS camera. An incubation time of 30 minutes to one hour at 4°C was sufficient to visualize “spiky” particles, indicating Fabs were bound to ZIKV. Molar ratios of 0.01-1 of Fab to E protein were assessed, with an increased molar ratio associated with the appearance of spikier virus particles (Figure 4.2).

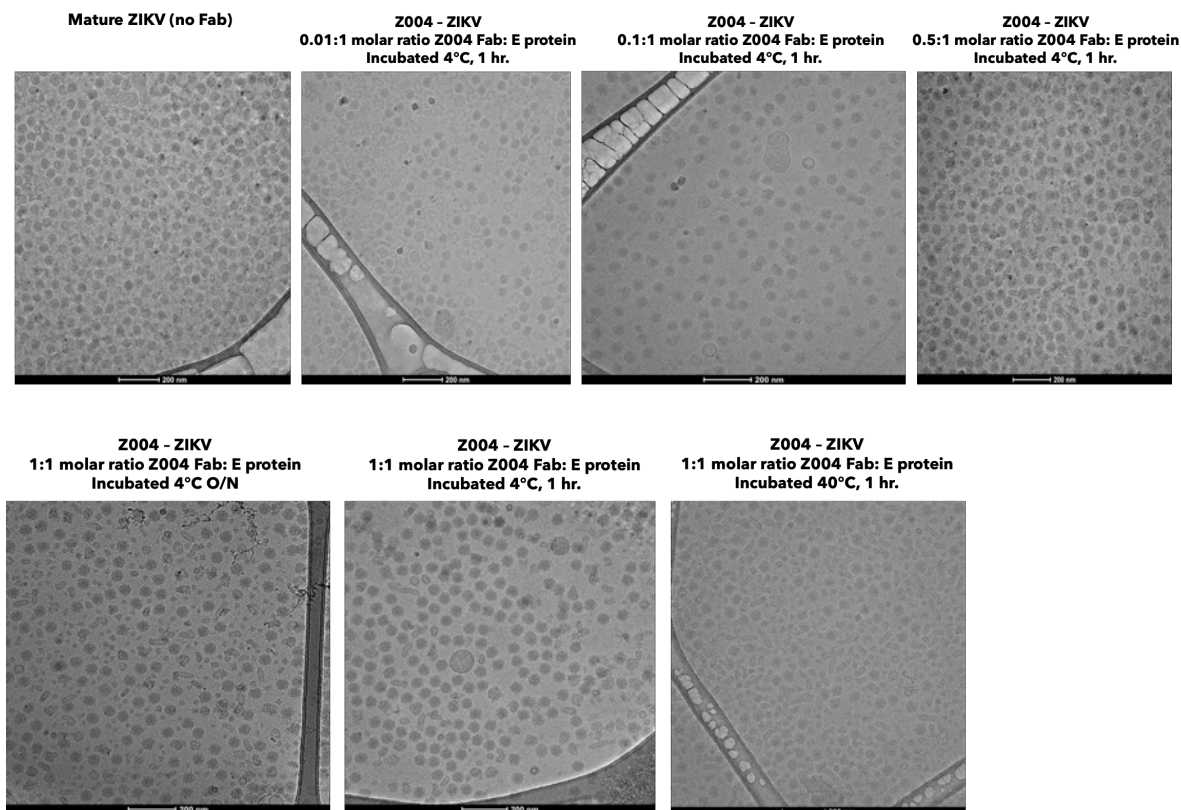
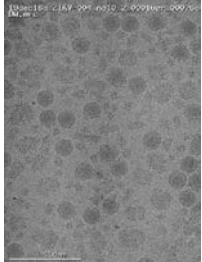
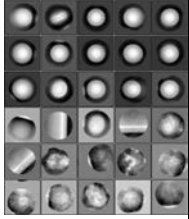
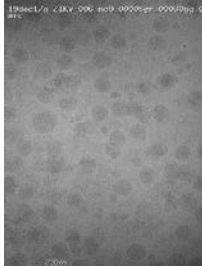
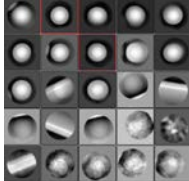
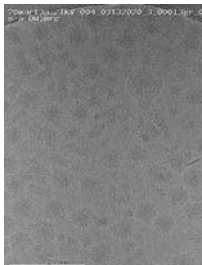
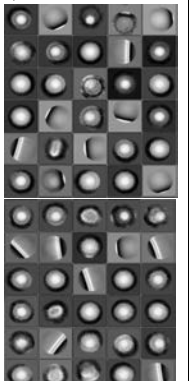
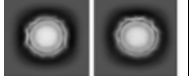
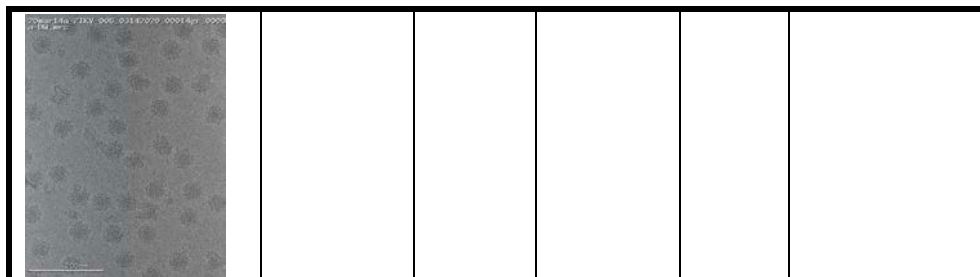


Figure 4.2. Electron micrographs of Z004 Fab–mature ZIKV.

Molar ratios of Fab to E protein ranging from 0.01 to 1, incubation temperatures of 4°C or 40°C, and incubation times of 1 hour or overnight (O/N) were analyzed.

Four data sets were then collected on a Titan Krios microscope with a K3 detector (Table 4.1). Processing for the first two datasets, Z004 Fab–ZIKV at a 0.1:1 molar ratio of Fab to E protein and Z006 Fab–ZIKV at a 0.01:1 ratio, resulted in a model without Fab bound, indicating the Fab to E protein molar ratio was too low. For the second two datasets, Z004 Fab–ZIKV and Z006 Fab–ZIKV, both at 0.5:1 Fab to E protein, the latter set was prioritized for processing due to the higher quality of the viruses on the micrographs. Both sets showed “spiky” particles, suggesting Fab was bound. For Z006 Fab–ZIKV, processing with cryoSPARC software showed a promising initial model with the lipid bilayer visible. However, further processing is necessary since the presence of heterogenous particles complicates model interpretation.

Table 4.1. Summary of Fab–ZIKV datasets collected with a Titan Krios microscope.					
Fab – ZIKV Complex	Fab: E protein molar ratio	Incubation conditions	Processing software	# images	# Particles & 2D classes
Z004 Fab–ZIKV 	0.1:1	4°C, 1 hr.	FindEM, Relion, JSPR	3,145	5,670 
Z006 Fab–ZIKV 	0.01:1	4°C, 2 hrs.	FindEM, Relion, JSPR	3,324	12,585 
Z004 Fab–ZIKV 	0.5:1	4°C, 1 hr.	FindEM, Relion, JSPR	1,349	2,658 
Z006 Fab–ZIKV	0.5:1	4°C, 1 hr.	CryoSPARC	1,013	20,792 



CHAPTER 5

***VH3-30* antibodies that target the SARS-CoV-2 RBD show diverse neutralization and cross-reactivity profiles**

Abstract

Neutralizing antibodies against the SARS-CoV-2 spike trimer, many recognizing the receptor-binding domain (RBD), correlate with protection from infection. While class 1 and class 2 anti-RBD antibodies that block ACE2 binding are strongly neutralizing, class 4 antibodies target less accessible regions of the RBD base, and generally show weaker, but more broadly cross-reactive, neutralization. Understanding how antibody properties and epitopes correlate with neutralization potency and breadth is critical for vaccine design and developing antibody therapeutics. Here we focused on *VH3-30*-derived antibodies, comparing potent neutralizers with tightly-binding, but weakly-neutralizing, antibodies. Single-particle cryo-electron microscopy structures of Fab–spike complexes showed that Fabs from five weakly-neutralizing and one potently-neutralizing *VH3-30* antibody caused dissociation of the spike trimer, with the potently-neutralizing antibody binding to a hybrid class 1/4 epitope. Analyses showed how variations in antibody light chains and CDRH3 lengths affected *VH3-30* Ab targeting of class 1-4 epitopes, and how epitopes correlated with spike trimer dissociation and neutralization across sarbecoviruses. The diverse epitopes,

cross-reactivity, and neutralization profiles of *VH3-30* Abs illustrate their importance for vaccine design and therapeutic antibody development.

Significance Statement

The detection of new SARS-CoV-2 variants and potential for new coronaviruses to spread from other species to humans has demonstrated the importance of developing therapeutic approaches that provide broad protection against infection and severe symptoms. Eliciting class 4 Abs is a potential therapeutic strategy since these antibodies bind epitopes on the RBD that are more conserved among coronaviruses and SARS-CoV-2 variants. By directly comparing the different epitopes, neutralization potencies and cross-reactivity profiles of *VH3-30* class 4 antibodies, we provide insight into the molecular features that determine the breadth and potency of antibody recognition and the potential for causing SARS-CoV-2 spike trimer dissociation.

Introduction

The previous SARS-CoV and Middle East Respiratory Syndrome coronavirus (MERS-CoV) epidemics and current SARS-CoV-2 pandemic demonstrated the necessity of investigating immune responses to betacoronavirus infection and vaccination^{95–97,99,100}. Given concerns regarding new SARS-CoV-2 variants and the possibility for newly-emerging zoonotic betacoronaviruses to cause future outbreaks^{104,105,107–110}, it is important to thoroughly understand possible strategies that may confer broad protection against different SARS-like betacoronavirus (sarbecovirus) strains. Determining how the properties and epitopes of antibodies (Abs) correlate with their neutralization mechanism and cross-reactivity is critical for informed design of vaccines and Ab therapeutics that effectively accomplish this aim.

Abs that target the receptor-binding domains (RBDs) of the SARS-CoV-2 spike (S) trimer represent an important component of the protective immune response against infection^{112–115,124–134}. The potent neutralization demonstrated by many of these Abs has been attributed to their ability to block the RBD from binding the SARS-CoV-2 host receptor, angiotensin-converting enzyme 2 (ACE2)^{114–117}, therefore preventing viral entry^{114,132,135–139}. RBDs can adopt ‘up’ and ‘down’ conformations on S trimer, but only bind ACE2 when in an ‘up’ conformation^{112–114,118–123}. Abs that target the RBD have been described using a simplified classification scheme: class 1 *VH3-53/VH3-63*-derived Abs with short heavy chain complementarity-determining region 3s (CDRH3s) that bind only ‘up’ RBDs at an epitope

overlapping with the ACE2 binding site, class 2 Abs that bind ‘up’ or ‘down’ RBDs and also overlap with the ACE2 binding site, class 3 Abs that do not block ACE2 and bind ‘up’ or ‘down’ RBDs on the surface adjacent to the glycan at residue N343, and class 4 Abs that usually exhibit weaker neutralization potencies and bind a cryptic surface of an ‘up’ RBD that faces the S trimer interior¹³².

While the class 4 surface of the RBD is less accessible than other RBD epitopes, it is more conserved than the class 1 and 2 epitopes and has been suggested as a potential target for vaccine design to elicit broadly neutralizing Abs against other sarbecovirus strains^{122,136,242–245}. Ab binding to class 4 cryptic epitopes has been proposed to disrupt the prefusion-conformation of the spike and potentially cause spike shedding as a neutralization mechanism^{122,136,137,244}. However, some class 4 Abs are only weakly neutralizing, possibly due to the reduced accessibility of the epitope^{122,134,135,137,244–247}. There are some exceptions that potently neutralize SARS-CoV-2, including COVA1-16 (half maximal inhibitory concentration, IC₅₀): 20 ng/mL)^{124,248}, H014 (~150-5,700 ng/ml; humanized mouse Ab)²⁴⁹, C118 (104 ng/mL)^{127,136}, C022 (74 ng/mL)^{127,136}, DH1047 (90-124 ng/mL)^{250,251}, ADG-2 (~1 ng/mL; engineered with direct evolution)²⁵², and ADI-56046 (10-100 ng/mL)²⁵³. Of these Abs, H014, C118, C022, DH1047, ADG-2, and ADI-56046 show relatively potent cross-neutralization of SARS-CoV and/or other sarbecoviruses^{127,136,249,250,252,253}.

Among RBD-targeting Abs, one of the germline heavy chain V gene segments that was reported as enriched or overrepresented compared to the human Ab repertoire is *VH3-30* and the closely-related *VH3-33* or *VH3-30-3* V gene segments^{124,126–129,134,254}. These and other Abs against SARS-CoV-2 show a relatively low number of somatic hypermutations compared to Abs isolated from individuals with other chronic infections^{124,126,127,245}. Notably, *VH3-30* Abs have been found to bind class 2, 3, and 4 epitopes on the RBD^{122,127,132,135,136,255–257}. While some *VH3-30* Abs have been reported as weak or non-neutralizing^{122,134,135,137}, potently-neutralizing *VH3-30* Abs have also been described, specifically P17 (class 2)²⁵⁶,

C002 (class 2)^{127,132}, C135 (class 3)^{127,132}, REGN10987 (class 3)^{255,258}, and C118 (class 4)^{127,136}. Understanding which Ab properties and epitopes correlate with potent versus weak neutralization and broad versus narrow cross-reactivity is important for guiding the design of vaccines intended to elicit broadly neutralizing *VH3-30* Abs.

Here we report binding, neutralization, and structural studies to compare the epitopes, cross-reactivity and characteristics of weakly versus potently neutralizing Abs with a *VH3-30* or a closely-related V gene segment. From a panel of *VH3-30* RBD-targeting Abs previously isolated from COVID-19 convalescent donors¹²⁷, we selected six Abs that bound comparably to SARS-CoV-2 RBD (half maximal binding (EC_{50} s) within 3.8-fold of each other¹²⁷), one of which was potently neutralizing: C149 (*IGHV3-30* or *IGHV3-30-5*), and five that were weakly or non-neutralizing: C008 (*IGHV3-30*), C027 (*IGHV3-30*), C030 (*IGHV3-30*), C113 (*IGHV3-33*), and C133 (*IGHV3-30-3*)¹²⁷. We performed structural, cross-reactivity, and neutralization studies for these six Abs and compared them with other *VH3-30* Abs that were previously structurally characterized, including C002 (*IGHV3-30* or *IGHV3-30-5*)^{127,132}, C118 (*IGHV3-30-3*)^{127,136}, C135^{127,132} (*IGHV3-30* or *IGHV3-30-3*), and REGN10987 (*VH3-30* or *VH3-30-3/VL2-14*)^{255,258} (SI Appendix, Table S5.1). Using single-particle cryo-electron microscopy (cryo-EM) and X-ray crystallography, we showed that the five weak neutralizers bind distinct cryptic class 4 epitopes and cause S trimer dissociation. We also determined the structure of the potent *VH3-30* neutralizer C149 bound to a hybrid RBD epitope midway between the class 1 and class 4 epitopes that is more accessible than class 4 epitopes, partly overlaps with the ACE2 epitope, and also causes S trimer dissociation. Our findings describe insights into the epitopes and properties of *VH3-30* Abs that correlate with weak versus potent neutralization and trimer dissociation. Furthermore, we demonstrated that the *VH3-30* class 4 weakly-neutralizing Abs showed diverse cross-reactivity, an important consideration for the development of vaccines aimed at eliciting a protective response against multiple sarbecovirus strains.

Results

VH3-30 Abs that bind SARS-CoV-2 RBD showed variable neutralization potencies. From a collection of 534 anti-RBD Abs isolated from convalescent COVID-19 donors, 105 were encoded by *VH3-30* or a closely-related V gene segment, and some of these exhibited weak or no neutralization in vitro (50% inhibitory concentrations, IC_{50} s, of >1000 ng/mL)¹²⁷. From this panel, we investigated five weak or non-neutralizers (C008, C027, C030, C113, and C133), and one potent neutralizer (C149), by performing SARS-CoV-2 and SARS-CoV pseudovirus-based neutralization assays²⁵⁹ starting at Ab concentrations higher than 1000 ng/mL. The IC_{50} s we determined under these conditions for C008 (7.39 μ g/mL), C027 (50.0 μ g/mL), C030 (352 μ g/mL), C113 (68.5 μ g/mL), and C133 (21.7 μ g/mL) showed that these Abs can neutralize SARS-CoV-2, although weakly (Figures 5.1A,C; Table 5.1). Our neutralization assays also confirmed that C149 (IC_{50} = 14.1 ng/mL) neutralizes SARS-CoV-2 (Figures 5.1A,C; Table 5.1) with a potency comparable to those of other *VH3-30* Abs, including C002 (8.9 ng/mL)¹²⁷, C135 (16.6 ng/mL)¹²⁷, REGN10987 (\sim 0.615 ng/mL)²⁵⁵, and C118 (440 ng/mL)¹³⁶ (Table 5.1). Of the six *VH3-30* Abs we investigated from the collection in Robbiani et al. (2020)¹²⁷, only C027 neutralized SARS-CoV (IC_{50} = 43.8 μ g/mL). The other Abs showed no neutralization above background levels observed for a negative control Ab against SARS-CoV at concentrations ≥ 500 μ g/mL (Figure 5.1B-C).

VH3-30 Abs exhibited cross-reactive binding to other sarbecovirus RBDs. We next assessed whether the six *VH3-30* Abs showed cross-reactive binding to a panel of sarbecovirus RBDs. ELISA measurements demonstrated that the *VH3-30* Abs showed variable cross-reactivity

profiles (Figure 5.1D; SI Appendix, Figure S5.1). While the potent neutralizer C149 did not show any cross-reactivity, the weakly neutralizing Abs C008, C027, C030, C113 and C133 all showed strong cross-reactivity to at least two other RBDs besides SARS-CoV-2 (Figure 5.1D; SI Appendix, Figure S5.1). The weakly neutralizing Ab C133 showed the broadest cross-reactivity with binding to all RBDs, although binding to SARS-CoV and Rs4081 was relatively reduced. Additionally, C133 was the only one of the six Fabs that showed binding to BM4831. The weakly neutralizing Abs C027 and C030 showed cross-reactivity to five RBDs (SARS-CoV, WIV1, SHC014, RaTG13 and Rs4081), although binding to SARS-CoV was again reduced. Cross-reactivity by C008 and C113 was more limited: C008 showed strong binding to WIV1 and SHC014 and reduced binding to RaTG13, which shares ~89% protein sequence similarity to SARS-CoV-2 RBD (SI Appendix, Figure S5.2). C113 demonstrated strong binding to RaTG13 and reduced binding to WIV1 and SHC014 (Figure 5.1D).

Structures of VH3-30 Fabs revealed RBD epitopes and evidence for S trimer dissociation.

To further investigate the different neutralization potencies and cross-reactive RBD-binding profiles, we used X-ray crystallography and single-particle cryo-EM to solve structures of Fab-RBD and Fab-S trimer complexes, respectively. We set up crystallization trials for each of the six Fabs in complex with SARS-CoV-2 RBD, obtaining crystals from which a structure solution was possible for two complexes: C133-RBD-C119 (where the Fab from the C119 neutralizing Ab^{127,132} was added to aid in crystallization) and C008-RBD, resulting in 3.15 Å and 3.0 Å structures, respectively (Figure 5.2A-B; SI Appendix, Tables S5.2-5.4, Figure S5.3-5.5). We also determined cryo-EM structures of Fabs in complex with SARS-CoV-2 6P S trimer²⁶⁰ for the weakly-neutralizing anti-RBD Abs C008, C027, C030, C113, and C133 and for the potently neutralizing Ab C149 (Figure 5.3; SI Appendix, Figure S5.3-5.5).

Classes corresponding to S trimers were observed in all cryo-EM datasets except C149; however, they were not complexed with Fab(s) with the exception of the C133-S complex, which showed a Fab-bound trimer with increased separation between RBDs compared with other anti-RBD Fab-S complexes. The cryo-EM dataset is still being processed. The crystal structure showed C133 bound low on the RBD at a class 4 epitope similar to that of the *VH3-30-18* Ab EY6A¹²² and non-*VH3-30* weakly-neutralizing Abs such as CR3022^{244,245}, S2A4¹³⁷, and S304¹³⁴ (Figures 5.2-5.4; SI Appendix, Figure S5.3-5.5).

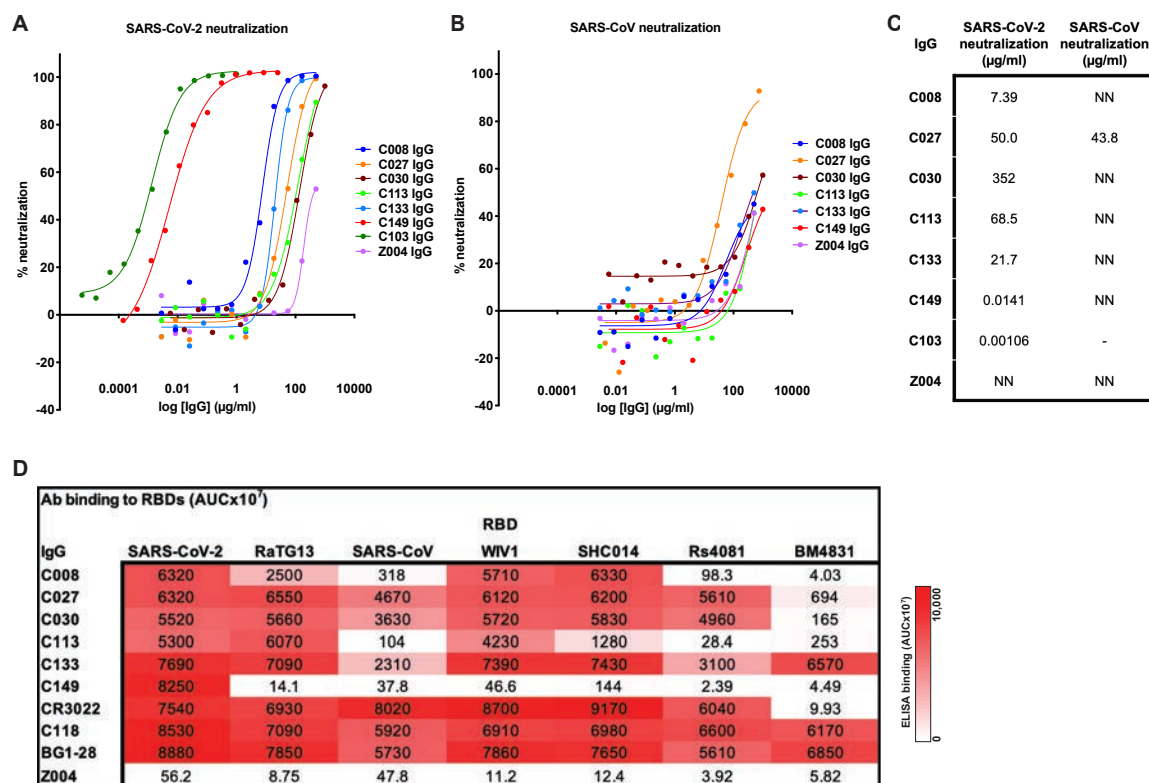


Figure 5.1. Neutralization potencies and binding affinities of anti-SARS-CoV-2 Abs.

Neutralization potencies of Abs against **A.** SARS-CoV-2 and **B.** SARS-CoV pseudoviruses.

Two independent neutralization experiments were performed; data from one experiment are shown with data points representing the mean of duplicates. **C.** IC₅₀ values reported as the

mean of two independent neutralization experiments. NN = non-neutralizing at ≥ 500 $\mu\text{g/mL}$. C103¹²⁷ IgG is a positive control for SARS-CoV-2 neutralization. **D.** Ab binding to sarbecovirus RBDs reported as area under the curve (AUC) calculated from the binding curves in SI Appendix, Figure S5.1. CR3022^{136,244,245}, C118¹³⁶, and BG1-28²⁶¹ IgGs served as positive controls. Z004 IgG is an anti-Zika Ab serving as a negative control³⁶.

Table 5.1. *VH3-30* and class 4 anti-SARS-CoV-2 Abs.

Ab type	Ab	Study	CDRH3 length	Class	Heavy chain V gene	Light chain V gene	SARS-CoV-2 neutralization IC50 (ng/ml)
VH3-30 class 1/4 potent neutralizers	C149	Robbiani et al. (2020), this study	18	1/4	VH3-30 or VH3-30-5	VK1-39	14.1
VH3-30 class 2 potent neutralizers	C002	Robbiani et al. (2020), Barnes et al. (2020)	17	2	VH3-30 or VH3-30-5	VK1-39	8.9
	P17	Yao et al. (2021)	12	2	VH3-30	-	~29
VH3-30 class 2 weak or non-neutralizers	COVOX-75	Dejnirattisai et al. (2021)	20	2	VH3-30	-	weak or non-neutralizing
VH3-30 class 3 potent neutralizers	C135	Robbiani et al. (2020), Barnes et al. (2020)	12	3	VH3-30 or VH3-30-3	VK1-5	16.6
	REGN10987	Hansen et al. (2020)	13	3	VH3-30 or VH3-30-3	VL2-14	~0.615
VH3-30 class 3 weak neutralizers	COVOX-45	Dejnirattisai et al. (2021)	14	3	VH3-30-3	-	2,005
VH3-30 class 4 potent neutralizers	C118	Robbiani et al. (2020), Jette et al. (2021)	20	4	VH3-30-3	VL4-69	104
	C008	Robbiani et al. (2020), this study	13	4	VH3-30 or VH3-30-5	VK1-5	625-7390
VH3-30 class 4 weak neutralizers	C027	Robbiani et al. (2020), this study	20	4	VH3-30-5	VK1-5	50,000
	C030	Robbiani et al. (2020), this study	20	4	VH3-30 or VH3-30-5	VK1-5	352,000
	C113	Robbiani et al. (2020), this study	18	4	VH3-33	VK1-5	68,500
	C133	Robbiani et al. (2020), this study	16	4	VH3-30-3	VK1-39	21,700
	EY6A	Zhou et al. (2020)	14	4	VH3-30-18	VK1-39	70-20,000
non-VH3-30 class 4 potent neutralizers	C022	Robbiani et al. (2020), Jette et al. (2021)	17	4	VH4-39	VK1-5	74
	COVA1-16	Brouwer et al. (2020), Liu et al. (2020)	22	4	VH1-46	VK1-33	20
	DH1047	Martinez et al. (2021), Li et al. (2021)	24	4	VH1-46	-	90-124
	ADI-56046	Wec et al. (2020)	18	4	VH3-53	-	10-100
	H014	Lv et al. (2020)	13	4	-	-	~150-5,700
	ADG-2	Rappazzo et al. (2021)	-	4	-	-	1
non-VH3-30 class 4 weak neutralizers	S304	Pinto et al. (2020)	14	4	VH3-13	VK1-39	>5000
	CR3022	Yuan et al. (2020), Huo et al. (2020)	12	4	VH5-51	VK4-1	114 - >400,000
	S2A4	Piccoli et al. (2020)	12	4	VH3-7	VL2-23	3500
	S2X35	Piccoli et al. (2020)	-	4	VH1-18	VL1-40	500

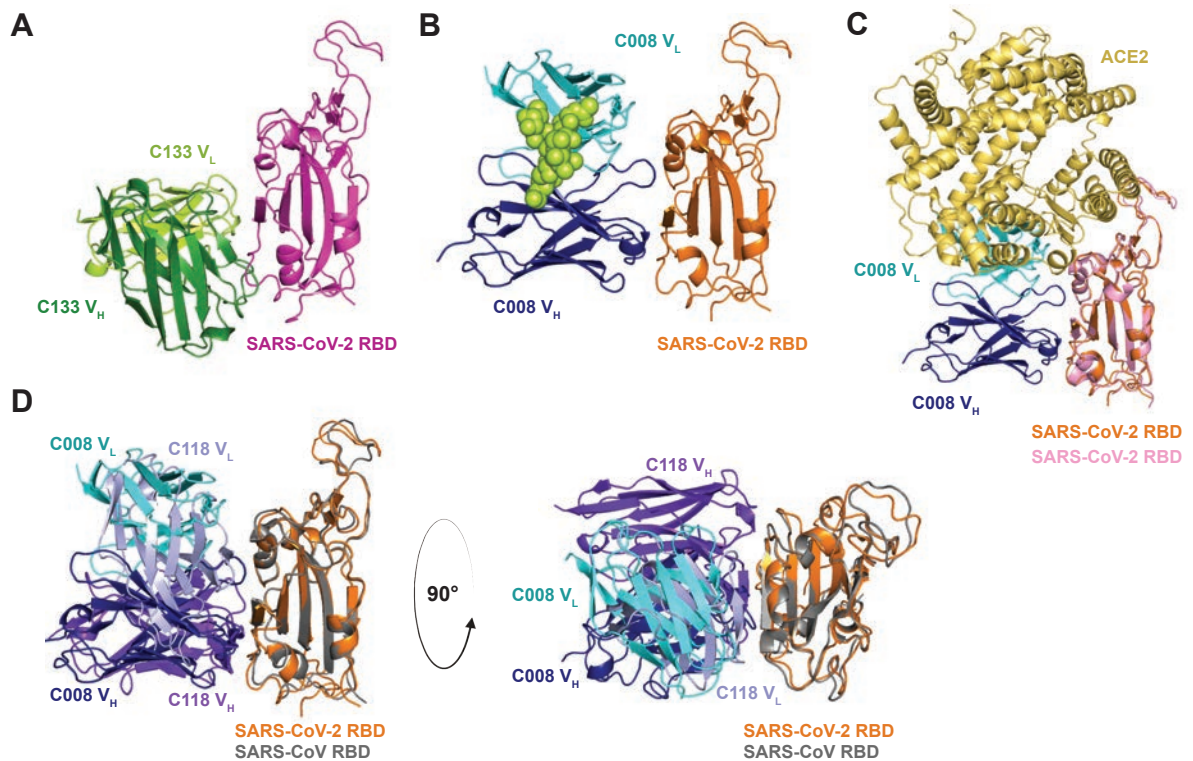


Figure 5.2. Crystal structures of C133 and C008 Fabs bound to SARS-CoV-2 RBD.

Cartoon representations of the V_HV_L portion of **A**. C133 Fab in complex with SARS-CoV-2 RBD. The C119 Fab that is also bound is not shown for clarity. **B**. C008 Fab in complex with SARS-CoV-2 RBD complex. The glycan at residue N26 is shown as green spheres. **C**. C008 V_HV_L–SARS-CoV-2 RBD is shown overlaid with the ACE2–RBD structure (PDB 6M0J) showing the clash between C008 V_L and ACE2. **D**. C008 V_HV_L–SARS-CoV-2 RBD is shown overlaid with C118 V_HV_L–SARS-CoV RBD.

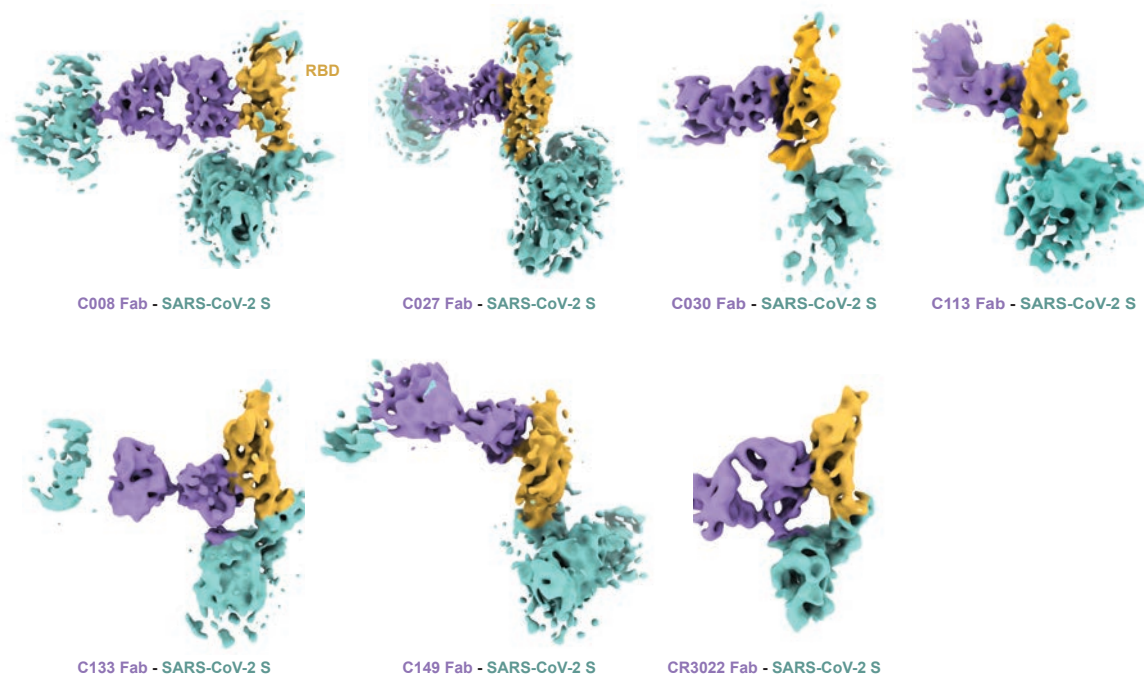


Figure 5.3. Cryo-EM density maps of SARS-CoV-2 S protomers bound by C008, C027, C030, C113, C133, C149, and CR3022 Fabs.

While C133-S was the only complex showing Fab-bound trimer, all six Fab-S complexes showed Fab bound to a dissociated spike protomer. Fabs from weakly neutralizing *VH3-30* Abs bound to S protomers showed variable class 4 epitopes where the RBD sequence is more conserved, consistent with their observed cross-reactivity^{122,136,245,249,250,252,253} (Figure 5.1D, 5.4). C027, C030, and C113 bound overlapping epitopes laterally oriented on the class 4 surface that are distinct from epitopes of other structurally-characterized class 4 Abs (Figure 5.4).

C008 bound more centrally on the class 4 region of the RBD, with an epitope similar to that of the *VH3-30-3* potentially-neutralizing Ab C118¹³⁶ as well as potentially neutralizing non-*VH3-*

30 Abs including C022¹³⁶, COVA1-16^{124,248}, H014²⁴⁹, and DH1047^{250,251} (Figure 5.2-5.4; SI Appendix, Figure S5.3-5.5). Since the C008 epitope partly overlapped with that of the more potently neutralizing *VH3-30-3* Ab C118¹³⁶, we superimposed the C008 V_H-V_L-SARS-CoV-2 RBD and C118 V_H-V_L-SARS-CoV crystal structures¹³⁶. The superimposition showed that C008 V_H-V_L was rotated 45-90° compared to C118 V_H-V_L with less overlap between the V_{HS} than the V_{LS} (Figure 5.2D). Comparisons of buried surface areas (BSAs) on the RBDs and interacting residues at the binding interfaces revealed that the C008 *VKI-5* V_L made fewer contacts with the RBD (7 vs. 11 residues) with 50% less BSA (160 Å² vs. 320 Å²) than C118 VL4-69 V_L (SI Appendix, Table S5.5). This difference was largely accounted for by increased contacts from the C118 V_L framework region 3 (FWRL3) and complementarity determining region 2 (CDRL2). While the BSA on the RBD contributed by the V_H domain was similar between C008 and C118, C008 showed more CDRH2 interactions whereas C118 showed more CDRH1 and CDRH3 interactions. Upon superimposing the RBDs of the C008-RBD and ACE2-RBD (PDB 6M0J)¹¹⁷ structures, the C008 V_L showed a clash with the ACE2 similar to that previously reported for C118 V_L¹³⁶ (Figure 5.2C). Apart from pairing with light chains derived from different V gene segments, other notable differences between C008 and C118 are the CDRH3 length (13 vs. 20 residues) and the presence of an N-linked glycan at C008 V_L residue N26 (Figure 5.2B, Table 5.1; SI Appendix, Tables S5.1, S5.5). This residue corresponds to a serine in V_{LS} of all other *VH3-30* Fab-RBD structures that we compared except REGN10987 (threonine)²⁵⁵ (SI Appendix, Figure S5.4).

Of the Fab-S protomer structures, the epitope of the potent neutralizer C149 was highest on the RBD, being located midway between the epitopes for class 1 and class 4 ant-RBD Abs, a previously-unreported binding site for anti-SARS-CoV-2 *VH3-30* Abs (Figures 5.3-5.4; SI Appendix, Figure S5.3-5.5). This epitope partly overlapped with the ACE2 binding site and with class 1 epitopes typically targeted by *VH3-53/VH3-63*-derived Abs¹³². The location of

the epitope high on the RBD where the sequence is less conserved, is consistent with the lack of cross-reactivity observed by C149^{122,136,242-245} (Figure 5.1D, 5.3-5.4). However, the C149 epitope also partly overlapped with epitopes of *VH3-30* and non-*VH3-30* class 4 Abs, but would be less buried at the S trimer center (Figures 5.4; SI Appendix, Figure S5.3-5.5).

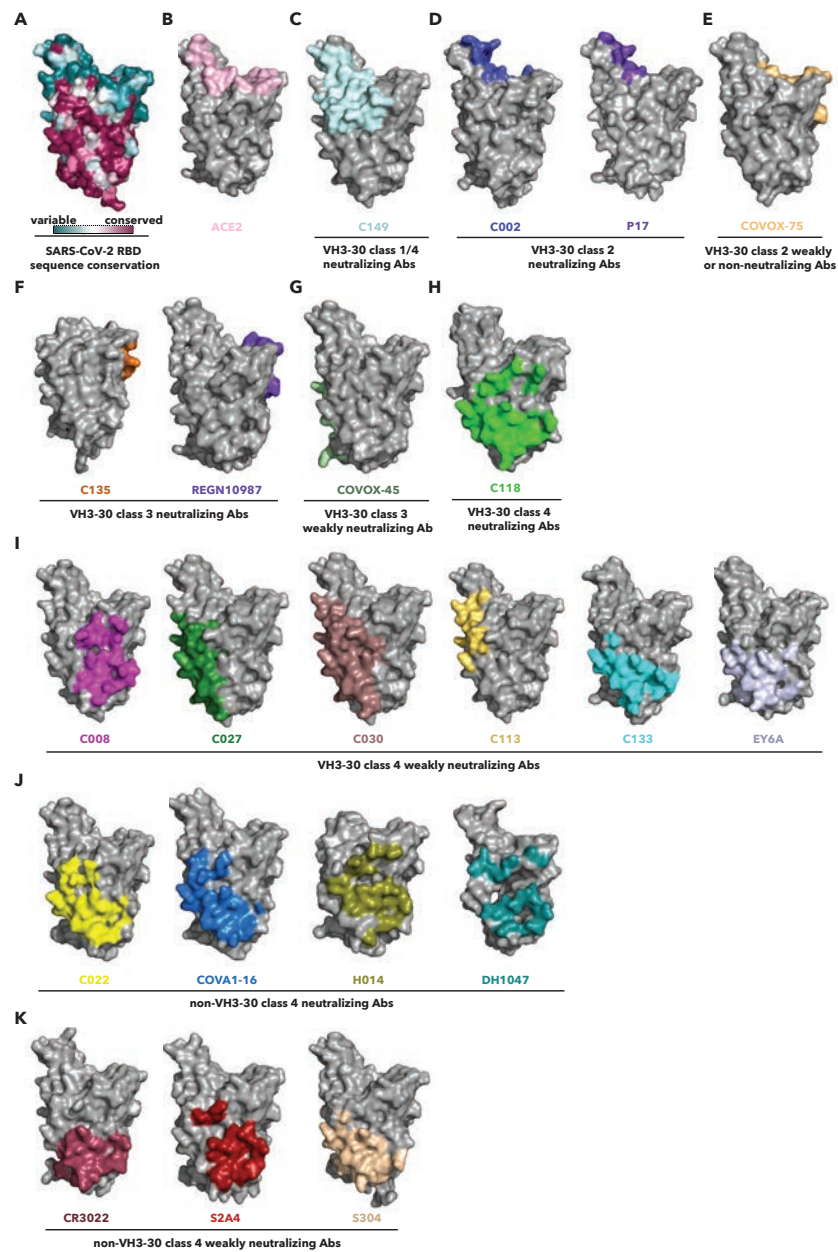


Figure 5.4. Comparison of Fab-RBD binding interfaces.

Surface representations are shown for the side of the RBD that faces the trimer center. **A.** Amino acid sequence conservation of seven RBDs (SI Appendix, Figure S5.2) plotted on a surface representation of a SARS-CoV-2 RBD (PDB 7BZ5). Surface representation of SARS-CoV-2 epitopes contact by: **B.** ACE2, **C.** *VH3-30* class 1/4 neutralizing Ab, **D.** *VH3-30* class 2 neutralizing Abs, **E.** *VH3-30* class 2 weakly or non-neutralizing Ab, **F.** *VH3-30* class 3 neutralizing Abs, **G.** *VH3-30* class 3 weakly neutralizing Ab, **H.** *VH3-30* class 4 neutralizing Ab, **I.** *VH3-30* class 4 weakly neutralizing Abs, **J.** non-*VH3-30* class 4 neutralizing Abs, and **K.** non-*VH3-30* class 4 weakly neutralizing Abs. All Ab epitopes are represented on SARS-CoV-2 RBDs except for C118, which is based on SARS-CoV RBD.

Since the C008 epitope partly overlaps that of the more potently neutralizing *VH3-30-3* Ab C118¹³⁶, we superimposed the C008 V_H - V_L -SARS-CoV-2 RBD and C118 V_H - V_L -SARS-CoV crystal structures¹³⁶. The superimposition showed that C008 V_H - V_L was rotated 45-90° compared to C118 V_H - V_L with the V_{HS} overlapping less than V_{LS} (Figure 5.4D). Comparisons of buried surface areas (BSAs) on the RBDs and interacting residues at the binding interfaces revealed that the C008 *VK1-5* V_L made fewer contacts with the RBD (7 vs. 11 residues) with 50% less BSA (160 Å² vs. 320 Å²) than C118 VL4-69 V_L (SI Appendix, Table S5.5). This difference was largely accounted for by increased contacts from the C118 V_L framework region 3 (FWRL3) and complementary determining region 2 (CDRL2). While the BSA on the RBD contributed by the V_H domain was similar between C008 and C118, C008 showed more CDRH2 interactions whereas C118 showed more CDRH1 and CDRH3 interactions. Upon superimposing the RBDs of the C008-RBD and ACE2-RBD (PDB 6M0J)¹¹⁷ structures, the C008 V_L showed a clash with the ACE2 similar to that previously

reported for C118 V_L¹³⁶ (Figure 5.4C). Apart from pairing with light chains derived from different V gene segments, other notable differences between C008 and C118 are the CDRH3 length (13 vs. 20 residues) and the presence of an N-linked glycan at C008 V_L residue N26 (Figure 5.4B, Table 5.1; SI Appendix, Tables S5.1, S5.5). This residue corresponds to a serine in V_Ls of all other *VH3-30* Fab–RBD structures that we compared except REGN10987 (threonine)²⁵⁵ (SI Appendix, Figure S5.2).

VH3-30 Abs show diverse cross-reactivity profiles against other sarbecoviruses. Since class 4 RBD epitopes are highly conserved among sarbecoviruses and have been proposed as a potential target for vaccine design to elicit a cross-reactive neutralizing response^{122,136,242–245}, we assessed whether the six *VH3-30* Fabs we structurally characterized showed cross-reactive binding to a panel of sarbecovirus RBDs as assessed by ELISA^{122,136,242–245,262,263}. ELISA measurements demonstrated that the *VH3-30* Fabs showed variable cross-reactivity profiles (Figure 5.1D; SI Appendix, Figure S5.4). The class 1/4 potent neutralizer C149 did not show any cross-reactivity, consistent with the location of the C149 epitope high on the RBD near the ACE2 binding site where the RBD sequence is less conserved^{122,136,242–245} (Figures 5.2–5.3). In contrast, the class 4 Fabs of weakly neutralizing Abs C008, C027, C030, C113, and C133 all showed strong cross-reactivity to at least two other RBDs besides SARS-CoV-2, consistent with the cross-reactivity previously reported for other class 4 Abs^{122,136,245,249,250,252,253}. The Fab of the weakly neutralizing Ab C133, which binds the lowest class 4 epitope on the RBD, showed the broadest cross-reactivity with binding to all RBDs, although binding to SARS-CoV and Rs4081 was relatively reduced. Additionally, C133 was the only one of the six Fabs that showed binding to BM4831. The weakly neutralizing Abs C027 and C030, which bind lower lateral epitopes on the RBD, showed cross-reactivity to five different RBDs (SARS-CoV, WIV1, SHC014, RaTG13, and Rs4081), although binding to SARS-CoV was again relatively reduced. Cross-reactivity by C008 and C113 was more limited: C008 showed strong binding to WIV1 and SHC014 and

reduced binding to RaTG13, which shares ~89% protein sequence similarity to SARS-CoV-2 RBD (SI Appendix, Figure S5.5). This contrasts with C118, which binds an overlapping epitope but cross-reacts with all the RBDs in the panel¹³⁶. C113 demonstrated strong binding to RaTG13 and reduced binding to WIV1 and SHC014 (Figure 5.1D).

Given that SARS-CoV and WIV1 RBD protein sequences are ~95% identical, it was interesting that Fabs of all five weakly-neutralizing Abs showed cross-reactive binding to WIV1, but reduced or no binding to SARS-CoV (Figure 5.1D, SI Appendix, Figure S5.5). The only two amino acids that differ between SARS-CoV and WIV1 that are near the RBD binding interface of the six *VH3-30* Abs we characterized are S373_{RBD} (near interface residues) and T430_{RBD} (an interacting residue) (numbering based on SARS-CoV-2 RBD) (SI Appendix, Figure S5.3, S5.5)^{103,109,262}. These residues (S373 and T430) are shared by SARS-CoV-2 and WIV1, but correspond to a phenylamine and methionine, respectively, in SARS-CoV. These differences may contribute to why these Abs bind SARS-CoV-2 and WIV1, but show reduced binding to SARS-CoV.

Discussion

Understanding the role of tightly binding but weakly neutralizing Abs in the immune response against SARS-CoV-2 and determining structural correlates of weak versus potent neutralization is important for the development of vaccines and Ab therapeutics. Here we performed cross-reactivity, neutralization, and structural studies for six *VH3-30* Abs (five weakly neutralizing and one potently neutralizing) isolated from COVID-19 convalescent donors¹²⁷ to compare with previously characterized *VH3-30* Abs. In addition to determining the different epitopes targeted by these Abs, we provided insights into the ability of *VH3-30* Abs to target diverse RBD epitopes with varied neutralization and cross-reactivity profiles.

Structural characterization of the binding epitopes of weakly neutralizing Abs with the *VH3-30* or a closely related V gene segment showed that all five Abs bound cryptic, but varied class 4 epitopes. Despite four of the five Abs sharing light chains derived from the same V_L gene segment (*VK1-5*) and three of the five sharing the same HC J gene segment (*JH4*02*), the Abs bound distinct epitopes with some overlap (Figure 5.4, Table 5.1; SI Appendix, Table S5.1). The Fab-bound protomers observed by cryo-EM for all five weakly neutralizing Fabs and the potent class 1/4 neutralizer C149 indicated that Fab binding causes the trimer to dissociate under conditions for cryo-EM. Spike trimer disruption has also been observed for the class 4 Ab CR3022²⁴⁴, and the cryo-EM structure of C118 Fab bound to SARS-CoV-2 showed Fab-bound trimer as well as Fab-bound protomer classes¹³⁶. Although it is unknown how spike trimer dissociation correlates with neutralization, it has been suggested that class 4 Fab binding may promote spike shedding or disruption of the prefusion conformation of the spike^{122,136,137,244}. Despite binding the lowest class 4 epitope on the RBD of all the Fabs we characterized, only the C133 Fab-S complex showed Fab-bound trimers. The finding that the C133-bound S trimer structure showed increased trimer opening similar to the C118-bound S trimer¹³⁶ is consistent with this mechanism. However, the location of the class 4

epitopes, buried at the trimer center, may also contribute to the reduced neutralization potency observed for several of these Abs.

Since the potential to hinder ACE2 binding is uniformly observed among strong class 4 neutralizers, this supports that ACE2 blocking is the most important determinant of whether a class 4 Ab can potently neutralize SARS-CoV-2^{136,248-250}. Structures of the class 4 neutralizers C118¹³⁶, C022¹³⁶, COVA1-16²⁴⁸, H014²⁴⁹, and DH1047²⁵¹ all showed Fab binding at angles that clashed with ACE2 when superimposed with an ACE2-bound RBD structure¹¹⁷. The neutralizing C149 antibody bound an epitope that reaches higher on the RBD than class 4 but lower than class 1 epitopes, thereby directly overlapping with part of the ACE2 epitope. The only other neutralizing *VH3-30* Abs that we identified that directly blocks part of ACE2 epitope were P17²⁵⁶ and C002¹³², class 2 anti-RBD Abs.

While the C008 epitope overlapped with that of all the class 4 potent neutralizers (C118¹³⁶, C022¹³⁶, COVA1-16²⁴⁸, H014²⁴⁹, and DH1047²⁵¹) and the Fab showed clashes when superimposed with the structure of ACE2-bound RBD¹¹⁷, C008 unexpectedly did not show potent neutralization. The neutralization demonstrated by C008 ($IC_{50} = 7390$ ng/mL) was ~7-48-fold more potent than the weakest class 4 neutralizers (C027, C030, C113, and C133), but weaker than the potent neutralizers (C118¹³⁶, C022¹³⁶, COVA1-16²⁴⁸, H014²⁴⁹, and DH1047²⁵¹) that bound similar epitopes (Figure 5.1, 5.4). The C008 V genes (*VH3-30/VKI-5*) are similar to many of the weak neutralizers (C027, C030, and C113) and may not be ideally suited for potent neutralization at this epitope. Notably, the potent neutralizer C008 shares a similar V_H V gene segment (*VH3-30-3*; 80% identity), while C022 shares a similar V_L V gene (*VKI-5*; 94% identity), but with a different light chain or heavy chain respectively (SI Appendix, Table S5.1). Compared to C118, the C008 V_L buried 50% less surface area on its RBD epitope, demonstrating the impact diverse light chain pairing can have on *VH3-30* epitope and neutralization potency (SI Appendix, Table S5.5). It is also possible that the N-

glycan on C008 V_L residue N26 may contribute to its lower potency, although it does not block the binding interface.

The class 4 epitopes can be further subclassified by Abs that bind low, laterally, centrally, or high on the class 4 surface (Figure 5.4). The low binders, including *VH3-30* Abs C133 and EY6A¹²² and non-*VH3-30* Abs CR3022^{244,245}, S2A4¹³⁷, and S304¹³⁴, tend to show weak or inconsistent neutralization against SARS-CoV-2¹³⁵ (Figures 5.1, 5.3, Table 5.1). This correlates with the reduced accessibility of this epitope at the trimer center and the increased distance from the ACE2 binding site. The lateral binders, *VH3-30* Abs C027, C030, and C113, bound the left lateral aspect of the class 4 surface and tend to be weakly neutralizing¹³⁵ (Figures 5.1, 5.4I). The central binders, *VH3-30* Abs C008 and C118¹³⁶ and non-*VH3-30* Abs C022¹³⁶, COVA1-16^{124,248}, H014²⁴⁹ and DH1047^{250,251}, show the potential to hinder ACE2 binding and tend to be potently neutralizing, with the exception of C008, as described above (Figures 5.1, 5.4H-J). Finally, the high binder, the class 1/4 *VH3-30* Ab C149, directly blocks the ACE2 epitope, but its epitope reaches lower on the RBD than other class 1 binders (Figure 5.4C).

The ability of potently and weakly neutralizing Abs derived from *VH3-30* or related V gene segments to bind diverse epitopes, the four class 4 subclasses and class 1-3 epitopes, is impacted by their varied light chain pairings (Figure 5.4; SI Appendix, Table S5.1). Anti-SARS-CoV-2 *VH3-30* Abs showed pairing with a variety of light chains, including but not limited to *VK1-39*, *VK1-5*, *VLI-5*, *VL2-14* and *VL4-69*^{126,127,129,254,264}. This is consistent with the ability of the *VH3-30* Abs with different light chain V genes to bind similar epitopes, but with varying neutralization potencies and different angles of approach. For example, C118¹³⁶ and C008 both bind central class 4 epitopes, and P17²⁵⁶, C002¹³² and COVOX-75¹³⁵ all bind class 2 epitopes, but only one or two of the Abs, respectively, are potently neutralizing in each case. The reduced potency of COVOX-75 was attributed to the finding that the majority of RBD interactions were with V_L outside the ACE2 binding site. The V_H interactions were

limited to the 20-residue long CDRH3 that may be displaced by ACE2 binding¹³⁵. When comparing *VH3-30* Abs, weak neutralizers showed more V_L BSA than potent neutralizers on average (360 vs. 230 Å² V_L BSA) (SI Appendix, Table S5.5). These observations indicate the light chain impacts where the *VH3-30* Ab binds and whether or not Abs bound at a particular epitope are neutralizing.

However, some *VH3-30* Abs paired with light chains of the same V gene can bind different epitopes; for example, the *VH3-30/VK1-5* Abs bind class 3 (C135) or class 4 (C008, C027, C030) epitopes, and the *VH3-30/VK1-39* Abs bind class 1/4 (C149), class 2 (C002) and class 4 (C133 and EY6A), indicating that other factors contribute to epitope variability. The anti-SARS-CoV-2 *VH3-30* Abs showed large CDRH3 length variability, ranging from 12-20 residues in the Abs we compared and in other studies¹³⁵ (Table 5.1; SI Appendix, Figures S5.3, S5.4, Table S5.5). Variation in the CDRH3 accounts for over 56-70% of the amino acid differences of the V_H of C135 compared to C008, C027 and C030 and 70-77% of the differences between C133, C149, C002, and EY6A (SI Appendix, Figures S5.3-5.4). For the *VH3-30* Abs compared in this study, average CDRH3 length was similar between potent (15 residues) and weak neutralizers (17 residues) (Table 5.1). Additionally, CDRH3 lengths by binding class were similar for class 1/4 (18), class 2 (16), and class 4 (17), but shorter for class 3 (13) *VH3-30* Abs (Table 5.1). The large variations in CDRH3 sequences are consistent with the unique ability of *VH3-30* Abs to bind multiple RBD epitopes.

Understanding which Abs are able to cross-react with other sarbecovirus RBDs is critical for vaccine development aimed at eliciting a broad immune response against multiple coronavirus strains. While it has been suggested that eliciting Abs that target the conserved class 4 epitope may be an effective therapeutic strategy^{122,136,242–245}, the ability of several weakly neutralizing class 4 Abs to show high affinity cross-reactive binding with weak or no cross-neutralization is an important consideration and possible complication for the effectiveness of this approach. Despite binding different class 4 RBD epitopes, all five

SARS-CoV-2 weakly-neutralizing Abs (C008, C027, C030, C113, and C133) showed strong cross-reactive binding to at least two different RBDs, but only C027 showed any cross-neutralization. The cross-neutralization by C027 against SARS-CoV ($IC_{50} = 43.8 \mu\text{g/mL}$) was 10-fold weaker than the cross-neutralization reported for the class 4 *VH3-30* potent SARS-CoV-2 neutralizer C118 against SARS-CoV ($IC_{50} = 3870 \text{ ng/mL}$)¹³⁶. These cross-reactive but not cross-neutralizing Abs may exhibit protective effects *in vivo* through Fc effector functions, but this requires further investigation²⁶⁵. The ACE2 blocking epitope targeted by the potent neutralizer C149 is more accessible but less conserved than class 4 epitopes, explaining the lack of cross-reactive binding observed by C149.

Given that SARS-CoV and WIV1 RBD protein sequences are ~95% identical, it was interesting that Fabs of all five weakly-neutralizing Abs showed cross-reactive binding to WIV1, but reduced or no binding to SARS-CoV (Figure 5.1D; SI Appendix, Figure S5.2). The only two amino acids that differ between SARS-CoV and WIV1 that are near the RBD binding interface of the six *VH3-30* Abs we characterized are S373_{RBD} (near interface residues) and T430_{RBD} (an interacting residue) (numbering based on SARS-CoV-2 RBD) (SI Appendix, Figure S5.2, S5.5)^{103,109,262}. These residues (S373 and T430) are shared by SARS-CoV-2 and WIV1, but correspond to a phenylamine and methionine, respectively, in SARS-CoV. These differences may contribute to why these Abs bind SARS-CoV-2 and WIV1, but show reduced binding to SARS-CoV.

Cross-reactive binding and neutralization against SARS-CoV and other sarbecoviruses was previously observed for anti-SARS-CoV-2 potentially-neutralizing class 4 Abs such as H014, C118, C022, DH1047, ADG-2, and ADI-56046^{127,136,249,250,252,253}. However, similar to our observation for the weakly neutralizing Ab C027, the potentially neutralizing class 4 Ab COVA1-16 cross-reacted with SARS-CoV, but showed only weak cross-neutralization ($IC_{50} > 1 \mu\text{g/mL}$)²⁴⁸. Despite binding a similar epitope and at a similar Fab orientation as C022¹³⁶, COVA1-16²⁴⁸ used different V genes and did not show the potent cross-neutralization of

SARS-CoV exhibited by C022^{136,248,266}. Comparisons of these Abs indicate that potent class 4 SARS-CoV-2 neutralizers use a variety of different V_H and V_L genes and are not all potent cross-neutralizers. Since both weak and potent class 4 SARS-CoV-2 neutralizers can show cross-reactive binding without cross-neutralization, efforts to use a conserved class 4-based immunogen for vaccine design may not necessarily elicit Abs that are broadly-neutralizing. The ability of class 4 Abs to bind highly similar epitopes does not indicate those Abs will show the same cross-neutralization profiles. Consequentially, these findings demonstrate the importance of understanding the structural correlates of diverse neutralization and cross-reactivity profiles in order to inform the design of effective vaccines and targeted Ab therapeutics.

Materials and Methods

Sequence alignments and analysis. Protein sequence alignments were performed with MUSCLE alignment²⁶⁷ using Geneious 11.0.5 software. V, D and joining J gene segment assignments were determined with IgBlast¹²⁷. The Kabat numbering scheme was used with ANARCI software²⁶⁸.

Protein expression. IgGs and Fabs were produced as previously described^{205,269}. Briefly, Fabs with a HC C-terminal His-tag and IgGs were expressed by transient transfection of Expi293F cells with equal amounts of HC and LC expression vectors. IgGs were purified from supernatants using a HiTrap MabSelect column (GE Healthcare), and Fabs were purified with Ni-NTA affinity chromatography. Fabs and IgGs were further purified with size exclusion chromatography (SEC) using a Superdex 200 column (GE Healthcare) in 20 mM Tris pH 8.0, 150 mM NaCl, 0.02% sodium azide.

RBDs with a C-terminal His-tag were produced as previously described^{132,136,202} by transient transfection of Expi293F cells. RBD constructs included the following residues: SARS-CoV-2 RBD (residues 328-533), SARS CoV RBD (residues 318-510), WIV-1 RBD (residues 307-528), SHC014 RBD (residues 307-524), RaTG13 RBD (residues 319-541), Rs4081 RBD (residues 310-515), and BM-4831 RBD (residues 310-530)^{202,262,263}. RBDs were purified from supernatant with Ni-NTA affinity chromatography and SEC using a Superdex 200 column (GE Healthcare) in 20 mM Tris pH 8.0, 150 mM NaCl, 0.02% sodium azide.

SARS-CoV-2 S trimer with ectodomain residues 16-1206 (GenBank MN985325.1) was produced as previously described^{132,133} with 6P stabilizing mutations^{5/21/22 3:53:00 PM}, a mutated furin cleavage site between S1 and S2, a C-terminal TEV site, a foldon trimerization motif, an octa-His tag, and an AviTag. S trimer was expressed by transient transfection of

Expi293F cells and purified with Ni-NTA affinity chromatography and SEC using a Superdex 200 column (GE Healthcare) in 20 mM Tris pH 8.0, 150 mM NaCl, 0.02% sodium azide. Peak fractions were identified by SDS-PAGE and combined.

Crystallization trials. For the C008 Fab–SARS-CoV-2 RBD complex, Fabs and RBD were incubated on ice for 1 hr with a Fab:RBD molar ratio of 2:1 for C008 Fab–SARS-CoV-2 RBD and 1.5:1 for C133 Fab–C119 Fab–SARS-CoV-2 RBD. The complexes were then purified by SEC on a Superdex 200 10/300 Increase column (GE Healthcare) and concentrated to 8 mg/mL. Crystallization trials were set up in sitting-drop MRC plates with a Mosquito micro-crystallization robot and stored at room temperature. Crystals were cryo-protected with 25% glycerol. Crystallization conditions corresponding to determined structures included 15% v/v 2-propanol, 0.1 M sodium citrate tribasic dihydrate pH 5.0, 10% w/v polyethylene glycol 10,000 3,350 (C008 Fab–SARS-CoV-2 RBD) and 0.1 M sodium citrate tribasic dihydrate pH 5.0, 10% w/v polyethylene glycol 6,000 (C133 Fab–C119 Fab–SARS-CoV-2 RBD).

X-ray structure determinations. X-ray data were collected at the Stanford Synchrotron Light Source (SSRL) beamline 12-1 on a Pilatus 6M pixel detector (Dectris). C008 Fab–SARS-CoV-2 RBD diffraction data were processed using the XDS package¹⁶⁰, and C133 Fab–C119 Fab–SARS-CoV-2 RBD complex data were processed using iMosflm¹⁶¹. Data were scaled using Aimless^{162,163}.

Structures were solved by molecular replacement (MR) with Phaser-MR¹⁶⁴. For the C008 Fab–SARS-CoV-2 RBD structure, the structure was first determined at 2.7 Å using C110 C_HC_L and V_HV_L (PDB 7K8P)¹³² as initial search models³⁶. This gave a partial solution with one Fab. The sequence was mutated to correspond to the sequence of the C008 Fab, and this was used to generate C008 V_HV_L and C_HC_L search models. These were used, along with SARS-CoV-2 RBD (PDB 7K8M)¹³², as search models in additional rounds of molecular

replacement. Three Fabs bound to RBD were identified in total. After a few rounds of rigid-body refinement with torsion-angle non-crystallographic symmetry restraints and group and individual B factors using phenix.refine¹⁶⁵, the R-free flags were transferred to the map processed at 3.0Å. Further refinement with torsion-angle non-crystallographic symmetry restraints, individual B factors and TLS parameters was performed using this map.

The C133 Fab–C119 Fab–SARS-CoV-2 RBD structure was determined by initially using a 3.5 Å map for molecular replacement with C110 C_HC_L and V_HV_L (PDB 7K8P)¹³², C119 C_HC_L and V_HV_L (PDB 7K8W)¹³², and SARS-CoV-2 RBD (PDB 7K8M)¹³² as search models. A partial solution with a correctly placed C110 C_HC_L and C110 V_HV_L was mutated to correspond to the sequence of C133 Fab, and this was used to generate C133 V_HV_L and C_HC_L search models. These were used, along with C119 C_HC_L and V_HV_L and SARS-CoV-2 RBD as search models for molecular replacement using a map processed at 3.15Å. Correctly placed Fabs and RBDs were used as partial solutions in iterative rounds of molecular replacement until all components, three RBDs bound by two Fabs each, were correctly placed. Refinement was performed using phenix.refine¹⁶⁵ with torsion-angle non-crystallographic symmetry restraints, group and individual B factors, and TLS parameters and with manual refinement in Coot²⁷⁰.

PDB accession codes and X-ray data collection and refinement statistics are in SI Appendix, Table S5.2. Figures were prepared using PyMOL (Version 2.1 Schrodinger, LLC)¹⁶⁶ or UCSF Chimera²⁷¹. Fab-RBD binding interfaces were mapped as residues within 4 Å. BSAs (calculated using a 1.4 Å probe) and interacting residues at Fab-RBD interfaces (calculated using a distance of <3.89 Å and an A-D-H angle >90° for H-bonds and a distance <4 Å for salt bridges) were determined with PDBePISA¹⁶⁸. The PDB accession codes of the structures used for RBD BSA representations and calculations are as follows: ACE2 (6M0J)¹¹⁷, EY6A (6ZCZ)¹²², C135 (7K8Z)¹³², C002 (7K8S)¹³², CR3022 (6W41)²⁴⁵, P17 (7CWO)²⁵⁶, COVOX-75 (7BEO)¹³⁵, COVOX-45 (7BEL)¹³⁵, COVA1-16 (7JMW)²⁴⁸, H014 (7CAH)²⁴⁹, DH1047

(7LD1)²⁵¹, S2A4 (7JVA)¹³⁷, REGN10987 (6XDG)²⁵⁵, and S304 (7JX3)¹³⁷. All BSA representations and calculations are based on Fab-bound structures of SARS-CoV-2 RBD except for C118, which is based on SARS-CoV^{136,272}. Amino acid sequence conservation was calculated with ConSurf²⁷³ and shown on a surface representation of a SARS-CoV-2 RBD (PDB 7BZ5)²⁷⁴.

Cryo-EM sample preparation. Fab was incubated with 3 mg/mL SARS-CoV-2 S trimer at a 1.2:1 molar ratio of Fab: protomer on ice for 30 minutes. A PELCO easiGLOW Glow Discharge Cleaning System (Ted Pella) was used to glow discharge 300 mesh, 1.2/1.3 QuantiFoil grids (Electron Microscopy Sciences) for 1 minute at 20 mA. Octyl-maltoside, fluorinated solution (Anatrace) was added to the complex at a final concentration of 0.02% w/v, immediately before applying 3.1 μ L of the complex to the grid. Samples were blotted for 2.5-3.5 s. with Whatman No. 1 filter paper before vitrification in 100% liquid ethane using a Mark IV Vitrobot (Thermo Fisher) at 22°C and 100% humidity.

Cryo-EM structure data collection, processing and analysis. Single-particle cryo-EM data were collected on a Talos Arctica transmission electron microscope (Thermo Fisher) operating at 200 kV. Movies were collected with SerialEM v3.7 automated data collection software²⁷⁵ using beam-image shift over a 3 by 3 pattern of 1.2 μ m holes with one exposure per hole. Movies were recorded in super-resolution mode (0.435 Å/pixel) on a K3 camera (Gatan). When data processing is completed, data collections parameters will be included.

Cryo-EM data processing was performed with cryoSPARC v2.15.0 and v3.2.0²⁷⁶. Movies were patch motion corrected for beam-induced motion after binning super-resolution movies. Non-dose-weighted images were used to estimate CTF parameters using the patch CTF estimation job, and micrographs with power spectra showing poor CTF fits or crystalline ice were discarded. Blob picker was used for reference-free selection of particles with a 140-240Å diameter using the circular blob option. Particles were extracted for subsequent 2D

classification. The best class averages were used to generate five *ab-initio* models (S trimer, Fab-bound S protomer, or junk/noise classes). All particles were then used in heterogeneous refinement against the five *ab initio* volumes generated with the smaller subset. Particles assigned to the volume with Fab-bound S protomer were further cleaned via iterative rounds of *ab-initio* reconstruction, heterogenous refinement, 2D classification, and homogenous refinement. Trimer classes were also further cleaned, but only in one case, for C133 Fab–SARS-CoV2 S6P, was a trimer found have Fab bound. To improve resolution at the Fab-RBD interfaces, volumes were segmented in UCSF Chimera²⁷¹ and the regions corresponding to the RBD domains and Fab V_H-V_L domains were extracted and used to generate a soft mask (5-pixel dilation radius, 10-pixel soft padding width). Local refinement with the mask resulted in modest improvements of the Fab-RBD interface. Cryo-EM processing is still in progress.

ELISAs. ELISAs were performed at previously described^{136,202}. RBDs at 2.5 µg/mL in 100 mM NaHCO₃ pH 9.8 was coated on Nunc MaxiSorp 384-well plates (Sigma) and stored at 4°C overnight. Plates were then blocked with 3% bovine serum albumin (BSA) in 20 mM Tris pH 8.0, 150 mM NaCl, 0.02% sodium azide, 0.1% Tween20 (TBS-T) for 1 hr. at room temperature. After blocking solution was removed, IgGs at 50 µg/mL were four-fold serially diluted in 3% BSA, TBS-T and added to plates at room temperature for 3 hr. Plates were then washed with TBS-T and incubated with a 1:15,000 dilution of secondary HRP-conjugated goat anti-human IgG (Southern Biotech) at room temperature for 45 minutes. Plates were washed with TBS-T, developed using SuperSignal ELISA Femto Maximum Sensitivity Substrate (ThermoFisher), and read at 425 nm. ELISAs were performed in duplicate. AUC measurements were determined after sigmoidal nonlinear regression (least-squares method without weighting with GraphPad Prism 9.0.0 software).

Neutralization assays. Abs were four-fold serially diluted in PBS and incubated with SARS-CoV or SARS-CoV-2 pseudotyped virus for 1 hr. at 37 °C. Pseudotyped HIV-1 lentiviral

reporter particles were prepared as previously described^{127,136,202,259} using genes encoded for S glycoproteins with deletions in the C-terminal cytoplasmic tail: a 21 amino acid deletion for SARS-CoV-2 and 19 amino acid deletion for SARS-CoV. The SARS-CoV-2 S gene also included the D614G mutation. Final starting concentrations against SARS-CoV-2 were 1 $\mu\text{g/mL}$ (C103 IgG, positive control)¹²⁷, 25 $\mu\text{g/mL}$ (C149 IgG), 500 $\mu\text{g/mL}$ (C008, C027, C113, C133, Z004³⁶ (negative control) IgGs), and 1000 $\mu\text{g/mL}$ (C030 IgG). Final starting concentrations against SARS-CoV were 500 $\mu\text{g/mL}$ (C008, C113, C133, Z004³⁶ (negative control) IgGs), 750 $\mu\text{g/mL}$ (C027 IgG), and 1000 $\mu\text{g/mL}$ (C030, C149 IgGs). The mixture of Ab and pseudotyped virus was added to HEK293T_{ACE2} cells¹²⁷ seeded the previous day on poly-Lysine-coated 96-well plates. After incubating for 48 hours at 37°C, target cells were lysed with Britelite Plus (Perkin Elmer) and luciferase activity was measured as relative luminescence units (RLUs) and normalized to values derived from cells infected with pseudotyped virus in the absence of Ab. The 50% inhibitory concentrations (IC₅₀) were determined using a 3-parameter (for SARS-CoV) or 4-parameter (for SARS-CoV-2) nonlinear regression (least-squares method without weighting) (GraphPad Prism 9.0.0). Experiments were repeated twice; curves from one experiment are shown in Figure 5.1A-B, and reported IC₅₀ values are the averaged IC₅₀s from the two independent experiments.

SI Appendix

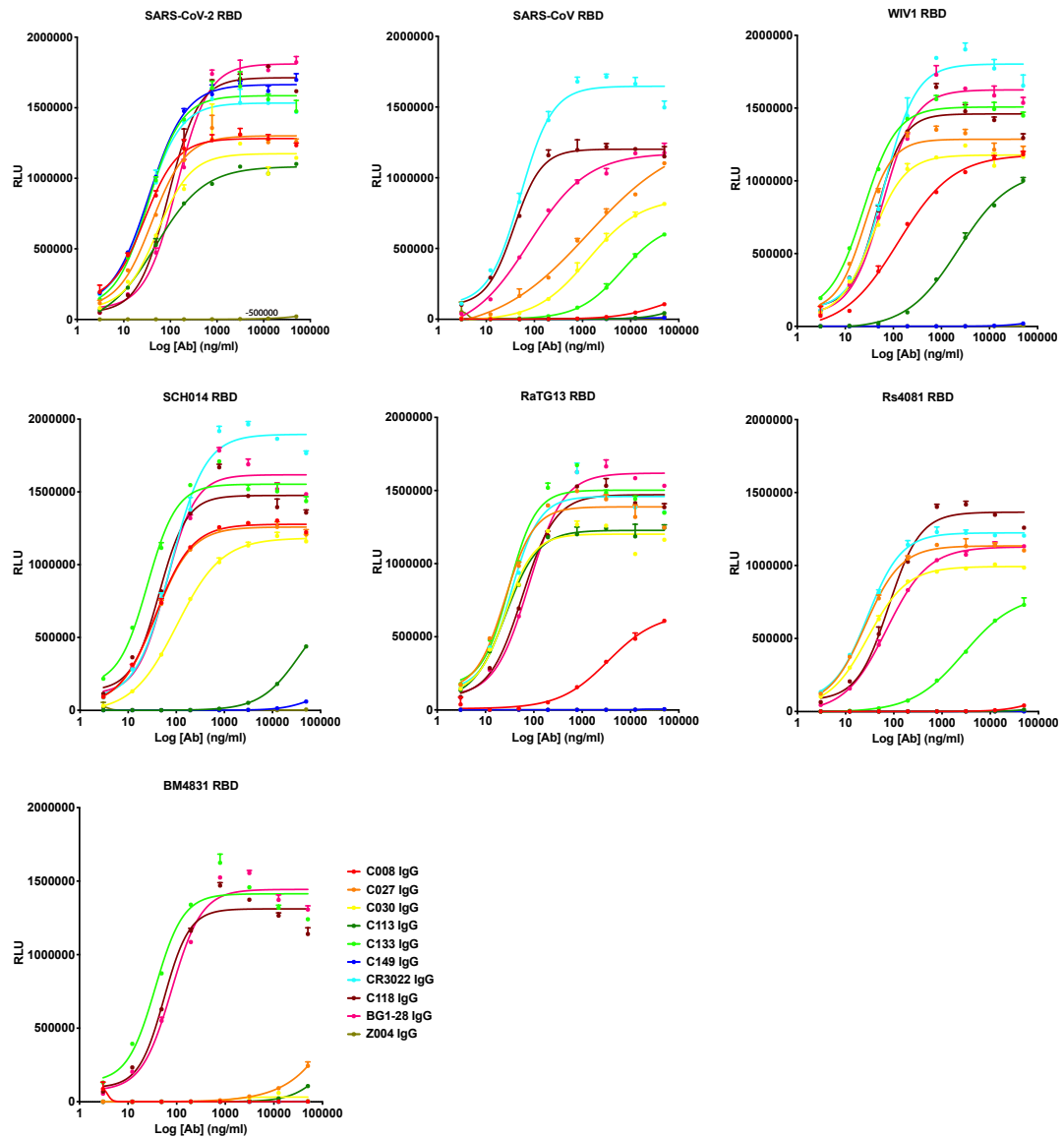


Figure S5.1. Ab binding to sarbecovirus RBDs.

ELISA curves for Ab binding to sarbecovirus RBDs performed in duplicate. CR3022, C118, and BG1-28 IgGs serve as positive controls. Z004 IgG is an anti-Zika Ab serving as a negative control. AUC calculations for these curves are shown in Figure 5.1D.

```

330      340      350      360      370      380      390      400      410
SARS-CoV-2 NITNLCPFGEVFNATRFASVYAWNRKRISNCVADY SVLYNSAS-FSTFKCYGVSPTKLNLDLCFTNVYADSFVIRGDEVQRQIAPG
RaTG13      NITNLCPFGEVFNATTFASVYAWNRKRISNCVADY SVLYNSTS-FSTFKCYGVSPTKLNLDLCFTNVYADSFVITGDEVQRQIAPG
SARS-CoV   NITNLCPFGEVFNATKFPSVYAWERKKISNCVADY SVLYNSTF-FSTFKCYGVSATKLNLDLCFNSVYADSFVVKGDDVQRQIAPG
WIV1       NITNLCPFGEVFNATTFPSVYAWERKRISNCVADY SVLYNSTS-FSTFKCYGVSATKLNLDLCFNSVYADSFVVKGDDVQRQIAPG
SHC014    NITNLCPFGEVFNATTFPSVYAWERKRISNCVADY SVLYNSTS-FSTFKCYGVSATKLNLDLCFNSVYADSFVVKGDDVQRQIAPG
Rs4081    NITNRCPFDKVFNASRFPNVYAWERTKISDCVADY TVLYNSTS-FSTFKCYGVSPSKLDLDCFTSVYADTFLIRSSSEVRQVAPG
BM4831    NITQLCPFNEVFNITSFPSVYAWERMRTN CVADY SVLYNSSASFSTFQCYGVSPTKLNLDLCFSSVYADYFVVKGDDVQRQIAPA

          420      430      440      450      460      470      480      490
SARS-CoV-2 QTGKIADYNYKLPDDFTGCVIAWNSNNLDSKVGGNYNLYRLFRKSNLKP FERDISTE IYQAGSTPCNGVEGFNCYFP LQSYGF
RaTG13      QTGKIADYNYKLPDDFTGCVIAWNSKHIDAKEGGNFNYLYRLFRKANLKP FERDISTE IYQAGSKPCNGQTGLNCCYPLYRYGF
SARS-CoV   QTGVIADYNYKLPDDFMGCVLAWNTRNIDATSTGNYNKYRSLRHGKLRP FERDISNVPFSPDGKPCPPPALNCCYWPLNDYGF
WIV1       QTGVIADYNYKLPDDFTGCVLAWNTRNIDATQTGNYNKYRSLRHGKLRP FERDISNVPFSPDGKPCPPPALNCCYWPLNDYGF
SHC014    QTGVIADYNYKLPDDFLGCVLAWNTNSKDSSTSGNYNLYRWVRRSKLNP YERDLSNDIYSPGGQSCS-AVGPNCYNPLRPYGF
Rs4081    ETGVIADYNYKLPDDFTGCVIAWNTAKQDQGG-----Y YRWSRKT KLKPFERDLTSDE-----NGVRTLSTYDF
BM4831    QTGVIADYNYKLPDDFTGCVIAWNTNSLDSN----EFYRRFRHGKIKPYGRDLSNVL FNP SGGTCS-AEGLNCCYKPLASYGF

          500      510      520
SARS-CoV-2 QPTNGVGYQPYRVVLSFELLHAPATV
RaTG13      YPTDGVGHQPYRVVLSFELLNAPATV
SARS-CoV   YTTTGIGYQPYRVVLSFELLNAPATV
WIV1       YITNGIGYQPYRVVLSFELLNAPATV
SHC014    FTTAGVGHQPYRVVLSFELLNAPATV
Rs4081    YPNVPIEYQATR VVLSFELLNAPATV
BM4831    TQSSGIGFQPYRVVLSFELLNAPATV

```

Figure S5.2. Alignment of RBDs used for cross-reactivity studies.

Differences between SARS-CoV and WIV1 are colored red.

V_H Alignment

	CDRH1	CDRH2
C149	QVQLVESGGGVVQPGRSLRLSCAASGFTFST--YGMHWVRQAPGKGLEWVAVISYDGSNKYFADSV	
C002	EVQLVESGGGVVQPGRSLRLSCAASGFTFSI--YGMHWVRQAPGKGLEWVAVISYDGSNKYYADSV	
P17	-QQLVESGGGVVQPGRSLRLSCAASGFTFSS--YAMHWVRQAPGKGLEWVAVISYDGSNKYYADSV	
COVOX-75	QVQLVESGGGVVQPGRSLRLSCAASGFTFNN--YPLHWVRQAPGKGEWVAVISQDGNKYYVDSV	
C135	QVQLVESGGGVVQPGRSLRLSCAASGFTFSS--YAMHWVRQAPGKGLEWVAVIPFDGRNKYYADSV	
REGN10987	QVQLVESGGGVVQPGRSLRLSCAASGFTFSS--YAMYWVRQAPGKGLEWVAVISYDGSNKYYADSV	
COVOX-45	QVQLVESGGGVVQPGRSLRLSCAASGFTFST--YAMHWVRQAPGKGLEWVAVISYDGSNKYYADSV	
C118	QVQLVESGGGVVQPGRSLRLSCAASGFTFSN--YAMHWVRQAPGKGLEWVAVISYDGSNKYYADSV	
C008	EVQLVESGGGVVQPGRSLRLSCAASGFTFSS--YGMHWVRQAPGKGLEWVAVISYDGSNKYYADSV	
C027	EVQLVESGGGVVQPGRSLRLSCAASGFTFSS--YGMHWVRQAPGKGLEWVAVISYDGSNKYYADSV	
C030	EVQLVESGGGVVQPGRSLRLSCAASGFTFSS--YGMHWVRQAPGKGLEWVAVISYDGSNKYYADSV	
C113	QVQLVESGGGVVQPGRSLRLSCAASGFTFSS--YGMHWVRQAPGKGLEWVAVIWDYDGSNKYYADSV	
C133	QVQLVESGGGVVQPGRSLRLSCAASGFTFSS--YAMHWVRQAPGKGLEWVAVILLYDGSNKYYADSV	
EY6A	EVQLVESGGGVVQPGRSLRLSCAASGFTFSS--YDMHWVRQAPGKGLEWVAVISYDGSNKYYADSV	
C022	QVQLQESGGLVQPKSETLSVCTVSGGSISSRYVWGWIRQPPGKLEWIGSIYYSGST--YINPSL	
COVA1-16	QVQLVQSGAEVKKPGASVKVSKKASGYTFTS--YYMHWVRQAPGQGLEWVMIINSSGGSTSYAQKF	
H014	-VQLVQSGAEVKKPGATVKISCKVSGYSFSS--YYIHWVRQAPGKSLWIGYIDPFGNGTSDNLFK	
DH1047	QVQLVQSGAEVKKPGASVQVCSQASANTFTN--HYIHWVRQAPGQGLEWVMIIPYTGNTIYAQGF	
CR3022	QMQLVQSGTEVKKPGESLKIISCKKSGYGFIT--YWIHWVRQMPGKLEWVMIIPYDSETRYSPSF	
S2A4	EVQLVESGGGLVQPGGSLRLSCAASGFTFSS--YDMHWVRQAPGKLEWVANIKQDGSSEKYYVDSV	
S304	EVQLVESGGGLVQPGGSLRLSCAASGFTFSS--YDMHWVRQTGKLEWVSTIGTAG-DTYYPSV	

	CDRH3
C149	KGRFTISRDNKNTLYLQMNSLRPEDTAVYYCAKVG--MEYSSGWYG--EEDIFWQGQTLVTVSS
C002	KGRFTISRDNKNTLYLQMNSLRAEDTAVYYCAKEG--RPSDIIVVV--VAFDYWGQGLTVTVSS
P17	KGRFTISRDNKNTLYLQMNSLRAEDTAVYYCARHA-----TLM-----NNKDIWGQGLTVTVSS
COVOX-75	KGRFTISRDNKNTLYLQMNRLRAEDTALYYCARDVVVVVAARNHYY--NGMDVWGQGTTVTVSS
C135	TGRFTISRDNKNTLYLQMNSLRAEDTAVYYCASSS-----GYL--FHSDYWGQGLTVTVSS
REGN10987	KGRFTISRDNKNTLYLQMNSLRTEEDTAVYYCASGS-----DYGD--YLLVYWGQGLTVTVSS
COVOX-45	KGRFTISRDNKNTLYLQMNSLRAEDTAVYYCAKGG--SYAAY--YYMDVWGKGTTVTVSS
C118	KGRFTISRDNKNTLYLQMNSLRAEDTALYYCASGYTGYDYFVRGDY--YGLDVWGQGTTVTVSS
C008	KGRFTISRDNKNTLYLQMNSLRAEDTAVYYCAREF----GDPEWY-----FDYWGQGLTVTVSS
C027	KGRFTISRDNKNTLYLQMNSLRAEDTAVYYCAKASGIYCSGGDCYS----YFFDYWGQGLTVTVSS
C030	KGRFTISRDNKNTLYLQMNSLRAEDTAVYYCAKASGIYCSGGNCYS----YFFDYWGQGLTVTVSS
C113	KGRFTISRDNKNTLYLQMNSLRAEDTAVYYCARGV--NPDDILTGV--DAFDIWGQGTMTVTVSS
C133	KGRFTISRDNKNTLYLQMNSLRAEDTAVYYCARDS----DVDTSMV--TWFDYWGQGLTVTVSS
EY6A	KGRFTISRDNKNTLYLQMNSLRAEDTAVYYCAKDG-----GKLWV--YFFDYWGQGLTVTVSS
C022	KSRVTISVDTSKNQFSLKLSVTAADTAVYYCARHAAAYYDRSGYYFI--EYFQHWGQGLTVTVSS
COVA1-16	QGRVTMTRDTSSTVYMELSSLRSEDVAVYYCARPPRNYDRSGYYQRA--EYFQHWGQGLTVTVSS
H014	KGAATLTADTSTDTAYMELSSLRSEDVAVYYCARSE-----YDPYYV-----MDYWGQGTTVTVSS
DH1047	QGRVTMTRDTSNTIYELSSLRSEDVAVYYCARDVRVDDSWSGYDLLSGGTYFDYWGQGLTVTVSS
CR3022	QGQVTISADKSLNTAYLQWSSLKASDTAIIYCACGS-----GIS--TFMDVWGQGTTVTVSS
S2A4	KGRFTISRDNKNSLFLQMNSLRAEDTAVYYCARVW-----WLR--GSFDYWGQGLTVTVSS
S304	KGRFTISRDAKNSLYLQMNSLRAGDTAVYYCARGD-----SSGYY--YFFDYWGQGLTVTVSS

Ab class:
VH3-30 class 1 strong neutralizers
VH3-30 class 2 strong neutralizers
VH3-30 class 2 weak neutralizers
VH3-30 class 3 strong neutralizers
VH3-30 class 3 weak neutralizers
VH3-30 class 4 strong neutralizers
VH3-30 class 4 weak neutralizers
Non-VH3-30 class 4 strong neutralizers
Non-VH3-30 class 4 weak neutralizers

Figure S5.3. Alignment for V_H protein sequences for a set of VH3-30 and/or class 4 Abs that bind the SARS-CoV-2 RBD.

V_H residues at the Fab-RBD interface are highlighted.

V_L Alignment

	CDRL1	CDRL2	CDRL3
C149	--DIQMTQSPSSLSASVGDRTITCRASQSI-----SSY-LNWFYQQKPKGKAPKLLIY----	AASSLQSGVPSRFSGS--GSGTDFTLTISLQPEDFATYYCQQSYRTPPL-TFGGGTKVEIK	
C002	--DIQLTQSPSSLSASVGDRTITCRASQSI-----SSY-LNWFYQQKPKGKAPKLLIY----	AASSLQSGVPSRFSGS--GSGTDFTLTISLQPEDFATYYCQQSYSTPR-TFGGQTKVEIK	
P17	GDIQLTQSPSSLSASVGDRTITCRASQSI-----SSY-LNWFYQQKPKGKAPKLLIY----	AASSLQSGVPSRFSGS--GSGTDFTLTISLQPEDFATYYCQQSYSTPR-TFGGQTKVEIK	
COVOX-75	--DIQLTQSPSSVSASVGDRTITCRASQGI-----SSW-LAWYQQKPKGKAPKLLIY----	AVSSLQSGVPSRFSGS--GSGTDFTLTISLQPEDFATYYCQQAKSFPE-TFGPGTKVEIK	
C135	--DIQMTQSPSTLSASVGDRTITCRASQSI-----SNW-LAWFQQKPKGKAPKLLIY----	EASSLESGVPSRFSGS--GSGTEFTLTISLQPDFFATYYCQQYNSYPW-TFGGQTKVEIK	
REGN10987	--QSALTQ-PASVSGSPGQSIITISCTGTSSD---VGGYNY-VSWYQQHPGKAPKLLMIY----	DVSKRPSGVSNRFSGS--KSGNTASLTISLQSEDEADYCNLSITSTWVFGGGTKLTVL	
COVOX-45	--DIQLTQSPSSLSASVGDRTITCQASQDI-----SNY-LNWFYQQKPKGKAPKLLIY----	DASNLETGVPSRFSGG--GSGTDFTFITISLQPEDIATYYCQQYDNLPL-TFGGGTKVDIK	
C118	--QPVLTSQSPA-SASLGASVKLTCTLSGGH-----SSYAIAWHQQQPEKGPRLMKLNTD	GSHSKGDGIPDRFSGS--SSGAERYLTISLQSEDEADYCCQTWGTGIL-VFGGGTKLTVL	
C008	--DIQMTQSPSTLSASVGDRTITCRANQSI-----SSW-LAWYQQKPKGKAPKLLIY----	KASSLESGVPSRFSGS--GSGTEFTLTISLQPDFFATYYCQQYNS--YWTFGQGTVEIK	
C027	--DIQMTQSPSTLSASVGDRTITCRASQSI-----SSW-LAWYQQKPKGKAPKLLIY----	KASSLESGVPSRFSGS--GSGTEFTLTISLQPDFFATYYCQQYNSYS--TFGQGTVEIK	
C030	--DIQMTQSPSTLSASVGDRTITCRASQSI-----SSW-LAWYQQKPKGKAPKLLIY----	KASSLESGVPSRFSGS--GSGTEFTLTISLQPDFFATYYCQQYNSYS--TFGQGTVEIK	
C113	--DIQMTQSPSTLSASVGDRTITCRASQSM-----SSW-LAWYQQKPGNAPKLLIY----	KASSLESGVPSRFSGS--GSGTEFTLTISLQPDFFATYYCQQHNSPL-TFGGQTKVEIK	
C133	--DIQMTQSPSSLSASVGDRTITCRASQSI-----SSY-LNWFYQQKPKGKAPKLLIY----	AASSLQSGVPSRFSGS--GSGTDFTLTISLQPEDFATYYCQQSYSTPPWTFGGQTKVEIK	
EY6A	--DIQMTQSPSSLSASVGDRTITCRASQSI-----SSY-LNWFYQQKPKGKAPKLLIY----	AASSLQSGVPSRFSGS--GSGTDFTLTISLQPEDFATYYCQQSYSTLALTFGGQTKVEIK	
C022	--DIQMTQSPSTLSASVGDSTVITCRASQSI-----SSW-LAWYQQKPKGKAPKLLIY----	KASSLESGVPSRFSGS--GSGTEFTLTISLQPDFFATYYCQQYNNRYR-TFGGQTKLEIK	
COVA1-16	--DIQLTQSPSSLSASVGDRTITCQASQDI-----SNY-LNWFYQQRPKGKAPKLLIY----	DASNLETGVPSRFSGS--GSGTDFTFITISLQPEDIATYYCQQYDNPPL-TFGGGTKLEIK	
H014	--IVLTQSPFQ-SVSPKEKVTITCRASQSI-----SSN-LHWYQQKPKGKAPKLLIK----	YASQISGIPDRFSGS--GSGTDFTLTINSLEAEDFGIYFCQQTNFWPY-IFGQGTKEIL	
DH1047	--DIVMTQSPDSLAVSLGERATINCRSSQSVLYSSNNENY-LAWYQQKPKGQPPKLLIY----	WASTRESGIPDRFSGS--GSGTDFTLTISRQAEDVAVYCCQQYYSLPR-TFGGQTKVEIK	
CR3022	--DIQLTQSPDSLAVSLGERATINCKSSQSVLYSSINKNY-LAWYQQKPKGQPPKLLIY----	WASTRESGVPDRFSGS--GSGTDFTLTISLQAEADVAVYCCQQYYSTPY-TFGGQTKVEIK	
S2A4	--NFMLTQ-PHSVSESPGKVTITISCTGSSGS-----IASNY-VQWYQQRPGSAPTTVIY----	EDNQRPSGVPDRFSGSIDSSNSASLTISGLKTEADYCCSYDSSNHVFGGGTKLTVL	
S304	--DIEMTQSPSSLSAAVGDRTITCRASQSI-----GSY-LNWFYQQKPKGKAPKLLIY----	AASSLQSGVPSRFSGS--GSGTDFTLTISLQPEDFAIYYCQQSYVSPTYTFPGTKVDIK	

Associated HC Ab class:

VH3-30 class 1 strong neutralizers
 VH3-30 class 2 strong neutralizers
 VH3-30 class 2 weak neutralizers
 VH3-30 class 3 strong neutralizers
 VH3-30 class 3 weak neutralizers
 VH3-30 class 4 strong neutralizers
 VH3-30 class 4 weak neutralizers
 Non-VH3-30 class 4 strong neutralizers
 Non-VH3-30 class 4 weak neutralizers

Figure S5.4. Alignment for V_L protein sequences for a set of VH3-30 and/or class 4 Abs that bind the SARS-CoV-2 RBD.

V_L residues at the Fab-RBD interface are highlighted.

```

330      340      350      360      370      380      390
C149    RFPNITNLCPFGVEFNATRFASVYAWNRKRISINCVADYSLVLYNSASFSTFKCYGVSPTRKNDLCLFTNVY
C002    RFPNITNLCPFGVEFNATRFASVYAWNRKRISINCVADYSLVLYNSASFSTFKCYGVSPTRKNDLCLFTNVY
P17     RFPNITNLCPFGVEFNATRFASVYAWNRKRISINCVADYSLVLYNSASFSTFKCYGVSPTRKNDLCLFTNVY
COV0X-75 RFPNITNLCPFGVEFNATRFASVYAWNRKRISINCVADYSLVLYNSASFSTFKCYGVSPTRKNDLCLFTNVY
C135    RFPNITNLCPFGVEFNATRFASVYAWNRKRISINCVADYSLVLYNSASFSTFKCYGVSPTRKNDLCLFTNVY
REGN10987 RFPNITNLCPFGVEFNATRFASVYAWNRKRISINCVADYSLVLYNSASFSTFKCYGVSPTRKNDLCLFTNVY
COV0X-45 RFPNITNLCPFGVEFNATRFASVYAWNRKRISINCVADYSLVLYNSASFSTFKCYGVSPTRKNDLCLFTNVY
C118    TNSNITNLCPFGVEFNATRFASVYAWNRKRISINCVADYSLVLYNSASFSTFKCYGVSPTRKNDLCLFTNVY
C008    RFPNITNLCPFGVEFNATRFASVYAWNRKRISINCVADYSLVLYNSASFSTFKCYGVSPTRKNDLCLFTNVY
C027    RFPNITNLCPFGVEFNATRFASVYAWNRKRISINCVADYSLVLYNSASFSTFKCYGVSPTRKNDLCLFTNVY
C030    RFPNITNLCPFGVEFNATRFASVYAWNRKRISINCVADYSLVLYNSASFSTFKCYGVSPTRKNDLCLFTNVY
C113    RFPNITNLCPFGVEFNATRFASVYAWNRKRISINCVADYSLVLYNSASFSTFKCYGVSPTRKNDLCLFTNVY
C133    RFPNITNLCPFGVEFNATRFASVYAWNRKRISINCVADYSLVLYNSASFSTFKCYGVSPTRKNDLCLFTNVY
EY6A    RFPNITNLCPFGVEFNATRFASVYAWNRKRISINCVADYSLVLYNSASFSTFKCYGVSPTRKNDLCLFTNVY
C022    RFPNITNLCPFGVEFNATRFASVYAWNRKRISINCVADYSLVLYNSASFSTFKCYGVSPTRKNDLCLFTNVY
COVA1-16 RFPNITNLCPFGVEFNATRFASVYAWNRKRISINCVADYSLVLYNSASFSTFKCYGVSPTRKNDLCLFTNVY
DH1047  RFPNITNLCPFGVEFNATRFASVYAWNRKRISINCVADYSLVLYNSASFSTFKCYGVSPTRKNDLCLFTNVY
CR3022  RFPNITNLCPFGVEFNATRFASVYAWNRKRISINCVADYSLVLYNSASFSTFKCYGVSPTRKNDLCLFTNVY
S2A4    RFPNITNLCPFGVEFNATRFASVYAWNRKRISINCVADYSLVLYNSASFSTFKCYGVSPTRKNDLCLFTNVY
S304    RFPNITNLCPFGVEFNATRFASVYAWNRKRISINCVADYSLVLYNSASFSTFKCYGVSPTRKNDLCLFTNVY

400      410      420      430      440      450      460
C149    ADSFVIRGDEVQRQIAPGQTGKIADYNYKLPDDFTGCVIAWNSNLD SKVGGNYLYRFRKSNLKPFPE
C002    ADSFVIRGDEVQRQIAPGQTGKIADYNYKLPDDFTGCVIAWNSNLD SKVGGNYLYRFRKSNLKPFPE
P17     ADSFVIRGDEVQRQIAPGQTGKIADYNYKLPDDFTGCVIAWNSNLD SKVGGNYLYRFRKSNLKPFPE
COV0X-75 ADSFVIRGDEVQRQIAPGQTGKIADYNYKLPDDFTGCVIAWNSNLD SKVGGNYLYRFRKSNLKPFPE
C135    ADSFVIRGDEVQRQIAPGQTGKIADYNYKLPDDFTGCVIAWNSNLD SKVGGNYLYRFRKSNLKPFPE
REGN10987 ADSFVIRGDEVQRQIAPGQTGKIADYNYKLPDDFTGCVIAWNSNLD SKVGGNYLYRFRKSNLKPFPE
COV0X-45 ADSFVIRGDEVQRQIAPGQTGKIADYNYKLPDDFTGCVIAWNSNLD SKVGGNYLYRFRKSNLKPFPE
C118    ADSFVIRGDEVQRQIAPGQTGKIADYNYKLPDDFTGCVIAWNSNLD SKVGGNYLYRFRKSNLKPFPE
C008    ADSFVIRGDEVQRQIAPGQTGKIADYNYKLPDDFTGCVIAWNSNLD SKVGGNYLYRFRKSNLKPFPE
C027    ADSFVIRGDEVQRQIAPGQTGKIADYNYKLPDDFTGCVIAWNSNLD SKVGGNYLYRFRKSNLKPFPE
C030    ADSFVIRGDEVQRQIAPGQTGKIADYNYKLPDDFTGCVIAWNSNLD SKVGGNYLYRFRKSNLKPFPE
C113    ADSFVIRGDEVQRQIAPGQTGKIADYNYKLPDDFTGCVIAWNSNLD SKVGGNYLYRFRKSNLKPFPE
C133    ADSFVIRGDEVQRQIAPGQTGKIADYNYKLPDDFTGCVIAWNSNLD SKVGGNYLYRFRKSNLKPFPE
EY6A    ADSFVIRGDEVQRQIAPGQTGKIADYNYKLPDDFTGCVIAWNSNLD SKVGGNYLYRFRKSNLKPFPE
C022    ADSFVIRGDEVQRQIAPGQTGKIADYNYKLPDDFTGCVIAWNSNLD SKVGGNYLYRFRKSNLKPFPE
COVA1-16 ADSFVIRGDEVQRQIAPGQTGKIADYNYKLPDDFTGCVIAWNSNLD SKVGGNYLYRFRKSNLKPFPE
DH1047  ADSFVIRGDEVQRQIAPGQTGKIADYNYKLPDDFTGCVIAWNSNLD SKVGGNYLYRFRKSNLKPFPE
CR3022  ADSFVIRGDEVQRQIAPGQTGKIADYNYKLPDDFTGCVIAWNSNLD SKVGGNYLYRFRKSNLKPFPE
S2A4    ADSFVIRGDEVQRQIAPGQTGKIADYNYKLPDDFTGCVIAWNSNLD SKVGGNYLYRFRKSNLKPFPE
S304    ADSFVIRGDEVQRQIAPGQTGKIADYNYKLPDDFTGCVIAWNSNLD SKVGGNYLYRFRKSNLKPFPE

470      480      490      500      510      520      530
C149    RDISTEIQAGSTPCNGVEGPNCFYPLQSYGFQPTNGVGYQPRVTVLSPELLHAPATVCGPKKSTNL
C002    RDISTEIQAGSTPCNGVEGPNCFYPLQSYGFQPTNGVGYQPRVTVLSPELLHAPATVCGPKKSTNL
P17     RDISTEIQAGSTPCNGVEGPNCFYPLQSYGFQPTNGVGYQPRVTVLSPELLHAPATVCGPKKSTNL
COV0X-75 RDISTEIQAGSTPCNGVEGPNCFYPLQSYGFQPTNGVGYQPRVTVLSPELLHAPATVCGPKKSTNL
C135    RDISTEIQAGSTPCNGVEGPNCFYPLQSYGFQPTNGVGYQPRVTVLSPELLHAPATVCGPKKSTNL
REGN10987 RDISTEIQAGSTPCNGVEGPNCFYPLQSYGFQPTNGVGYQPRVTVLSPELLHAPATVCGPKKSTNL
COV0X-45 RDISTEIQAGSTPCNGVEGPNCFYPLQSYGFQPTNGVGYQPRVTVLSPELLHAPATVCGPKKSTNL
C118    RDISTEIQAGSTPCNGVEGPNCFYPLQSYGFQPTNGVGYQPRVTVLSPELLHAPATV
C008    RDISTEIQAGSTPCNGVEGPNCFYPLQSYGFQPTNGVGYQPRVTVLSPELLHAPATVCGPKKSTNL
C027    RDISTEIQAGSTPCNGVEGPNCFYPLQSYGFQPTNGVGYQPRVTVLSPELLHAPATVCGPKKSTNL
C030    RDISTEIQAGSTPCNGVEGPNCFYPLQSYGFQPTNGVGYQPRVTVLSPELLHAPATVCGPKKSTNL
C113    RDISTEIQAGSTPCNGVEGPNCFYPLQSYGFQPTNGVGYQPRVTVLSPELLHAPATVCGPKKSTNL
C133    RDISTEIQAGSTPCNGVEGPNCFYPLQSYGFQPTNGVGYQPRVTVLSPELLHAPATVCGPKKSTNL
EY6A    RDISTEIQAGSTPCNGVEGPNCFYPLQSYGFQPTNGVGYQPRVTVLSPELLHAPATVCGPKKSTNL
C022    RDISTEIQAGSTPCNGVEGPNCFYPLQSYGFQPTNGVGYQPRVTVLSPELLHAPATVCGPKKSTNL
COVA1-16 RDISTEIQAGSTPCNGVEGPNCFYPLQSYGFQPTNGVGYQPRVTVLSPELLHAPATVCGPKKSTNL
DH1047  RDISTEIQAGSTPCNGVEGPNCFYPLQSYGFQPTNGVGYQPRVTVLSPELLHAPATVCGPKKSTNL
CR3022  RDISTEIQAGSTPCNGVEGPNCFYPLQSYGFQPTNGVGYQPRVTVLSPELLHAPATVCGPKKSTNL
S2A4    RDISTEIQAGSTPCNGVEGPNCFYPLQSYGFQPTNGVGYQPRVTVLSPELLHAPATVCGPKKSTNL
S304    RDISTEIQAGSTPCNGVEGPNCFYPLQSYGFQPTNGVGYQPRVTVLSPELLHAPATVCGPKKSTNL

```

Class of the Ab bound to the SARS-CoV-2 RBD:	
VH3-30	class 1 strong neutralizers
VH3-30	class 2 strong neutralizers
VH3-30	class 2 weak neutralizers
VH3-30	class 3 strong neutralizers
VH3-30	class 3 weak neutralizers
VH3-30	class 4 strong neutralizers
VH3-30	class 4 weak neutralizers
Non-VH3-30	class 4 strong neutralizers
Non-VH3-30	class 4 weak neutralizers

Figure S5.5. SARS-CoV-2 RBD protein interface residues bound by Abs.

The interacting Ab is indicated on the left. RBD residues at the Fab-RBD interface interacting with the V_H are highlighted and the residues interacting with the V_L are underlined. All sequences correspond to SARS-CoV-2 RBD except the one bound by C118, which corresponds to SARS-CoV.

Table S5.1. Germline gene assignments for *VH3-30* and class 4 Abs that bind the SARS-CoV-2 RBD

	Ab (Donor ^{**})	Class	HC germline (% identity)			LC germline (% identity)		# of HC amino acid mutations from germline			# of LC amino acid mutations from germline		
			V gene	D gene	J gene	V gene	J gene	FWRH1 FWRH2 FWRH3	CDRH1 CDRH2 CDRH3	FWRL1 FWRL2 FWRL3	CDRL1 CDRL2 CDRL3		
VH3-30 class 1/4 Abs	C149 (COV47)	1/4	IGHV3-30*03 or IGHV3-30*18 or IGHV3-30-5*01 (97.9%)	IGHD6-19*01 (90.5%)	IGHJ4*02 (89.6%)	IGKV1-39*01 or IGKV1D-39*01 (98.6%)	IGKJ4*01 (100%)	0 0 2	1 0 1	0 1 0	0 0 1		
VH3-30 class 2 Abs	C002 (COV21)	2	IGHV3-30*03 or IGHV3-30*18 or VHV3-30-5*01 (99.3%)	IGHD2-15*01 (88.2%)	IGHJ4*02 (91.7%)	IGKV1-39*01 (99.6%)	IGKJ1*01 (100%)	1 0 0	1 0 1	1 0 0	0 0 0		
	P17*	2	IGHV3-30										
	COVOX75*	2	IGHV3-30										
VH3-30 class 3 Abs	C135 (COV72)	3	IGHV3-30*04 or IGHV3-30-3*01 or IGHV3-30-3*03 (97.9%)	IGHD3-22*01 (81.3%)	IGHJ4*02 (93.8%)	IGKV1-5*03 (98.9%)	IGKJ1*01 (97.4%)	0 0 1	0 3 0(1)	0 1 0	1 1 0(1)		
	REGN10987*	3	IGHV3-30*04 or IGHV3-30-3*03 (98.6%)	IGHD4-17*01 (92.3%)	IGHJ4*02 (89.4%)	IGLV2-14 (97.6%)	IGLJ3*02 (100%)	0 1 1	1 0 0(1)	0 0 2	0 0 3(4)		
	COVOX45*	3	IGHV3-30-3										
VH3-30 class 4 Abs	C008 (COV21)	4	IGHV3-30*03 or IGHV3-30*18 or IGHV3-30-5*01 (98.3%)	IGHD4-17*01 (89.2%)	IGHJ4*02 (95.8%)	IGKV1-5*03 (99.6%)	IGKJ1*01 (100%)	1 1 0	0 1 0	1 1 0	0 0 0(1)		
	C027 (COV21)	4	IGHV3-30-5*01 (99.7%)	IGHD2-15*01 (77.4%)	IGHJ4*02 (100%)	IGKV1-5*03 (100%)	IGKJ1*01 (100%)	1 0 0	0 0 1	0 0 0	0 0 0		
	C030 (COV21)	4	IGHV3-30*03 or IGHV3-30*18 or IGHV3-30-5*01 (99.7%)	IGHD2-15*01 (87.1%)	IGHJ4*02 (100%)	IGKV1-5*03 (99.6%)	IGKJ1*01 (100%)	1 0 0	0 0 1	0 0 0	0 0 0		
	C113 (COV107)	4	IGHV3-33*01 or IGHV3-33*06 (99.3%)	IGHD3-9*01 (89.6%)	IGHJ3*02 (98.0%)	IGKV1-5*03 (98.9%)	IGKJ4*01 (100%)	0 0 0	2 0 0	0 1 0	1 0 1(3)		
	C133 (COV72)	4	IGHV3-30-3*01 (99.7%)	IGHD5-19*01 (86.7%)	IGHJ5*01 or IGHJ5*02 (88.2%)	IGKV1-39*01 or IGKV1D-39*01 (100%)	IGKJ1*01 (100%)	0 0 0	0 1 0	0 0 0	0 0 0		
	C149 (COV47)	4	IGHV3-30*03 or IGHV3-30*18 or IGHV3-30-5*01 (97.9%)	IGHD6-19*01 (90.5%)	IGHJ4*02 (89.6%)	IGKV1-39*01 or IGKV1D-39*01 (98.6%)	IGKJ4*01 (100%)	0 0 2	1 0 1	0 1 0	0 0 1		
	C118 (COV107)	4	IGHV3-30-3*01 (99.0%)	IGHD5-12*01 (90.9%)	IGHJ6*02 (83.9%)	IGLV4-69*01 (99.3%)	IGLJ3*01 (97.2%)	0 0 1	1 0 0(1)	1 0 0	0 0 1		
	EY6A*	4	IGHV3-30-18 (3 SHM)			IGKV1-39 (100%)							
Non-VH3-30 class 4 Abs	C022 (COV21)	4	IGHV4-39*01 (97.9%)	IGHD3-22*01 (76.7%)	IGHJ1*01 (94.2%)	IGKV1-5*03 (99.3%)	IGKJ2*01 (97.4%)	2 0 0	1 0 0	1 0 0	0 0 1(1)		
	CR3022	4	IGHV5-51*01 or IGHV5-51*03 or IGHV5-51*04 or IGHV5-51*06 (80.2%)	IDH2-15*01 (58.8%)	JH3*01 (88.0%)	IGKV4-1*01 (76.1%)	IGKJ2*01 (86.5%)	3 0 2	3 1 0(1)	2 0 0	1 0 0		
	COVA1-16*	4	IGHV1-46 (99.0%)	IGHD3-22	IGHJ-1	IGKV1-33 (98.6%)	IGKJ4	0 0 0	0 1 ?	1 1 1	0 0 1		
	H014*	4											
	S2A4*	4	IGHV3-7			IGLV2-23							
	S304*	4	IGHV3-13			IGKV1-39							
	DH1047*	4	IGHV1-48										

*nucleotide sequence not found; information based on publication and structure or left blank.

**Donor ID listed for Abs from Robbiani et al. (2020).

Table S5.2. X-ray diffraction data and refinement statistics for Fab–RBD crystal structures

	C133 Fab–C119 Fab– SARS-CoV-2 RBD	C008 Fab– SARS-CoV-2 RBD
Data collection		
Space group	I2	P1
Cell dimensions		
<i>a, b, c</i> (Å)	155.3 135.9 215.3	91.6 104.1 107.8
α, β, γ (°)	90, 107.2, 90	96.4, 102.0, 110.9
Resolution (Å)	39.74-3.15 (3.22-3.15)	39.29-3.00 (3.07-3.00)
Total reflections	389233 (24198)	248966 (16521)
Unique reflections	70417 (7128)	64594 (6145)
Redundancy	5.5 (5.5)	3.9 (3.7)
Completeness (%)	95.1 (96.7)	88.1 (68.9)
<i>I</i> / $\sigma(I)$	6.0 (1.6)	3.5 (0.9)
Wilson B-factor (Å ²)	52.4	69.5
<i>R</i> _{merge} (%)	0.29 (1.16)	0.42 (5.81)
<i>R</i> _{meas} (%)	0.32 (1.28)	0.49 (6.82)
<i>R</i> _{pim} (%)	0.13 (0.54)	0.25 (3.55)
CC1/2	0.96 (0.36)	0.91 (0.40)
Refinement		
Resolution (Å)	38.74-3.15 (3.26 - 3.15)	38.43-3.00 (3.11 - 3.00)
No. reflections	70386 (7126)	62825 (4888)
<i>R</i> _{work} (%)	21.1 (32.2)	20.7 (40.8)
<i>R</i> _{free} (%)	25.6 (37.6)	23.7 (47.4)
No. atoms		
Peptide	24338	14626
Ligand	94	295
Water	0	0
B-factors (Å ²)		
Peptide	56.9	79.6
Ligand	106	115.8
Water	0	0
R.M.S. deviations		
Bond lengths (Å)	0.002	0.002
Bond angles (°)	0.55	0.60
Ramachandran statistics		
Ramachandran favored (%)	95.5	96.6
Ramachandran allowed (%)	4.27	3.38
Ramachandran outliers (%)	0.19	0.05
Rotamer outliers (%)	3.16	0.25
Clashscore	5.36	5.23
Number of TLS** groups	15	11

Each structure was derived from a single crystal.

*Highest resolution shell statistics shown in parentheses.

**Translation/Libration/Screw

Table S5.3. Pairwise superimpositions and rmsd calculations of C008 V_HV_L and RBD chains in the C008 Fab–RBD crystal structure

C008 V_HV_L–RBD chain Set 1	C008 V_HV_L–RBD chain Set 2	Cα atom count	rmsd (Å)
A and B (V _H V _L); G (RBD)	C and D (V _H V _L); H (RBD)	353	0.20
A and B (V _H V _L); G (RBD)	E and F (V _H V _L); U (RBD)	390	0.37
E and F (V _H V _L); U (RBD)	C and D (V _H V _L); H (RBD)	373	0.32

Table S5.4. Pairwise superimpositions and rmsd calculations of C133 VHVL and RBD chains in the C133 Fab–C119 Fab–RBD crystal structure

C133 V_HV_L–RBD chain Set 1	C133 V_HV_L–RBD chain Set 2	Cα atom count	rmsd (Å)
A and B (V _H V _L); C (RBD)	D and E (V _H V _L); F (RBD)	410	0.89
A and B (V _H V _L); C (RBD)	G and H (V _H V _L); I (RBD)	206	0.29
D and E (V _H V _L); F (RBD)	G and H (V _H V _L); I (RBD)	201	0.26

Table S5.5. BSA and interacting residues for Fab–SARS-CoV-2 structures

			Fab								RBD		
			V _H BSA				V _L BSA				Total BSA (Å ²) (# of Fab interface residues)	Surface area (Å ²) buried by V _H (# of RBD interface residues)	Surface area (Å ²) buried by V _L (# of RBD interface residues)
Ab Class	BSA Å ² (# of V _H interface residues)	FWRH1 FWRH2 FWRH3 (# interface residues)	CDRH1 CDRH2 CDRH3 (# interface residues)	CDRH1 CDRH2 CDRH3 (# interface residues)	BSA Å ² (# of V _L interface residues)	FWRL1 FWRL2 FWRL3 (# interface residues)	CDRL1 CDRL2 CDRL3 (# interface residues)	CDRL1 CDRL2 CDRL3 (# interface residues)	BSA (Å ²)	BSA (Å ²)			
											VH3-30 class 1/4 Abs	C149*** 1/4	
VH3-30 class 2 Abs	C002 PDB 7K8S	2	740 (22)	20 (1) 30 (2) 30 (1)	5/8 3/8 10/17	220 130 310	190 (6)	0 (0) 0 (0) 0 (0)	1/6 0/3 5/9	60 0 130	930 (28)	720 (23)	190 (5)
	P17 PDB 7CWO	2	660 (20)	0 (0) 30 (2) 40 (1)	4/8 6/8 7/12	110 170 310	230 (8)	0 (0) 0 (0) 20 (1)	2/6 0/3 5/9	80 0 130	890 (28)	640 (23)	230 (9)
	COVOX75 PDB 7BEO	2	450 (11)	0 (0) 0 (0) 30 (1)	0/8 0/8 10/20	0 0 420	330 (11)	0 (0) 0 (0) 30 (2)	3/6 1/3 5/9	140 20 130	780 (22)	430 (16)	350 (12)
VH3-30 class 3 Abs	C135** PDB 7K8Z	3	310 (10)	0 (0) 6 (0) 0 (0)	3/8 4/8 2/12	50 170 90	320 (8)	0 (0) 0 (0) 0 (0)	1/6 0/3 5/9	70 0 120	630 (16)	330 (11)	230 (4)
	REGN10987 PDB 6XDG	3	480 (16)	0 (0) 20 (2) 50 (1)	3/8 5/8 5/13	70 180 160	100 (5)	0 (0) 0 (0) 0 (0)	2/9 0/0 3/10	20 0 80	580 (21)	510 (14)	110 (5)
	COVOX45 PDB 7BEL	3	750 (23)	90 (2) 0 (0) 8 (1)	5/8 5/8 10/14	100 70 480	390 (14)	0 (0) 90 (3) 110 (4)	3/6 1/3 3/8	90 40 60	1140 (37)	720 (17)	370 (11)
VH3-30 class 4 Abs	C008	4	790 (18)	0 (0) 0 (0) 30 (2)	4/8 5/8 7/13	200 250 320	160 (7)	0 (0) 40 (1) 5 (1)	3/6 1/3 1/8	70 40 6	950 (25)	740 (25)	160 (7)
	C027***	4											
	C030***	4											
	C113***	4											
	C133	4	670 (21)	0 (0) 50 (2) 150 (3)	3/8 5/8 7/16	20 220 270	440 (12)	40 (2) 0 (0) 0 (0)	3/6 0/3 7/10	100 0 300	1,110 (33)	620 (22)	380 (17)
	C118*	4	750 (17)	0 (0) 0 (0) 0 (0)	5/8 3/8 9/20	350 100 440	320 (11)	0 (0) 20 (1) 130 (5)	0/7 5/7 0/9	0 160 0	1,070 (28)	640 (21)	340 (12)
	EY6A PDB 6ZCZ	4	570 (16)	0 (0) 1 (1) 150 (3)	1/8 5/7 6/14	20 150 260	470 (11)	20 (2) 0 (0) 0 (0)	4/6 0/3 5/10	140 0 300	1,040 (27)	560 (21)	370 (15)
Non-VH3-30 class 4 Abs	C022	4	790 (22)	20 (2) 0 (0)	6/10 1/7 13/21	240 1 530	210 (7)	0 (0) 50 (1) 140 (5)	0/6 1/3 0/9	0 30 140	1,000 (29)	720 (27)	210 (7)
	CR3022 PDB 6W41	4	590 (19)	4 (1) 0 (0) 3 (1)	6/8 4/8 7/12	270 110 200	430 (13)	0 (0) 50 (2) 30 (3)	7/12 1/3 7/9	290 60 310	1,020 (32)	590 (19)	400 (16)
	COVA1-16 PDB 7JMW	4	670 (20)	0 (0) 0 (0) 0 (0)	4/8 0/8 13/22	110 0 560	150 (5)	0 (0) 30 (1) 120 (4)	0/6 0/3 0/9	0 0 0	820 (25)	630 (21)	150 (5)
	H014 PDB 7CAH	4	720 (21)	0 (0) 20 (1) 150 (5)	3/8 6/8 6/13	30 200 310	310 (8)	0 (0) 0 (0) 0 (0)	2/6 1/3 5/9	10 10 290	1030 (29)	680 (25)	290 (13)
	S2A4 PDB 7JVA	4	390 (9)	0 (0) 0 (0) 30 (1)	1/8 3/8 4/12	20 30 300	460 (16)	0 (0) 1 (1) 60 (4)	5/8 2/3 4/10	250 60 90	850 (25)	380 (12)	430 (15)
	S304 PDB 7JX3	4	510 (17)	0 (0) 4 (1) 70 (1)	3/8 6/7 6/14	50 160 230	450 (13)	10 (1) 0 (0) 0 (0)	5/6 0/3 7/10	130 0 300	960 (30)	500 (19)	370 (16)
	DH1047 PDB 7LD1	4	530 (13)	0 (0) 0 (0) 100 (3)	0/8 3/8 7/24	0 80 350	260 (9)	30 (1) 0 (0) 0 (0)	4/12 0/3 4/9	140 0 90	790 (22)	490 (22)	270 (14)

*C118 RBD interacting residues and BSA are based on SARS-CoV and not SARS-CoV-2

**C135 VH interacting residues and BSA are an underestimate since there are missing RBD residues in the PDB structure

***left blank until data processing is complete

CHAPTER 6

Quantification of viral production in marine sediment near a methane seep using bio-orthogonal non-canonical amino acid tagging

Abstract

As the most abundant biological entities in the ocean, viruses significantly alter microbial populations and food webs, and therefore, carbon and nutrient cycling. With an estimated 10^{28} daily viral infections, viruses are thought to be responsible for ~50% of microbial mortality. Marine sediment, accumulated on the ocean floor, is a large carbon sink where organic carbon is buried and degraded; consequentially, assessing the impact of viruses on microbes in marine sediment is particularly important. Viral production is often assessed by a sediment dilution-based method that relies on nucleic acid staining over a time series. An alternative method for quantifying viral production utilizes biorthogonal non-canonical amino acid tagging (BONCAT) to fluorescently label viruses after lysis of translationally-active host microorganisms²⁷⁷. Here we showed preliminary results towards a comparison of the two methods, dilution-based and BONCAT, for quantifying viral production in marine sediment near a deep-sea methane seep in Monterey, California. Understanding the efficacy and limits of these methods is important for accurately quantifying viral production and obtaining deeper insight into virus-host interactions critical for nutrient cycling and biogeochemical cycles.

Introduction

The effects of viruses in marine ecosystems. At an average concentration of 10 million per milliliter of surface seawater, viruses are the smallest, yet most abundant biological entities in the ocean, outnumbering bacteria by approximately ten-fold²⁷⁸. These highly abundant entities play critical roles in bacterial mortality, microbial population dynamics, food webs, horizontal gene transfer, and biogeochemical cycling. With $\sim 10^{28}$ viral infections occurring per day, viruses are responsible for an estimated 50% of marine bacterial mortality with 20-30% of bacterial cells infected at any time^{278,279}. Lysis of infected bacteria results in the release of up to three gigatons of carbon into the ocean each year^{278,280}. Consequentially, viral lysis is a major player in altering microbial populations and rapid recycling of carbon and other nutrients in the ocean^{281,282}. Although more is known about viruses in the upper water column, understanding of viral production and infection rates, host specificity, and viral diversity in marine sediment remains limited.

Viruses in marine sediment may impact biogeochemical cycles. Marine sediment accumulated on the ocean floor is a primary source of carbon burial and degradation²⁸⁰. As the largest biome in the world, marine sediment is host to an abundance of viruses (benthic viruses) responsible for prokaryotic mortality^{280,283}. Through virus-induced bacterial lysis, viruses transform heterotrophic production into enormous amount of dissolved organic material important for sustaining resource-limited benthic ecosystems^{280,283}. The impact of viruses on bacteria and archaea in sediment near methane seeps is of particular interest. Microorganisms consume methane through anaerobic oxidation, preventing this greenhouse gas with potent warming potential from reaching the atmosphere²⁸⁴⁻²⁸⁶. Therefore, it is important to fully understand virus-host interactions that influence these microbial communities²⁸⁰. To evaluate the biogeochemical impact of virus-host interactions in sediment near methane seeps, it is essential to develop accurate methods to measure viral production rates and virus-induced mortality.

The dilution-based method quantifies viral production by nucleic acid staining. The dilution-based approach is the current conventional method for determining viral production. This approach is based on time course incubations of sediment diluted with virus-free seawater followed by recovery of virus, a second dilution, staining of viral particles using nucleic acid stain (SYBR Gold) fluorochromes, and counting virus-like particles (VLPs) with epifluorescence microscopy²⁸³. The rationale for this method is that by reducing environmental virus and host densities by dilution, the effect of new infections is minimized, thus permitting measurement of the number of viruses released from their hosts at the end of the lytic cycle. Viral loss from protozoa and other predators or possible enzymatic degradation will also be minimized²⁸³. However, this method relies on the assumption that all stained nucleic acid-containing particles are viruses, and newly produced viruses cannot be distinguished from viruses already present at the start of the incubation.

BONCAT facilitates quantification of viral production by labeling newly-translated viral proteins. Fluorescence-based biorthogonal non-canonical amino acid tagging (BONCAT) can be used to directly quantify viral production and detect newly synthesized viral proteins in environmentally-relevant virus-host model systems²⁷⁷. BONCAT works through addition of a non-canonical amino acid, specifically the methionine derivative L-homopropargylglycine (HPG) in this case, which is taken up by translationally active cells²⁸⁷. HPG is incorporated into newly synthesized proteins in bacteria and archaea, including those of new viral proteins. To visualize viral production over time, samples are passed through a 0.2- μm filter to remove cells. Then, upon addition of fluorescence-based click-reaction reagents, including an azide-containing fluorescent dye, a copper-catalyzed reaction links this azide with the alkyne in HPG (Figure 6.1). Newly-produced VLPs can be visualized with epifluorescence microscopy, and viral production can be quantified by imaging at timepoints over the course of an incubation²⁷⁷.

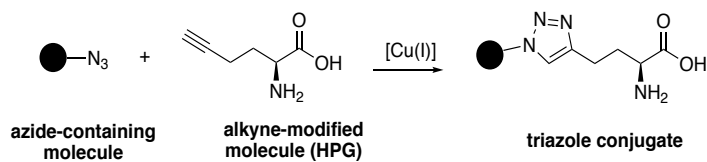


Figure 6.1. BONCAT click chemistry using the non-canonical amino acid HPG.

The key difference between the dilution-based method and BONCAT is the reliance on nucleic acid staining versus protein labeling to quantify viruses, requiring that BONCAT stained viruses are produced from metabolically active hosts that have taken up HPG. To assess differences in outcomes and the accuracy of viral quantification techniques, here we showed progress comparing the dilution-based and BONCAT approaches for quantification of viral production in environmental water and marine sediment samples. We evaluated sediment from the top 20 cm of a core extracted from a microbial mat of an active methane seep site, located at a depth of 965.8 m in the Monterey submarine canyon, to provide insight on the impact of viruses on microorganisms associated with these productive zones of greenhouse gas emission.

Results

Evaluating BONCAT and the dilution-based method of virus quantification in environmental water samples. Comparisons of BONCAT and the dilution-based method were initially practiced using a readily available environmental sample: water from the Caltech Turtle Pond. Microcosm incubations of 250 mL pond water without HPG and 250 mL with 50 μ M HPG were prepared and harvested at 0, 6, 9, and 12 hours and 1 week timepoints. At each timepoint, 1 mL of each sample was 0.2 μ m-filtered (to remove cells) for BONCAT, 1 mL of each unfiltered sample was harvested for the dilution method, and 1 mL of each unfiltered sample was fixed with 4% paraformaldehyde (PFA) for later assessment of bacterial counts.

For the dilution method, samples without HPG were prepared in a dilution series to identify the optimal dilution that would allow enumeration of between 20 and 40 VLPs per optical field²⁸³. A twofold dilution series, ranging from 15-fold to 480-fold, was used to prepare six dilutions of the sample in virus-free salt mix buffer (100 mM NaCl, 8 mM MgSO₄, 50 mM Tris-Cl pH 7.5). This was followed by DNase treatment to remove free nucleic acids and then nucleic acid staining with SYBR Gold. VLPs were visualized using a 100x oil immersion objective on an upright epifluorescence microscope (Olympus BX51). Images were collected using CellSens software (Olympus) and a QIClick Mono 12-bit CCD digital camera (QIMaging) using a FITC filter (480/40 excitation and 535/50 nm emission to monitor SYBR Gold nucleic acid staining) (Figure 6.2). Images were analyzed in Image J, and signal in images with a FITC filter were counted as VLPs. The optimal dilution for this sample was determined to be ~60-fold, yielding 20 to 40 VLPs in the optical field.

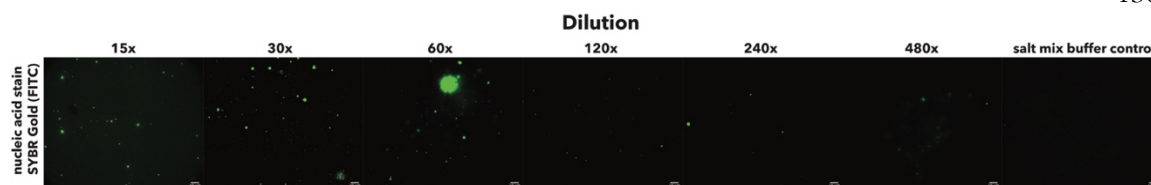


Figure 6.2. Nucleic acid-stained VLPs in an environmental water sample dilution series.

Water from the Caltech Turtle Pond was diluted and nucleic acids were stained with SYBR Gold (detected with a FITC filter; **green**). The dilution factor can be optimized to separate VLPs from cells and enable counting of individual VLPs. The scale bar is 10 μm .

To practice the BONCAT protocol with environmental samples, 1 μm alkyne-conjugated magnetic beads (positive controls) were added to filtered pond water that was previously incubated with and without HPG. Samples underwent a copper-catalyzed click reaction to label HPG-incorporated proteins (and the positive control, alkyne-conjugated magnetic beads) with diazo biotin-azide. A fluorescent streptavidin-Alexa Fluor 647 conjugate was then added to bind the biotin to facilitate visualization. This was followed by nucleic acid counter-staining with SYBR Gold (Figure 6.3). Samples were visualized with an Olympus BX51 epifluorescence microscope (100x oil objective as described above), and images were collected using CellSens software (Olympus) and a QIClick Mono 12-bit CCD digital camera (QIMaging) using a FITC filter (480/40 nm excitation and 535/50 nm emission to monitor SYBR Gold nucleic acid staining) and a Cy5 filter (620/60 nm excitation and 700/75 nm emission to monitor BONCAT-labeling). Images were analyzed in Image J, and overlapping signal in the images from FITC and Cy5 filters were counted as VLPs. The successful visualization of BONCAT-labeled VLPs and nucleic acid staining demonstrated the feasibility of proceeding with marine sediment samples.

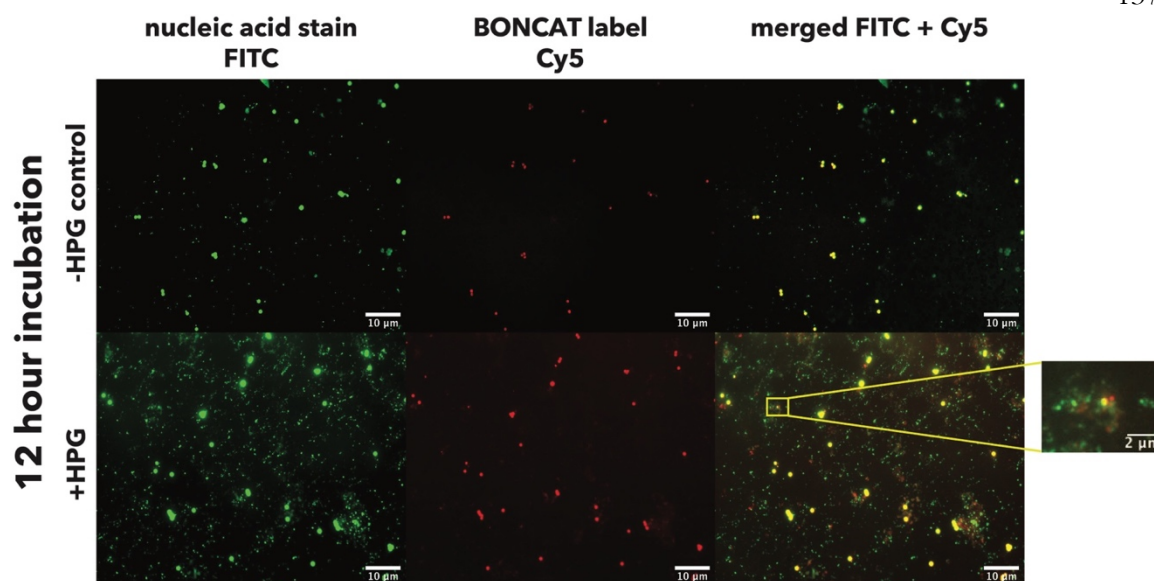


Figure 6.3. Visualization of newly-produced VLPs in BONCAT-labeled environmental water samples.

Water samples from the Caltech Turtle Pond were incubated with or without HPG before staining with SYBR Gold (detected with a FITC filter; **green**) and click-addition of a fluorophore to newly translated proteins (detected with a Cy5 filter; **red**). Here, the 12 hour timepoint is displayed. Merged images from FITC and Cy5 filters display successful BONCAT labeling (**yellow**). One μm azide-beads were added to both samples as a positive control, and are displayed **yellow** as expected. Newly produced VLPs, $\sim 50 \text{ nm}^{288}$ are also displayed **yellow**, as shown in the enlarged inset on the right.

Preparing incubations of sediment from an active methane seep. After testing BONCAT and the dilution-based methods on environmental water samples, we set up incubations of a marine sediment sample relevant for understanding the impact of viruses on microorganisms from methane seeps. Sediment below a sulfide-oxidizing microbial mat

from an active methane seep in the Monterey Submarine Canyon (36 46.5799 N 122 5.0935 W, depth of 965.8 m) was collected using a push coring device operated by a remotely operated vehicle in December, 2018 and stored near the in situ temperature (4°C) under anaerobic conditions. Using N₂-sparged 0.02 µm-filtered virus-free seawater collected from the same site, the anoxic sediment from 0-20 cm horizons was diluted by ~50% and split into 120 individual 4.5 mL anaerobic incubations (in 50 mL rubber-stoppered glass serum bottles on ice): half with 50 µM HPG added and half without HPG (three replicates per method per timepoint) (Figure 6.4). Nitrogen gas was exchanged for methane, and incubations were stored in the dark at 4°C.

Harvesting incubation timepoints. Individual incubations with and without HPG were harvested at 0, 48, 51, 54, 57, and 72 hours, and 1, 2, 3, and 4 weeks (Figure 6.4). For each timepoint, six of the incubations with HPG and six of the incubations without HPG were harvested with the aim of having sufficient samples available to test the two different virus quantification methods (BONCAT versus dilution-based) and two different methods of virus recovery from sediment (centrifugation versus tetrasodium pyrophosphate) in triplicate. Both short (hours) and long (weeks) incubation times were utilized to facilitate comparison with previous dilution-based studies²⁸³. No samples were harvested during the 1-48 hours after the start of the incubation to allow sediment to be refreshed from the previously “dormant” state during storage.

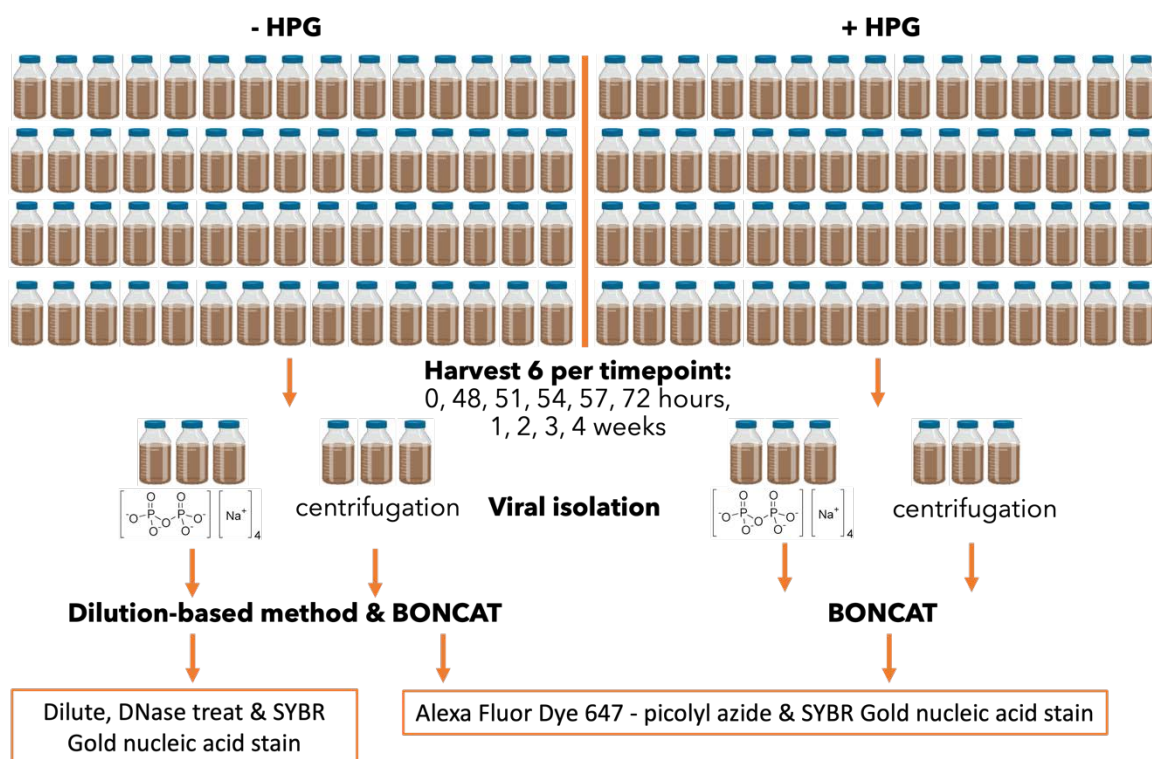


Figure 6.4. Incubation setup of sediment slurry from Monterey Submarine Canyon.

Sediment slurry was split into 120 individual 4.5 mL anaerobic incubations in serum bottles, half with 50 μ M HPG and half without HPG. Samples were harvested in triplicate at ten different timepoints (0, 48, 51, 54, 57, and 72 hours, and 1, 2, 3, and 4 weeks) with and without HPG and for two different possible methods of virus recovery (centrifugation or addition of tetrasodium pyrophosphate before centrifugation). Not all samples were ultimately processed.

Samples were harvested by pouring the 4.5 mL of sediment slurry from each serum bottle into individual 15 mL Falcon Conical Centrifuge Tubes on ice. To assist with transferring residual sediment, 2-3 mL of virus-free seawater (4°C) was added to the serum bottles (1

mL at a time) and then the bottles were shaken and the remaining sample was added to the Falcon tube. This addition of 2-3 mL of virus-free seawater was done during the transfer for all timepoints except the 0 hour timepoint, for which 2 mL of seawater was added directly to the Falcon tubes. The Falcon tubes were then vigorously shaken to evenly mix the sediment and virus-free seawater. To prepare a fixed sample cellular background, 500 μ l aliquots of each sediment slurry were removed and combined with 500 μ l 4% PFA, 1x PBS in 2 mL Eppendorf tubes and stored at 4°C overnight. The remaining sediment slurry in the Falcon tubes was frozen in liquid nitrogen and stored at -20°C. The next day, the fixed cellular background samples were centrifuged at 14,000g for 5 minutes in an Eppendorf 5425 centrifuge and PFA supernatant was removed. Residual PFA was removed by resuspending the pellets in 1 mL 1x PBS with a Vortex mixer and pipetting. Samples were again centrifuged (14,000g, 5 minutes) and PBS supernatant was removed. These wash steps, resuspension in PBS and centrifugation, were repeated a second time. The pellets were then resuspended in 1 mL of 50% EtOH, 50% 1x PBS, frozen in liquid nitrogen, and stored at -20°C.

Virus recovery from sediment using centrifugation. Three harvested sediment slurry samples with HPG and three without HPG from each of the 10 timepoint (0, 48, 51, 54, 57, and 72 hours, and 1, 2, 3, and 4 weeks) were thawed on ice for recovery of the virus from the sediment using centrifugation. The other half of the samples were left frozen at -20°C for possible use at a later date if a different method of virus recovery (addition of tetrasodium pyrophosphate before centrifugation) is needed. The 60 samples were centrifuged at 800g, 4°C for 2 minutes using a Beckman Coulter Allegra X-15R centrifuge to isolate the virus in the seawater supernatant from the sediment pellet. The volume in each Falcon tube was recorded (Table 6.1) before the supernatant was extracted with a pipet. For the supernatant samples with HPG, two 500 μ l aliquots were prepared for BONCAT: one was passed through a 0.2- μ m filter and one was unfiltered. For supernatant

samples without HPG, four 500 μ l aliquots were prepared: one filtered and one unfiltered for BONCAT (to serve as the negative controls to account for autofluorescence) and one filtered and one unfiltered for the dilution-based method.

Table 6.1. Volumes of sediment slurry samples with VLPs recovered from sediment using centrifugation

Tube ID	Timepoint	Replicate #	Volume (mL) of seawater added to sediment incubation	Sediment slurry volume (mL)	
				- HPG	+ HPG
0hr-1	0 hr.	1	2	3.75	4.75
0hr-2	0 hr.	2	2	4.25	4.25
0hr-3	0 hr.	3	2	4.00	4.50
3hr-1	3 hr.	1	2	5.75	5.50
3hr-2	3 hr.	2	2	4.75	5.25
3hr-3	3 hr.	3	2	5.50	5.50
6hr-1	6 hr.	1	2	5.25	5.75
6hr-2	6 hr.	2	2	5.75	6.00
6hr-3	6 hr.	3	2	5.50	5.50
9hr-1	9 hr.	1	2	5.25	5.50
9hr-2	9 hr.	2	2	5.25	5.50
9hr-3	9 hr.	3	2	5.25	5.50
12hr-1	12 hr.	1	2	5.50	5.50
12hr-2	12 hr.	2	2	5.25	5.25
12hr-3	12 hr.	3	2	5.25	5.50
24hr-1	24 hr.	1	2	5.50	5.50
24hr-2	24 hr.	2	2	5.25	5.00
24hr-3	24 hr.	3	2	4.50	5.25
1wk-1	1 week	1	2	5.25	5.25
1wk-2	1 week	2	2	5.00	5.25
1wk-3	1 week	3	3	6.50	6.25
2wk-1	2 weeks	1	2	5.50	5.25
2wk-2	2 weeks	2	2	5.25	5.25

2wk-3	2 weeks	3	2	4.50	5.50
3wk-1	3 weeks	1	2	5.25	5.50
3wk-2	3 weeks	2	2	5.25	5.00
3wk-3	3 weeks	3	2	5.25	5.75
4wk-1	4 weeks	1	2	5.25	5.50
4wk-2	4 weeks	2	2	5.00	5.25
4wk-3	4 weeks	3	2	5.50	5.50

Loading samples onto Anodiscs for BONCAT. One 0.2- μm filtered supernatant sample with HPG and one filtered supernatant sample without HPG from each of four timepoints (72 hours and 1, 2, and 3 weeks) as well as a salt mix buffer control were loaded onto Whatman Anodisc inorganic filter membranes (25 mm, pore size 0.02 μm) in preparation for BONCAT. The samples were prepared by diluting 20 μL into 5 mL of 0.02- μm -filtered salt mix buffer to help ensure the VLPs would be equally distributed on Anodisc surface. Anodiscs were first washed using a filter tower with an attached vacuum pump. The fritted glass support base was washed with Nanopure water before a Durapore 5 μm PVDF or PES membrane (25 mm) filter was placed on top. The filter was then wet with 1 mL of 0.02 μm -filtered water using a pipet before the Anodisc was placed face up on top of the filter. Due to prior instances of contamination, the Anodiscs were slowly washed multiple times in a drop-wise fashion with a pipet as follows: 1 mL of 0.02 μm -filtered 1x PBS, 1 mL of 50% ethanol (EtOH), 1 mL of 70% EtOH, and 1 mL of 80% EtOH. The 5 mL of sample was then slowly loaded onto the Anodisc in a circular dropwise fashion, letting the liquid pass through the filter before applying more, to help ensure the VLPs would be evenly distributed. The Anodisc was then washed with 1 mL 0.02 μm -filtered 1x PBS two times. Once dried, the Anodisc was lifted off the support base by grasping the rim with clean forceps and transferred to a petri dish for storage at 4°C until proceeding with the click reaction (no longer than one day later).

BONCAT labelling of samples on Anodiscs. BONCAT labeling was performed by a copper-catalyzed click reaction to label HPG-incorporated proteins with Alexa Fluor Dye 647 conjugated to picolyl azide (spectrally almost identical to Cy5 dye). A 250 μl click cocktail was prepared by combining 0.5 μl of 10 mM Alexa Fluor 647 picolyl-azide fluorophyl in DMSO, 2.5 μl of 0.2 μm -filtered 50 mM THPTA, and 1.25 μl of freshly prepared 20 mM copper sulfate in 0.02 μm -filtered water. The click cocktail was incubated at room temperature in the dark for 3 minutes before 12.5 μl of freshly prepared 100 mM aminoguanidine in 0.02 μm -filtered 1x PBS, 12.5 μl of freshly prepared 100 mM sodium ascorbate in 0.02 μm -filtered PBS, and 221 μl of 0.02 μm -filtered 1x PBS were added. The click cocktail was mixed by tube inversion and Vortex machine and kept in the dark. A 25 μl aliquot was placed on a petri dish, and the Anodisc (with previously loaded sample) was carefully placed face up over the click cocktail aliquot, making sure no air bubbles were present. The Anodisc was then covered with a glass square coverslip to prevent possible oxidation and stored in the dark for 30 minutes. The Anodiscs were then transferred to a new petri dish and washed three times, first with 0.02 μm -filtered 1x PBS, then 0.02 μm -filtered water, and finally 0.02 μm -filtered 50% EtOH, by filling the petri dish with enough solution to completely cover the Anodisc, keeping the dish in the dark for 3 minutes, and then carefully pouring out the solution.

Nucleic acid staining. Once BONCAT-labelled Anodiscs dried, nucleic acid staining was performed with SYBR Gold. A 25x working solution of SYBR Gold Samples was prepared in 0.02 μm -filtered water. A 25 μl aliquot was then placed in a drop on the petri dish and the Anodisc was placed face up on top. After staining for 15 minutes at room temperature in the dark, the Anodisc was transferred and washed in a new petri dish by filling the dish with 0.02 μm -filtered water, waiting three minutes, and carefully pouring out the solution. These wash steps were repeated a second time with 50% ethanol. The Anodiscs were then transferred to dry on a glass slide. A 30 μl aliquot of antifade (0.01% PPD, p-

phenylendiamine in 50% 1x PBS, 50% glycerol) was placed on the Anodisc and covered with a glass coverslip. Slides were stored at 4°C until imaging.

Imagine VLPs. VLPs on Anodiscs were visualized with an Olympus BX51 epifluorescence microscope (100x oil objective as described above), and 20-25 images per Anodisc were collected using Ocular software (QImaging) and a Retiga R6 camera (QImaging) using a FITC filter (480/40 nm excitation and 535/50 nm emission to monitor SYBR Gold nucleic acid staining) and a Cy5 filter (620/60 nm excitation and 700/75 nm emission to monitor BONCAT-labeling). Images were analyzed in Image J, and VLPs were manually counted as overlapping signal in the FITC filter and Cy5 filter (Figure 6.5, Table 6.2). The averaged counts and standard deviation of newly produced VLPs from five images at each timepoint were plotted, revealing that the number of newly-produced VLPs increases until around two weeks (Figure 6.6). By three weeks, the number decreases, likely due to the diminished availability of HPG for incorporation into new viral proteins. The standard deviation between the five images/timepoint ranged from 0.4 to 1.3 counts for samples without HPG and 4.4 to 23.4 counts for samples with HPG (Table 6.2).

Table 6.2. VLP counts determined by overlapping FITC and Cy5 signal on five images per Anodisc

Frame	72 hours		1 week		2 weeks		3 weeks	
	+HPG	- HPG	+ HPG	- HPG	+ HPG	- HPG	+ HPG	- HPG
1	3	0	35	0	51	3	59	3
2	5	0	32	1	100	0	52	0
3	2	1	58	0	105	2	50	0
4	13	0	40	0	97	2	60	1
5	4	1	50	0	108	0	53	1
Average	5.4	0.4	43.0	0.2	92.2	1.4	54.8	1.0
Standard deviation	4.4	0.5	10.8	0.4	23.4	1.3	4.4	1.2

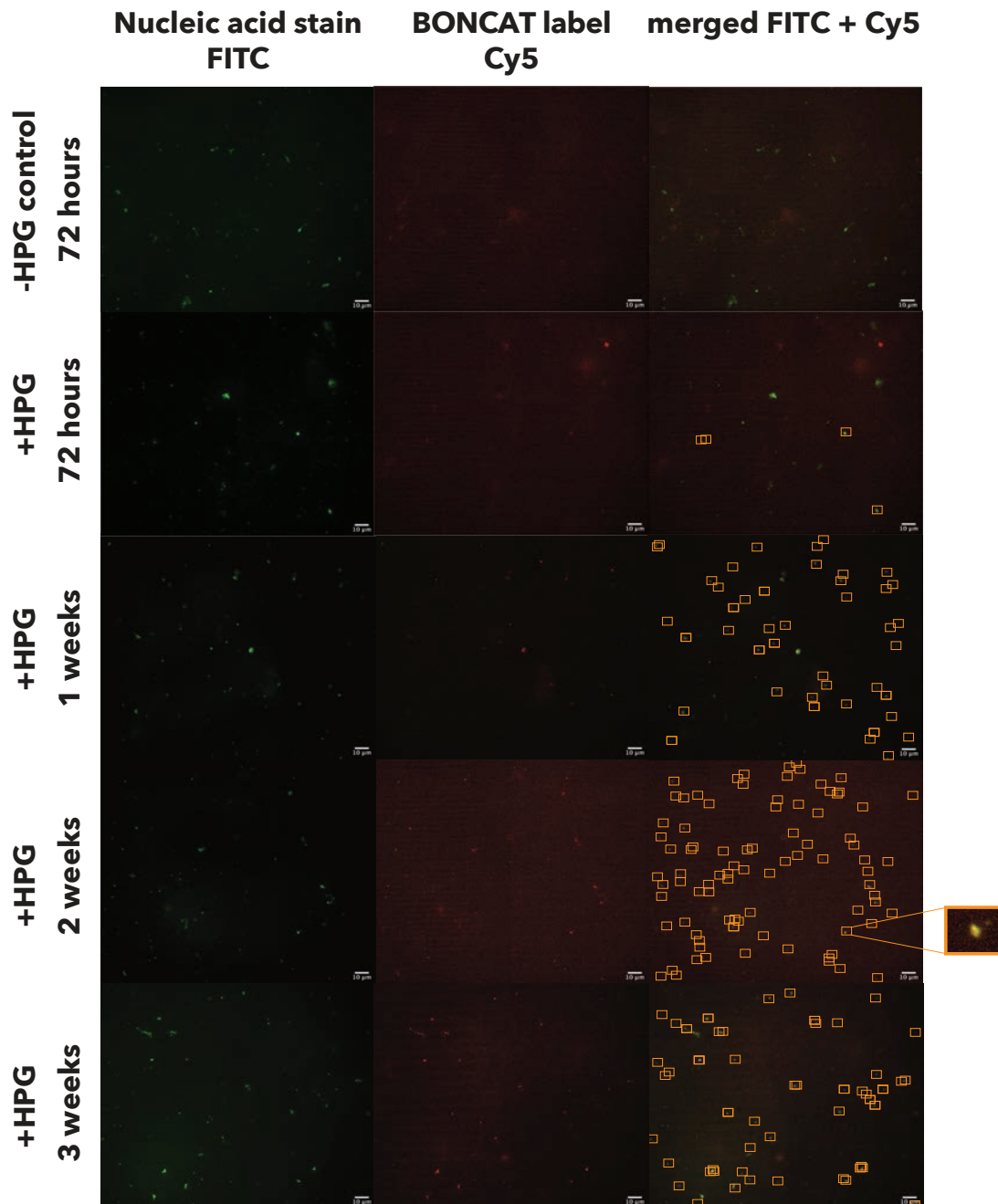


Figure 6.5. Visualization and quantification of BONCAT-labeled VLPs in marine sediment.

Sediment extracted from a methane seep was anaerobically incubated with or without HPG and harvested at successive timepoints for nucleic acid staining with SYBR Gold (detected with a FITC filter; **green**) and click-addition of a fluorophore to newly synthesized proteins (detected with a Cy5 filter; **red**). Representative merged images from FITC and Cy5 filters display successful BONCAT labeling (**yellow**). Newly produced VLPs, $\sim 50 \text{ nm}^{288}$, are indicated in orange squares. The scale bar is $10 \mu\text{m}$.

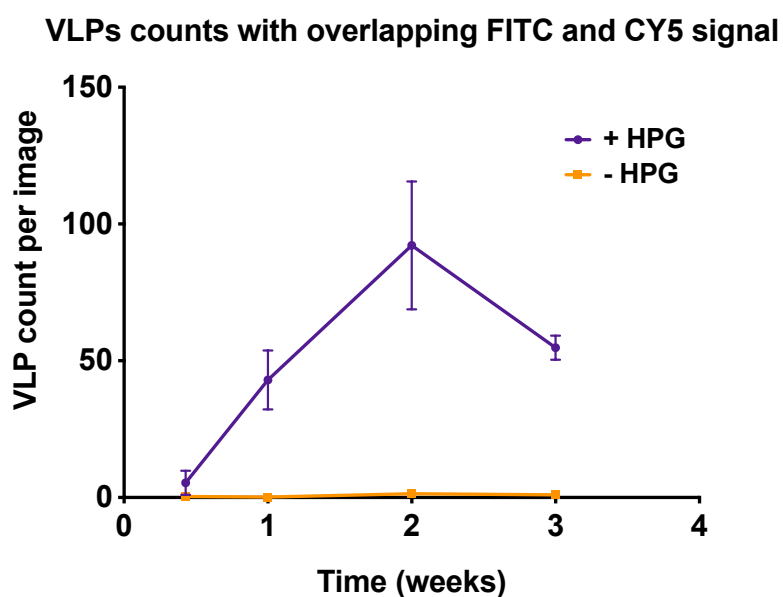


Figure 6.6. BONCAT-labeled VLP quantification in marine sediment near a methane seep.

Averaged VLP counts from five images per Anodisc with (+) and without (-) HPG plotted over time. Consistent with independent observations in the lab, VLP counts fall after two weeks for the +HPG sample as HPG supply diminishes. Note this is based on a single biological replicate.

Future directions

The preliminary experiments showed promise for successfully quantifying viral production in marine sediment for comparison of the dilution-based and BONCAT methods. However, multiple challenges were encountered during attempts to repeat these experiments with additional replicates and timepoints. One problem was contamination visualized on the Anodiscs that auto-fluoresced, particularly with the Cy5 filter. Efforts to plasma clean the Anodiscs, replace all reagents, 0.02 μm -filter solutions, and continue the extensive washing steps described for the preliminary experiments did not fully resolve this problem. Another problem was low signal to background noise when trying to identify VLPs. Even for the successful quantification described above, attempts to automate identification of VLPs failed due to low signal and necessitated manual counting. Low signal was a problem for both the FITC and Cy5 signals, but more so for Cy5. Use of an alternative dye, Cal Fluor 488, instead of Alexa Fluor 647 conjugated to picolyl-azide, did not resolve this problem. The delay in processing additional replicates, storage of unfixed samples at -20°C , and background autofluorescence may all have contributed to this low signal. The dilution-method, which only uses nucleic acid staining, also showed low signal with the FITC filter; the length of DNase treatment may have been an additional parameter contributing to the signal problem for the dilution-based method. In an attempt to address the problem of auto-fluorescent contamination on Anodiscs, in-solution BONCAT was tried. This approach BONCAT-labels and nucleic acid-stains samples in-solution by using a 100 kDa Amicon filter device and visualizing the sample directly on glass slides in the presence of an analytical standard (Sigma micro particles based on silicon dioxide). While P1 bacteriophage controls could be detected with the FITC filter, the signal was too low to detect VLPs in the sediment sample; the signal in the FITC filter using in-solution BONCAT was even lower than when using Anodiscs. Overall, the multiple wash steps, extensive time for manual counting, and

challenges with contamination and low signal limit the ability use BONCAT in a high-throughput format for VLP quantification.

Despite the challenges, the promising initial results suggest BONCAT could be a useful tool for quantifying virus production in marine sediment samples. For a thorough comparison of the dilution-based method versus BONCAT, a repeated experiment with fresh sediment incubations may benefit from the following changes to the experimental setup: 1) only include samples in duplicate for one method of virus recovering (instead of two) at only six timepoints (0 and 72 hours, and 1, 2, 3 and 4 weeks) to maintain a feasible processing timeline, 2) store samples at 4°C and perform VLP quantification analysis within 24-48 hours after harvesting, and 3) minimize the number of wash steps for loading samples on Anodiscs and dilute the VLP aliquot into a volume smaller than 5 mL, since loading samples onto Anodiscs is currently the most time consuming step in this experiment apart from manually counting VLPs. Additionally, aspects of analysis not yet explored for the Monterey Submarine Canyon sediment samples included evaluating the fixed cellular background samples, measuring the sediment wet weight to determine the total VLP count per mg of sediment, and performing additional optimization of the procedure to recover VLPs from sediment. While centrifugation was the method used to recover VLPs in these experiments, the addition of tetrasodium pyrophosphate before centrifugation could also be evaluated. Further efforts to evaluate the utility of BONCAT compared to dilution-based approaches may inform optimal methodology for quantification of viral production and facilitate evaluation of the impact of viruses on microbial communities in marine sediment. Coupling these approaches with additional studies may provide insight into how virus production correlates with virus morphology, sediment depth, and virus-host dynamics.

BIBLIOGRAPHY

1. Koonin, E. V., Senkevich, T. G. & Dolja, V. V. The ancient Virus World and evolution of cells. *Biol Direct* **1**, 29 (2006).
2. Breitbart, M. & Rohwer, F. Here a virus, there a virus, everywhere the same virus? *Trends in Microbiology* **13**, 278–284 (2005).
3. Sender, R., Fuchs, S. & Milo, R. Revised Estimates for the Number of Human and Bacteria Cells in the Body. *PLOS Biology* **14**, e1002533 (2016).
4. Mokili, J. L., Rohwer, F. & Dutilh, B. E. Metagenomics and future perspectives in virus discovery. *Current Opinion in Virology* **2**, 63–77 (2012).
5. Xu, G. J. *et al.* Comprehensive serological profiling of human populations using a synthetic human virome. *Science* **348**, aaa0698 (2015).
6. Kernbauer, E., Ding, Y. & Cadwell, K. An enteric virus can replace the beneficial function of commensal bacteria. *Nature* **516**, 94–98 (2014).
7. Barr, J. J. *et al.* Bacteriophage adhering to mucus provide a non-host-derived immunity. *Proc. Natl. Acad. Sci. U.S.A.* **110**, 10771–10776 (2013).
8. Barton, E. S., White, D. W. & Virgin, H. W. Herpesvirus Latency and Symbiotic Protection from Bacterial Infection. *Viral Immunol* **22**, 3–4 (2009).
9. Xu, P. *et al.* Virus infection improves drought tolerance. *New Phytol.* **180**, 911–921 (2008).

10. Lenman, A. *et al.* Polysialic acid is a cellular receptor for human adenovirus 52. *PNAS* **115**, E4264–E4273 (2018).
11. Hastie, E. & Grdzlishvili, V. Z. Vesicular stomatitis virus as a flexible platform for oncolytic virotherapy against cancer. *J Gen Virol* **93**, 2529–2545 (2012).
12. Andtbacka, R. H. I. *et al.* Talimogene Laherparepvec Improves Durable Response Rate in Patients With Advanced Melanoma. *JCO* **33**, 2780–2788 (2015).
13. Dolgin, E. The secret social lives of viruses. *Nature* **570**, 290–292 (2019).
14. Kuno, G., Chang, G.-J. J., Tsuchiya, K. R., Karabatsos, N. & Cropp, C. B. Phylogeny of the Genus Flavivirus. *J Virol* **72**, 73–83 (1998).
15. Heinz, F. X. & Stiasny, K. Flaviviruses and flavivirus vaccines. *Vaccine* **30**, 4301–4306 (2012).
16. Faria, N. R. *et al.* Genomic and epidemiological monitoring of yellow fever virus transmission potential. *Science* **361**, 894–899 (2018).
17. Roehrig, J. T. West Nile Virus in the United States — A Historical Perspective. *Viruses* **5**, 3088–3108 (2013).
18. Bhatt, S. *et al.* The global distribution and burden of dengue. *Nature* **496**, 504–507 (2013).
19. Pierson, T. C. & Diamond, M. S. The emergence of Zika virus and its new clinical syndromes. *Nature* **560**, 573–581 (2018).

20. Pierson, T. C. & Diamond, M. S. The continued threat of emerging flaviviruses. *Nat Microbiol* **5**, 796–812 (2020).
21. Prasad, V. M. *et al.* Structure of the immature Zika virus at 9 Å resolution. *Nat Struct Mol Biol* **24**, 184–186 (2017).
22. Sirohi, D. *et al.* The 3.8 Å resolution cryo-EM structure of Zika virus. *Science* **352**, 467–70 (2016).
23. Heinz, F. X. & Stiasny, K. The Antigenic Structure of Zika Virus and Its Relation to Other Flaviviruses: Implications for Infection and Immunoprophylaxis. *Microbiol Mol Biol Rev* **81**, (2017).
24. Laureti, M., Narayanan, D., Rodriguez-Andres, J., Fazakerley, J. K. & Kedzierski, L. Flavivirus Receptors: Diversity, Identity, and Cell Entry. *Front Immunol* **9**, 2180 (2018).
25. Stadler, K., Allison, S. L., Schlich, J. & Heinz, F. X. Proteolytic activation of tick-borne encephalitis virus by furin. *J Virol* **71**, 8475–8481 (1997).
26. Yu, I. M. *et al.* Structure of the immature dengue virus at low pH primes proteolytic maturation. *Science* **319**, 1834–7 (2008).
27. Yu, I.-M. *et al.* Association of the pr Peptides with Dengue Virus at Acidic pH Blocks Membrane Fusion. *J Virol* **83**, 12101–12107 (2009).
28. Sevvana, M. *et al.* Refinement and Analysis of the Mature Zika Virus Cryo-EM Structure at 3.1 Å Resolution. *Structure* **26**, 1169-1177.e3 (2018).

29. Kuhn, R. J., Dowd, K. A., Beth Post, C. & Pierson, T. C. Shake, rattle, and roll: Impact of the dynamics of flavivirus particles on their interactions with the host. *Virology* **479–480**, 508–17 (2015).
30. Nelson, S. *et al.* Maturation of West Nile virus modulates sensitivity to antibody-mediated neutralization. *PLoS Pathog* **4**, e1000060 (2008).
31. Dowd, K. A., DeMaso, C. R. & Pierson, T. C. Genotypic Differences in Dengue Virus Neutralization Are Explained by a Single Amino Acid Mutation That Modulates Virus Breathing. *MBio* **6**, e01559-15 (2015).
32. Fibriansah, G. *et al.* Structural Changes in Dengue Virus When Exposed to a Temperature of 37°C. *J Virol* **87**, 7585–7592 (2013).
33. Austin, S. K. *et al.* Structural basis of differential neutralization of DENV-1 genotypes by an antibody that recognizes a cryptic epitope. *PLoS Pathog* **8**, e1002930 (2012).
34. Cockburn, J. J. *et al.* Mechanism of dengue virus broad cross-neutralization by a monoclonal antibody. *Structure* **20**, 303–14 (2012).
35. Kostyuchenko, V. A. *et al.* Structure of the thermally stable Zika virus. *Nature* **533**, 425–8 (2016).
36. Robbiani, D. F. *et al.* Recurrent Potent Human Neutralizing Antibodies to Zika Virus in Brazil and Mexico. *Cell* **169**, 597-609.e11 (2017).
37. Zhao, H. *et al.* Mechanism of differential Zika and dengue virus neutralization by a public antibody lineage targeting the DIII lateral ridge. *J Exp Med* **217**, (2020).

38. Zanusso, C. *et al.* First report of autochthonous transmission of Zika virus in Brazil. *Mem. Inst. Oswaldo Cruz* **110**, 569–572 (2015).
39. Duffy, M. R. *et al.* Zika virus outbreak on Yap Island, Federated States of Micronesia. *N Engl J Med* **360**, 2536–43 (2009).
40. Cao-Lormeau, V.-M. *et al.* Zika Virus, French Polynesia, South Pacific, 2013. *Emerg Infect Dis* **20**, 1085–1086 (2014).
41. Oehler, E. *et al.* Zika virus infection complicated by Guillain-Barré syndrome – case report, French Polynesia, December 2013. *Eurosurveillance* **19**, 20720 (2014).
42. Musso, D. Zika Virus Transmission from French Polynesia to Brazil. *Emerging Infect. Dis.* **21**, 1887 (2015).
43. Dick, G. W. A. Zika virus (II). Pathogenicity and physical properties. *Trans R Soc Trop Med Hyg* **46**, 521–534 (1952).
44. Dick, G. W. A., Kitchen, S. F. & Haddock, A. J. Zika Virus (I). Isolations and serological specificity. *Trans R Soc Trop Med Hyg* **46**, 509–520 (1952).
45. Simpson, D. I. H. Zika virus infection in man. *Transactions of the Royal Society of Tropical Medicine and Hygiene* **58**, 335–338 (1964).
46. Foy, B. D. *et al.* Probable non-vector-borne transmission of Zika virus, Colorado, USA. *Emerg Infect Dis* **17**, 880–2 (2011).
47. Suy, A. *et al.* Prolonged Zika Virus Viremia during Pregnancy. *N Engl J Med* **375**, 2611–2613 (2016).

48. Barzon, L. *et al.* Infection dynamics in a traveller with persistent shedding of Zika virus RNA in semen for six months after returning from Haiti to Italy, January 2016. *Euro surveillance : bulletin Europeen sur les maladies transmissibles = European communicable disease bulletin* **21**, 30316 (2016).
49. Murray, K. O. *et al.* Prolonged Detection of Zika Virus in Vaginal Secretions and Whole Blood. *Emerg Infect Dis* **23**, 99–101 (2017).
50. Beckham, J. D., Pastula, D. M., Massey, A. & Tyler, K. L. Zika Virus as an Emerging Global Pathogen: Neurological Complications of Zika Virus. *JAMA Neurol* **73**, 875–879 (2016).
51. Brasil, P. *et al.* Guillain-Barré syndrome associated with Zika virus infection. *The Lancet* **387**, 1482 (2016).
52. Miner, J. J. & Diamond, M. S. Zika Virus Pathogenesis and Tissue Tropism. *Cell Host Microbe* **21**, 134–142 (2017).
53. Li, C. *et al.* Zika Virus Disrupts Neural Progenitor Development and Leads to Microcephaly in Mice. *Cell Stem Cell* **19**, 120–126 (2016).
54. Brasil, P. *et al.* Zika Virus Infection in Pregnant Women in Rio de Janeiro. *N Engl J Med* **375**, 2321–2334 (2016).
55. Miner, J. J. *et al.* Zika Virus Infection during Pregnancy in Mice Causes Placental Damage and Fetal Demise. *Cell* **165**, 1081–1091 (2016).

56. Coyne, C. B. & Lazear, H. M. Zika virus - reigniting the TORCH. *Nat Rev Microbiol* **14**, 707–715 (2016).
57. Pierson, T. C., Fremont, D. H., Kuhn, R. J. & Diamond, M. S. Structural insights into the mechanisms of antibody-mediated neutralization of flavivirus infection: implications for vaccine development. *Cell Host Microbe* **4**, 229–38 (2008).
58. Barba-Spaeth, G. *et al.* Structural basis of potent Zika-dengue virus antibody cross-neutralization. *Nature* **536**, 48–53 (2016).
59. Dai, L. *et al.* Structures of the Zika Virus Envelope Protein and Its Complex with a Flavivirus Broadly Protective Antibody. *Cell Host Microbe* **19**, 696–704 (2016).
60. Oliphant, T. *et al.* Development of a humanized monoclonal antibody with therapeutic potential against West Nile virus. *Nat. Med.* **11**, 522–530 (2005).
61. Wang, L. *et al.* Structural Basis for Neutralization and Protection by a Zika Virus-Specific Human Antibody. *Cell Rep* **26**, 3360-3368.e5 (2019).
62. Keeffe, J. R. *et al.* A Combination of Two Human Monoclonal Antibodies Prevents Zika Virus Escape Mutations in Non-human Primates. *Cell Rep* **25**, 1385-1394.e7 (2018).
63. Beasley, D. W. & Barrett, A. D. Identification of neutralizing epitopes within structural domain III of the West Nile virus envelope protein. *J Virol* **76**, 13097–100 (2002).

64. Crill, W. D. & Roehrig, J. T. Monoclonal antibodies that bind to domain III of dengue virus E glycoprotein are the most efficient blockers of virus adsorption to Vero cells. *J Virol* **75**, 7769–73 (2001).
65. Zhao, H. *et al.* Structural Basis of Zika Virus-Specific Antibody Protection. *Cell* **166**, 1016–27 (2016).
66. Nybakken, G. E. *et al.* Structural basis of West Nile virus neutralization by a therapeutic antibody. *Nature* **437**, 764–769 (2005).
67. Yu, L. *et al.* Delineating antibody recognition against Zika virus during natural infection. *JCI Insight* **2**, (2017).
68. Stettler, K. *et al.* Specificity, cross-reactivity, and function of antibodies elicited by Zika virus infection. *Science* **353**, 823–6 (2016).
69. Sapparapu, G. *et al.* Neutralizing human antibodies prevent Zika virus replication and fetal disease in mice. *Nature* **540**, 443–447 (2016).
70. Wahala, W. M. P. B., Kraus, A. A., Haymore, L. B., Accavitti-Loper, M. A. & de Silva, A. M. Dengue virus neutralization by human immune sera: Role of envelope protein domain III-reactive antibody. *Virology* **392**, 103–113 (2009).
71. Sukupolvi-Petty, S. *et al.* Type- and Subcomplex-Specific Neutralizing Antibodies against Domain III of Dengue Virus Type 2 Envelope Protein Recognize Adjacent Epitopes. *Journal of Virology* **81**, 12816–12826 (2007).

72. Van Rompay, K. K. A. *et al.* A combination of two human monoclonal antibodies limits fetal damage by Zika virus in macaques. *Proceedings of the National Academy of Sciences* (2020) doi:10.1073/pnas.2000414117.
73. Chang, H.-H. *et al.* Systematic analysis of protein identity between Zika virus and other arthropod-borne viruses. *Bull World Health Organ* **95**, 517-525I (2017).
74. Ye, Q. *et al.* Genomic characterization and phylogenetic analysis of Zika virus circulating in the Americas. *Infection, Genetics and Evolution* **43**, 43–49 (2016).
75. Vaughn, D. W. *et al.* Dengue viremia titer, antibody response pattern, and virus serotype correlate with disease severity. *J. Infect. Dis.* **181**, 2–9 (2000).
76. Bardina, S. V. *et al.* Enhancement of Zika virus pathogenesis by preexisting antinflavivirus immunity. *Science* **356**, 175–180 (2017).
77. Harrison, S. C. Immunogenic cross-talk between dengue and Zika viruses. *Nat Immunol* **17**, 1010–2 (2016).
78. Priyamvada, L. *et al.* Human antibody responses after dengue virus infection are highly cross-reactive to Zika virus. *Proc Natl Acad Sci U S A* **113**, 7852–7 (2016).
79. Rogers, T. F. *et al.* Zika virus activates de novo and cross-reactive memory B cell responses in dengue-experienced donors. *Sci Immunol* **2**, (2017).
80. Halstead, S. B. Neutralization and antibody-dependent enhancement of dengue viruses. *Adv Virus Res* **60**, 421–67 (2003).

81. Dejnirattisai, W. *et al.* Dengue virus sero-cross-reactivity drives antibody-dependent enhancement of infection with zika virus. *Nat Immunol* **17**, 1102–8 (2016).
82. Wahala, W. M. & Silva, A. M. The human antibody response to dengue virus infection. *Viruses* **3**, 2374–95 (2011).
83. Morens, D. M. Antibody-dependent enhancement of infection and the pathogenesis of viral disease. *Clin. Infect. Dis.* **19**, 500–512 (1994).
84. Redoni, M. *et al.* Dengue: Status of current and under-development vaccines. *Reviews in Medical Virology* **30**, e2101 (2020).
85. Sridhar, S. *et al.* Effect of Dengue Serostatus on Dengue Vaccine Safety and Efficacy. *New England Journal of Medicine* (2018) doi:10.1056/NEJMoa1800820.
86. Hadinegoro, S. R. *et al.* Efficacy and Long-Term Safety of a Dengue Vaccine in Regions of Endemic Disease. <http://dx.doi.org/10.1056/NEJMoa1506223>
<https://www.nejm.org/doi/10.1056/NEJMoa1506223> (2015)
doi:10.1056/NEJMoa1506223.
87. Shukla, R., Ramasamy, V., Shanmugam, R. K., Ahuja, R. & Khanna, N. Antibody-Dependent Enhancement: A Challenge for Developing a Safe Dengue Vaccine. *Front. Cell. Infect. Microbiol.* **10**, (2020).
88. Nisalak, A. *et al.* Forty Years of Dengue Surveillance at a Tertiary Pediatric Hospital in Bangkok, Thailand, 1973–2012. *The American Journal of Tropical Medicine and Hygiene* **94**, 1342–1347 (2016).

89. SANGKAWIBHA, N. *et al.* RISK FACTORS IN DENGUE SHOCK SYNDROME: A PROSPECTIVE EPIDEMIOLOGIC STUDY IN RAYONG, THAILAND: I. THE 1980 OUTBREAK. *American Journal of Epidemiology* **120**, 653–669 (1984).
90. Katzelnick, L. C. *et al.* Zika virus infection enhances future risk of severe dengue disease. *Science* **369**, 1123–1128 (2020).
91. Halstead, S. B. In Vivo Enhancement of Dengue Virus Infection in Rhesus Monkeys by Passively Transferred Antibody. *The Journal of Infectious Diseases* **140**, 527–533 (1979).
92. Waggoner, J. J. *et al.* Antibody-Dependent Enhancement of Severe Disease Is Mediated by Serum Viral Load in Pediatric Dengue Virus Infections. *The Journal of Infectious Diseases* **221**, 1846–1854 (2020).
93. Katzelnick, L. C. *et al.* Antibody-dependent enhancement of severe dengue disease in humans. *Science* **358**, 929–932 (2017).
94. Salje, H. *et al.* Reconstruction of antibody dynamics and infection histories to evaluate dengue risk. *Nature* **557**, 719–723 (2018).
95. Drosten, C. *et al.* Identification of a novel coronavirus in patients with severe acute respiratory syndrome. *N Engl J Med* **348**, 1967–1976 (2003).
96. Ksiazek, T. G. *et al.* A novel coronavirus associated with severe acute respiratory syndrome. *N Engl J Med* **348**, 1953–1966 (2003).

97. Zaki, A. M., van Boheemen, S., Bestebroer, T. M., Osterhaus, A. D. M. E. & Fouchier, R. A. M. Isolation of a novel coronavirus from a man with pneumonia in Saudi Arabia. *N Engl J Med* **367**, 1814–1820 (2012).
98. Huang, C. *et al.* Clinical features of patients infected with 2019 novel coronavirus in Wuhan, China. *The Lancet* **395**, 497–506 (2020).
99. Zhu, N. *et al.* A Novel Coronavirus from Patients with Pneumonia in China, 2019. *N Engl J Med* **382**, 727–733 (2020).
100. Zhou, P. *et al.* A pneumonia outbreak associated with a new coronavirus of probable bat origin. *Nature* **579**, 270–273 (2020).
101. Haagmans, B. L. *et al.* Middle East respiratory syndrome coronavirus in dromedary camels: an outbreak investigation. *The Lancet Infectious Diseases* **14**, 140–145 (2014).
102. Memish, Z. A. *et al.* Middle East Respiratory Syndrome Coronavirus in Bats, Saudi Arabia - Volume 19, Number 11—November 2013 - Emerging Infectious Diseases journal - CDC. doi:10.3201/eid1911.131172.
103. Ge, X.-Y. *et al.* Isolation and characterization of a bat SARS-like coronavirus that uses the ACE2 receptor. *Nature* **503**, 535–538 (2013).
104. Hu, B. *et al.* Discovery of a rich gene pool of bat SARS-related coronaviruses provides new insights into the origin of SARS coronavirus. *PLoS Pathog* **13**, e1006698 (2017).
105. Li, W. *et al.* Bats are natural reservoirs of SARS-like coronaviruses. *Science* **310**, 676–679 (2005).

106. Yang, X.-L. *et al.* Isolation and Characterization of a Novel Bat Coronavirus Closely Related to the Direct Progenitor of Severe Acute Respiratory Syndrome Coronavirus. *J Virol* **90**, 3253–3256 (2015).
107. Wang, N. *et al.* Serological Evidence of Bat SARS-Related Coronavirus Infection in Humans, China. *Virol Sin* **33**, 104–107 (2018).
108. Zhou, H. *et al.* Identification of novel bat coronaviruses sheds light on the evolutionary origins of SARS-CoV-2 and related viruses. *bioRxiv* 2021.03.08.434390 (2021) doi:10.1101/2021.03.08.434390.
109. Menachery, V. D. *et al.* SARS-like WIV1-CoV poised for human emergence. *PNAS* **113**, 3048–3053 (2016).
110. Menachery, V. D. *et al.* A SARS-like cluster of circulating bat coronaviruses shows potential for human emergence. *Nature Medicine* **21**, 1508–1513 (2015).
111. Tortorici, M. A. & Veisler, D. Structural insights into coronavirus entry. *Adv Virus Res* **105**, 93–116 (2019).
112. Wrapp, D. *et al.* Cryo-EM structure of the 2019-nCoV spike in the prefusion conformation. *Science* **367**, 1260–1263 (2020).
113. Walls, A. C. *et al.* Structure, Function, and Antigenicity of the SARS-CoV-2 Spike Glycoprotein. *Cell* **181**, 281-292.e6 (2020).
114. Liu, L. *et al.* Potent neutralizing antibodies against multiple epitopes on SARS-CoV-2 spike. *Nature* **584**, 450–456 (2020).

115. Zost, S. J. *et al.* Potently neutralizing and protective human antibodies against SARS-CoV-2. *Nature* **584**, 443–449 (2020).
116. Hoffmann, M. *et al.* SARS-CoV-2 Cell Entry Depends on ACE2 and TMPRSS2 and Is Blocked by a Clinically Proven Protease Inhibitor. *Cell* **181**, 271-280.e8 (2020).
117. Lan, J. *et al.* Structure of the SARS-CoV-2 spike receptor-binding domain bound to the ACE2 receptor. *Nature* **581**, 215–220 (2020).
118. Kirchdoerfer, R. N. *et al.* Pre-fusion structure of a human coronavirus spike protein. *Nature* **531**, 118–121 (2016).
119. Yuan, Y. *et al.* Cryo-EM structures of MERS-CoV and SARS-CoV spike glycoproteins reveal the dynamic receptor binding domains. *Nat Commun* **8**, 15092 (2017).
120. Li, Z. *et al.* The human coronavirus HCoV-229E S-protein structure and receptor binding. *eLife* **8**, e51230 (2019).
121. Walls, A. C. *et al.* Cryo-electron microscopy structure of a coronavirus spike glycoprotein trimer. *Nature* **531**, 114–117 (2016).
122. Zhou, D. *et al.* Structural basis for the neutralization of SARS-CoV-2 by an antibody from a convalescent patient. *Nature Structural & Molecular Biology* **27**, 950–958 (2020).
123. Roy, S., Jaiswar, A. & Sarkar, R. Dynamic Asymmetry Exposes 2019-nCoV Prefusion Spike. *J. Phys. Chem. Lett.* **11**, 7021–7027 (2020).

124. Brouwer, P. J. M. *et al.* Potent neutralizing antibodies from COVID-19 patients define multiple targets of vulnerability. *Science* **369**, 643–650 (2020).
125. Cao, Y. *et al.* Potent Neutralizing Antibodies against SARS-CoV-2 Identified by High-Throughput Single-Cell Sequencing of Convalescent Patients' B Cells. *Cell* **182**, 73-84.e16 (2020).
126. Kreer, C. *et al.* Longitudinal Isolation of Potent Near-Germline SARS-CoV-2-Neutralizing Antibodies from COVID-19 Patients. *Cell* **182**, 843-854.e12 (2020).
127. Robbiani, D. F. *et al.* Convergent antibody responses to SARS-CoV-2 in convalescent individuals. *Nature* **584**, 437–442 (2020).
128. Rogers, T. F. *et al.* Isolation of potent SARS-CoV-2 neutralizing antibodies and protection from disease in a small animal model. *Science* **369**, 956–963 (2020).
129. Seydoux, E. *et al.* Analysis of a SARS-CoV-2-Infected Individual Reveals Development of Potent Neutralizing Antibodies with Limited Somatic Mutation. *Immunity* **53**, 98-105.e5 (2020).
130. Shi, R. *et al.* A human neutralizing antibody targets the receptor-binding site of SARS-CoV-2. *Nature* **584**, 120–124 (2020).
131. Zost, S. J. *et al.* Rapid isolation and profiling of a diverse panel of human monoclonal antibodies targeting the SARS-CoV-2 spike protein. *Nat Med* **26**, 1422–1427 (2020).
132. Barnes, C. O. *et al.* SARS-CoV-2 neutralizing antibody structures inform therapeutic strategies. *Nature* **588**, 682–687 (2020).

133. Barnes, C. O. *et al.* Structures of Human Antibodies Bound to SARS-CoV-2 Spike Reveal Common Epitopes and Recurrent Features of Antibodies. *Cell* **182**, 828-842.e16 (2020).
134. Pinto, D. *et al.* Cross-neutralization of SARS-CoV-2 by a human monoclonal SARS-CoV antibody. *Nature* **583**, 290–295 (2020).
135. Dejnirattisai, W. *et al.* The antigenic anatomy of SARS-CoV-2 receptor binding domain. *Cell* **184**, 2183-2200.e22 (2021).
136. Jette, C. A. *et al.* Broad cross-reactivity across sarbecoviruses exhibited by a subset of COVID-19 donor-derived neutralizing antibodies. *bioRxiv* 2021.04.23.441195 (2021) doi:10.1101/2021.04.23.441195.
137. Piccoli, L. *et al.* Mapping Neutralizing and Immunodominant Sites on the SARS-CoV-2 Spike Receptor-Binding Domain by Structure-Guided High-Resolution Serology. *Cell* **183**, 1024-1042.e21 (2020).
138. Huang, K.-Y. A. *et al.* Breadth and function of antibody response to acute SARS-CoV-2 infection in humans. *PLOS Pathogens* **17**, e1009352 (2021).
139. Tortorici, M. A. *et al.* Ultrapotent human antibodies protect against SARS-CoV-2 challenge via multiple mechanisms. *Science* **370**, 950–957 (2020).
140. Victora, G. D. & Nussenzweig, M. C. Germinal Centers. *Annual Review of Immunology* **30**, 429–457 (2012).

141. Scharf, L. *et al.* Structural basis for HIV-1 gp120 recognition by a germ-line version of a broadly neutralizing antibody. *Proc Natl Acad Sci U S A* **110**, 6049–54 (2013).
142. Scharf, L. *et al.* Structural basis for germline antibody recognition of HIV-1 immunogens. *Elife* **5**, (2016).
143. West, A. P., Diskin, R., Nussenzweig, M. C. & Bjorkman, P. J. Structural basis for germline gene usage of a potent class of antibodies targeting the CD4 binding site of HIV-1 gp120. *Proc Natl Acad Sci U S A Plus* **109**, E2083-90 (2012).
144. Wu, X. *et al.* Focused Evolution of HIV-1 Neutralizing Antibodies Revealed by Structures and Deep Sequencing. *Science* **333**, 1593–1602 (2011).
145. Simonich, C. A. *et al.* Kappa chain maturation helps drive rapid development of an infant HIV-1 broadly neutralizing antibody lineage. *Nature Communications* **10**, 2190 (2019).
146. Ye, J., Ma, N., Madden, T. L. & Ostell, J. M. IgBLAST: an immunoglobulin variable domain sequence analysis tool. *Nucleic Acids Res* **41**, W34–W40 (2013).
147. Chen, J., Sawyer, N. & Regan, L. Protein–protein interactions: General trends in the relationship between binding affinity and interfacial buried surface area. *Protein Science* **22**, 510–515 (2013).

148. Gao, F. *et al.* Development of a potent and protective germline-like antibody lineage against Zika virus in a convalescent human. *bioRxiv* 661918 (2019) doi:10.1101/661918.
149. Foote, J. & Milstein, C. Conformational isomerism and the diversity of antibodies. *PNAS* **91**, 10370–10374 (1994).
150. Thorpe, I. F. & Brooks, C. L. Molecular evolution of affinity and flexibility in the immune system. *PNAS* **104**, 8821–8826 (2007).
151. Wedemayer, G. J., Patten, P. A., Wang, L. H., Schultz, P. G. & Stevens, R. C. Structural Insights into the Evolution of an Antibody Combining Site. *Science* **276**, 1665–1669 (1997).
152. Escolano, A., Dosenovic, P. & Nussenzweig, M. C. Progress toward active or passive HIV-1 vaccination. *The Journal of experimental medicine* **214**, 3–16 (2017).
153. Tai, W. *et al.* Critical neutralizing fragment of Zika virus EDIII elicits cross-neutralization and protection against divergent Zika viruses. *Emerg Microbes Infect* **7**, 7 (2018).
154. Yang, M., Dent, M., Lai, H., Sun, H. & Chen, Q. Immunization of Zika virus envelope protein domain III induces specific and neutralizing immune responses against Zika virus. *Vaccine* **35**, 4287–4294 (2017).

155. Yang, M., Lai, H., Sun, H. & Chen, Q. Virus-like particles that display Zika virus envelope protein domain III induce potent neutralizing immune responses in mice. *Scientific Reports* **7**, 7679 (2017).
156. Robbiani, D. F. *et al.* Risk of Zika microcephaly correlates with features of maternal antibodies. *J Exp Med* **216**, 2302–2315 (2019).
157. Klein, F. *et al.* Enhanced HIV-1 immunotherapy by commonly arising antibodies that target virus escape variants. *The Journal of experimental medicine* **211**, 2361–72 (2014).
158. Nelson, C. A., Lee, C. A. & Fremont, D. H. Oxidative Refolding from Inclusion Bodies. in *Structural Genomics and Drug Discovery: Methods and Protocols* (ed. Anderson, W. F.) 145–157 (Springer New York, 2014). doi:10.1007/978-1-4939-0354-2_11.
159. Huang, J. *et al.* Identification of a CD4-Binding-Site Antibody to HIV that Evolved Near-Pan Neutralization Breadth. *Immunity* **45**, 1108–1121 (2016).
160. Kabsch, W. XDS. *Acta Cryst D* **66**, 125–132 (2010).
161. Battye, T. G. G., Kontogiannis, L., Johnson, O., Powell, H. R. & Leslie, A. G. W. iMOSFLM: a new graphical interface for diffraction-image processing with MOSFLM. *Acta Crystallogr. D Biol. Crystallogr.* **67**, 271–281 (2011).
162. Evans, P. Scaling and assessment of data quality. *Acta Cryst D* **62**, 72–82 (2006).

163. Evans, P. R. An introduction to data reduction: space-group determination, scaling and intensity statistics. *Acta Crystallogr. D Biol. Crystallogr.* **67**, 282–292 (2011).
164. McCoy, A. J. *et al.* Phaser crystallographic software. *J Appl Cryst* **40**, 658–674 (2007).
165. Adams, P. D. *et al.* PHENIX: a comprehensive Python-based system for macromolecular structure solution. *Acta Cryst D* **66**, 213–221 (2010).
166. Schrödinger, LLC. The PyMOL Molecular Graphics System, Version 1.8. (2015).
167. Waterhouse, A. *et al.* SWISS-MODEL: homology modelling of protein structures and complexes. *Nucleic Acids Res.* **46**, W296–W303 (2018).
168. Krissinel, E. & Henrick, K. Inference of macromolecular assemblies from crystalline state. *J. Mol. Biol.* **372**, 774–797 (2007).
169. McGee, C. E. *et al.* Infection, Dissemination, and Transmission of a West Nile Virus Green Fluorescent Protein Infectious Clone by *Culex pipiens quinquefasciatus* Mosquitoes. *Vector-Borne and Zoonotic Diseases* **10**, 267–274 (2009).
170. Rompay, K. K. A. V. *et al.* A Combination of Two Human Monoclonal Antibodies Limits Fetal Damage by Zika Virus in Macaques. *bioRxiv* 2020.01.31.926899 (2020) doi:10.1101/2020.01.31.926899.
171. Guzman, M. G., Gubler, D. J., Izquierdo, A., Martinez, E. & Halstead, S. B. Dengue infection. *Nat Rev Dis Primers* **2**, 1–25 (2016).

172. Musso, D., Ko, A. I. & Baud, D. Zika Virus Infection — After the Pandemic. *New England Journal of Medicine* **381**, 1444–1457 (2019).
173. Rapid risk assessment: Zika virus epidemic in the Americas: potential association with microcephaly and Guillain-Barré syndrome - 4th update, 10 December 2015. *European Centre for Disease Prevention and Control*
<https://www.ecdc.europa.eu/en/publications-data/rapid-risk-assessment-zika-virus-epidemic-americas-potential-association> (2015).
174. Mlakar, J. *et al.* Zika Virus Associated with Microcephaly.
<https://doi.org/10.1056/NEJMoa1600651>
<https://www.nejm.org/doi/10.1056/NEJMoa1600651> (2016)
doi:10.1056/NEJMoa1600651.
175. Suthar, M. S., Diamond, M. S. & Gale Jr, M. West Nile virus infection and immunity. *Nat Rev Microbiol* **11**, 115–128 (2013).
176. Petersen, L. R., Brault, A. C. & Nasci, R. S. West Nile Virus: Review of the Literature. *JAMA* **310**, 308–315 (2013).
177. Monath, T. P. & Vasconcelos, P. F. C. Yellow fever. *J Clin Virol* **64**, 160–173 (2015).
178. da Fonseca, N. J. *et al.* Sequence, structure and function relationships in flaviviruses as assessed by evolutive aspects of its conserved non-structural protein domains. *Biochemical and Biophysical Research Communications* **492**, 565–571 (2017).

179. Dejnirattisai, W. *et al.* Cross-Reacting Antibodies Enhance Dengue Virus Infection in Humans. *Science* **328**, 745–748 (2010).
180. Alwis, R. de *et al.* Dengue Viruses Are Enhanced by Distinct Populations of Serotype Cross-Reactive Antibodies in Human Immune Sera. *PLOS Pathogens* **10**, e1004386 (2014).
181. Cattarino, L., Rodriguez-Barraquer, I., Imai, N., Cummings, D. A. T. & Ferguson, N. M. Mapping global variation in dengue transmission intensity. *Science Translational Medicine* **12**, (2020).
182. Faria, N. R. *et al.* Establishment and cryptic transmission of Zika virus in Brazil and the Americas. *Nature* **546**, 406–410 (2017).
183. Beltramello, M. *et al.* The Human Immune Response to Dengue Virus Is Dominated by Highly Cross-Reactive Antibodies Endowed with Neutralizing and Enhancing Activity. *Cell Host & Microbe* **8**, 271–283 (2010).
184. Cryptic Properties of a Cluster of Dominant Flavivirus Cross-Reactive Antigenic Sites. *Journal of Virology* <https://journals.asm.org/doi/abs/10.1128/JVI.00080-06>.
185. Rey, F. A., Stiasny, K., Vaney, M.-C., Dellarole, M. & Heinz, F. X. The bright and the dark side of human antibody responses to flaviviruses: lessons for vaccine design. *EMBO reports* **19**, 206–224 (2018).

186. Persistence of Circulating Memory B Cell Clones with Potential for Dengue Virus Disease Enhancement for Decades following Infection. *Journal of Virology* <https://journals.asm.org/doi/abs/10.1128/JVI.06335-11>.
187. Terzian, A. C. B. *et al.* Viral Load and Cytokine Response Profile Does Not Support Antibody-Dependent Enhancement in Dengue-Primed Zika Virus–Infected Patients. *Clinical Infectious Diseases* **65**, 1260–1265 (2017).
188. Santiago, G. A. *et al.* Prior Dengue Virus Infection Is Associated With Increased Viral Load in Patients Infected With Dengue but Not Zika Virus. *Open Forum Infectious Diseases* **6**, (2019).
189. Michlmayr, D. *et al.* Comprehensive Immunoprofiling of Pediatric Zika Reveals Key Role for Monocytes in the Acute Phase and No Effect of Prior Dengue Virus Infection. *Cell Reports* **31**, (2020).
190. Halai, U.-A. *et al.* Maternal Zika Virus Disease Severity, Virus Load, Prior Dengue Antibodies, and Their Relationship to Birth Outcomes. *Clinical Infectious Diseases* **65**, 877–883 (2017).
191. Rodriguez-Barraquer, I. *et al.* Impact of preexisting dengue immunity on Zika virus emergence in a dengue endemic region. *Science* **363**, 607–610 (2019).
192. Gordon, A. *et al.* Prior dengue virus infection and risk of Zika: A pediatric cohort in Nicaragua. *PLOS Medicine* **16**, e1002726 (2019).

193. Wen, J. *et al.* Dengue virus-reactive CD8 + T cells mediate cross-protection against subsequent Zika virus challenge. *Nat Commun* **8**, 1459 (2017).
194. López-Sagaseta, J., Malito, E., Rappuoli, R. & Bottomley, M. J. Self-assembling protein nanoparticles in the design of vaccines. *Computational and Structural Biotechnology Journal* **14**, 58–68 (2016).
195. Slifka, M. K. & Amanna, I. J. Role of Multivalency and Antigenic Threshold in Generating Protective Antibody Responses. *Front. Immunol.* **10**, (2019).
196. Brune, K. D. & Howarth, M. New Routes and Opportunities for Modular Construction of Particulate Vaccines: Stick, Click, and Glue. *Front. Immunol.* **9**, (2018).
197. Brune, K. D. *et al.* Plug-and-Display: decoration of Virus-Like Particles via isopeptide bonds for modular immunization. *Sci Rep* **6**, 19234 (2016).
198. Bruun, T. U. J., Andersson, A.-M. C., Draper, S. J. & Howarth, M. Engineering a Rugged Nanoscaffold To Enhance Plug-and-Display Vaccination. *ACS Nano* **12**, 8855–8866 (2018).
199. Zakeri, B. *et al.* Peptide tag forming a rapid covalent bond to a protein, through engineering a bacterial adhesin. *Proc Natl Acad Sci U S A* **109**, E690-7 (2012).
200. Tan, T. K. *et al.* A COVID-19 vaccine candidate using SpyCatcher multimerization of the SARS-CoV-2 spike protein receptor-binding domain induces potent neutralising antibody responses. *Nat Commun* **12**, 542 (2021).

201. Zhang, B. *et al.* A platform incorporating trimeric antigens into self-assembling nanoparticles reveals SARS-CoV-2-spike nanoparticles to elicit substantially higher neutralizing responses than spike alone. *Sci Rep* **10**, 18149 (2020).
202. Cohen, A. A. *et al.* Mosaic nanoparticles elicit cross-reactive immune responses to zoonotic coronaviruses in mice. *Science* **371**, 735–741 (2021).
203. Kanekiyo, M. *et al.* Mosaic nanoparticle display of diverse influenza virus hemagglutinins elicits broad B cell responses. *Nat Immunol* **20**, 362–372 (2019).
204. Rahikainen, R. *et al.* Overcoming Symmetry Mismatch in Vaccine Nanoassembly through Spontaneous Amidation. *Angew Chem Int Ed Engl* **60**, 321–330 (2021).
205. Esswein, S. R. *et al.* Structural basis for Zika envelope domain III recognition by a germline version of a recurrent neutralizing antibody. *PNAS* (2020) doi:10.1073/pnas.1919269117.
206. Slon-Campos, J. L. *et al.* A protective Zika virus E-dimer-based subunit vaccine engineered to abrogate antibody-dependent enhancement of dengue infection. *Nat Immunol* **20**, 1291–1298 (2019).
207. Ramasamy, V. *et al.* A tetravalent virus-like particle vaccine designed to display domain III of dengue envelope proteins induces multi-serotype neutralizing antibodies in mice and macaques which confer protection against antibody dependent enhancement in AG129 mice. *PLoS Negl Trop Dis* **12**, e0006191 (2018).

208. Watanabe, S. *et al.* Dengue Virus Infection with Highly Neutralizing Levels of Cross-Reactive Antibodies Causes Acute Lethal Small Intestinal Pathology without a High Level of Viremia in Mice. *J Virol* **89**, 5847–5861 (2015).
209. Zhang, N., Li, C., Jiang, S. & Du, L. Recent Advances in the Development of Virus-Like Particle-Based Flavivirus Vaccines. *Vaccines (Basel)* **8**, (2020).
210. Shanmugam, R. K. *et al.* Pichia pastoris-expressed Zika virus envelope domain III on a virus-like particle platform: design, production and immunological evaluation. *Pathogens and Disease* **77**, (2019).
211. Cimica, V. *et al.* Zika Virus-Like Particle (VLP) vaccine displaying Envelope (E) protein CD loop antigen elicits protective and specific immune response in a murine model. *Biochemical and Biophysical Research Communications* **529**, 805–811 (2020).
212. Fluckiger, A.-C. *et al.* ENVELOPED VIRUS-LIKE PARTICLES (eVLPs) EXPRESSING MODIFIED FORMS OF ZIKA VIRUS PROTEINS E AND NS1 PROTECT MICE FROM ZIKA VIRUS INFECTION. *bioRxiv* 666966 (2019) doi:10.1101/666966.
213. Espinosa, D. *et al.* Passive Transfer of Immune Sera Induced by a Zika Virus-Like Particle Vaccine Protects AG129 Mice Against Lethal Zika Virus Challenge. *EBioMedicine* **27**, 61–70 (2018).
214. Cabral-Miranda, G. *et al.* Correction: Zika Virus-Derived E-DIII Protein Displayed on Immunologically Optimized VLPs Induces Neutralizing Antibodies without

- Causing Enhancement of Dengue Virus Infection. *Vaccines* 2019, 7, 72. *Vaccines* **8**, 94 (2020).
215. Cielens, I. *et al.* Mosaic RNA Phage VLPs Carrying Domain III of the West Nile Virus E Protein. *Mol Biotechnol* **56**, 459–469 (2014).
216. Chua, A. J. *et al.* A novel platform for virus-like particle-display of flaviviral envelope domain III: induction of Dengue and West Nile virus neutralizing antibodies. *Virology Journal* **10**, 129 (2013).
217. Ohtaki, N. *et al.* Immunogenicity and efficacy of two types of West Nile virus-like particles different in size and maturation as a second-generation vaccine candidate. *Vaccine* **28**, 6588–6596 (2010).
218. Qiao, M. *et al.* Induction of Sterilizing Immunity against West Nile Virus (WNV), by Immunization with WNV-Like Particles Produced in Insect Cells. *The Journal of Infectious Diseases* **190**, 2104–2108 (2004).
219. Shukla, R. *et al.* Pichia pastoris-Expressed Bivalent Virus-Like Particulate Vaccine Induces Domain III-Focused Bivalent Neutralizing Antibodies without Antibody-Dependent Enhancement in Vivo. *Front. Microbiol.* **8**, (2018).
220. Rajpoot, R. K., Shukla, R., Arora, U., Swaminathan, S. & Khanna, N. Dengue envelope-based ‘four-in-one’ virus-like particles produced using Pichia pastoris induce enhancement-lacking, domain III-directed tetravalent neutralising antibodies in mice. *Sci Rep* **8**, 8643 (2018).

221. Khetarpal, N. *et al.* Recombinant Dengue Virus 4 Envelope Glycoprotein Virus-Like Particles Derived from *Pichia pastoris* are Capable of Eliciting Homotypic Domain III-Directed Neutralizing Antibodies. *The American Journal of Tropical Medicine and Hygiene* **96**, 126–134 (2017).
222. Mani, S. *et al.* *Pichia pastoris*-Expressed Dengue 2 Envelope Forms Virus-Like Particles without Pre-Membrane Protein and Induces High Titer Neutralizing Antibodies. *PLOS ONE* **8**, e64595 (2013).
223. Crill, W. D., Hughes, H. R., Delorey, M. J. & Chang, G.-J. J. Humoral immune responses of dengue fever patients using epitope-specific serotype-2 virus-like particle antigens. *PLoS One* **4**, e4991 (2009).
224. Poddar, A. *et al.* Virus-like particles derived from *Pichia pastoris*-expressed dengue virus type 1 glycoprotein elicit homotypic virus-neutralizing envelope domain III-directed antibodies. *BMC Biotechnology* **16**, 50 (2016).
225. Arora, U., Tyagi, P., Swaminathan, S. & Khanna, N. Virus-like particles displaying envelope domain III of dengue virus type 2 induce virus-specific antibody response in mice. *Vaccine* **31**, 873–878 (2013).
226. Arora, U., Tyagi, P., Swaminathan, S. & Khanna, N. Chimeric Hepatitis B core antigen virus-like particles displaying the envelope domain III of dengue virus type 2. *Journal of Nanobiotechnology* **10**, 30 (2012).

227. Tripathi, L. *et al.* *Pichia pastoris*-expressed dengue 3 envelope-based virus-like particles elicit predominantly domain III-focused high titer neutralizing antibodies. *Front. Microbiol.* **6**, (2015).
228. Keeble, A. H. *et al.* Approaching infinite affinity through engineering of peptide–protein interaction. *PNAS* **116**, 26523–26533 (2019).
229. Diamond, M. S., Ledgerwood, J. E. & Pierson, T. C. Zika Virus Vaccine Development: Progress in the Face of New Challenges. *Annu. Rev. Med.* **70**, 121–135 (2019).
230. de Silva, A. M. & Harris, E. Which Dengue Vaccine Approach Is the Most Promising, and Should We Be Concerned about Enhanced Disease after Vaccination? The Path to a Dengue Vaccine: Learning from Human Natural Dengue Infection Studies and Vaccine Trials. *Cold Spring Harb Perspect Biol* **10**, (2018).
231. Screaton, G., Mongkolsapaya, J., Yacoub, S. & Roberts, C. New insights into the immunopathology and control of dengue virus infection. *Nat Rev Immunol* **15**, 745–59 (2015).
232. McCracken, M. K. *et al.* Impact of prior flavivirus immunity on Zika virus infection in rhesus macaques. *PLoS Pathog* **13**, (2017).
233. De Góes Cavalcanti, L. P. *et al.* Zika virus infection, associated microcephaly, and low yellow fever vaccination coverage in Brazil: is there any causal link? *J Infect Dev Ctries* **10**, 563–566 (2016).

234. Schultz, E. M., Jones, T. J. & Barr, K. L. Post-Vaccination Yellow Fever Antibodies Enhance Zika Virus Infection in Embryoid Bodies. (2020) doi:10.20944/preprints202007.0105.v1.
235. Thompson, J. D., Higgins, D. G. & Gibson, T. J. CLUSTAL W: improving the sensitivity of progressive multiple sequence alignment through sequence weighting, position-specific gap penalties and weight matrix choice. *Nucleic Acids Research* **22**, 4673–4680 (1994).
236. Cohen, A. A. *et al.* Construction, characterization, and immunization of nanoparticles that display a diverse array of influenza HA trimers. *PLOS ONE* **16**, e0247963 (2021).
237. Zhang, X. *et al.* Structure of acidic pH dengue virus showing the fusogenic glycoprotein trimers. *J. Virol.* **89**, 743–750 (2015).
238. Wang, Q. *et al.* Molecular determinants of human neutralizing antibodies isolated from a patient infected with Zika virus. *Sci Transl Med* **8**, 369ra179 (2016).
239. Hasan, S. S. *et al.* A human antibody against Zika virus crosslinks the E protein to prevent infection. *Nat Commun* **8**, 14722 (2017).
240. Zhang, S. *et al.* Neutralization mechanism of a highly potent antibody against Zika virus. *Nat Commun* **7**, 13679 (2016).
241. Wang, J. *et al.* A Human Bi-specific Antibody against Zika Virus with High Therapeutic Potential. *Cell* **171**, 229-241.e15 (2017).

242. Tian, X. *et al.* Potent binding of 2019 novel coronavirus spike protein by a SARS coronavirus-specific human monoclonal antibody. *Emerging Microbes & Infections* **9**, 382–385 (2020).
243. Jaimes, J. A., André, N. M., Chappie, J. S., Millet, J. K. & Whittaker, G. R. Phylogenetic Analysis and Structural Modeling of SARS-CoV-2 Spike Protein Reveals an Evolutionary Distinct and Proteolytically Sensitive Activation Loop. *Journal of Molecular Biology* **432**, 3309–3325 (2020).
244. Huo, J. *et al.* Neutralization of SARS-CoV-2 by Destruction of the Prefusion Spike. *Cell Host & Microbe* **28**, 445-454.e6 (2020).
245. Yuan, M. *et al.* A highly conserved cryptic epitope in the receptor binding domains of SARS-CoV-2 and SARS-CoV. *Science* **368**, 630–633 (2020).
246. Meulen, J. ter *et al.* Human Monoclonal Antibody Combination against SARS Coronavirus: Synergy and Coverage of Escape Mutants. *PLOS Medicine* **3**, e237 (2006).
247. Wu, N. C. *et al.* A natural mutation between SARS-CoV-2 and SARS-CoV determines neutralization by a cross-reactive antibody. *PLOS Pathogens* **16**, e1009089 (2020).
248. Liu, H. *et al.* Cross-Neutralization of a SARS-CoV-2 Antibody to a Functionally Conserved Site Is Mediated by Avidity. *Immunity* **53**, 1272-1280.e5 (2020).

249. Lv, Z. *et al.* Structural basis for neutralization of SARS-CoV-2 and SARS-CoV by a potent therapeutic antibody. *Science* **369**, 1505–1509 (2020).
250. Martinez, D. R. *et al.* A broadly neutralizing antibody protects against SARS-CoV, pre-emergent bat CoVs, and SARS-CoV-2 variants in mice. *bioRxiv* 2021.04.27.441655 (2021) doi:10.1101/2021.04.27.441655.
251. Li, D. *et al.* The functions of SARS-CoV-2 neutralizing and infection-enhancing antibodies in vitro and in mice and nonhuman primates. *bioRxiv* (2021) doi:10.1101/2020.12.31.424729.
252. Rappazzo, C. G. *et al.* Broad and potent activity against SARS-like viruses by an engineered human monoclonal antibody. *Science* **371**, 823–829 (2021).
253. Wec, A. Z. *et al.* Broad neutralization of SARS-related viruses by human monoclonal antibodies. *Science* **369**, 731–736 (2020).
254. Yuan, M. *et al.* Structural basis of a shared antibody response to SARS-CoV-2. *Science* **369**, 1119–1123 (2020).
255. Hansen, J. *et al.* Studies in humanized mice and convalescent humans yield a SARS-CoV-2 antibody cocktail. *Science* **369**, 1010–1014 (2020).
256. Yao, H. *et al.* Rational development of a human antibody cocktail that deploys multiple functions to confer Pan-SARS-CoVs protection. *Cell Res* **31**, 25–36 (2021).
257. Yuan, M. *et al.* Structural and functional ramifications of antigenic drift in recent SARS-CoV-2 variants. *Science* (2021) doi:10.1126/science.abh1139.

258. Baum, A. *et al.* Antibody cocktail to SARS-CoV-2 spike protein prevents rapid mutational escape seen with individual antibodies. *Science* **369**, 1014–1018 (2020).
259. Crawford, K. H. D. *et al.* Protocol and Reagents for Pseudotyping Lentiviral Particles with SARS-CoV-2 Spike Protein for Neutralization Assays. *Viruses* **12**, 513 (2020).
260. Hsieh, C.-L. *et al.* Structure-based design of prefusion-stabilized SARS-CoV-2 spikes. *Science* **369**, 1501–1505 (2020).
261. Scheid, J. F. *et al.* B cell genomics behind cross-neutralization of SARS-CoV-2 variants and SARS-CoV. *Cell* **184**, 3205-3221.e24 (2021).
262. Letko, M., Marzi, A. & Munster, V. Functional assessment of cell entry and receptor usage for SARS-CoV-2 and other lineage B betacoronaviruses. *Nat Microbiol* **5**, 562–569 (2020).
263. Andersen, K. G., Rambaut, A., Lipkin, W. I., Holmes, E. C. & Garry, R. F. The proximal origin of SARS-CoV-2. *Nat Med* **26**, 450–452 (2020).
264. Ju, B. *et al.* Human neutralizing antibodies elicited by SARS-CoV-2 infection. *Nature* **584**, 115–119 (2020).
265. Song, G. *et al.* Cross-reactive serum and memory B cell responses to spike protein in SARS-CoV-2 and endemic coronavirus infection. *bioRxiv* 2020.09.22.308965 (2020) doi:10.1101/2020.09.22.308965.

266. Liu, H. *et al.* A combination of cross-neutralizing antibodies synergizes to prevent SARS-CoV-2 and SARS-CoV pseudovirus infection. *Cell Host & Microbe* **29**, 806-818.e6 (2021).
267. Edgar, R. C. MUSCLE: multiple sequence alignment with high accuracy and high throughput. *Nucleic Acids Res* **32**, 1792–1797 (2004).
268. Dunbar, J. & Deane, C. M. ANARCI: antigen receptor numbering and receptor classification. *Bioinformatics* **32**, 298–300 (2016).
269. Scharf, L. *et al.* Antibody 8ANC195 reveals a site of broad vulnerability on the HIV-1 envelope spike. *Cell reports* **7**, 785–95 (2014).
270. Emsley, P., Lohkamp, B., Scott, W. G. & Cowtan, K. Features and development of Coot. *Acta Crystallogr D Biol Crystallogr* **66**, 486–501 (2010).
271. Pettersen, E. F. *et al.* UCSF Chimera—A visualization system for exploratory research and analysis. *Journal of Computational Chemistry* **25**, 1605–1612 (2004).
272. Walls, A. C. *et al.* Unexpected Receptor Functional Mimicry Elucidates Activation of Coronavirus Fusion. *Cell* **176**, 1026-1039.e15 (2019).
273. Landau, M. *et al.* ConSurf 2005: the projection of evolutionary conservation scores of residues on protein structures. *Nucleic Acids Research* **33**, W299–W302 (2005).
274. Wu, Y. *et al.* A noncompeting pair of human neutralizing antibodies block COVID-19 virus binding to its receptor ACE2. *Science* **368**, 1274–1278 (2020).

275. Mastrorarde, D. N. Automated electron microscope tomography using robust prediction of specimen movements. *J Struct Biol* **152**, 36–51 (2005).
276. Punjani, A., Rubinstein, J. L., Fleet, D. J. & Brubaker, M. A. cryoSPARC: algorithms for rapid unsupervised cryo-EM structure determination. *Nat Methods* **14**, 290–296 (2017).
277. Pasulka, A. L. *et al.* Interrogating marine virus-host interactions and elemental transfer with BONCAT and nanoSIMS-based methods. *Environ Microbiol* **20**, 671–692 (2018).
278. Breitbart, M., Bonnain, C., Malki, K. & Sawaya, N. A. Phage puppet masters of the marine microbial realm. *Nat Microbiol* **3**, 754–766 (2018).
279. Suttle, C. A. Marine viruses--major players in the global ecosystem. *Nat Rev Microbiol* **5**, 801–12 (2007).
280. Danovaro, R. *et al.* Major viral impact on the functioning of benthic deep-sea ecosystems. *Nature* **454**, 1084–7 (2008).
281. Wilhelm, S. W. & Suttle, C. A. Viruses and Nutrient Cycles in the Sea: Viruses play critical roles in the structure and function of aquatic food webs. *BioScience* **49**, 781–788 (1999).
282. Fuhrman, J. A. Marine viruses and their biogeochemical and ecological effects. *Nature* **399**, 541–8 (1999).

283. Dell'Anno, A., Corinaldesi, C., Magagnini, M. & Danovaro, R. Determination of viral production in aquatic sediments using the dilution-based approach. *Nat Protoc* **4**, 1013–22 (2009).
284. Levin, L. A. *et al.* Hydrothermal Vents and Methane Seeps: Rethinking the Sphere of Influence. *Front. Mar. Sci.* **3**, (2016).
285. Levin, L. A. Ecology of Cold Seep Sediments: Interactions of Fauna with Flow, Chemistry and Microbes. in (2005). doi:10.1201/9781420037449-3.
286. McGlynn, S. E., Chadwick, G. L., Kempes, C. P. & Orphan, V. J. Single cell activity reveals direct electron transfer in methanotrophic consortia. *Nature* **526**, 531–535 (2015).
287. Dieterich, D. C. *et al.* Labeling, detection and identification of newly synthesized proteomes with bioorthogonal non-canonical amino-acid tagging. *Nat Protoc* **2**, 532–40 (2007).
288. Brum, J. R., Schenck, R. O. & Sullivan, M. B. Global morphological analysis of marine viruses shows minimal regional variation and dominance of non-tailed viruses. *ISME J* **7**, 1738–51 (2013).